Searches for dark matter and single top-quarks with the ATLAS experiment

Dissertation

zur Erlangung des akademischen Grades
Doctor Rerum Naturalium (Dr. rer. nat.)

im Fach Physik

eingereicht an der
Mathematisch-Naturwissenschaftlichen Fakultät der
Humboldt-Universität zu Berlin

von

M.Sc. Ben Brüers

Präsidentin der Humboldt-Universität zu Berlin
Prof. Dr. Julia von Blumenthal

Dekanin der Mathematisch-Naturwissenschaftlichen Fakultät
Prof. Dr. Caren Tischendorf

Gutachter/innen:

1. Dr. Priscilla Pani
2. Prof. Dr. Johannes Albrecht
3. Prof. Dr. Thomas Lohse

Tag der mündlichen Prüfung: 03.03.2023

Abstract

Dark matter (DM) remains one of the unrevealed mysteries of the universe. Even though it constitutes $\sim 85\%$ of the matter, considerably little is known about DM, despite its significant influence on the dynamics of galaxies and the expansion of the universe. The search for DM at colliders marks an important pillar in exploring all possible realisations of DM. A search for DM particles with the ATLAS experiment at the LHC is presented in this thesis. The full run-II dataset of $\sqrt{s} = 13\,\text{TeV}$ proton-proton collisions with an integrated luminosity of $139\,\text{fb}^{-1}$ collected from 2015 to 2018 is used. A model with an extended Higgs-sector is probed in the search. In this 2HDM+a model, a second Higgs doublet, a pseudo-scalar DM mediator and a fermionic DM particle are added to the Standard Model of particle physics (SM). DM particles produced in association with a top-quark and a W-boson are searched for. The top-quark decays into a W-boson and a b-quark. This gives a total of two W-bosons in signal events. Both of these can decay into quarks or leptons. Depending on the decays of the W-bosons, the final state of this search is characterised by zero, one or two charged leptons. Three analysis channels are defined according to the charged lepton multiplicity and referred to as 0L, 1L and 2L channel. The search presented in this thesis focusses on the 1L channel. In addition, all final states are statistically combined to provide the most stringent exclusion limits in terms of 2HDM+a model based DM models. The 1L channel exploits that one of the W-bosons can, if decaying hadronically and having a relatively high-p_{T}, be reconstructed in a large-radius jet and be identified using a procedure called W-tagging. This significantly increases the signal-to-background ratio. Selected events must have high missing transverse momentum due to the elusive nature of DM particles and at least one b-tagged small-radius jet. Consistency between the SM prediction and the data is observed and exclusion limits at 95 % CL on the normalisation of BSM signals are derived. The analysis of the full run-II dataset and the statistical combination of all final states constrain large areas of the parameter space. Masses m_a up to 400 GeV as well as masses $m_{H^\pm}$ below 300 GeV and beyond 2000 GeV and values of $\tan\beta$ up to 2.2 are excluded. Interesting opportunities to further explore challenging corners of the parameter space arise, e.g. extending the sensitivity at high values of $\tan\beta$.

Kurzfassung

Dunkle Materie (DM) ist eines der ungelösten Geheimnisse des Universums. Obwohl sie etwa 85% der Materie ausmacht und einen signifikanten Einflusses auf die Dynamik von Galaxien und auf die Expansion des Universums hat, ist vergleichsweise wenig über die DM bekannt. Die Suche nach DM mit Kolliderexperimenten stellt einen wichtigen Bestandteil dar, um alle möglichen Realisierungen der DM zu überprüfen. Diese Arbeit handelt von einer Suche nach DM-Teilchen mit dem ATLAS-Experiment am LHC. Es wird der komplette Run-II Datensatz von $\sqrt{s} = 13\,\text{TeV}$ Proton-Proton-Kollisionen mit einer integrierten Luminsität von $139\,\text{fb}^{-1}$, aufgezeichnet zwischen 2015 und 2018, dafür verwendet. In der Suche wird eine Theorie überprüft, in der das Standardmodell der Teilchenphysik um ein weiteres Higgs-Doublet, einen pseudoskalaren DM-Mediator und ein fermionisches DM-Teilchen erweitert wird (2HDM+a Modell). Es wird nach DM-Teilchen, die gemeinsam mit einem Top-Quark und einem W-Boson produziert werden, gesucht. Das Top-Quark zerfällt in ein W-Boson und ein b-Quark. Das ergibt insgesamt zwei W-Bosonen in Signalereignissen. Diese zerfallen jeweils entweder in zwei Quarks oder zwei Leptonen. Abhängig von den Zerfällen der W-Bosonen sind im Endzustand kein, ein oder zwei geladene Leptonen zu finden. Die drei Analysekanäle 0L, 1L und 2L werden dementsprechend definiert. Die Suche, die in dieser Arbeit vorgestellt wird, konzentriert sich auf den 1L-Kanal. Zudem werden die entwickelten Signalregionen dieses Kanals in der Arbeit mit Signalregionen des 0L- und 2L-Kanals statistisch kombiniert. Dies erlaubt es die derzeit stringentesten Ausschlussgrenzen auf 2HDM+a Modell basierte DM Modelle zu setzen. Der 1L-Kanal nutzt aus, dass das W-Boson, sofern es hadronisch zerfällt und einen relativ großen Transversalimpuls hat, in einem large-radius Jet rekonstruiert werden kann. Dieser large-radius Jet kann mittels einer Methode, die W-Tagging heißt, identifiziert werden. Dies erhöht das Verhältnis von Signal zu Untergrund erheblich. In dem 1L Kanal werden nur Kollisionsereignisse mit einem großen fehlenden Transversalimpuls aufgrund der DM-Teilchen sowie mit mindestens einem identifizierten b-Jet ausgewählt. Die Daten stimmen gut mit der Standardmodellvorhersage überein und 95 % Konfidenzintervall Ausschlussgrenzen werden auf die Normalisierung von BSM Signalen gesetzt. Die Analyse der kompletten Run-II Daten und die statistische Kombination aller Endzustände erlaubt es den möglichen Parameterraum des Modells stark einzuschränken. Massen des $H^{\pm}$-Bosons unter 300 GeV und über 2000 GeV sowie Massen des a-Bosons bis zu 400 GeV und Werte von $\tan\beta$ bis 2.2 können ausgeschlossen werden. Weiterhin ist es möglich besonders herausfordernde Bereiche des Parameterraumes genauer zu untersuchen. So wird zum Beispiel die Sensitivität bei hohen $\tan\beta$ erheblich erweitert.

Selbstständigkeitserklärung

Hiermit erkläre ich, die Dissertation selbstständig und nur unter Verwendung der angegebenen Hilfen und Hilfsmittel angefertigt zu haben. Ich habe mich nicht anderwärts um einen Doktorgrad in dem Promotionsfach beworben und besitze keinen entsprechenden Doktorgrad. Die Promotionsordnung der Mathematisch-Naturwissenschaftlichen Fakultät, veröffentlicht im Amtlichen Mitteilungsblatt der Humboldt-Universität zu Berlin Nr. 42 am 11. Juli 2018, habe ich zur Kenntnis genommen.

I declare that I have completed the thesis independently using only the aids and tools specified. I have not applied for a doctor's degree in the doctoral subject elsewhere and do not hold a corresponding doctor's degree. I have taken due note of the Faculty of Mathematics and Natural Sciences PhD Regulations, published in the Official Gazette of Humboldt-Universität zu Berlin no. 42 on July 11 2018.

Berlin, 24th April 2023

Ben Brüers

Contents

List of abbreviations

2HDM two Higgs doublet model

2HDM+a model two Higgs doublet plus pseudo-scalar mediator model

ALICE A Large Ion Collider Experiment; one of the experiments at the Large Hadron Collider (LHC)

ALP axion-like particle

ATLAS A Large Toroidal Aparatus; one of the experiments at the LHC

BBN Big Bang nucleosynthesis

BSM beyond the Standard Model

CERN European Council for Nuclear Research

CL confidence level

CMB cosmic microwave background

CMS Compact Muon Solonoid; one of the experiments at the LHC

CR control region

CSC cathode strip chamber; a device of the muon system of the A Large Toroidal Aparatus (ATLAS) detector

DD direct detection

DGLAP Dokshitzer-Gribov-Lipatov-Altarelli-Parisi

DM dark matter

ECAL electromagnetic calorimeter

EFT effective field theory

FCal forward calorimeter

FCNC flavour-changing neutral current

FSR final state radiation

HCAL hadronic calorimeter

HEC hadronic end-cap calorimeter

HLT high-level trigger

IBL Insertable B-Layer; the inner most part of the inner detector (ID)

ID inner detector; the inner most part of the ATLAS detector

IDD indirect detection

ISR initial state radiation

JER jet energy resolution

JES jet energy scale

JMR jet mass resolution

JMS jet mass scale

JVT jet vertex tagger

fJVT forward jet vertex tagger

L1 trigger Level-I trigger

ΛCDM standard model of cosmology

LCW local hadronic cell weighting

LEP Large Electron-Positron Collider

LHC Large Hadron Collider

LHCb Large Hadron Collider beauty; one of the experiments at the LHC

LL leading logarithm

LO leading order

MACHO massive compact halo object

MC Monte Carlo

MDT monitored drift tube; a device of the muon system of the ATLAS detector

MOND modified Newtonian dynamics

NLL next-to-leading logarithm

NLO next-to-leading order

NNLL next-to-next-to-leading logarithm

NNLO next-to-next-to-leading order

NWA narrow-width approximation

OS opposite sign

PBH primordial black hole

PDF parton distribution function

QCD quantum chromodynamics

QFT quantum field theory

RGS random grid search

ROI region-of-interest

RPC resistive plate chamber; a device of the muon system of the ATLAS detector

SCT semiconductor tracker; the part of the ID made of Silicon strip detectors

SF same flavour

SM Standard Model of particle physics

SR signal region

TGC thin gap chamber; a device of the muon system of the ATLAS detector

TRT transition radiation tracker; the outer most part of the ID and its only gaseous detector component

UFO Universal FeynRules Output; a file format used as input to an event generators. It contains all the Feynman rules relevant to a theoretical model.

VEV vacuum expectation value

VR validation region

WIMP weakly interacting massive particle

Chapter 1

Introduction

Dark matter (DM) - there are probably only few who can resist asking themselves "What is that supposed to be?" Scientific research about DM centers much around this question, though the understanding of DM, which constitutes roughly 27 % of the energy in the universe [1], has progressed significantly in the past decades [2]. Zwicky, who famously used the term in his 1933 publication [3], concluded from the observation that the velocity dispersion in galaxy clusters is much higher than expected from the luminosity, that additional, non-luminous matter must exist, which prevents the galaxies from escaping the cluster [4]. He speculated that this additional matter were faint stars and other non-luminous astrophysical objects [5]. Today it has become clear that DM is probably not constituted of such objects [6, 7]. Rather, measurements of the cosmic microwave background (CMB) in the context of the well-tested standard model of cosmology (ΛCDM) suggest that DM is made of non-baryonic matter [1]. A typical assumption is that this non-baryonic matter is made of weakly interacting massive particles (WIMPs), i.e. of particles that are massive and have masses and interactions strengths comparable to those of weak force mediators.

The Standard Model of particle physics (SM) [8–11] is a theory describing the smallest known parts of matter: the fundamental particles and their interactions. The dynamics of these particles can be described very successfully with the SM. Yet, there is good reason to believe that the SM is incomplete. At present, the SM does not provide a candidate to explain the non-baryonic DM for example. Instead, an extension of the SM appears to be necessary to describe DM.

Multiple models predicting hypothetical DM particles and extending the SM have been developed [12]. Due to the many unknowns concerning the nature of DM particles, these models often aim at making as few assumptions as possible about DM. So-called simplified models assume that DM particles are WIMPs that couple to SM particles via an additional mediator particle [13]. Theoretical inconsistencies of these simplified models at high energies have motivated the introduction of more elaborate models [13]. One of these models is the two Higgs doublet plus pseudo-scalar mediator model (2HDM+a model) [14]. In the 2HDM+a model, the SM Higgs-boson sector is extended by a second Higgs doublet, which leads to the introduction of four additional spin-0 particles, the scalar H, the pseudoscalar A and the two charged bosons $H^{\pm}$. A pseudoscalar mediator particle a, which mixes with the A-boson is further added. The a- and the A-boson interact with a fermionic DM particle candidate in the model and allow for the production of DM particles from SM particles. The 2HDM+a model offers a rich phenomenology that can be probed at particle colliders.

The 2HDM+a model gives rise to three signatures that feature DM particles in the final state and the resonant production of one of the additional Higgs bosons:

the mono-Higgs, the mono-Z and the tW+DM signatures [14, 15]. These three signatures have the largest cross-sections in the 2HDM+a model with respect to the associated production of SM and DM particles. Using them allows probing the model over a wide range of its parameter space. While the mono-Higgs and mono-Z signatures have already been extensively studied in multiple publications [16–20], the tW+DM signature was uncovered until recently [21, 22]. A search for DM in the tW+DM signature with the ATLAS experiment is presented in this thesis. The work of this thesis has been published in References [21, 22] and special focus is on the search published in Reference [22]. It is based on the full 139 fb^{-1} run-II dataset of proton-proton collisions at a centre-of-mass energy of 13 TeV recorded between 2015 and 2018 with the ATLAS detector [23] at the LHC [24]. The LHC is located close to European Council for Nuclear Research (CERN) in the vicinity of Geneva.

The tW+DM signature is characterised by the associated production of a top-quark, a W-boson and DM particles. The W-boson and the DM particles stem for example from the decay of an $H^{\pm}$-boson. As the DM particles are assumed to be weakly interacting, they escape the detector without depositing energy and without producing a directly detectable signal. Since the proton beams collide head-on, the momenta in the plane transverse to the direction of the beams of all produced particles must sum to zero. Due to the elusive nature of DM particles, the sum of the momenta in the transverse plane of all reconstructed particles will not equal zero in events with DM particles. Instead large missing transverse momentum ($\vec{p}_{\text{T}}^{\,\text{miss}}$, magnitude $E_{\text{T}}^{\text{miss}}$) is expected in signal events. Since the top-quark most likely decays into a W-boson and a b-quark [25], two W-bosons emerge in the tW+DM signature. Either of these W-bosons can decay into a pair of quarks, or into a charged lepton and a neutrino. Zero, one or two charged leptons are therefore expected in the final state. Three channels, referred to as 0L, 1L and 2L channel, are defined according to the number of reconstructed charged leptons in the final state. All three channels are used to search for DM particles in this thesis. Special focus is on the 1L channel. In this channel at least one W-boson decays into quarks. Depending on the masses of the $H^{\pm}$-boson and the mediator a, the W-boson emerging from the decay of the resonantly produced $H^{\pm}$-boson can have a relatively high momentum for example. If that is the case and the W-boson decays into quarks, dedicated techniques using so-called large-radius jets and W-tagging can be used to reconstruct and identify such W-bosons. The usage of these techniques significantly enhances the presence of signal over the background.

Signal enhanced phase space regions are presented for the 1L channel in this thesis. They are constructed to be statistically independent from the 0L channel region which is also introduced. The two channels are statistically combined to increase the sensitivity towards beyond the Standard Model (BSM) physics. The 2L channel signal enhanced region introduced in Reference [21], is statistically independent from the 1L and 0L channel regions. Therefore, all three channels are statistically combined, reaching the strongest sensitivity to date towards the 2HDM+a model in the tW+DM signature.

This thesis is structured as follows. The SM is introduced in Chapter 2. The evidence for DM, possible DM candidates and the principles of DM searches are discussed in Chapter 3. The 2HDM+a model, its parameters and the different signatures to search for DM particles in the context of the 2HDM+a model are introduced in Chapter 4. Special attention is given to the tW+DM signature. Chapter 5 is devoted to the description of the LHC and the ATLAS detector, which are used to collect the data analysed in this thesis. The data is complemented by simulated proton-proton collision events, which are used to define the signal enriched regions, estimate the background and to derive systematic uncertainties. The event simulation is the topic of Chapter 6. Chapter 7 discusses how particles or more generally "objects" are reconstructed from the electric signals produced by particles

traversing the detector. The search for DM particles in the tW+DM signature is presented in Chapters 8 to 12. The signal characteristics, the dominant background contributions, the analysis strategy and the statistical analysis are discussed in Chapter 8. Signal enriched phase space regions for the 1L and 0L channels are presented in Chapter 9. The estimation of the background is the topic of Chapter 10. Results obtained from the combination of the 1L and 0L channels are shown in Chapter 11. The 2L channel analysis regions as well as the statistical combination of 0L, 1L and 2L channel signal enriched regions are discussed in Chapter 12. Exclusion limits on the 2HDM+a model parameters from the combination are also shown in this chapter. Finally, Chapter 13 summarises the findings of this thesis and gives an outlook.

Contribution of the author

The author was one of the main analysers of the search presented in this thesis. He was responsible for the 1L channel and developed the signal regions (SRs), the control regions (CRs) and the validation regions (VRs) unless indicated otherwise.

The statistical analysis implemented in the `HistFitter` framework [26] was setup in close collaboration between the main analysers. The author contributed to deriving the distributions of multiple variables in the SRs, CRs and VRs using the results of the background-only fit. Furthermore, the author was a lead developer of the software to produce and visualise the 2HDM+a model model exclusion limits. The author performed the statistical combination of the 0L, 1L and 2L channels and developed a software tool employing the `pyHF` software [27, 28] to construct the combined likelihood.

Concerning uncertainties, the author was responsible for deriving background modelling uncertainties for the $t\bar{t}$, single top quark and $t\bar{t} + Z$ processes from simulated samples. The author furthermore took care of evaluating experimental uncertainties from numerous sources and tested and validated that they were being accounted for correctly.

Chapter 2

The Standard Model of particle physics

In the Standard Model of particle physics (SM) [8–11] all observable matter is constituted of a set of fundamental particles [29]. These particles are subject to four fundamental interactions, of which three are included in the SM. Developed in the 1960' and 1970', the SM has shown to precisely describe the outcome of numerous experiments at energies spread over multiple orders of magnitude. Several particles predicted by the SM were only much later discovered, demonstrating the success of the SM. This chapter begins with an overview of the fundamental particles and the theoretical foundation of the SM. Then, specific aspects, namely the Higgs mechanism [30–34], the strong interaction, cross-section calculations at hadron colliders and shortcomings of the SM are discussed.

2.1 The fundamental particles

The fundamental particles of the SM [8–11] are made up of the half-integer spin fermions and the bosons which have an integer spin.

The bosons of spin-1 are the mediating particles of the three fundamental interactions in the SM: the electromagnetic, the weak and the strong interaction [35]. The mediating particle of the electromagnetic interaction is the photon (γ), which is massless and only couples to particles with a non-zero electrical charge q, while not carrying any charge. The massive Z, W^+- and W^--bosons are the force carriers of the weak interaction. The W^+- and W^- bosons only couple to particles with a non-zero weak isospin, while the Z-boson only couples to particles with a non-zero combination of the weak isospin and the hypercharge Y. Interactions among the mediators of the weak interaction are possible. Finally, the mediators of the strong interaction, the massless gluons, couple only to colour-charged particles and carry colour-charge themselves. Due to the colour-charge of the gluons, a gluon can interact with other gluons.

One boson of spin-0 is contained in the SM, the Higgs-boson [30–34]. It gives the particles their masses (see Section 2.3) and couples to all massive particles, though it is not clear whether this also applies to neutrinos [35].

Quarks and leptons constitute the fermions [35]. Both quarks and leptons come in three generations of two particles, with higher generation particles having a higher mass. That gives a total of six quarks (u, d), (c, s), (t, b) and six leptons (e, ν_e), (μ, ν_μ), (τ, ν_τ), with pairs of two indicating the particles of one generation. For each fermion an anti-particle of the same mass, but opposite quantum numbers

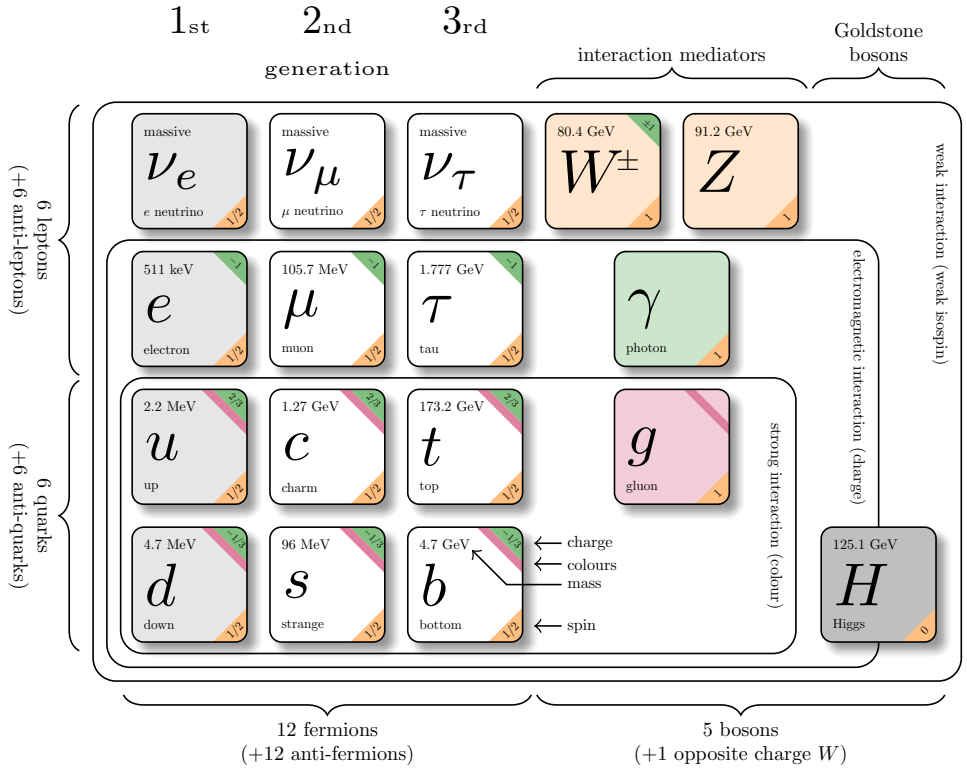

Figure 2.1: Particle content of the SM. Adapted from Reference [37].

(charge, colour charge, weak isospin, etc.) exists in the SM, though neutrinos may be their own anti-particles.

The electromagnetic and weak interaction are the only interactions leptons participate in [35]. While the neutrinos ν_e, ν_μ and ν_τ have no electric charge and cannot interact electromagnetically, the electron e, the muon μ and the τ-lepton have an electric charge of $q = -1e$. Neutrinos were originally assumed to be massless in the SM, even though neutrino oscillations have shown that they must be massive [36].

Quarks can interact electromagnetically, weakly and strongly [35]. Their electrical charge is either $^2/_3e$ (u, c, t) or $-^1/_3e$ (d, s, b). All particles contained in the SM are summarised in Figure 2.1.

2.2 Theoretical foundation

The SM is based on a Lagrangian $\mathcal{L}_{\text{SM}}$, composed of the Lagrangian $\mathcal{L}_{\text{QCD}}$ of the strong interaction and of the Lagrangian $\mathcal{L}_{\text{EW}}$ of the electroweak theory [8–11, 35, 38]. The electroweak theory is the combination of the theories of the electromagnetic and the weak interaction. The Lagrangian $\mathcal{L}_{\text{SM}}$ is invariant under local gauge transformations with the symmetry group

$$\underbrace{SU(3)_C}_{\text{QCD}} \times \underbrace{SU(2)_L \times U(1)_Y}_{\text{electroweak}} .$$

Along with the invariance of the Lagrangian under this symmetry group come several gauge fields, of which the mediating bosons of the SM interactions are made up.

The Lagrangian $\mathcal{L}_{\mathrm{QCD}}$ of the strong interaction, where the subscript QCD stands for quantum chromodynamics, the quantum field theory (QFT) of the strong interaction, is locally gauge invariant under the $SU(3)_C$ symmetry group [35]. The C on $SU(3)_C$ stands for the colour charge, which must be non-zero for particles interacting with the eight gauge fields of QCD. The gauge fields represent the gluons. As a consequence of the non-commutative nature of the $SU(3)_C$, making QCD a so-called non-abelian gauge theory, gluons can interact among each other.

The Lagrangian $\mathcal{L}_{\mathrm{EW}}$ of the electroweak theory is invariant under local gauge transformations with the symmetry group $SU(2)_L \times U(1)_Y$ [35]. The gauge fields of the $SU(2)_L$ and the $U(1)_Y$ are denoted by W_μ^a $(a = 1 \ldots 3)$ and B_μ. They only couple to particles which have a non-zero weak isospin component T_a or weak hypercharge $Y = 2(q - T_3)$, respectively. The observable bosons of the electromagnetic and the weak interaction, the γ, Z- and $W^\pm$-bosons, are linear combinations of the fields W_μ^a and B_μ, as is discussed in Section 2.3. As the $SU(2)_L$ is a non-abelian group interactions among the electroweak bosons are possible.

The subscript L on the $SU(2)_L$ indicates that only left-handed chiral[1] fermion states couple to the gauge fields W_μ^a [35]. It is implemented by dividing all fermions into left-handed chiral (subscript L) states which form $SU(2)_L$ doublets and chirality right handed (subscript R) states, which form $SU(2)_L$ singlets:

$$\underset{e_R}{\begin{pmatrix}\nu_e\\ e\end{pmatrix}_L} \quad \underset{\mu_R}{\begin{pmatrix}\nu_\mu\\ \mu\end{pmatrix}_L} \quad \underset{\tau_R}{\begin{pmatrix}\nu_\tau\\ \tau\end{pmatrix}_L} \qquad \underset{u_R, d_R}{\begin{pmatrix}u\\ d'\end{pmatrix}_L} \quad \underset{c_R, s_R}{\begin{pmatrix}c\\ s'\end{pmatrix}_L} \quad \underset{t_R, b_R}{\begin{pmatrix}t\\ b'\end{pmatrix}_L}$$

Right-handed neutrinos have not been included here as they cannot participate in any SM interaction (all quantum numbers are zero) and their existence is not clear. One consequence of the gauge fields W_μ^a only coupling to left-handed chiral fermion states is the experimentally observed parity violation in the weak interaction [39, 40]. The so-called weak quark eigenstates d', s' and b' appearing in the isospin doublets are linear combinations of the mass eigenstates d, s and b with the coefficients being given by the Cabibbo-Kobayashi-Maskawa (CKM) matrix [41, 42]. These weak eigenstates reflect that W-bosons can couple to quarks of different generations (as long as their charge difference is one), though an interaction of same generation quarks is most likely.

2.3 The Higgs mechanism

The mediating particles of the weak interaction are massive [35]. The introduction of mass terms for the bosons is not ad-hoc possible in the SM, as such terms violate the local gauge invariance. The Higgs mechanism solves this problem, by introducing an additional field that spontaneously breaks the gauge symmetry. It goes back to the 1964 works of Brout and Englert [33], Higgs [32] and Guralnik, Kibble and Hagen [34], building on ideas of Goldstone [31] and Nambu [30].

The Higgs mechanism introduces a scalar isospin-doublet field ϕ with complex components [43]

$$\phi(x) = \frac{1}{\sqrt{2}} \begin{pmatrix} \phi_1(x) + i\phi_2(x) \\ \phi_3(x) + i\phi_4(x) \end{pmatrix}$$

and real-valued fields $\phi_1, \phi_2, \phi_3, \phi_4$. The dynamics of ϕ is determined by following

[1] Using the projection operators $\frac{1}{2}(1 \mp \gamma_5)$, every fermion field can be separated into left-handed chiral $(-)$ and right-handed $(+)$ states, with γ_5 being the fifth Dirac matrix.

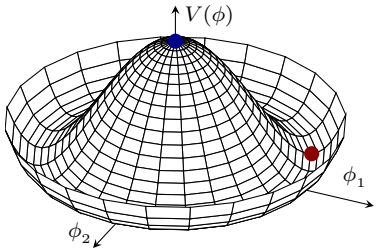

Figure 2.2: The Higgs potential $V(\phi)$ has a maximum at $\phi = 0$ (blue dot) and degenerate minima at $\phi^\dagger\phi = -\mu^2/2\lambda$ (e.g. red dot). Modified from Reference [44].

Lagrangian

$$\mathcal{L}_H = \underbrace{(D_\mu\phi)^\dagger(D^\mu\phi)}_{\text{kinetic}} - \underbrace{(\mu^2\phi^\dagger\phi + \lambda(\phi^\dagger\phi)^2)}_{=:V(\phi),\ \text{potential}}, \tag{2.1}$$

$$D_\mu = \partial_\mu - ig_W\hat{T}_a \cdot W_\mu^a - i\frac{g'\hat{Y}}{2}B_\mu, \tag{2.2}$$

with the complex, mass-dimension parameter μ, the quartic coupling λ and the coupling constants g_W and g' of the fields W_μ^a and B_μ. $\hat{Y}$ is the weak hypercharge operator.

The kinetic energy of ϕ and its couplings to the gauge fields of the electroweak theory are given by the term in Equation (2.1) involving the covariant derivative (Equation (2.2)) [35]. The second and third term in Equation (2.1) form the Higgs potential $V(\phi)$, which determines the vacuum expectation value (VEV) of ϕ. The potential is illustrated in two dimensions in Figure 2.2 for $\mu^2 < 0$ and $\lambda > 0$. At $\phi = 0$ the potential has a local maximum and is minimal at the circle of radius $\phi^\dagger\phi = -\mu^2/2\lambda$. In four dimensions, the minima are distributed across a three-dimensional hypersphere.

In the vacuum state, ϕ takes one of the infinite number of non-zero minima [35]. This is called spontaneous symmetry breaking. Expanding ϕ around the vacuum state, which is chosen to be $\begin{pmatrix}0 & v/\sqrt{2}\end{pmatrix}^t$ and using the so-called unitary gauge (see e.g. Reference [35] for a pedagogical explanation) the field ϕ can be rewritten at every point x as:

$$\phi(x) = \frac{1}{\sqrt{2}}\begin{pmatrix}0\\ v + h(x)\end{pmatrix}.$$

The excitations of the Higgs field ϕ are described by the function $h(x)$. It can be identified with the Higgs-boson field. Furthermore, v satisfies $v^2 = -\mu^2/\lambda$.

With this gauging, the covariant derivative term of the Higgs Lagrangian (Eq. (2.1)) can be simplified and mass terms for the electroweak bosons arise [35]. The $W^\pm$-boson fields are defined as $W_\mu^\pm = \frac{1}{\sqrt{2}}(W_\mu^{(1)} \mp iW_\mu^{(2)})$. Their masses are given by $m_W = \frac{v}{2}g_W$. The photon field A_μ and the Z-boson field Z_μ^0 are obtained from linear combinations of $W_\mu^{(3)}$ and B_μ:

$$\begin{pmatrix}A_\mu\\ Z_\mu\end{pmatrix} = \frac{1}{\sqrt{g_W^2 + g'^2}}\begin{pmatrix}g_W & g'\\ -g' & g_W\end{pmatrix}\begin{pmatrix}B_\mu\\ W_\mu^{(3)}\end{pmatrix} = \begin{pmatrix}\cos(\theta_W) & \sin(\theta_W)\\ -\sin(\theta_W) & \cos(\theta_W)\end{pmatrix}\begin{pmatrix}B_\mu\\ W_\mu^{(3)}\end{pmatrix},$$

with the Weinberg angle θ_W being defined as $\tan\theta_W \coloneqq \frac{g'}{g_W}$. While the mass of the Z-boson is given by $m_Z = \frac{v}{2}\sqrt{g_W^2 + g'^2}$, the photon is massless. Adding the

Higgs field ϕ with four degrees of freedom allows introducing mass terms for the mediating bosons of the weak interaction, while preserving local gauge invariance.

Furthermore, the Higgs-boson field emerges. The mass of the Higgs-boson is encoded in the Higgs potential, which in the unitary gauge reads (ignoring constant terms) [35]:

$$V(\phi) = \underbrace{\lambda v^2 h(x)^2}_{\text{Higgs mass}} + \underbrace{\lambda v h(x)^3}_{\text{trinlinear}} + \underbrace{\frac{\lambda}{4} h(x)^4}_{\text{quartic}}.$$

The first term determines the mass $m_h = \sqrt{2\lambda}v$ of the Higgs-boson. The second and third term are trilinear and quartic Higgs self-couplings, respectively. A particle compatible with the Higgs-boson was discovered in 2012 by the ATLAS and Compact Muon Solonoid (CMS) experiments [45, 46], supporting the validity of the Higgs mechanism.

Similarly to the weak bosons, mass terms for the fermions also break the local gauge invariance, if they are added naively to the SM [9, 35]. Fortunately, fermion masses can be introduced in a straight forward way by utilising the Higgs field. For the lepton doublet $L = \begin{pmatrix}\nu & \ell\end{pmatrix}_L^t$ and the quark doublet $Q = \begin{pmatrix}u & d\end{pmatrix}_L^t$ of each generation, the Higgs Lagrangian $\mathcal{L}_H$ is extended by following term:

$$\mathcal{L}_g = -y_\ell(\bar{L}\phi\ell_R + h.c.) - y_u(\bar{Q}\tilde{\phi}u_R + h.c.) - y_d(\bar{Q}\phi d_R + h.c.). \tag{2.3}$$

In this equation, y_ℓ, y_u and y_d are the so-called Yukawa couplings of ℓ, u and d, hermitian conjugate is abbreviated by $h.c.$ and $\tilde{\phi} \coloneqq -i\sigma_2\phi^*$ with σ_2 the second Pauli matrix. After spontaneous symmetry breaking and using the unitary gauge, $\mathcal{L}_g$ becomes

$$\mathcal{L}_g = \sum_{f=\{\ell,u,d\}} \underbrace{-m_f\bar{f}f}_{\text{mass}} - \underbrace{\frac{m_f}{v}\bar{f}fh}_{\text{Higgs coupling}}, \tag{2.4}$$

with m_f the fermion masses, related to the Yukawa couplings by $y_f = \frac{\sqrt{2}m_f}{v}$. The first term in the sum of Equation (2.4) is the mass term for each fermion and the second term is the coupling of the fermions to the Higgs field.

2.4 The strong interaction

One feature of the strong interaction is that the force between two colour charged particles increases as these are spatially separated [35]. This is in contrast to the electromagnetic interaction for example, which has a decreasing force as a function of the distance. Both behaviours can be explained by a phenomenon called screening [47]. Given a particle with a negative electric charge and no color charge, virtual electron-positron pairs emerge in the surrounding vacuum. The positive electric charges screen the negative electric charge of the particle and reduce the effective electric charge. For a colour charged particle virtual gluon loops arise in the vacuum, which have the opposite effect: they represent additional coloured particles to interact with and enhance the effective colour charge. The amount of screening increases with the distance from the particle and this results in the described distance relations of the strong and electromagnetic force between two particles.

Due to the increase of the strong force with the distance, spatially separating two colour-charged particles leads to an incrementing potential energy [35, 48]. When this energy becomes sufficiently large, additional colour-charged particles are

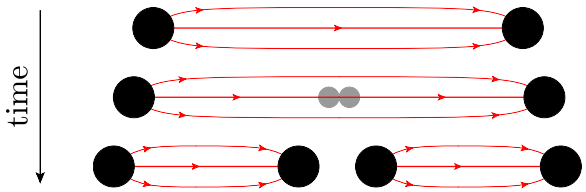

Figure 2.3: As the distance between two coloured particles increases, the force does, too and eventually leads to the production of additional coloured particles. Figure modified from Reference [25].

produced as illustrated in Figure 2.3. Eventually, colour neutral, bound states form, referred to as hadrons. The behaviour leads to the absence of isolated colour charges, which is coined confinement. According to the number of quarks contained, hadrons are classified as mesons (a quark-antiquark pair) and baryons (three quarks). Four quark compounds (tetraquarks) and five quark compounds (pentaquarks) have also been observed [49–52]. At hadron colliders, where individual quarks and gluons are produced, confinement leads to the development of collimated hadron sprays. Such a spray of hadrons is called a jet. Jets are discussed in more detail in Chapter 7.

Another particular feature of the strong interaction is that its coupling strength diverges as the square of the transferred momentum Q between two interacting particles decreases [35]. This is contrast to the electromagnetic coupling strength, which decreases as Q^2 decreases. The coupling strengths α_{EM} (electromagnetic) and α_{S} (strong interaction) have the following form at lowest order:

$$\alpha(Q^2) = \frac{\alpha(\mu^2)}{1 + \beta_0 \alpha(\mu^2) \ln(Q^2/\mu^2)}, \tag{2.5}$$

with $\alpha(\mu^2)$ being the coupling strength evaluated at the reference momentum square μ^2. The factor β_0 differs between the electromagnetic interaction and QCD. For the electromagnetic interaction, $\beta_0^{\mathrm{EM}} = -1/3\pi$, while $\beta_0^{\mathrm{QCD}} = (11N_c - 2n_f)/12\pi$ for QCD with $N_c = 3$ being the number of colours and n_f the number of quark flavours that can be produced at energy transfers Q. While β_0^{EM} is negative, β_0^{QCD} is > 0. This makes α_{EM} increase towards higher Q^2, while α_{S} diminishes, as shown in Figure 2.4.

As shown in the figure, α_{EM} is well below one. Therefore, calculations can be carried out perturbatively [35]. This is different for QCD. Perturbative QCD calculations can only be made for high Q^2, where $\alpha_{\mathrm{S}} \ll 1$. This is called asymptotic freedom. For values of $|Q| \lesssim 1\,\mathrm{GeV}$ however, α_{S} becomes $\gtrsim 1$, so no perturbative QCD calculations are possible at small Q^2. Instead phenomenological approaches and lattice QCD are used to make predictions in this non-perturbative regime. For a recent review of lattice QCD see e.g. Reference [25].

2.5 Cross-section calculations at proton colliders

Protons are collided at the LHC[2]. Protons are made of three so-called valence quarks u, u, d, as well as gluons from interactions of the quarks, other "sea" quarks from gluon splittings, as well as leptons and gauge bosons from quark decays, quark interactions and particle emissions [25]. In proton collisions, any of the constituents (partons) of the two protons can interact with each other.

The distribution of parton i carrying a momentum fraction x in a collision with momentum transfer Q^2 is given by the parton distribution functions (PDFs)

[2]The LHC is described in more detail in Section 5.1.

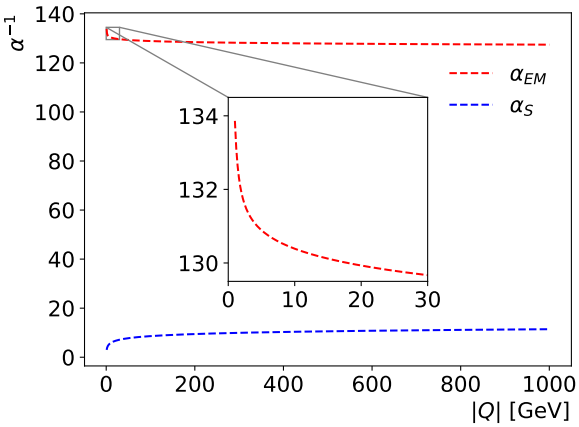

Figure 2.4: The inverse electromagnetic coupling constant decreases as a function of $|Q|$ (α_{EM} increases), while the inverse strong coupling constants increases (α_{S} decreases). α_{S} is calculated according to Equation (2.5) with $\mu = m_Z$ and inputs from [25], while higher order corrections are included for α_{EM} [53, 54] with inputs from [25, 55].

$f_i(x, Q^2)$ [25, 35]. Due to non-perturbative nature of QCD at low Q^2 (Section 2.4), PDFs cannot be deduced from theory. Deep inelastic scattering experiments, which collide protons with other particles such as electrons, determine them though, for example. To transfer the measured PDFs, which are determined at some specific Q^2, to the wanted Q^2, the Dokshitzer-Gribov-Lipatov-Altarelli-Parisi (DGLAP) equations [56–60] are employed.

Due to the so-called factorisation theorem [61], the cross-section of producing some final state X in proton-proton collisions can be split into non-perturbative parts, given by PDFs, and a perturbatively calculable term $\sigma_{i,j\to X}$ [62]:

$$\sigma_X = \sum_{i,j} \int_0^1 \int_0^1 \sigma_{i,j\to X}(x_i p_1, x_j p_2, \mu_R, \mu_F) f_i(x_i, \mu_F) f_j(x_j, \mu_F) \mathrm{d}x_i \mathrm{d}x_j. \quad (2.6)$$

The factorisation scale μ_F is the energy scale at which the perturbative and non-perturbative parts are split. The sum in the equation runs over all partons i and j of the two protons, x_i and x_j are the parton momentum fractions, $\sigma_{i,j\to X}$ is the cross-section of the partons to produce X and p_1 and p_2 are the proton momenta. A perturbative expansion in α_{S} allows evaluating the cross-section $\sigma_{i,j\to X}$ [25]. Due to the dependence on α_{S}, the cross-section $\sigma_{i,j\to X}$ is a function of the so-called renormalisation scale μ_R, which is the scale entering into the calculation of α_{S} ($\mu_R^2 = Q^2$ in Equation (2.5)). The evaluation of $\sigma_{i,j\to X}$ involves the matrix element of $i, j \to X$, which can be derived using the corresponding Feynman diagrams [62].

In what concerns this thesis, $\sigma_{i,j\to X}$ is evaluated either at leading order (LO) in α_{S} using only the Feynman diagrams of $i, j \to X$ containing the least powers of α_{S}; at next-to-leading order (NLO) if adding Feynman diagrams with one additional factor of α_{S}, i.e. containing an extra QCD loop or an additional QCD particle emission; or at next-to-next-to-leading order (NNLO) if adding diagrams with one and two additional powers of α_{S} with respect to LO [25]. As an example, an LO, NLO and NNLO diagram of the $q\bar{q} \to q'\bar{q}'$ process are shown in Figure 2.5.

Kinematic constraints on the final state X can lead to the appearance of terms of the form $(\alpha_{\mathrm{S}} L^2)^n$ at each order n in the perturbative expansion of $\sigma_{i,j\to X}$, with L being the logarithm of a function depending on energy scales [25]. The expression

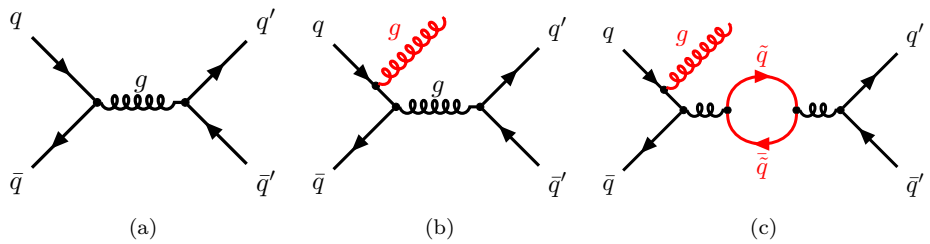

Figure 2.5: Feynman diagrams of the $q\bar{q} \to q'\bar{q}'$ process. In (a) an LO diagram is shown while an NLO and NNLO diagram are shown in (b) and (c), respectively. The additional radiations and loops in the NLO and NNLO diagrams are highlighted in red.

$\alpha_S L^2$ can become very large and endanger the validity of a fixed order cross-section calculation. A technique called resummation allows taking the most dominant of such terms at all powers of α_S into account. Depending on the powers of L considered, the accuracy of the resummation is referred to as leading logarithm (LL), next-to-leading logarithm (NLL) or next-to-next-to-leading logarithm (NNLL).

2.6 Physics beyond the Standard Model

The SM has been shown to describe the physics of the fundamental particles very accurately. However, there are good reasons to believe that the SM is incomplete [63]:

- The Lagrangian of QCD contains CP-violating terms, which can be probed by measuring the electric dipole moment of the neutron [25]. It turns out that the neutron dipole moment is approximately zero and that there is no CP-violation in QCD. The fine-tuning of the CP-violating phase θ of QCD to zero is referred to as the strong CP-problem. It is taken as motivation to question the completeness of the SM, assuming that a more fundamental principle constrains $\theta = 0$.

- To obtain the observable Higgs-boson mass m_h, loop corrections to the bare Higgs-boson mass $m_{h,\text{bare}}$ have to be taken into account [63, 64]:

$$m_h^2 = m_{h,\text{bare}}^2 + \Delta m_h^2.$$

  The largest corrections come from top-quark loops and depend on the energy scale Λ up to which the SM is valid

$$(\Delta^{\text{top-loop}} m_h)^2 \simeq -\frac{3G_F m_t^2}{\pi^2\sqrt{2}}\Lambda^2 \simeq -0.075\Lambda^2,$$

  with G_F the Fermi constant and m_t the top-quark mass. The scale Λ may be as large as the Planck scale (1×10^{19} GeV), but even if assuming that $\Lambda = 5$ TeV, the bare Higgs mass has to be tuned very finely such that m_h equals the measured value of 125 GeV [45, 46]. This unnatural assignment over multiple orders of magnitude is called the hierarchy problem. The hierarchy problem is taken as a hint towards the incompleteness of the SM, assuming that an extension of the SM can resolve the unnatural assignment of the bare Higgs-boson mass.

- Ideally, a fundamental theory would have as few free parameters as possible [35]. The SM has 19 free parameters[3]. This large number of parameters is taken as cause to ask whether there is a more fundamental theory containing the SM and in which (most of) the values of the SM parameters can be derived.

- Neutrino masses were not originally included in the SM. Neutrino oscillations however suggest neutrinos to be massive [36]. It is not clear what the correct way of introducing neutrino masses to the SM is [35].

- Gravitational interactions of the fundamental particles are not described in the SM. Adding gravity to the SM is however desirable to describe all known fundamental interactions between particles in a consistent theory.

- Cosmological observations suggest that the universe contains significantly more matter than antimatter [63]. The so-called Sakharov-conditions [65] state how this asymmetry could be explained. For example, the violation of the CP-symmetry could lead to the observed matter-antimatter asymmetry. Though CP-violation can be measured in meson mixing [66] and be related to a CP-violating phase in the CKM-matrix, the amount of violation in the SM is insufficient to explain the large matter-antimatter asymmetry.

- The existence of DM is evident from multiple astrophysical observations, such as the dynamics of galaxies in galaxy clusters, galaxy rotation curves and gravitational lensing [2]. Recent studies indicate that DM makes up roughly 27 % of the energy content in the universe [67]. The SM is currently not able to explain DM, indicating that an extension is necessary. A common assumption is that DM is made of weakly interacting massive particles and multiple extensions of the SM under this assumption have been developed. This thesis presents a search for DM particles predicted by one of these SM extensions. The SM extension is introduced in Chapter 4. The evidence for DM, models describing it and strategies to search for DM are discussed in the following chapter.

[3]These are 9 quark and lepton masses, 4 CKM parameters, 3 coupling strengths, the Higgs mass and VEV, the QCD CP-violating phase [35].

Chapter 3

Dark matter and its modelling

Dark matter (DM) remains one of the mysteries to unravel in the universe. Despite there being compelling evidence for its existence, see Sections 3.1 and 3.2, surprisingly little is known about its nature, in particular its interaction with Standard Model of particle physics (SM) particles. This chapter gives an overview of DM, what is known, theories of its nature and finally about experiments targeting to measure interactions of SM and DM particles.

3.1 Astrophysical evidence for dark matter

Multiple astrophysical measurements indicate that additional matter that interacts gravitationally and not by one of the three SM forces (hence being optically non-visible) exists in the universe, referred to as dark matter (DM) [2]. One of the first and most famous hints for DM were found by Fritz Zwicky in his 1933 publication on the Coma cluster of galaxies [3, 4]. Zwicky calculated the velocity dispersion of the galaxy cluster using two methods. First he used the number of visible galaxies to calculate a total mass and converted this into a velocity dispersion using the virial theorem. Second he estimated the dispersion using the Doppler shift of spectral lines of observable galaxies. The velocity dispersion resulting from the second method was much higher than what was predicted by the first. Zwicky's conclusion was that additional non-luminous ("dark"), but gravitationally interacting matter has to exist to prevent the cluster from falling apart.

The rotational velocity of gas clouds surrounding stars in galaxies was studied by Vera Rubin and Kent Ford as a function of their distance r from the galactic center in the early 70' [2, 68]. From Newtonian gravity, a velocity profile inversely proportional to $\sqrt{r}$ is expected:

$$v(r) = \sqrt{\frac{GM(r)}{r}},$$

with G the gravitational constant and $M(r)$ the sum of the masses of all galaxy constituents with distance $\leq r$ from the center. Given the astrophysical relation between mass and luminosity, the mass $M(r)$ can be estimated from the observed stars in the galaxy and becomes approximately constant for all r greater than the radial extent r_0 of the galaxy bulge. Correspondingly, $v(r)$ is expected to decrease with $1/\sqrt{r}$ for $r > r_0$. Opposed to this, Rubin and collaborators found that the rotational velocity of the gas clouds remains roughly constant as a function of distance,

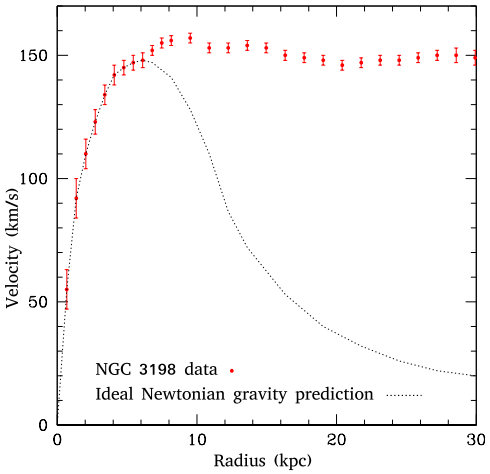

Figure 3.1: Dark matter supposedly alters the rotational velocity in the NGC 3198 galaxy and makes it flat as a function of r beyond the galaxy bulge, compared to the expected velocity from Newtonian gravity, which falls as $1/\sqrt{r}$ [2, 69].

Figure 3.2: A gravitational lens, here the luminous red galaxy LRG 3-757 (central bright yellow/red spot), deflects the light of a blue galaxy behind it resulting in the blue ring [73].

similar to what is shown in Figure 3.1. This supports Zwicky's interpretation of additional non-visible matter binding the gas clouds at $r > r_0$ to the galaxy. Furthermore, the result shows that the non-visible matter mass has to increase linearly with r.

Some years after Vera Rubin had made her observation, gravitational lenses were discovered [2, 70, 71], opening new opportunities to compare the mass determined from luminosity and from gravitation. A gravitational lens is a massive astrophysical object, e.g. a galaxy cluster, a galaxy or a star, that by the laws of general relativity [72] deflects the light of luminous objects, as depicted in Figure 3.2 for a rather extreme case. The deflection depends on the mass of the deflecting object and conversely allows estimating its mass. Much greater lensing masses than luminous masses are found in multiple examples. This additionally supports the hypothesis that matter not interacting by one of the three SM forces, but gravitationally, i.e. DM, exists.

More recently, the so-called bullet cluster collision has provided additional evid-

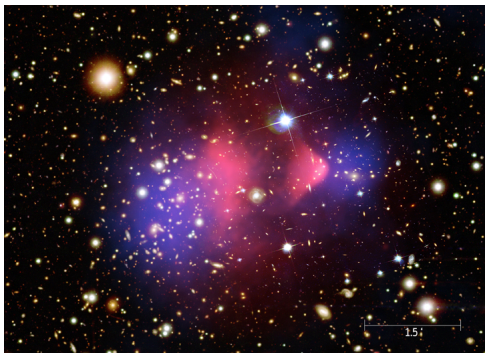

Figure 3.3: As the main cluster (left) and the bullet subcluster (right) of the E0657-558 galaxy cluster collided, the X-ray emitting plasmas, which are the bulk of the baryonic matter and indicated by the pink shade, were displaced from the areas of highest gravitational potential, marked by the blue shade, supporting the DM hypothesis [79].

ence for the DM hypothesis [2, 74, 75]. The bullet cluster is a subcluster of the E0657-558 cluster of galaxies. It collided with the main cluster of E0657-558 roughly 100 million years ago. Galaxies in galaxy clusters are surrounded by an X-ray emitting plasma, which makes up the dominant part of the baryonic matter, being two to 15 times more massive than the stars [76–78]. While the galaxies did not interact when passing by each other in the cluster collision, the two plasmas did. They heated up and slowed down with respect to the motion of the galaxies. The result is two sources of X-rays, which are displaced from the galaxies. If there is no DM, the spatial distribution of the X-rays and of the gravitational potential should coincide. The gravitational potential can be inferred from gravitational lensing. As shown in Figure 3.3, the areas with the highest gravitational potential are shifted from the strongest X-ray emitting sources and the significance of the shift is 8σ [75]. This observation remarkably supports Zwicky's interpretation that additional, non-luminous, gravitationally interacting matter exists.

3.2 Cosmological evidence for dark matter

Cosmological measurements complement the astrophysical evidence for DM. Shortly after the big bang, the universe was filled by a plasma consisting of interacting charged particles and force mediating photons [2]. As the universe expanded and cooled down, charge-neutral atoms formed and the photons were released from the interactions and freely traversed the universe. Due to the expansion of the universe and the corresponding redshift, these photons become apparent nowadays as low frequency (microwave) electromagnetic radiation, called cosmic microwave background (CMB) [80]. The CMB has a nearly perfect black body frequency spectrum with an almost uniformly distributed temperature of $T = (2.725\,48 \pm 0.000\,57)\,\mathrm{K}$ [81] across the sky. Temperature non-uniformities appear at the order of $10\,\mu\mathrm{K}$ and are called anisotropies. The distribution of the anisotropies across the sky as measured by the Planck space observatory [1] is shown in Figure 3.4.

The CMB anisotropies have their origins in early universe fluctuations of the mass density and of the temperature. By measuring the anisotropy power spectrum, the baryon and DM mass densities relative to the critical density ρ_c, denoted as Ω_b and Ω_χ, can be determined. This assumes the validity of the ΛCDM [83], where DM is one of the components besides Dark Energy (Λ) and the SM matter. As an example for how the densities impact the power spectrum, the ΛCDM pre-

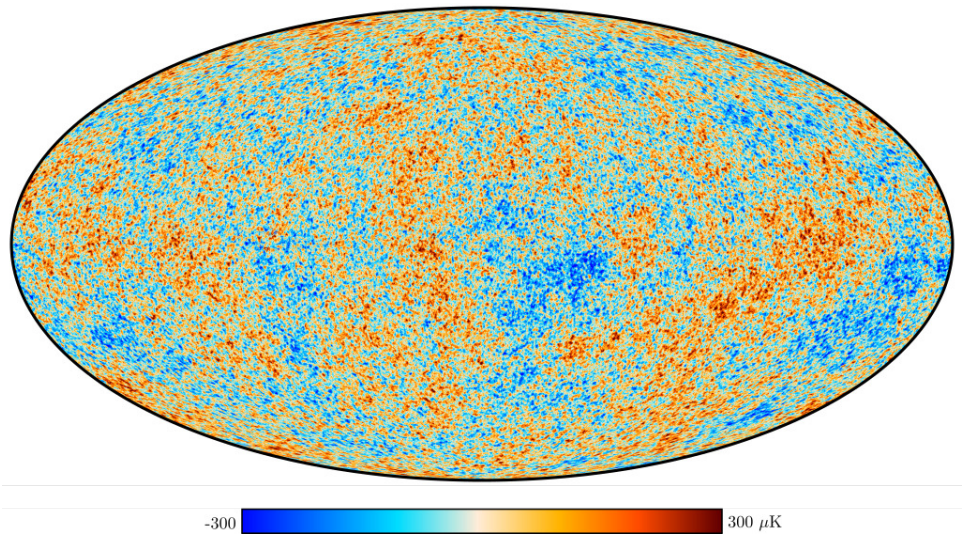

Figure 3.4: Mollweide projection map [82] of the sky with the CMB temperature anisotropy being shown by the colouring [67].

dictions for different Ω_b and Ω_χ are shown in Figure 3.5. Recent Planck observatory measurements yield [67]

$$\Omega_b h^2 = 0.022\,37 \pm 0.000\,15, \qquad \Omega_\chi h^2 = 0.1200 \pm 0.0012,$$

with h the reduced Hubble constant[1]. Using $h = 0.6735 \pm 0.0054$ [67], one obtains the baryon and DM densities:

$$\Omega_b = 0.0493 \pm 0.0006, \qquad \Omega_\chi = 0.265 \pm 0.004.$$

These results remarkably support the DM hypothesis, i.e. that additional, gravitationally interacting matter exists and complement the astrophysical observations. Furthermore, the CMB measurements provide information on the DM quantity: DM must be roughly five times more common than the SM baryons. Yet, these conclusions require to assume the validity of the ΛCDM.

A confirmation of the ΛCDM can be found in the Big Bang nucleosynthesis (BBN) [2]. During the BBN, baryons bounded to light elements such as deuterium, helium and lithium in the first minutes after the big bang. By measuring the abundance of light elements in certain primordial parts of the universe, $\Omega_b h^2$ can be determined [25]:

$$\Omega_b h^2 = 0.0224 \pm 0.0007.$$

This value is perfectly consistent with the CMB result and supports the validity of the ΛCDM.

3.3 The composition of dark matter

While the observations presented in Sections 3.1 and 3.2 indicate the existence of additional matter that interacts gravitationally, but not by the three SM forces, the observations do not constrain the nature of DM.

[1] With H the Hubble constant describing the expansion rate of the universe, $h = \frac{H}{100\,\mathrm{km/s/Mpc}}$ [85].

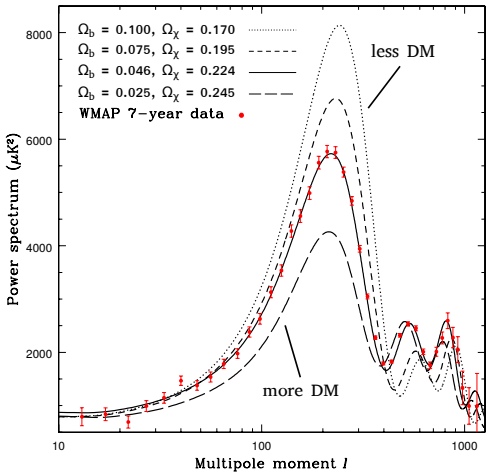

Figure 3.5: Comparison of the anisotropy power spectrum from the seven year data of the WMAP experiment [2, 84] (a predecessor of the Planck observatory) and from four ΛCDM predictions, each with different Ω_b and Ω_χ. The multipole moment is shown on the x-axis, which represents spherical Fourier modes, with small values corresponding to large angular scales and vice versa [80].

Considering the astrophysical DM evidence, the additional matter could be due to non-luminous astrophysical objects, such as planets, black holes, brown dwarfs, etc. [4]. These objects are referred to as massive compact halo objects (MACHOs). Exploiting that MACHOs are detectable by their gravitational lensing, surveys for MACHOs have been conducted [2, 6, 7]. The surveys yield a small number of MACHOs in the universe, so small that they can only be a negligible fraction of the DM. Besides, MACHOs as DM are in conflict with the CMB anisotropy measurements, as being baryonic matter.

Other astrophysical objects that could explain (some of) the DM are primordial black holes (PBHs) [80, 86]. PBHs are hypothetical black holes that formed in the very early universe, so early that they do not contribute to the baryon density derived from the CMB anisotropies. They can be very light, so light they cannot be excluded by the MACHO surveys [4]. In addition to the MACHO surveys, the PBH abundance can be constrained e.g. by gamma-ray and gravitational wave measurements, see Reference [87] for a recent review. The constraints allow setting limits on the DM fraction made up of PBHs as a function of the PBH mass. That PBHs cannot be more than 10 % of the DM for most of the PBH mass range is shown in a recent summary plot [88].

Since astrophysical objects do not seem to explain the bulk of DM, non-baryonic particles become of interest as potential large DM compound. From the SM particles, charged leptons cannot compose DM, as DM does not interact electromagnetically. Mesons are not candidate particles for DM, as they are not stable, but DM appears to be [2]. Neutrinos, not interacting electromagnetically, represent DM particle candidates on the other hand. However, they move with a relativistic speed (making them “hot” DM), which is not compatible with the assumption of a non-relativistic DM speed (“cold” DM) in the ΛCDM [4, 80]. That DM is not “hot”, is confirmed by simulations of the large-scale structure of the universe, which very accurately reproduce the observations if assuming that DM is “cold” [12, 89–93]. Furthermore, due to their light masses and the resulting small mass density, neutrinos can only make up $< 2\,\%$ of the DM [1]. Summarising, none of the known SM particles represents a candidate that can describe a large fraction of the DM.

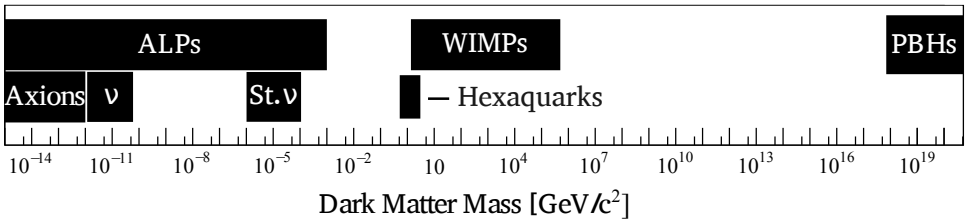

Figure 3.6: The DM candidates presented in the text span a broad mass range of more than 30 orders of magnitude. Sterile neutrinos are abbreviated by "St. ν". Figure adapted from Reference [80], with inputs from References [12, 94].

There are speculations that DM is made of exotic, composite, undiscovered SM particles. For example, it was recently discussed whether DM could be hexaquarks [94], which seems unlikely given oxygen nucleus lifetime measurements [95].

It appears almost inevitable that an extension of the SM is necessary to explain the bulk of the DM. Extensions of the SM offering at least one candidate particle for DM are introduced in the following. Figure 3.6 compares the typical mass ranges of all DM particle candidates that are discussed in this section.

Axions are candidate particles for DM that were predicted while attempting to solve strong-CP parameter fine-tuning problem in QCD (see Section 2.6) [2, 96]. They are very light (typical mass orders are sub-eV), spin-zero particles and interact with photons due to their mixing with SM mesons [25]. Together with their generalisation, the axion-like particles (ALPs), axions represent light-weight, "cold" DM particle candidates. Whilst very heavy (O(GeV)) ALPs are subject to searches at colliders such as the LHC [97], lighter masses are covered by dedicated experiments, such as ADMX [98] and ALPS [99]. For a recent review of axions and ALPs see e.g. Reference [25].

Sterile neutrinos, are hypothetical, right-handed (chirality), massive fermions [100]. They couple to the SM e.g. by oscillating to SM (left-handed) neutrinos. Sterile neutrinos allow postulating a DM particle candidate with a mass of $\sim 1\,\mathrm{keV}$ [100] and are searched for by the ATLAS experiment [101], but also by experiments specialised in neutrino physics, e.g. MicroBooNE [102].

A weakly interacting massive particle (WIMP) [12, 103–109] is a DM particle candidate, which has an interaction strength and mass in the same order of magnitude as the weak force has. WIMPs naturally yield the observed DM density. This is called the WIMP "miracle" and detailed next section. They emerge from a variety of SM extensions, e.g. Supersymmetry, theories with extra dimensions and the model introduced in Chapter 4 (see Reference [12] for more examples and more details on the first two). Due to their properties, WIMPs are very suitable search candidates for a variety of experiments including those at colliders [83]. An overview of the different types of experiments searching for WIMPs is given in Section 3.5.

For completeness, it shall be mentioned here that there are theories which modify gravity instead of requiring extra matter to explain the observations described in Sections 3.1 and 3.2. These are for example the modified Newtonian dynamics (MOND) theory [110–112] and its relativistic extension, TeVeS [113]. The bullet cluster collision [75] is regarded as strong indication against these theories [2]. In a nutshell, the argument is that if MOND or TeVeS were correct, one would expect that the X-rays trace the gravitational potential. However, this argument is discussed controversially and TeVeS may be able to explain the offset anyway, see e.g. Reference [114] for a comprehensive summary. An additional argument against MOND is the insufficient description of galaxy cluster dynamics [114], while it is opposed that the ΛCDM model has flaws on galactic scales, which again is discussed

lively as reviewed in Reference [115]. For the rest of this thesis it is assumed that DM is constituted of additional matter, to be precise of additional particles.

3.4 The dark matter density and weakly interacting massive particles

This section discusses the thermal production of DM [12], which allows explaining the DM density observed today based on DM particles[2]. It is shown that WIMPs, characterised by their weak-scale interaction strength and mass, give a density compatible with the observed one in this thermal production framework.

The following assumptions are made by the thermal production paradigm (usually called the WIMP paradigm) [12, 103–109]:

- DM particles are stable.
- The only way DM particles can be produced, is found in the early, radiation dominated era of the universe by the annihilation of SM or DM particles and the subsequent pair-production of DM particles.
- The annihilation and production rates of DM particles are equal in the early universe.

Furthermore, it is assumed here for simplicity that all DM is made of particles of one non-SM species.

The aim is to derive an expression for today's DM density Ω_χ under these premises. To do so, the dynamics of the DM particle number density n_χ, which is the number of DM particles in a unit volume, is studied. While Ω_χ does not change as the volume of the universe expands, the unit volume in the denominator of n_χ is stretched by the expansion and n_χ decreases [12].

In the thermal DM production mechanism, n_χ reduces due to the decrease of the temperature T of the universe as it expands [116]: when T is greater than the DM particle mass m_χ (setting $k_\mathrm{B} = 1$ here), the kinetic energy of the annihilating SM (and DM) particles is sufficient to pair-produce DM particles. As the universe cools, the energy available in SM particle-antiparticle collisions gets reduced and at some point, when $T \ll m_\chi$, the frequency of producing DM particle pairs becomes very low. Effectively, DM particles are not produced any more, but continue annihilating. The rate of DM particles annihilating is proportional to n_χ and thus diluted by the expansion of the universe [12]. At some point, the expansion rate of the universe H (the Hubble constant) becomes greater than the annihilation rate. In other words, the universe expands faster than DM particles can annihilate. The annihilation of DM particles stops and the number of DM particles in the universe becomes constant. This is called freeze-out. As the expansion of the universe does not stop, the DM particle number density n_χ keeps decreasing.

After gaining a qualitative understanding of the freeze-out, a quantitative assessment is given in the following. The temporal evolution of n_χ can be described by the Boltzmann equation [12]:

$$\frac{\mathrm{d}n_\chi}{\mathrm{d}t} = -3Hn_\chi - \langle\sigma_{\chi\bar{\chi}}v\rangle(n_\chi^2 - n_\mathrm{eq}^2), \tag{3.1}$$

with $\langle\sigma_{\chi\bar{\chi}}v\rangle$ the velocity averaged total DM particle annihilation cross-section [13] and v the velocity of the DM particles. The terms on the right-hand-side of Equation (3.1) correspond the dependencies of n_χ on: the expansion of the universe, and the annihilation and production of DM particles.

[2] More production mechanisms are discussed e.g. in Reference [12].

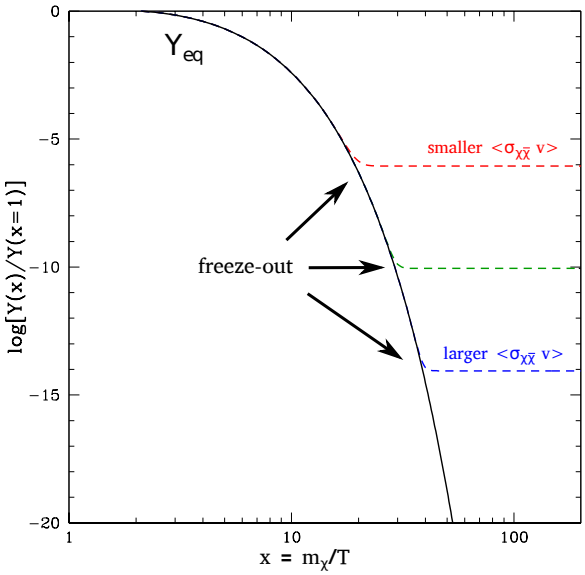

Figure 3.7: The co-moving DM number density Y follows the equilibrium density Y_{eq} as a function of DM mass divided by the temperature, until the freeze-out occurs [2, 85]. At the freeze-out Y plateaus. The equilibrium density is shown by the black line, while solutions of the Boltzmann equation for different $\langle\sigma_{\chi\bar{\chi}}v\rangle$ are shown by the coloured dashed lines.

It is common to define the number density per co-moving volume $Y = \frac{n_\chi}{s}$ [85], with s the entropy density and to solve the Boltzmann equation for Y [12]. The co-moving number density Y can be regarded as the number density corrected for the increase of the unit volume as the universe expands. Y becomes constant after the freeze-out.

Three numerical solutions for Y, each solving the Boltzmann equation for a different $\langle\sigma_{\chi\bar{\chi}}v\rangle$, are shown in Figure 3.7 as a function of the DM mass over the temperature [2, 85]. As can be seen, Y resembles the exponential drop predicted in the equilibrium of the DM particle annihilation and production rate and becomes constant after the freeze-out. The temperature at which the freeze-out occurs, depends on $\langle\sigma_{\chi\bar{\chi}}v\rangle$. For larger $\langle\sigma_{\chi\bar{\chi}}v\rangle$, the annihilation continues until lower temperatures, resulting in a lower co-moving number density.

The co-moving number density after freeze-out can be determined from the numerical solution of Equation (3.1) and expressed in terms of the DM density Ω_χ times h^2, with h being the reduced Hubble constant [117]:

$$\frac{\Omega_\chi h^2}{0.12} = \frac{1}{\left\langle \frac{\sigma_{\chi\bar{\chi}}}{1\,\mathrm{pb}} \cdot \frac{v/c}{0.1} \right\rangle} \stackrel{!}{=} 1. \tag{3.2}$$

The DM density on the left-hand-side is divided by the measured value. Hence, the equation needs to equal one. It turns out that particles with a coupling in the same range as the weak force ($O(1/10)$ [25]) and a mass of $O(100\,\mathrm{GeV})$ can fulfil Equation (3.2) and explains why they are called WIMPs. The fact that DM particle candidates with weak scale couplings and masses naturally give the correct DM density is referred to as WIMP "miracle". WIMPs make excellent candidates for DM particle searches [83]. Concepts of such searches are discussed in Section 3.5.

An example of how a WIMP can fulfil Equation (3.2) is given in the following. As DM particles do most likely not participate in SM interactions, it appears plausible to introduce a massive mediating particle in addition to the DM particle. This

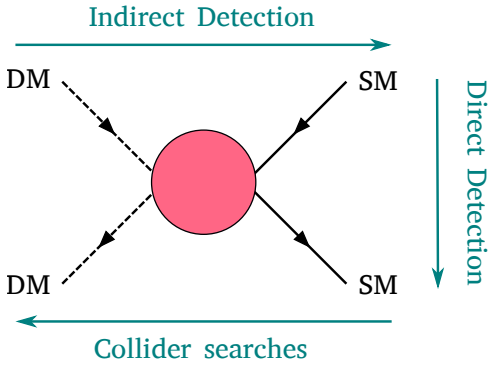

Figure 3.8: The different types of DM particle search experiments target complementary interactions of DM and SM particles.

mediator interacts with SM and DM particles and is the only particle directly interacting with DM particles. Analogous to the weak force bosons, the interaction strength of such a mediator to SM and DM particles can be steered by the mediator mass. To assure that the DM particle is stable, the mediator mass m_M must be greater than m_χ. Let the coupling strengths of the mediator to DM and SM particles be λ_χ and λ_{SM}, respectively. The annihilation cross-section of such a mediator+DM particle model is proportional to $\lambda_\chi^2 \lambda_{\mathrm{SM}}^2 m_\chi^2 / m_M^4$ [118]. Inputting a DM-mediator coupling of one, a SM-mediator coupling in the weak force range, $m_\chi = 100\,\mathrm{GeV}$ and $m_M = 500\,\mathrm{GeV}$, this gives

$$\sigma_{\chi\bar{\chi}} \sim \lambda_\chi^2 \lambda_{\mathrm{SM}}^2 \frac{m_\chi^2}{m_M^4} = 0.6\,\mathrm{pb}.$$

For velocities of $v/c \simeq 0.1$, such a DM particle model can roughly fulfil Equation (3.2). The appearance of the mediator mass to the negative fourth power indicates the importance on the self-interaction probability of DM particles.

3.5 Searching for dark matter particles

WIMPs have served as motivation for a vast number of experiments searching for DM particles [4]. The experiments can be categorised according to the interaction of DM and SM particles they aim for as Figure 3.8 illustrates. Scattering of DM and SM particles is targeted by direct detection (DD) experiments, production of SM particles from annihilating DM particles by indirect detection (IDD) experiments and the production of DM from SM particles by experiments at particle colliders [2]. For all of these experiments, background and DM particle events need to be carefully distinguished. In the following, the principles of DD, IDD and DM particles searches at colliders are outlined.

3.5.1 Direct detection

Direct detection (DD) experiments [80] search for the scattering of DM and SM particles. They assume that DM particles are abundant in the vicinity of earth or even permeate it and occasionally interact with its matter [2]. The scattering probability depends on the velocity distribution and the local density of DM.

The detection principle of DD is that DM particles scatter off the nuclei in the detection volume, yielding phonons (atomic lattice vibrations), atomic excitations and atom ionisations [2]. Phonons can be detected by the change in the temperature

of the detector material they induce. Atomic excitations can be detected by scintillation light. Electrons liberated in atom ionisations can be detected by making use of charge sensitive electrodes.

Background sources in DD experiments mainly originate from cosmic radiation and radioactive decays [80]. Therefore, DD experiments are typically situated underground, are shielded, use elaborate coincidence and veto systems as well as very pure materials of stable elements, for example.

Among the most well known DD experiments are SuperCDMS [119], EDELWEISS [120], XENON1T [121], LUX [122] and DAMA [123]. While an excess compatible with DM has been observed in annular modulation studies by DAMA [124], no independent confirmation has been possible so far [25] and the results are livelily debated.

3.5.2 Indirect detection

The products emerging from annihilating DM particles are the target of indirect detection (IDD) experiments [25]. Such annihilations occur e.g. in areas with high DM densities, such as the sun or the center of the milky way [2]. The annihilating DM particles produce SM particle pairs, such as photons, quarks, bosons etc. These particles or their decay products can e.g. yield gamma-rays, neutrinos or antimatter fluxes.

Gamma-rays from DM particle annihilation are expected to be e.g. due to photons resulting from quark hadronisation [25]. Searches for them assume that they arise from the galactic center of the milky way, dwarf galaxies and clusters of galaxies, for example. Distinct kinematic features of gamma-rays produced by DM, such as high energies or entire energy ranges of enhanced spectral activity ("boxes") [125], make them distinguishable from backgrounds. Multiple experiments, such as the FERMI-LAT satellite [126], search for these gamma-rays.

The annihilation of DM particles, for example in the sun, can also yield neutrinos [25]. Depending on the DM capture and annihilation rate in the sun, high fluxes of highly energetic neutrinos are expected, well separable from the nuclear reaction solar neutrinos of lower energies. Searches for these neutrinos are conducted e.g. by the IceCube [127] and Super-Kamiokande experiments [128], so far without any significant excess [129, 130].

The low abundance and well understood sources of antimatter in the universe motivate the search for antimatter excesses due to DM particle annihilation [2]. Common search candidates are positron and antiprotons. Since these are charged and deflected in the universe, antimatter searches usually do not focus on dedicated areas of the sky. To reduce the background of antimatter from collisions of cosmic particles with the atmosphere, DM annihilation antimatter searches are typically found in the upper atmosphere (e.g. the HEAT balloon [131]) or in space (e.g. PAMELA [132], AMS [133]), though ground-based experiments do exist (e.g. HESS [134]). A considerable excess of positrons has been reported by multiple experiments [135–141]. Whether the excess hints to DM particles is under vibrant discussion, see e.g. Reference [25] for a recent summary.

3.5.3 Collider searches

DM searches at colliders assume that DM particles can be produced in the high-energetic collisions of SM particles [142]. The following description focusses on WIMP DM and on an LHC-like collider with equal energies of the two colliding beams. As WIMPs interact weakly with SM matter, no visible signal in the collision-point surrounding detectors is expected from the DM particles, as Figure 3.9a sketches. If solely WIMPs are produced in a collision, this signal absence

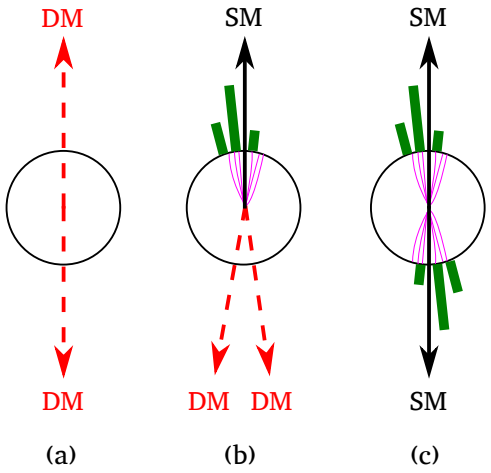

Figure 3.9: View transverse to the beam pipe of some collider experiment. The red lines show particles escaping detection, the purple lines indicate reconstructed tracks, the green boxes illustrate energy deposits in the calorimeters. (a) DM particles escape the detector without energy deposition. (b) DM particles recoil against a jet. (c) Example for two jets emerging from a mediator decay.

poses a challenge: most experiments at hadron colliders rely on a signal from one or more energy-depositing particle(s) to initiate the read-out and storage of a collision event ("trigger"[3]). If no visible signal is produced, no trigger can be issued. Furthermore, even if DM particles were discovered by analysing events without a visible signal, many of its properties could not be investigated without studying events in which additional particles are produced.

It is therefore necessary to study the production of DM particles in association with other particles, such as photons, quarks (experimentally detected as jets), W-bosons, etc., see Figure 3.9b [142]. Since the colliding particles carry no momentum in the plane transverse to the directions of the beams, the sum of all emerging particle momenta projected to this plane must equal zero. Due to the elusive nature of DM particles, they yield an imbalance of the sum of the measured momenta in this transverse plane, as Figure 3.10 illustrates. The negative of this sum is called missing transverse momentum $\vec{p}_{\mathrm{T}}^{\,\mathrm{miss}}$ and is the key signal used by direct WIMP searches at colliders.

Certain extensions of the SM predict that DM and SM particles only couple via a mediating particle [142]. This mediator can be searched for by exploiting that if produced by SM particles, it can also decay into SM particles. These so-called resonant searches involve all sort of SM particles as outcome, such a quark pairs for example, yielding a dijet signature in the detector.

Since they depend on the SM particles that DM particles are produced with or the SM particles the mediator decays into, i.e. the detector signature, WIMP searches at colliders rely heavily on the model describing the DM. At current collision energies, these DM models are typically less generic than at DD and IDD experiments. The DM models probed at colliders typically have to be more complex and make more assumptions on the DM particle interactions. Yet, as shown in Figure 3.11, collider experiments complement the DD and IDD searches for these more specific DM models. Collider experiments may be able to efficiently probe DM properties, if candidates were observed with DD or IDD [142].

[3]Note that experiments are often able to trigger on particles depositing no energy in a detector ("$E_{\mathrm{T}}^{\mathrm{miss}}$ triggers"), but this typically requires the presence of visible particles to infer on the invisible particles.

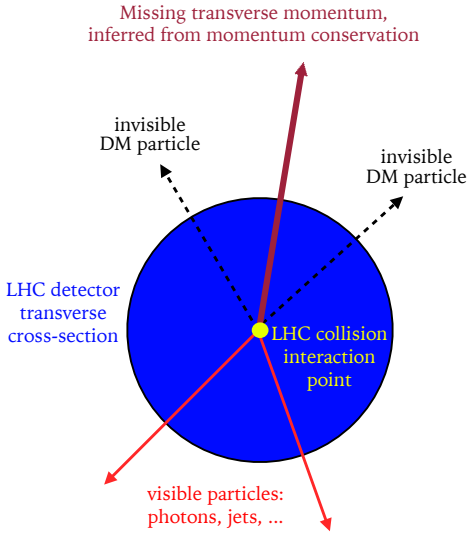

Figure 3.10: The DM particles do not produce a visible signature in the detector, leading to a non-zero sum of measured momenta in the plane transverse to the beam axis [142].

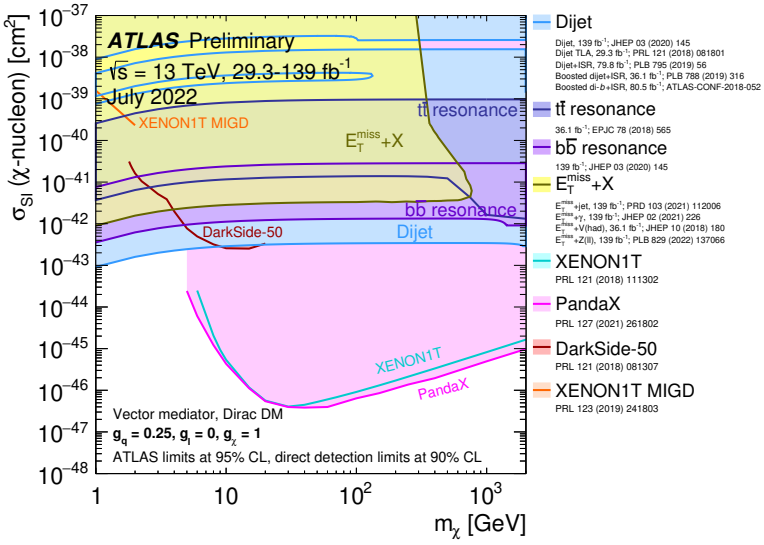

Figure 3.11: DD experiments (XENON1T, PandaX, DarkSide) exclude lower DM-nucleon interaction cross-sections σ_{SI} for DM particle masses $> 5\,\mathrm{GeV}$ than the ATLAS experiment collider searches do (dijet, $t\bar{t}$, $b\bar{b}$, $E_{\mathrm{T}}^{\mathrm{miss}} + X$) [143]. The collider searches exclude lower σ_{SI} for $m_{\chi} \leq 5\,\mathrm{GeV}$. The shaded areas are the excluded regions. Dijet and $E_{\mathrm{T}}^{\mathrm{miss}} + X$ represent the union of multiple searches, with $E_{\mathrm{T}}^{\mathrm{miss}} = |\vec{p}_{\mathrm{T}}^{\,\mathrm{miss}}|$ and "X" standing for a jet, a photon or a vector-boson. The vector mediator simplified DM model used in the plot is described in Chapter 4. The DD exclusion limits are at 90 % confidence level (CL), while the ATLAS limits are at 95 % CL.

Chapter 4

Extended Higgs sector dark matter models

Searches for WIMPs at colliders depend on the signature investigated and hence on the model describing the dark matter (DM) particles. Due to the many unknowns concerning DM, it is important that collider searches are kept as model independent as possible. This is achieved by relying on generic model building frameworks.

The most generic DM models are based on effective field theories (EFTs) [144, 145]. Although such models were employed in previous studies [145–150], they have been shown to suffer from validity problems at current LHC energies [151–153].

The next most generic type of DM models are so-called simplified DM models [154–158], in which a particle mediating the interaction of SM and DM particles is introduced. The mediator can be classified in terms of its spin and CP properties. Simplified DM models make valid predictions at the centre-of-mass energies of the LHC, but are generally not UV-complete [15, 159]. They contain unitarity violating amplitudes, which lead to diverging cross-sections as a function of the centre-of-mass energy, such that the models are not valid at all energy scales.

In this thesis, one of the simplest UV-complete extensions of simplified DM models is probed. This 2HDM+a model [14, 15] is based on an extension of the Higgs sector by a second Higgs doublet [14, 160–167]. Models in which the SM is extended by a second Higgs doublet are referred to as two Higgs doublet models (2HDMs) [168, 169]. In 2HDMs both of the Higgs doublets develop non-zero VEVs v_1 and v_2 with $v^2 = v_1^2 + v_2^2 = (246\,\text{GeV})^2$ and conventionally, the ratio of the two VEVs, $\tan\beta \coloneqq \frac{v_2}{v_1}$, is used as a free parameter. Five spin-0 mass eigenstates arise after symmetry breaking in 2HDMs. These are the CP-even h and H, the CP-odd A and the two charged, equal-mass bosons $H^\pm$. Imposing the alignment limit [14, 15], h is identified in the following as the SM Higgs boson [45, 46]. The remaining spin-0 bosons are referred to as Higgs partners or simply additional Higgs-bosons. Furthermore, the decoupling limit [170] is assumed, in which the additional Higgs-bosons are heavier than the SM one.

Strong experimental constraints on the absence of flavour-changing neutral currents (FCNCs) restrict the Yukawa coupling structure of the Higgs doublets to the fermions to four scenarios [171, 172]. In each scenario, the up- and down-type quarks as well as the charged leptons can couple to only one of the two Higgs doublets. Yukawa type-II couplings [169, 170] are employed here [15], where the up-type quarks couple only to one of the Higgs doublets and all other massive fermions couple only to the other doublet [14].

As in the case of DM simplified models [154, 155, 157, 158], a mediator particle, here assumed to be a pseudoscalar, is added in the 2HDM+a model [14]. This

field interacts with the Higgs doublets and Yukawa-like with the DM particle χ, which is assumed to be a Dirac fermion. The mediator a mixes with the CP-odd Higgs-boson A with mixing angle θ. The mixing angle determines the interaction strength of both a and A to DM particles. For $\sin\theta = 0$, only the a-boson couples to DM, while the interaction strength of both bosons to DM is equal for $\sin\theta = 1/\sqrt{2}$ (maximal mixing condition). Since the Feynman diagrams featuring the associated production of DM particles and SM particles with the largest cross-sections (see Section 4.2) have vanishing amplitudes in the extreme case of $\sin\theta = 0$, non-zero values of $\sin\theta = 0.35$ and $\sin\theta = 1/\sqrt{2} \simeq 0.7$ are considered in the following [15].

4.1 Parameter constraints

The 2HDM+a model has a total of 14 free parameters. In addition to the previously mentioned v, $\tan\beta$ and $\sin\theta$, these are the masses m_h, m_H, m_A, $m_{H^\pm}$ and m_a, the quartic couplings of the Higgs potential λ_3, λ_{P1} and λ_{P2}, and the DM particle coupling and mass y_χ and m_χ. Constraints on some of these parameters arise from previous searches and measurements as well as from theoretical and simplification arguments, following the recommendations from the LHC DM working group [15]. They are summarised in Table 4.1.

The additional Higgs-bosons H, A and $H^\pm$ impact higher order loop corrections to the weak interaction boson propagators [14]. These corrections are constrained by precision measurements in the electroweak SM sector and require that $m_H = m_{H^\pm}$ or that $m_{H^\pm} = m_A$. To fulfil these requirements and to simplify the parameter space under study [173], $m_H = m_{H^\pm} = m_A$ is imposed in the models considered in this thesis [15].

Constraints on the mediator mass m_a arise from searches for invisible decays of the SM Higgs-boson [174, 175], due to the decays $h \to aa^* \to \chi\bar{\chi}\chi\bar{\chi}$ and $h \to a\chi\bar{\chi} \to \chi\bar{\chi}\chi\bar{\chi}$ [14, 15]. Assuming $m_a \geq 100\,\text{GeV}$ largely evades these restrictions, as the decays $h \to aa^*$ and $h \to a\chi\bar{\chi}$ become strongly suppressed in that case[1].

To ensure stability of the vacuum, the Higgs potential of the 2HDM+a model has to be bounded from below [170]. This can be translated into a lower bound on the quartic coupling λ_3 appearing in the Higgs potential [15, 170]. At the same time, to ensure perturbativity, λ_3 may not be $\geq 4\pi$. Following the suggestion in Reference [15], λ_3 is set to 3. For $\sin\theta = 0.7$, this value $\lambda_3 = 3$ guarantees the stability of the vacuum for $m_H = m_{H^\pm} = m_A \lesssim 600\,\text{GeV}$, though the range of valid m_H can be increased by almost a factor two by incrementing λ_3 to eight [15, 22]. Furthermore, as pointed out in Reference [177] for 2HDMs, the introduction of additional quartic terms in the Higgs potential can weaken the condition on m_H [164].

The remaining quartic couplings λ_{P1} and λ_{P2} are set equal to λ_3, to keep the decay widths of the H- and A-bosons as small as possible [15]. This is motivated by the use of the narrow-width approximation (NWA), which is a standard technique, significantly simplifying the cross-section calculation of complicated decay processes [178]. The NWA is only applicable if the decay width Γ of a particle is sufficiently smaller than its mass m, i.e. $\Gamma \lesssim m/3$ [14].

Finally, the DM coupling and mass are fixed to simplify further studies. The coupling y_χ is set to one, its value does not have a significant impact on the distribution of the observables at colliders, where DM is not detected by its interaction with the detector[2] [15]. The DM mass m_χ is set to 10 GeV, for which the decay $a \to \bar{\chi}\chi$ remains allowed for all $m_a \geq 100\,\text{GeV}$. Deduced results are however valid for any DM mass, as long as $m_a > 2 \cdot m_\chi$.

[1] A recent study targeting mediator masses below 100 GeV can be found in Reference [176].
[2] y_χ plays a much more important role for e.g. DD experiments.

Constrained parameters

Parameter	*Definition*	*Constrained due to*
$m_h = 125\,\text{GeV}$	SM Higgs-boson mass	Alignment limit / Higgs-boson discovery
$m_H = m_A = m_{H^\pm}$	Higgs-boson masses	Electroweak measurements
$m_a \geq 100\,\text{GeV}$	Mediator mass	$h \to$ invisible
$v = 246\,\text{GeV}$	Higgs VEV	Electroweak and Higgs physics
$\cos(\beta - \alpha) = 0$	α: CP-even Higgs-boson mixing angle	Alignment limit / Previous searches
$\lambda_3 = \lambda_{P1} = \lambda_{P2} = 3$	Quartic Higgs-boson couplings	Vacuum stability (λ_3), NWA (λ_{P1}, λ_{P2})
$y_\chi = 1$	Yukawa coupling of the DM particle	No significant impact on collider searches
$m_\chi = 10\,\text{GeV}$	DM particle mass	$m_a > 2 \cdot m_\chi$

Parameters left free

Parameter	*Definition*
$m_H = m_A = m_{H^\pm}$	Masses of H, A and $H^\pm$
m_a	Mediator mass
$\sin\theta$	CP-odd Higgs-boson mixing
$\tan\beta$	Ratio of Higgs doublet VEVs

Table 4.1: Summary of the parameters of the 2HDM+a model [14], their definitions and constraints [15].

Summarising, several constraints have been placed on the 2HDM+a model parameters, originating from previous measurements and theoretical and simplification considerations. Four parameters are left free for study: $m_{H^\pm}$, m_a, $\sin\theta$ and $\tan\beta$.

4.2 Anatomy of the model

There is a rich phenomenology associated to the 2HDM+a model with final states containing only SM particles, as well as final states in which DM particles are produced in association with SM particles [15, 22]. The most important final states for DM searches arise from the Feynman diagrams shown in Figures 4.1a, 4.1c and 4.1e, featuring the on-shell production of each of the heavy Higgs partners A, H and $H^\pm$, respectively. These heavy Higgs partners interact as follows in the Feynman diagrams:

- The A-boson decays into the mediator a and a SM Higgs-boson. As long as the DM mass is smaller than half of the mediator mass, the a-boson almost exclusively decays into two DM particles. The resulting signature is called "mono-Higgs signature".

- The H decays into a mediator a and a Z-boson ("mono-Z signature").

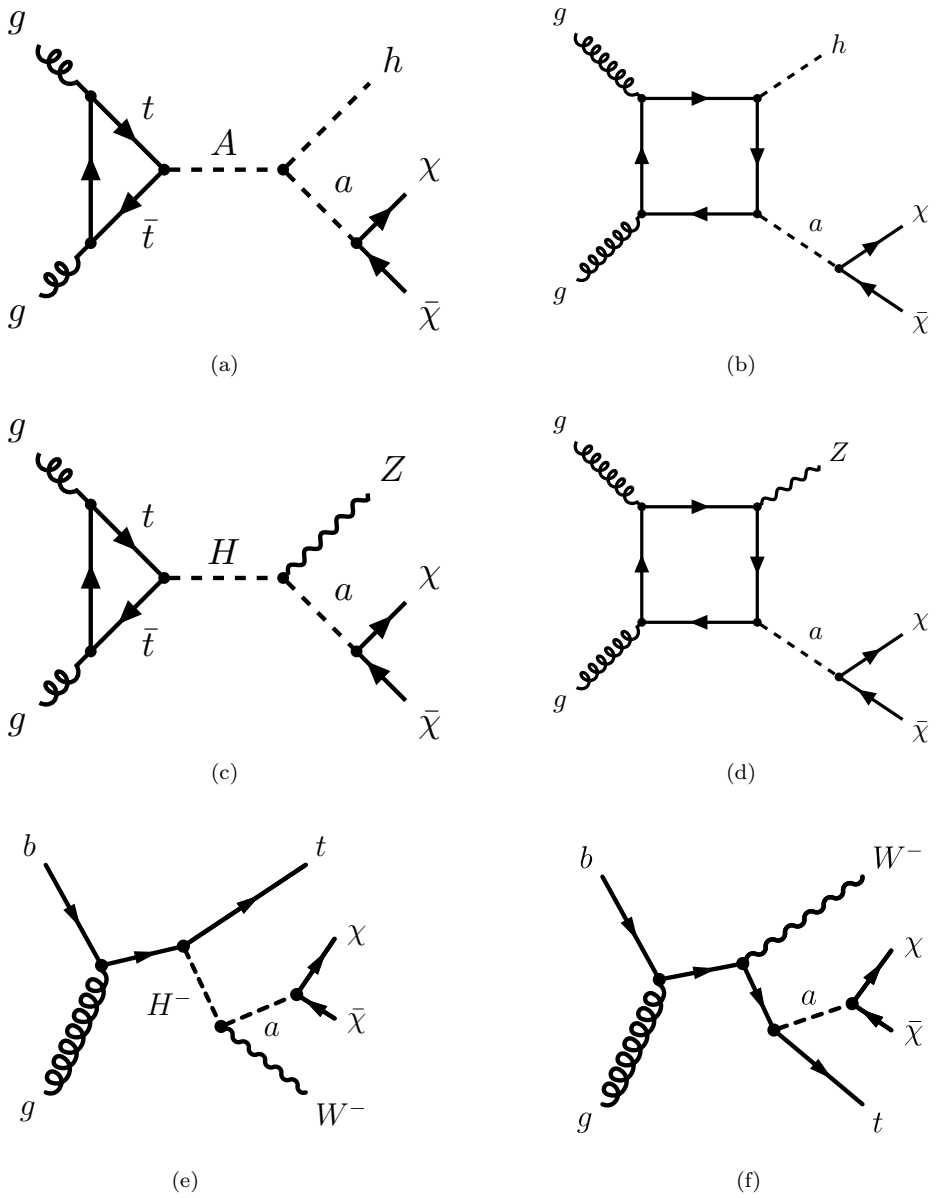

Figure 4.1: 2HDM+a model Feynman diagrams for the mono-Higgs (top), mono-Z (middle) and tW+DM (bottom) signatures [21]. Diagrams on the left are resonantly enhanced in the 2HDM+a model.

Figure 4.2: 2HDM+a model Feynman diagrams for the $t\bar{t}$+DM signature. Except for A-boson contributions, both diagrams are also valid in the simplified DM model presented in the introduction of this chapter.

- The $H^{\pm}$-boson is produced in association with a top-quark and decays into the mediator a (decaying to $\chi\bar{\chi}$) and a W-boson ("tW+DM signature").

For all three signatures, the resonant diagrams, shown in Figures 4.1a, 4.1c and 4.1e interfere with the non-resonant production of the same final states, shown in Figures 4.1b, 4.1d and 4.1f.

Apart from the DM particle signatures with resonantly enhanced diagrams, there are also signatures without resonant diagrams [15]. Among these is the $t\bar{t}$+DM signature, i.e. the associated production of a top-quark pair and DM particles. The most important Feynman diagrams of the $t\bar{t}$+DM signature are shown in Figures 4.2a and 4.2b. As the top-quarks most commonly decay into a W-boson and a b-quark [25], the $t\bar{t}$+DM and the tW+DM signature differ by one b-quark in the final state. This kinematic similarity is exploited to enhance the sensitivity of the search presented in this thesis.

The mono-Higgs and mono-Z signatures have already been studied extensively in the past and shown to be very powerful to constrain the free model parameters [16–20]. This thesis hence focusses on the exploitation of the last and experimentally overlooked final state involving the associate production of DM particles, a top-quark and a W-boson. The work of this thesis was included in two publications [21, 22]. It is detailed in Chapters 8-12, with special focus on the search published in Reference [22].

4.2.1 The tW+DM signature

It is worth noticing, specifically for the tW+DM final state that the search for processes involving a single top-quark are generally challenging, having large backgrounds from SM processes with very high cross-sections such as $t\bar{t}$ and the associated production of vector-bosons and jets.

As top-quarks almost exclusively decay into a W-boson and a b-quark [25], the tW+DM final state contains two W-bosons. The topology of these W-bosons is unbalanced in terms of their boost. The W-boson from the $H^{\pm}$-boson decay Figure 4.1e or the $b \to Wt$ vertex in the a-boson diagram Figure 4.1f is likely to have a relatively high transverse momentum above 200 GeV as shown in Figure 4.3a. On the other hand, the W-boson from the top-quark is less likely to be very energetic, see Figure 4.3b[3]. In contrast, the two W-bosons emerging in SM $t\bar{t}$ events for

[3]A more detailed study on the momentum of the W-bosons is presented in Section 8.2.

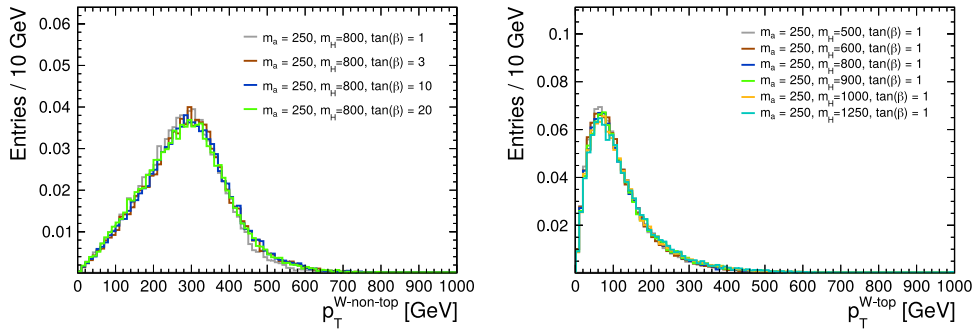

(a) (b)

Figure 4.3: (a) The sum of the transverse momentum (p_{T}) distributions of the W-boson from the $H^{\pm}$-boson decay and the W-boson from the $b \to Wt$ vertex in the a-boson diagram and (b) the p_{T} distribution of the W-boson from the top-quark decay. Distributions are shown at particle level (see Chapter 6) for multiple 2HDM+a model signal samples generated with varying (a) $\tan\beta$ and (b) $m_{H^{\pm}}$. Unless indicated otherwise, the signal samples are generated with the 2HDM+a model parameters $m_a = 250\,\mathrm{GeV}$, $m_{H^{\pm}} = 800\,\mathrm{GeV}$, $\tan\beta = 1$ and $\sin\theta = 0.7$. The simulation setup to produce the signal samples is presented in Chapter 6. All distributions are normalised to unity. More parameter dependencies of the p_{T} of the W-bosons are studied in Section 8.2.

example have a more equal boost. This signal feature is exploited in the analysis presented in Chapters 8-12.

The cross-section of the resonant diagram Figure 4.1e depends on the branching ratio of the $H^{\pm} \to aW^{\pm}$ vertex. This branching ratio is a function of the free 2HDM+a model parameters as follows: for the masses $m_{H^{\pm}}$ and m_a, the branching ratio decreases as the difference $\Delta = m_{H^{\pm}} - (m_a + m_W)$ decreases, with m_W the W-boson mass, and becomes zero, if $\Delta = 0$ [14, 21]. The branching ratio $\mathrm{BR}(H^{\pm} \to aW^{\pm})$ increases as $\sin\theta$ does. Finally, the $\mathrm{BR}(H^{\pm} \to aW^{\pm})$ depends on $\tan\beta$, as the $H^{\pm} \to aW^{\pm}$ vertex competes with the $H^{\pm} \to tb$ vertex and the decay width of the latter depends on $\tan\beta$ [14, 179].

The cross-sections of both tW+DM diagrams (Figs. 4.1e, 4.1f) grow with $\sin\theta$ [179, 180]. For models considered in this thesis either $\sin\theta = 0.35$ is assumed, or, to maximally enhance the total cross-section of the process of interest, the maximal mixing condition is ($\sin\theta = 0.7$).

Figure 4.4a shows the cross-section of the tW+DM signature as a function of $\tan\beta$ for $m_{H^{\pm}} = 500\,\mathrm{GeV}$, $m_a = 150\,\mathrm{GeV}$ and $\sin\theta = 1/\sqrt{2}$ [179]. The total tW+DM cross-section (solid red line) is dominated by the contribution from the resonant $H^{\pm}$-boson diagram (dashed pink line). For heavier $H^{\pm}$, the non-resonant diagram (Figure 4.1f) gains importance. This can be seen in Figure 4.4b for $m_{H^{\pm}} = 1000\,\mathrm{GeV}$: the resonant diagram cross-section reduces by a factor ten compared to $m_{H^{\pm}} = 500\,\mathrm{GeV}$ and only makes up roughly 50 % of the total cross-section.

Figures 4.4a and 4.4b also reveal a significant $\tan\beta$ dependence of the cross-section. All cross-sections have their maximum at the lowest value of $\tan\beta$ and a local minimum at $\tan\beta \simeq 5-7$. The cross-section of the resonant tW+DM diagram has a local maximum at $\tan\beta \simeq 30$, which also becomes visible in the total cross-section. In essence, this functional form is a consequence of the Yukawa type-II couplings of the 2HDM+a model. These make the couplings of top-quarks to the Higgs boson partners and the mediator proportional to $\cot\beta$ and those of b-quarks

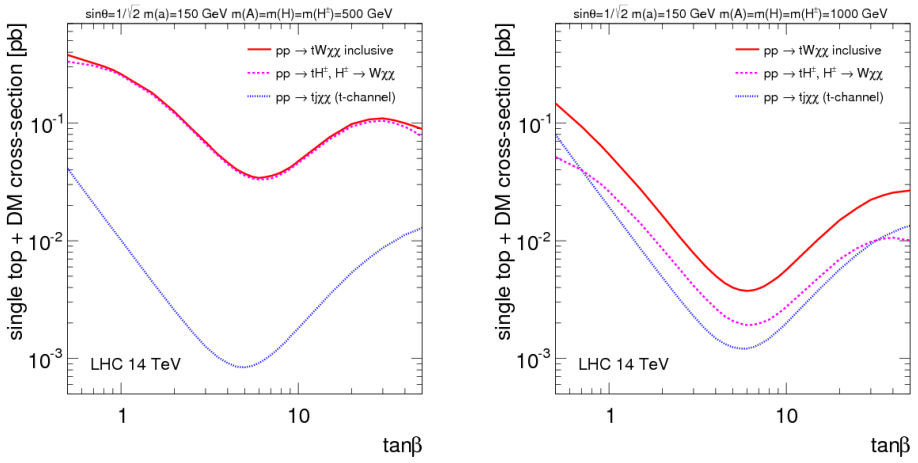

(a) (b)

Figure 4.4: Cross-sections of the tW+DM and tj+DM signatures in the 2HDM+a model as a function of $\tan\beta$ for $\sin\theta = 1/\sqrt{2}$, $m_a = 150\,\text{GeV}$ and (a) $m_A = m_H = m_{H^\pm} = 500\,\text{GeV}$ and (b) $m_A = m_H = m_{H^\pm} = 1000\,\text{GeV}$ [179]. The total tW+DM signature cross-section is indicated by the red solid line, the cross-section of the resonant diagram in Figure 4.1e is shown by the pink dashed line and the total cross-section of the tj+DM signature is shown by the blue dotted line. The cross-section calculation assumes a proton-proton collider with a centre-of-mass energy of 14 TeV.

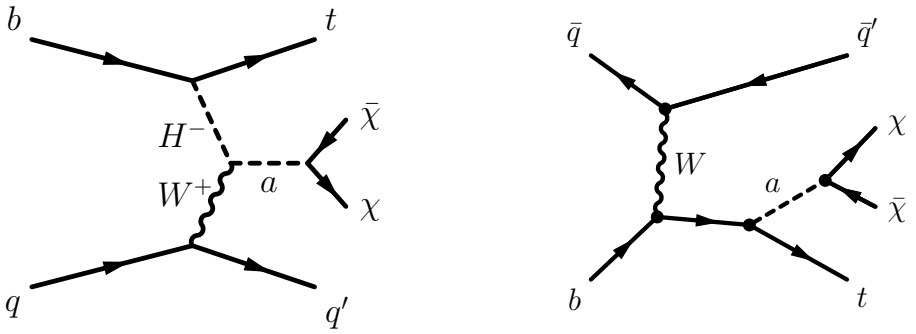

Figure 4.5: 2HDM+a model Feynman diagrams for the tj+DM signature [21].

proportional to $\tan\beta$, though the factors enter the cross-sections non-trivially [179]. For completeness, the total cross-section of another signature involving a charged Higgs-boson is shown by the dotted blue line visible in Figures 4.4a and 4.4b. This signature is characterised by the presence of a single top-quark, a lighter quark (yielding a jet) and DM particles in the final state ("tj+DM signature"). The two dominant Feynman diagrams of the tj+DM signature are shown in Figures 4.5a and 4.5b. As can be seen in Figures 4.4a and 4.4b, the total tj+DM signature cross-section is at least a factor two below the one of the tW+DM signature.

In the analysis presented in this thesis, the 2HDM+a model is studied in the tW+DM signature in two-dimensional planes of model parameters. In the m_a-$m_{H^\pm}$ plane, the mediator and $H^\pm$-boson masses are varied between 100 GeV–600 GeV and 400 GeV–2000 GeV, respectively, while $\tan\beta$ is fixed to one. In the two $m_{H^\pm}$-$\tan\beta$ planes probed, the charged Higgs-boson mass and $\tan\beta$ are scanned between 300 GeV–2000 GeV and 0.3–30, while the a-boson mass equals either 150 GeV or 250 GeV. All three planes are investigated for $\sin\theta = 0.35$ and $\sin\theta = 0.7$.

Chapter 5

The ATLAS experiment at the LHC

Data from proton-proton interactions recorded by the A Large Toroidal Aparatus (ATLAS) detector [23] at the Large Hadron Collider (LHC) [24] between 2015 and 2018 is analysed in this thesis. This chapter provides an overview of the LHC and a description of the ATLAS detector.

5.1 The Large Hadron Collider

Protons and heavy ions are collided at so far unrivalled centre-of-mass energies by the LHC [24]. It is located close to the European Council for Nuclear Research (CERN) facilities on the Swiss-French border in the vicinity of Geneva. The LHC has a circumference of 27 km and is located roughly 100 m underground in the former Large Electron-Positron Collider (LEP) tunnel [181]. Particles are accelerated in two beam pipes in opposite directions. Superconducting radio frequency cavities are used for the acceleration. To make the particles follow a circular orbit, 1232 superconducting NbTi dipole magnets are employed, operating at temperatures lower than 2 K and providing field strengths of up to 8.33 T.

Protons and heavy ions are accelerated in bunches of particles [24]. A proton bunch contains about 1.15×10^{11} protons. At centre-of-mass energies of 14 TeV, these proton bunches are roughly 1.06 ns long (4σ). Up to 2808 proton bunches are circulating simultaneously in the LHC, separated by at least 24.95 ns and distributed across 3564 positions.

Protons pass through a chain of pre-accelerators, illustrated in Figure 5.1, before entering the LHC [24]. Initially, the protons are produced by ionising hydrogen atoms. These are fed into the Linac 2 accelerator[1], which raises their kinetic energy to 50 MeV. Subsequently, the Proton Synchrotron Booster (1.4 GeV), the Proton Synchrotron (PS, 25 GeV) and Super Proton Synchrotron (SPS, 450 GeV) increase the energy of the protons. Eventually, the SPS injects the protons into the LHC, where the protons are accelerated to their final energies.

The LHC beams are collided at four interaction points, where experiments are placed [24]. The four major experiments at the LHC are the ATLAS experiment [23], the CMS experiment [185], the Large Hadron Collider beauty (LHCb) experiment [186] and the A Large Ion Collider Experiment (ALICE) [187]. ATLAS and CMS are multi-purpose experiments. They focus on precision measurements of

[1]Since 2020, the Linac 4 accelerator replaces Linac 2 and speeds up protons to 160 MeV [183, 184]. In the data analysed in this thesis, Linac 2 was still in use.

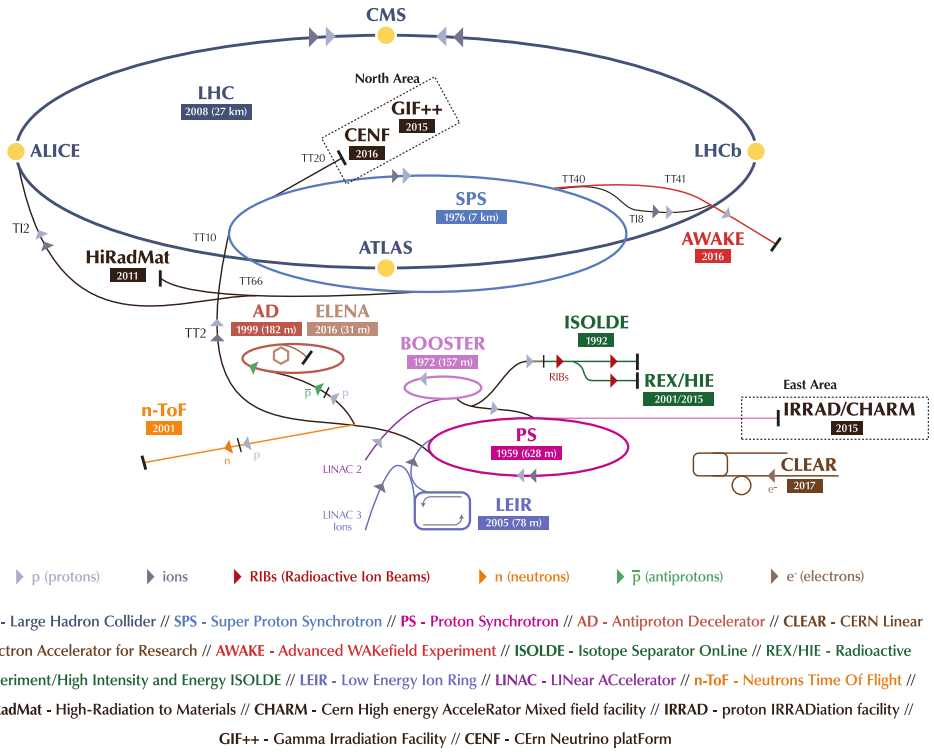

LHC - Large Hadron Collider // SPS - Super Proton Synchrotron // PS - Proton Synchrotron // AD - Antiproton Decelerator // CLEAR - CERN Linear Electron Accelerator for Research // AWAKE - Advanced WAKefield Experiment // ISOLDE - Isotope Separator OnLine // REX/HIE - Radioactive EXperiment/High Intensity and Energy ISOLDE // LEIR - Low Energy Ion Ring // LINAC - LINear ACcelerator // n-ToF - Neutrons Time Of Flight // HiRadMat - High-Radiation to Materials // CHARM - Cern High energy AcceleRator Mixed field facility // IRRAD - proton IRRADiation facility // GIF++ - Gamma Irradiation Facility // CENF - CErn Neutrino platForm

Figure 5.1: Overview of the accelerators and experiments related to the LHC. Adapted from Reference [182].

the SM, in particular Higgs boson properties and search for physics beyond the SM, such as supersymmetric and DM particles. LHCb's main targets are rare b-hadron decays and CP-violation. ALICE investigates heavy ion collisions and studies the quark gluon plasma and properties of QCD.

5.1.1 Energy, luminosity and pile-up

Most studies of physics processes at colliders are based upon the number N_X of collisions yielding some final state X. At the LHC, the rate R_X of producing X is given by

$$R_X = \frac{\mathrm{d}N_X}{\mathrm{d}t} = L \cdot \sigma_X(\sqrt{s})$$

with $\sigma_X(\sqrt{s})$ being the cross-section of producing X, previously discussed in Equation (2.6), and L the luminosity.

The cross-section $\sigma_X(\sqrt{s})$ is a function of the collider's centre-of-mass energy $\sqrt{s}$. More explicitly: the centre-of-mass energy plays an important role in how likely it is to produce a final state and even which heavy particles can be produced. Furthermore, the kinematics of particles in X depend on $\sqrt{s}$. The centre-of-mass energy is a paramount quantity at colliders.

The LHC collided protons with a centre-of-mass energy of $\sqrt{s} = 7\,\mathrm{TeV}$ in 2010 and 2011 and $\sqrt{s} = 8\,\mathrm{TeV}$ in 2012 [188]. This time period is called run-I. Between 2015 and 2018, which is called run-II, the centre-of-mass energy was increased to $\sqrt{s} = 13\,\mathrm{TeV}$ [189], corresponding to a kinetic energy of 6.5 TeV per proton beam. For run-III, which started in 2022, the centre-of-mass energy is $\sqrt{s} = 13.6\,\mathrm{TeV}$ [190].

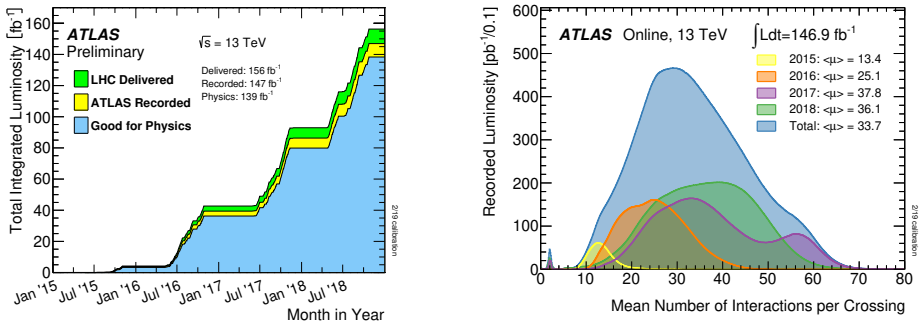

(a) (b)

Figure 5.2: (a) The integrated luminosity between 2015 and 2018 at the ATLAS experiment [199]. The integrated luminosity of the LHC collisions at the ATLAS detector is shown in green, of the collisions recorded in yellow and the integrated luminosity of the collisions usable for physics analyses is shown in blue. (b) The μ distribution measured by the ATLAS detector during LHC run-II [199].

In heavy ion collisions, centre-of-mass energies of up to 5.44 TeV per colliding nucleon pair have been achieved [189, 191]. Proton-proton interactions from LHC run-II are analysed in this thesis.

In addition to the centre-of-mass energy, the rate R_X depends on the luminosity. The luminosity depends on beam parameters: the number of bunches n_b in the LHC, the number of protons n_1 and n_2 per bunch, the revolution frequency f_r of the bunches as well as the size of the transversal overlap Σ_x and Σ_y of the two beams in x- and y-direction [192, 193]

$$L = \frac{n_b n_1 n_2 f_r}{4\pi \Sigma_x \Sigma_y}.$$

The transversal overlap of the beams is measured in so-called van-der-Meer scans [194], in which the luminosity is calibrated [195–197]. A peak luminosity of $L = 1.9 \times 10^{34}\,\mathrm{cm}^{-2}\,\mathrm{s}^{-1}$ [197, 198] was reached at the ATLAS detector in 2018, exceeding the maximum design luminosity of $L = 1 \times 10^{34}\,\mathrm{cm}^{-2}\,\mathrm{s}^{-1}$ [24].

From the rate R_X, the number of collisions N_X containing the final state X can be calculated by $N_X = \sigma_X(\sqrt{s}) \int L dt$ [35]. As N_X is essential at collider experiments, the integrated luminosity $\mathcal{L} := \int L dt$ is, too. Figure 5.2a shows the increase of the integrated luminosity between 2015 and 2018.

Data from collisions collected with the ATLAS detector may not be suitable for studying physics processes [200]. For example, some important detector components may not have been functioning during certain time periods. Therefore, the integrated luminosity of the collision data to be used for physics analyses is smaller than the integrated luminosity of the total number of recorded collisions as shown in Figure 5.2a. The integrated luminosity of the collision data suitable for physics analyses corresponds to $139\,\mathrm{fb}^{-1}$ [197, 198, 200] for run-II. More information on the conditions defining collision data as suitable for analyses can be found in Reference [200].

Dense bunches of protons are collided at the interaction points by the LHC. As a consequence, there can be multiple proton-proton interactions per bunch crossing [23]. The average number of proton-proton interactions per bunch crossing is denoted by μ [196]. It scales linearly with the luminosity. The distribution of μ is shown in Figure 5.2b for the ATLAS detector during LHC run-II. The average was $\langle\mu\rangle = 33.7$ [199].

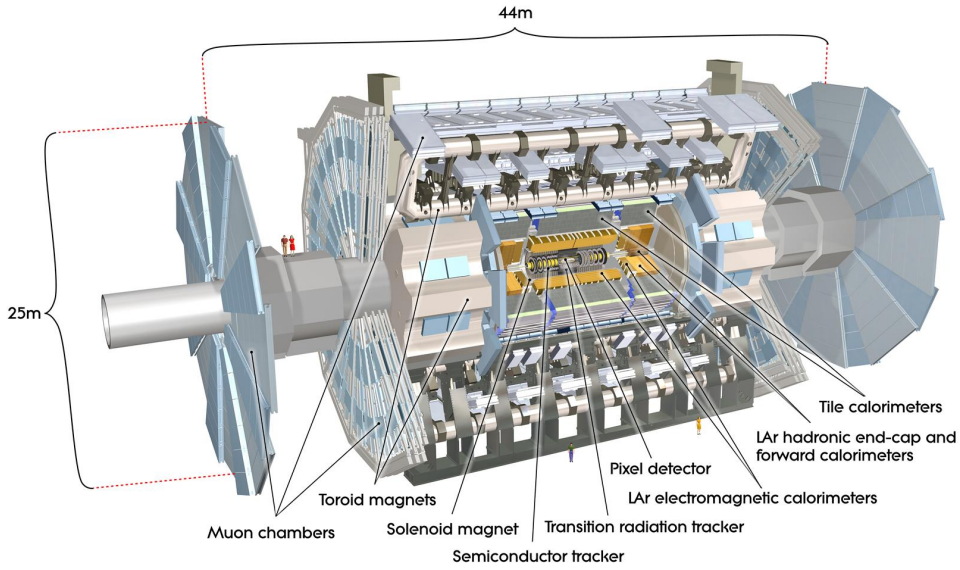

Figure 5.3: Overview of the ATLAS detector [23].

Typically, only the most energetic interaction per bunch crossing, called the hard-scatter, is analysed. Pile-up refers to the additional proton-proton interactions. A higher number of pile-up interactions increases the number of particles depositing energy in the detector. Therefore a higher μ also complicates the process of reconstructing the particles produced in the hard-scatter.

5.2 The ATLAS detector

The aim of the ATLAS experiment [23] is to study the SM and to search for physics beyond it at unprecedented centre-of-mass energies and luminosities. A cylindrically symmetric detector is employed, placed at the so-called interaction point one of the LHC. The ATLAS detector is the largest at the LHC, extending 25 m in height and being 44 m long. Its mass is roughly 7000 t. Figure 5.3 gives an overview of the ATLAS detector.

The sub-detector closest to the beam pipe is the inner detector (ID) [23]. Purpose of the ID is the precise measurement of the trajectory of charged particles, referred to as tracks. A 2 T solenoid magnet surrounds the ID. It bends the trajectory of charged particles, allowing particle momenta to be determined from the tracks.

The calorimeter system surrounds the ID [23]. Its function is to measure the energy of particles. It is divided into the electromagnetic calorimeter (ECAL) and the hadronic calorimeter (HCAL).

The muon system is placed outside of the calorimeters and aims at precise muon momentum measurements [23]. It further provides triggering signals. The muon system consists of gas-filled tracking detectors and large air-coil toroid magnets.

All sub-detectors are split into a central part, the barrel, made of cylindrically layers of instrumentation around the beam-pipe; and two outer parts, the end-caps. The end-caps are placed on the left and on the right of the barrel and consist of disc- or wheel-shaped structures of instrumentation centred around the beam pipe.

5.2.1 Coordinates and variables

The coordinate system is centred at the interaction point within the ATLAS detector [23]. The x-axis points to the centre of the LHC, the y-axis upwards and the z-axis along the beam pipe. Spherical coordinates r, ϕ and θ and the pseudo-rapidity $\eta \coloneqq -\ln\left(\tan\left(\frac{\theta}{2}\right)\right)$ are defined. The beam axis is given by $\eta = \pm\infty$ and the x-y-plane, referred to as the transverse plane, is located at $\eta = 0$. Using η instead of θ is motivated by the roughly even distribution of jets as a function of η [35]; and by the relation of η to the rapidity y. Differences of the rapidity y are invariant under Lorentz boosts in z-direction. For massless particles, $\eta = y$ and thus η can be treated as an approximation of the rapidity y for highly energetic particles.

Angular distances between particles are often of interest. They are commonly measured by the quantity $\Delta R \coloneqq \sqrt{\Delta\eta^2 + \Delta\phi^2}$ [23].

The protons colliding inside of the ATLAS detector only have momentum components in the z-direction. Given the particles emerging from a collision, the sum of their momenta in the transverse plane $\vec{p}_{\mathrm{T}} \coloneqq \begin{pmatrix} p_x & p_y \end{pmatrix}^{\mathrm{t}}$ must therefore yield zero [201]. Some particles, such as neutrinos or hypothetical DM particles, escape the ATLAS detector unimpededly. The transverse momentum sum of all escaping particles can be determined from the total transverse momentum sum having to be zero. It is given by the negative sum of the transverse momenta of all detected particles. This quantity is called missing transverse momentum and in a simplified form given by $\vec{p}_{\mathrm{T}}^{\,\mathrm{miss}} \coloneqq -\sum_{\mathrm{detected}} \vec{p}_{\mathrm{T}}^{\,i}$. It is very important for DM particle searches. The absolute value of $\vec{p}_{\mathrm{T}}^{\,\mathrm{miss}}$ is denoted by $E_{\mathrm{T}}^{\mathrm{miss}} \coloneqq |\vec{p}_{\mathrm{T}}^{\,\mathrm{miss}}|$.

5.2.2 The inner detector

Determining the tracks of charged particles is the function of the ATLAS ID [23]. A precise determination of tracks is desirable for a variety of applications:

- Due to the magnetic field of the solenoid, the momentum of a particle can be measured from a track.
- Tracks can be used to reconstruct the vertices of the proton-proton interactions and of particle decays inside of the ATLAS detector volume. Decay vertex reconstruction plays an important role in the identification of jets containing b-hadrons for example, as discussed further in Section 7.4.3.
- Also important for the identification of jets containing b-hadrons is the so-called perigee point $\vec{p}_0$, which is a property of a track [202, 203]. The perigee point $\vec{p}_0$ is the point of closest approach of a track to the z-axis. It has two commonly used derivations. The transverse impact parameter d_0 is the distance in the transverse plane of $\vec{p}_0$ from the z-axis. The longitudinal impact parameter z_0 is the z-axis coordinate of $\vec{p}_0$. Both d_0 and z_0 are sketched in Figure 5.4.

The ID is comprised, from inner to outer, of the so-called Insertable B-Layer (IBL), the pixel detector, the semiconductor tracker (SCT) and the transition radiation tracker (TRT), as shown in Figures 5.5 and 5.6. With the exception of the TRT, the ID is made of silicon-based detectors.

The IBL

The IBL is the innermost layer of the ID, placed 3.3 cm from the beam pipe in one concentric layer of instrumentation [206, 207]. The aim of the IBL [208], installed in the first long shutdown of the LHC, is to increase the robustness and precision of the tracking, in particular if the number of pile-up interactions is high. The IBL

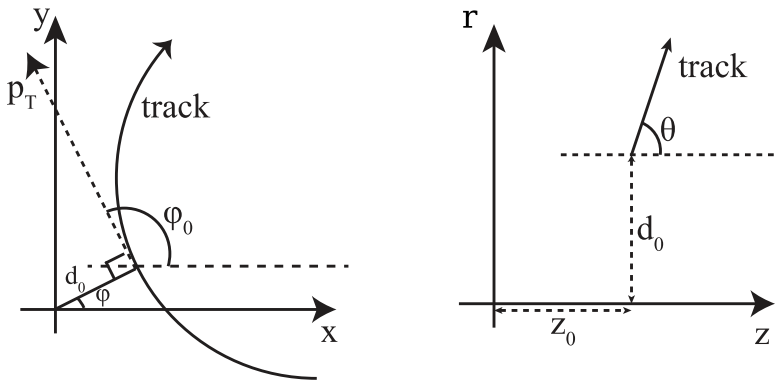

Figure 5.4: Sketch of the transversal impact parameter d_0 (left) and the longitudinal impact parameter z_0 (right). Modified from Reference [204].

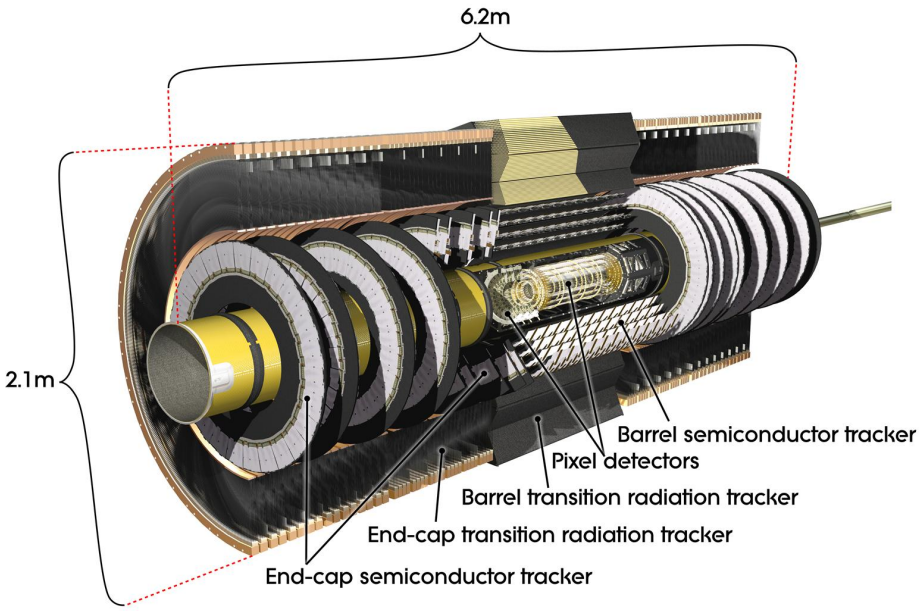

Figure 5.5: Overview of the ATLAS ID [23]. The IBL is not shown in the figure.

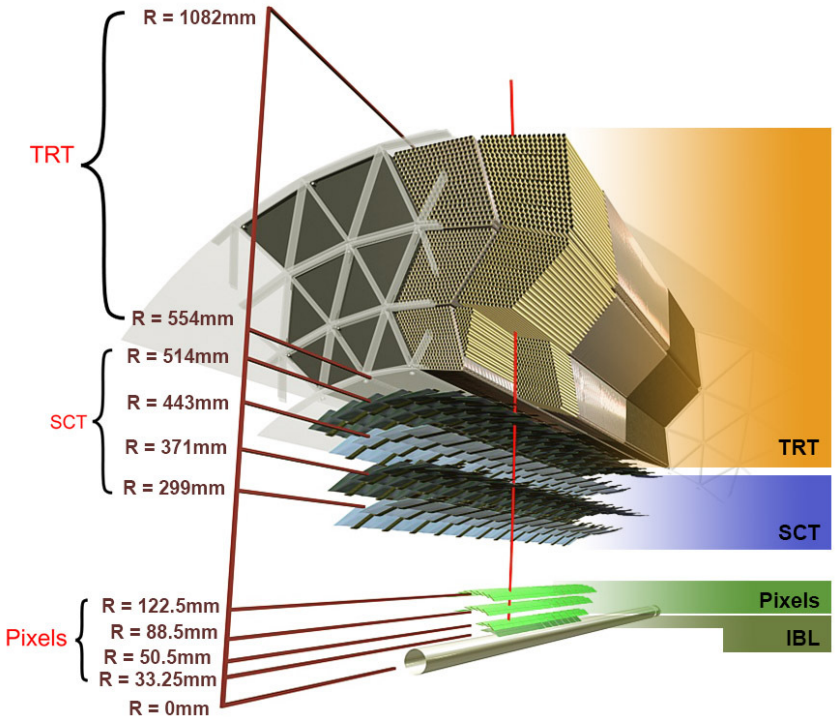

Figure 5.6: Layers of the ID barrel [205].

covers $|\eta| \leq 3$ and uses pixelated silicon sensors with a pitch of 50 µm × 250 µm ($(r-\phi) \times z$). With the installation of the IBL, the impact parameter resolution of the ATLAS detector could be significantly decreased [209].

The pixel detector

The pixel detector is made of three concentric layers of instrumentation in the barrel and of three discs in each end-cap with sensors parallel to the transverse plane [23]. The barrel layers are placed at radii of 50.5 mm, 88.5 mm and 122.5 mm, as shown in Figure 5.6. The discs are located between $|z| = 495\,\text{mm}$–$650\,\text{mm}$ and cover $r = 88.8\,\text{mm}$–$149.6\,\text{mm}$. That gives a coverage of $|\eta| \leq 2.5$ for the pixel detector.

Pixelated silicon sensors are employed by the pixel detector [23]. The pixel pitch is either 50 µm × 400 µm (∼ 90 % of the pixels) or 50 µm × 600 µm. The short side of the pixels is oriented along $r-\phi$ in both the barrel and the end-caps. The intrinsic position resolution of the pixel detector is 10 µm in $r-\phi$ and 115 µm in z (r) in the barrel (end-caps).

The SCT

The SCT uses silicon strip sensors distributed across four layers in the barrel and nine discs in each end-cap [23]. The barrel layers range from $r = 299\,\text{mm}$ to $r = 514\,\text{mm}$ and cover $z < 749\,\text{mm}$, while the discs are placed between $|z| = 853.8\,\text{mm}$ and $|z| = 2720.2\,\text{mm}$. This allows the SCT to cover $|\eta| \leq 2.5$.

Strip modules are rectangularly shaped in the barrel with up to 12 cm long strips aligned in z-direction and trapezoidal shaped in the end-caps with radially oriented strips [23]. The strip pitch of the SCT is 80 µm. A three-dimensional coordinate is

obtained by the SCT by installing two strip sensors back-to-back at a stereo angle of 40 mrad. The intrinsic position resolution of the SCT is 17 µm in $r-\phi$ and 580 µm in z (r) in the barrel (end-caps).

The TRT

The TRT is made of gas flooded straw-tube detectors with a diameter of 4 mm [23]. The length of the tubes is 144 cm in the barrel and 37 cm in the end-caps. The tubes are aligned parallel to the beam pipe in the barrel and radially in the end-caps. The TRT covers $|\eta| \leq 2$. Only $r \times \phi$ ($\phi \times z$) coordinates of traversing charged particles are determined by the TRT in the barrel (end-caps). The position resolution per straw-tube in the TRT is 130 µm [23, 210]. This much worse resolution compared to the other parts of the ID is largely mitigated by a particle traversing at least 22 straw-tubes.

Besides offering position information, the TRT can also aid the identification of charged particles by exploiting transition radiation [23]. Particles traversing polypropylene fibres (foils) in the barrel (end-caps) produce this transition radiation. Its intensity is proportional to $\gamma = \frac{E}{mc^2}$ [211]. If additionally measuring the energy of the traversing particle, its mass can be calculated from the transition radiation and the particle can be identified.

5.2.3 The calorimeter system

While measuring the momentum, the ID does not provide any information about the energy of a particle. To identify a particle by its four-momentum square, this information is however needed. Calorimeters are energy measurement devices. Particles entering a calorimeter produce a cascade ("shower") of secondary particles [211]. These loose energy via ionisation or other processes and are finally stopped. By measuring the amount of charge induced by the ionisation for example, the energy of the incoming particle can be determined.

The ATLAS detector uses so-called sampling calorimeters for energy measurements [23]. Sampling calorimeters are comprised of alternating layers of absorber and active materials [211]. Particle showers are produced in the absorber material layers and the charge induced by ionisation for example is measured in the active material layers.

An overview of the calorimeter system in the ATLAS detector is given in Figure 5.7 [23]. It covers $|\eta| \leq 4.9$. Electron and photon energy measurements are the primary target of the ATLAS ECAL, while the main purpose of the ATLAS HCAL is hadron energy measurements. The calorimeter components are described in the sequel.

The ECAL

Lead and liquid argon comprise the absorber and active material of the ATLAS ECAL [23]. An incoming electron or photon produces bremsstrahlung photons or an electron-positron (e^+e^-) pair in the absorber, respectively [211]. These again produce bremsstrahlung photons and e^+e^--pairs, resulting in an electromagnetic shower. Ionisation produced by this shower in the liquid argon is registered by electrodes.

The ECAL barrel covers $|\eta| < 1.475$. It is surrounded by two end-caps. The end-caps extend the coverage in the area $1.375 < |\eta| < 3.2$ [23]. Calorimeter cell sizes range between 0.025×0.025 and 0.1×0.1 in $\eta \times \phi$ in the ECAL. The structure of the absorber material and of the electrodes is accordion like, allowing for a crackless coverage in ϕ. A so-called pre-sampler is installed in the area of $|\eta| < 1.8$ to

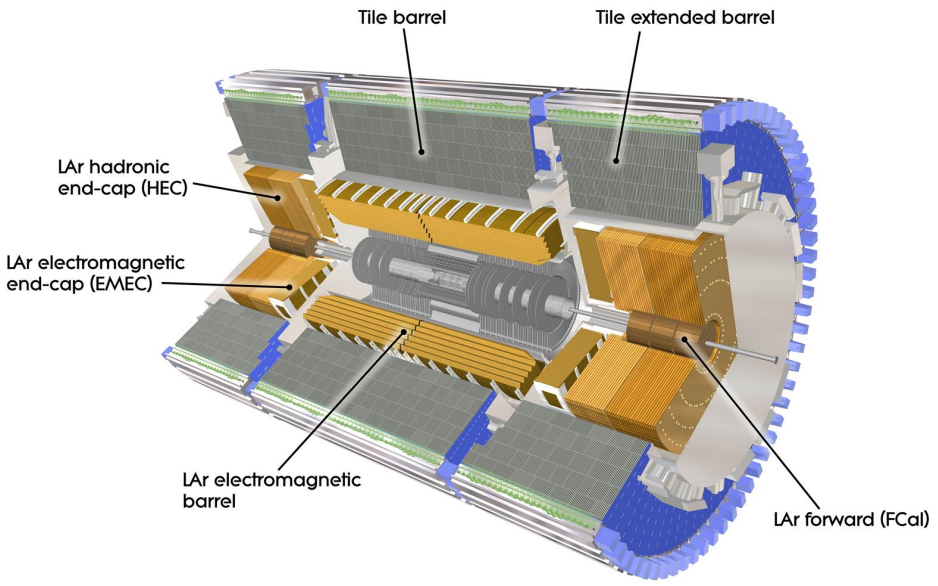

Figure 5.7: Overview of the calorimeter system of the ATLAS detector [23].

estimate the energy a particle lost before reaching the ECAL [23]. One layer of liquid argon and read-out electrodes make up the pre-sampler.

The radiation length X_0 gives the average distance a highly energetic electron traverses a material before having lost $1 - 1/e$ of its energy because of bremsstrahlung [211]. The radiation length is also $7/9$ of the mean free path of a high energy photon before converting to an electron-positron pair in a material. To contain electromagnetic showers initiated by electrons and photons over a wide energy range as completely as possible, it is desirable for the thickness of the ECAL to be a high multiple of X_0. The material in the ECAL sums to $22 \cdot X_0$ or more [23].

The HCAL

Since hadrons can interact via the strong interaction, hadronic showers are much more complex than electromagnetic ones, involving the production of other particles like pions and kaons, electromagnetic showers, the excitation of nuclei, etc. [35, 211]. The HCAL has been designed to precisely measure the energy of hadrons [23]. Different materials are used in hadronic calorimeters compared to electromagnetic calorimeters, accounting for the different nature of hadronic showers.

Steel and scintillating tiles comprise the absorber and active material of the ATLAS HCAL in the barrel and in the so-called tile extended barrel [23]. The light produced by the hadronic showers in the tiles is transported to photomultipliers via wavelength shifting fibres. Together, the HCAL barrel and tile extended barrel cover $|\eta| \leq 1.7$.

A hadronic end-cap calorimeter (HEC) is installed behind each of the two ECAL end-caps [23]. Copper is used as absorber and liquid argon as active material. It covers $1.5 < |\eta| < 3.2$.

A forward calorimeter (FCal), comprised of three layers, is also located in the calorimeter end-caps [23]. The first layer employs copper as absorber material, while the remaining two use tungsten. All three layers employ liquid argon as active material. The aim of the first layer is electromagnetic calorimetry, while the

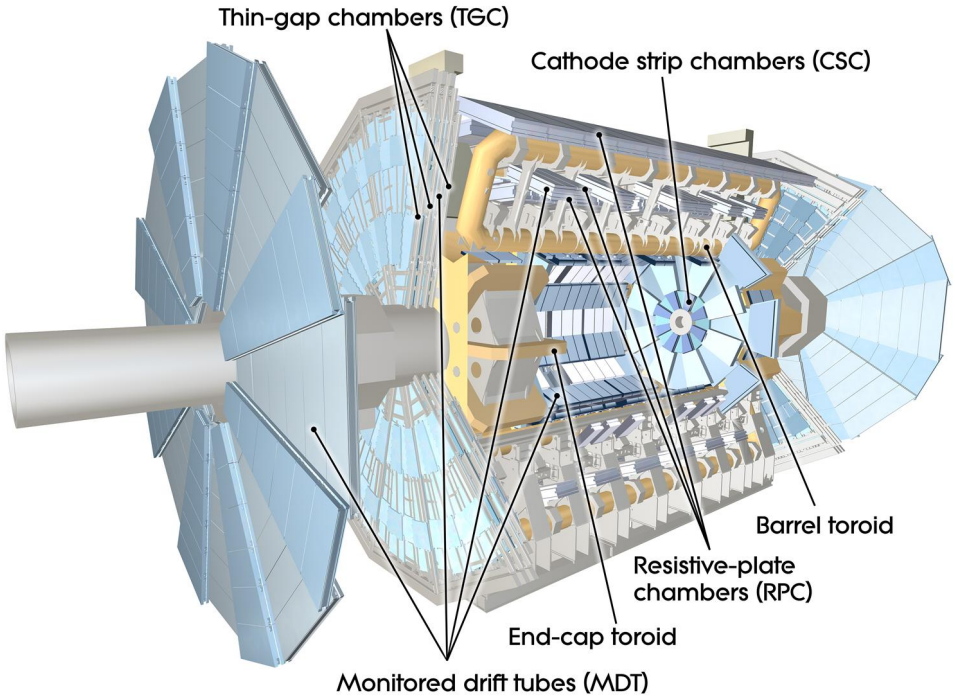

Figure 5.8: Overview of the ATLAS detector muon system [23].

latter two target hadronic calorimetry [212]. The FCals covers $3.1 < |\eta| < 4.9$.

The average distance a highly energetic hadron travels in a material before interacting inelastically with a nucleus is given by the absorption length λ [211]. To capture a large part of the hadronic showers and to prevent punch-throughs to the muon system, the thickness of the calorimeter system ought to be a high multiple of λ [23]. In the ATLAS detector, the muon system is shielded at $|\eta| = 0$ by more than 11λ of which more than 9.7λ are available for energy measurements.

5.2.4 The muon system

Goal of the muon system is the measurement of muon momenta and the generation of triggering signals [23]. It is installed outside of the calorimeter system, which muons can traverse due to their relatively small energy loss in matter.

The muon trajectories are bent by a toroid magnet system, comprised of a barrel and two end-caps [23]. The superconducting toroid magnets generate a magnetic field which is mostly perpendicular to the possible muon tracks. Thanks to the air-core of the toroids, the amount of multiple scattering is kept minimal, which is beneficial for the resolution of the muon momentum measurement.

Gas-filled tracking detectors are installed in three layers in the muon system barrel and in four layers in the end-caps [23]. Aim is to provide position information to measure the muon momentum and to obtain information for the trigger. The triggering components cover $|\eta| < 2.4$, while the tracking units provide coverage over $|\eta| < 2.7$. All triggering devices are used to complement the position information of the tracking components. An overview of the muon system of the ATLAS detector is shown in Figure 5.8.

In the barrel of the muon system, chambers of monitored drift tubes (MDTs) are installed for the purpose of tracking in concentric layers at radii of 5 m, 7.5 m and 10 m from the beam pipe [23]. At the outer two radii, resistive plate chambers

(RPCs) are mounted, too, which are used for triggering and to complement the position information of the MDTs.

An MDT chamber is made of three to eight layers of 3 cm drift tubes [23]. A tube has a spatial resolution of 80 µm resulting in a resolution per chamber of ~ 35 µm. RPCs consist of two resistive plates, enclosing a gas. Strips are installed on the outsides of the plates, perpendicular in orientation between the two plates. Penetrating muons ionise the gas and this induces a signal on the strips.

Four wheels at $|z|$-coordinates of 7.4 m ("small wheel"), 10.8 m, 14 m ("big wheel") and 21.5 m make up the end-caps of the muon system [23]. MDT chambers are used at high radii in the wheel closest to the interaction point for tracking. At low radii, covering $2 < |\eta| < 2.7$, cathode strip chambers (CSCs) are used instead of MDT chambers. MDTs would saturate at the high rates present in this range of $|\eta|$. One layer of thin gap chambers (TGCs) is placed in front of the MDT chambers in the first wheel for the sake of triggering and to complement the position information of the tracking devices. MDT chambers for tracking and multiple layers of TGCs for triggering are installed in the third wheel with respect to the interaction point. The second and fourth wheel consist of tracking MDT chambers only.

A CSC is a multi-wire proportional chamber [23]. Strip-segmented cathodes are used on either side of the strips, with the strips being oriented in orthogonal directions. Only the strips are read out. The CSCs are installed such that the wires are oriented radially. CSCs provide a resolution of 40 µm in r and 5 mm in ϕ. TGCs are also multi-wire proportional chambers. A three dimensional position information is obtained by reading out wires (r-coordinate) and pick-up strips (ϕ-coordinate). TGCs have a high time resolution of 4 ns and a spatial resolution of 2 mm–7 mm.

5.2.5 Trigger system

Bunch crossings occur up to every 25 ns or at rates up to 40 MHz at the ATLAS detector [23]. The amount of data produced by this high rate of bunch crossings exceeds the storage capabilities of the ATLAS detector. In addition, the majority of bunch crossings feature only low proton-proton momentum transfers and are therefore not of interest to most physics analyses. A selection system, called trigger system, is employed to only store data from bunch crossings with interesting outcomes and to reduce the amount of data written to disc.

It is split into two steps [213, 214]. Collision events are first filtered by the Level-I trigger (L1 trigger) and then by the high-level trigger (HLT). Signals from the muon trigger chambers and calorimeters are employed by the hardware-based L1 trigger among information from smaller sub-detectors. It identifies events in a fast way in which e.g. electrons, muons, jets, etc. are produced [23]. For a selected event, region-of-interests (ROIs), containing the geographical information relevant for the selection by the L1 trigger, are output. The rate of events to be considered for storage is decreased to at most 100 kHz by the L1 trigger. The second step of the trigger chain is the HLT, which processes events accepted by the L1 trigger. While the L1 trigger only uses information from a subset of the ATLAS detector, the software based HLT can employ information from the whole detector. A more elaborate analysis of an event is performed by the HLT, also using particle reconstruction techniques similar to the ones described in Chapter 7. The average acceptance rate of the HLT is 1.2 kHz, corresponding to a data rate of $1.2\,\mathrm{GB\,s^{-1}}$ being written to disc [214].

Chapter 6

Event simulation

Simulated proton-proton interaction events are used in the search for DM particles presented in Chapters 8-12. They are employed to construct kinematic phase space regions enhanced in signal events, to estimate contributions from background events and to evaluate systematic uncertainties.

The event simulation emulates the proton-proton interactions in the detector with the goal of predicting the emerging particles, their kinematics and the detector response. Its theoretical foundation is the SM described in Chapter 2 and, if simulating events involving BSM physics, the corresponding model. Due to the complexity of the integrals emerging from the QFT calculations and the difficulty of evaluating some of the occurring random variables, Monte Carlo (MC) techniques are employed in the simulation [25].

A general overview of the event simulation is given in the following section. Specific parts of the simulation are described in more detail thereafter.

6.1 Overview of the event simulation

Figure 6.1 sketches the typical particles simulated in the simulation of a proton-proton interaction event [215]. The dark green ellipses illustrate incoming protons and their respective PDFs. Partons emerge from these protons and are indicated by the dark blue lines. These partons interact. The most energetic interaction of the partons, yielding the process of interest, is marked by the dark red dot. The outgoing particles produced in this hard parton scatter are indicated by light red lines and are two top-quarks, a Higgs-boson and a gluon in this sketch. The top-quarks and the Higgs-boson decay into lighter quarks and bosons at the light red dots. As discussed in Section 2.5, the cross-section of producing some final state X in a proton-proton interaction can be calculated by employing the parton distribution functions (PDFs) and the cross-sections $\sigma_{i,j\to X}$ of the partons i and j producing X. The cross-sections $\sigma_{i,j\to X}$ can be calculated by integrating the matrix elements, derived from the corresponding Feynman diagrams, over the phase space [62]. The matrix elements are computed at a fixed order in perturbation theory, e.g. at next-to-leading order (NLO). They allow generating the hard-scatter event which contains all of the particles described up to this stage.

Higher order emissions and (gluon or photon) splittings to the finite order hard-scatter events are accounted for by the parton showering [25]. The radiations and splittings are denoted as final state radiation (FSR) if affecting the outgoing particles from the hard-scatter, and as initial state radiation (ISR) if affecting the incoming partons. The radiations and gluon splittings added by the parton showering are illustrated by light red and dark blue lines in Figure 6.1. The parton

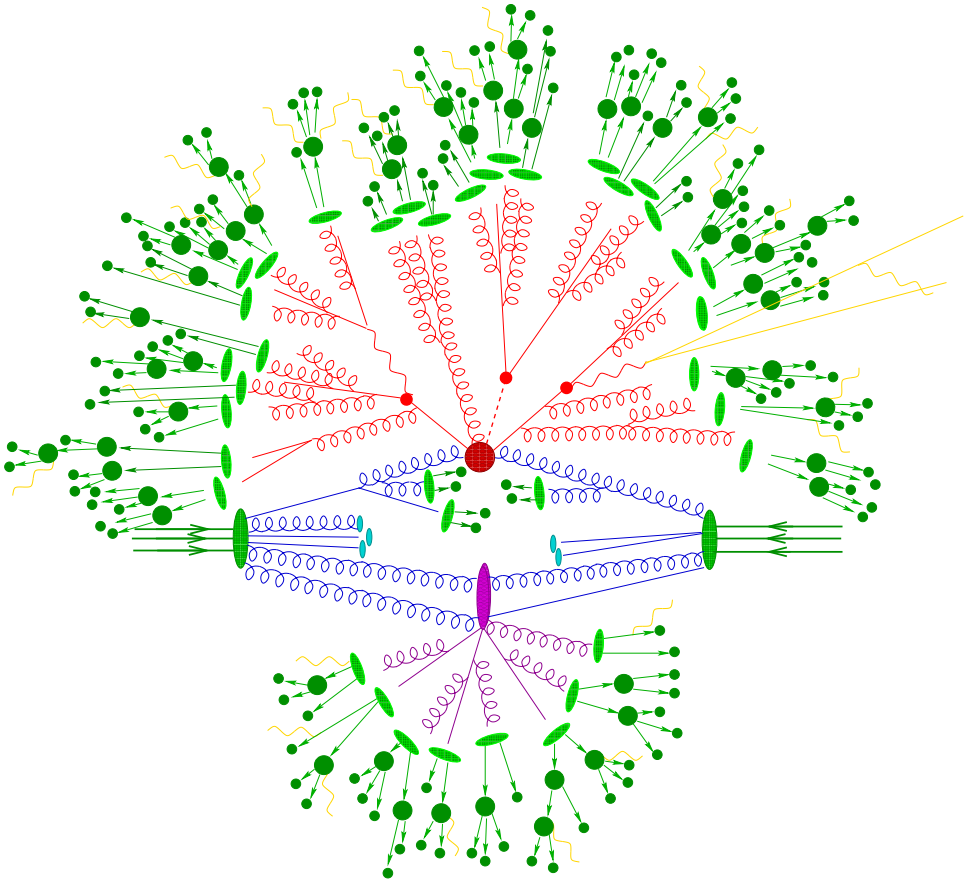

Figure 6.1: Event simulation illustration of a $t\bar{t} + h$ event [215]. Partons from the protons and the ISR are shown by dark blue lines. The large dark red circle indicates the most energetic parton interaction. The emerging particles decay at the light red circles. Outgoing particles from these decays and final state radiation (FSR) partons are indicated by light red lines. Resulting hadrons are illustrated by light green ellipses and their decays in dark green. Photon and leptons are drawn in yellow. Additional parton-parton interactions (purple ellipsis) and the hadronisation of further proton remnants (light blue ellipses) form the underlying event.

showering is described in more detail in Section 6.2.

The output of the parton showering are multiple particles, among them individual quarks and gluons. Due to the QCD confinement discussed in Section 2.4, quarks cannot be observed individually. Instead, hadrons are observed in the detector and these are highlighted by the light green ellipses in Figure 6.1. The formation of hadrons is modelled in the hadronisation step of the simulation [25], described in Section 6.4.

Not all of the hadrons that are formed are stable, i.e. they may decay before passing through the sensitive detector volume [25]. Likewise, the τ-lepton is not stable. The decays of instable particles are also accounted for in the simulation and the decay products are indicated in Figure 6.1 by the dark green circles.

Several parton interactions can occur in a proton-proton interaction [25]. They are simulated by the so-called underlying event simulation and are indicated by the purple ellipsis with the outgoing partons, hadrons and hadron decay products in the figure. Further proton remnants and the hadrons they form, illustrated by the light blue ellipses, are also accounted for by the underlying event simulation. More details on the underlying event are given in Section 6.3.

The previously described steps of the simulation yield the energies, momenta, and spatial coordinates of hadrons, leptons, and, if applicable, BSM particles, which propagate through the detector. This stage of the event simulation is called particle level. To emulate the signals produced by these particles in the ATLAS detector, a dedicated detector simulation is used. Events from simultaneous proton-proton interactions in the detector are also accounted for in this step of the simulation. The detector simulation is discussed in Section 6.6.

6.2 Parton showering and matching

The parton shower accounts for higher order perturbative corrections to the hard-scatter event obtained from fixed order matrix elements [62]. It adds low-energetic (soft) and small-angle (collinear) particle emissions to the incoming and outgoing particles of the hard-scatter [25]. For simplicity, only quark and gluon emissions are discussed here. The reader is referred to Reference [25] and references therein for the treatment of electroweak emissions.

The parton emissions and gluon splittings accounted for by the parton shower are added according to an evolution scale [62]. This scale can e.g. be proportional to the square of the angle θ between the original particle and the emitted one. For each particle that is outgoing from the hard-scatter, the parton showering iteratively constructs a tree of radiations and splittings, reducing the evolution scale from step to step. The cross-section of additional radiations and gluon splittings increases as the evolution scale decreases. For example, if the evolution scale is proportional to θ^2, the probability of producing a collinear emission increases as θ^2 decreases. To avoid the resulting divergences, a cut-off parameter Λ is introduced at which the parton showering stops. Introducing Λ is also physically motivated: very collinear radiation for example, yielding two very close by particles, may not be resolvable. Other models are used to describe the evolution of the quarks and gluons at lower scales, see Section 6.4.

The technical working principle of the parton shower is as follows [25]. For each quark or gluon at the scale Q^2, the parton shower probabilistically estimates the scale q^2 of the resulting particles if emitting a gluon or if the gluon splits into two quarks. The probability depends on the Sudakov form factors [25]. If the scale q^2 of the resulting particles is above the cut-off scale Λ, typically $\Lambda \simeq 1\,\text{GeV}$, then the additional gluon emission or gluon splitting is accepted. The parton showering continues to add emissions and to split gluons of the resulting particles. Additional

radiations or splittings are not added to the parton if $q^2 < \Lambda$.

Gluon emissions and splittings are also considered for the partons incoming to the hard-scatter [25]. In this case, the evolution of emissions and splittings is propagated from the hard-scatter partons backwards until obtaining the partons emerging from the proton. This reversed approach is used because of computational benefits [62]. As dealing with proton constituents, this modelling of the ISR depends on PDFs.

Parton showering algorithms are constructed to be precise for collinear and soft emissions [62]. Harder and wider-angle radiations are more accurately modelled if including additional partons in the final state in the matrix element calculations used for the hard-scatter event. To achieve the best accuracy for extra radiations, it is therefore beneficial to combine both techniques. Combining them is however not trivial and dedicated matching algorithms are used to do so, for example parts of the phase space may be accounted for twice. Common methods used for the matching are `CKKW` [216], `MC@NLO` [217] and `Powheg` [218].

6.3 Underlying event simulation

The underlying event is further activity in a proton-proton interaction event not covered by the hard-scatter and parton shower [25]. Additional parton-parton interactions contributing to the underlying event are described by the so-called multiple parton-parton interaction (MPI) model. In this model, the additional parton interactions originate primarily from t-channel diagrams featuring the exchange of a gluon. While they may lead to the production of jets, the more sizeable consequence is the correction of global event quantities, such as the number of hadrons.

6.4 Fragmentation and hadronisation

Parton showering algorithms add particle radiations and gluon splittings to a hard-scattering event down to a cut-off scale Λ [62]. Beyond this scale, perturbative calculations as used in the matrix elements and in the parton shower cannot be employed any more. Instead, phenomenological fragmentation models are used to describe the formation of hadrons from the partons output by the parton showering as necessitated by QCD confinement. The Lund string model [48] and the cluster model [219] are introduced here.

The string model exploits that the potential $V(r)$ between two quarks, spatially separated by the distance r, can be described by $V(r) = \kappa r$, i.e. it increases with the distance [25]. Interactions between quarks are described by a string, which's tension increases as the quarks are spatially separated, until the energy stored is sufficient to create a quark-antiquark pair, as depicted in Figure 2.3 on page 10. The string is then split into two strings, with a quark and an antiquark on the respective ends of the new strings. In the string model, the string splitting continues until the invariant mass of a quark-antiquark pair is in the order of the mass of some meson. The production of baryons can also be incorporated into the string model, e.g. by allowing for the production of two quark-antiquark pairs in a string splitting.

In the first step of the cluster model, all gluons output by the parton showering are decayed into a quark-antiquark pair [25]. Quark-antiquark pairs are subsequently defined as a cluster. These clusters are iteratively split, until the energy of all clusters is below 3 GeV–4 GeV. Mesons and excited mesons are formed from the final clusters and the exited mesons are forced to decay, giving the final set of hadrons.

6.5 Process simulation programs used in the ATLAS experiment

Multiple programs are used by the ATLAS experiment for the generation of simulated events. The most common programs are introduced in the following.

The MadGraph5_aMC@NLO [220] and PowHeg-Box [218, 221, 222] programs allow for the calculation of matrix elements and cross-sections up to NLO precision and the generation of hard-scatter events. They use the `MC@NLO` [217] and `Powheg` [218] methods, respectively, for the parton shower matching.

Pythia [223], Herwig [224, 225] and Sherpa [215, 226] are multi-purpose event generators, which can calculate matrix elements, cross-sections and generate hard-scatter events, as well as perform the parton showering, hadronisation, hadron and τ-lepton decays as well as the underlying event simulation. Pythia and Herwig are mainly used for the parton shower, hadronisation and underlying event simulation in this thesis. Pythia uses the string model for the hadronisation, while Herwig uses the cluster model. Sherpa is used with all of its functionalities. It supports the calculation of matrix elements up to NLO precision and uses the cluster model for the hadronisation [227].

Due to the multiple parameter dependencies of the different simulation programs, the predictions obtained from the programs are compared to data and the parameters are tuned such that the predictions and the data agree [25]. Sets of tuned parameters are published for each of the multi-purpose event generators.

6.6 Detector simulation

The final particles output by the simulation programs described in Section 6.5 are processed with the ATLAS detector simulation [228] to obtain an emulated detector response. Firstly, the energy depositions of the particles in the sensitive volumes of the detector are estimated using the `Geant4` framework [229]. Energy deposits accounting for the impact of pile-up interactions and other effects, such as beam-gas, are overlaid. The combined energy depositions are then transformed into electric signals and digital output signals for all of the detector components. This then provides an emulation of the output of the detector with respect to the simulated event.

`Geant4` derives the energy deposits in a very detailed manner and is computationally expensive, particularly to simulate the calorimeter response [228]. Therefore, the computationally less expensive version `AF2` of the detector simulation software was developed, employing a parametrised approximation of the shower profile in the calorimeters, with the drawback of degraded spatial calorimeter information. Samples using the full and the `AF2` detector simulation are employed in the analysis presented in this thesis.

6.7 Simulated samples

Multiple samples of simulated events are used in the analysis presented in this thesis. The software used to generate these samples is described in this section.

To generate 2HDM+a model samples, the Feynman rules of the model have to be known. They are implemented in a Universal FeynRules Output (UFO) [230] file, produced with the `FeynRules 2` [231] and `NLOCT` [232] packages and provided [233] by the authors of Reference [14]. Using the UFO, the 2HDM+a model tW+DM signal samples are produced at LO accuracy in the matrix element with MadGraph5_aMC@NLO v2.6.2 and v2.7.3 [220] interfaced to Pythia v8.212 [234, 235]

and v8.244, respectively. The NNPDF3.0 [236] five-flavour scheme[1] set of PDFs, accurate to NLO, is input into MadGraph5_aMC@NLO. MadSpin [238, 239] is used to model top-quark decays, thereby retaining spin-correlations and effects due to the finite decay width. Pythia is used for the parton showering, hadronisation and underlying event simulation. The LO accurate NNPDF2.3 [240] set of PDFs as well as the A14 parameter tune [241] are input to Pythia. EvtGen v1.6 and v1.7 [242] are used for the decays of heavy flavour hadrons. The total cross-section output by MadGraph5_aMC@NLO is used to normalise the generated events. For those signal samples generated with MadGraph5_aMC@NLO 2.7.3, the reweighting technique described in Reference [243] is used to obtain samples with $\tan\beta = 0.3$–3 and $\sin\theta = 0.35$ or 0.7 from samples generated with $\tan\beta = 1$ and $\sin\theta = 0.35$.

Furthermore, 2HDM+a model $t\bar{t}$+DM signal samples are used in the analysis presented in this thesis. These samples are produced by reweighting and merging samples [15, 173] generated for the simplified DM model with a pseudoscalar mediator [154–158] introduced in Chapter 4. The dominant Feynman diagrams in the simplified model contributing to the $t\bar{t}$+DM signature are equivalent to the 2HDM+a model diagrams shown in Figure 4.5. They do not contain A-boson contributions however and just feature the pseudoscalar mediator a, which is produced in association with a $t\bar{t}$ pair and decays into DM particles. In the 2HDM+a model, diagrams featuring the associated production of a $t\bar{t}$ pair and an A-boson decaying into DM particles must be additionally accounted for. An approximate 2HDM+a model $t\bar{t}$+DM signal sample can be obtained from a simplified model sample by following procedure [15, 173]:

- For each combination of m_a, m_A, $\tan\beta$ and $\sin\theta$ for which a 2HDM+a model sample is to be produced, two simplified model samples with a mediator mass of m_a and m_A, respectively, are generated.
- The cross-section of each of the simplified model samples is normalised to the cross-section of the 2HDM+a model $t\bar{t}$+DM production, where either only the a-boson or the A-boson decays to DM particles. To be explicit, the cross-section $\sigma_{\text{Simp}}(m_\alpha)$ of the simplified model sample generated with mediator mass m_α is multiplied by the factor $\sigma^{\alpha\to\chi\bar{\chi}}_{\text{2HDM+a}}(m_a, m_A, \tan\beta, \sin\theta)/\sigma_{\text{Simp}}(m_\alpha)$, with either $\alpha = a$ or $\alpha = A$. The expression $\sigma^{\alpha\to\chi\bar{\chi}}_{\text{2HDM+a}}(m_a, m_A, \tan\beta, \sin\theta)$ denotes the 2HDM+a model cross-section of the $t\bar{t}$+DM signature where exclusively the α-boson decays to DM particles.
- The two reweighted simplified model samples are merged and yield the final 2HDM+a model sample.

The simplified model $t\bar{t}$+DM samples are produced at LO accuracy in the matrix element using MadGraph5_aMC@NLO v2.7.3 [220] including up to one additional parton emission in the final state. The hard-scatter events are interfaced to Pythia 8.244 [234, 235] for the parton shower, hadronisation and underlying event simulation. The PDFs and tuning sets are equal to the ones employed for the tW+DM signal. As for the tW+DM signal, MadSpin [238, 239] is used to model the top-quark decays. The UFO [156, 244] found in the link in Reference [245] is employed to produce the simplified model $t\bar{t}$+DM samples. The simplified model cross-sections are derived with MadGraph5_aMC@NLO and the version proposed in Reference [246]. They are accurate to NLO. The 2HDM+a model cross-sections are calculated at LO with MadGraph5_aMC@NLO v2.7.3 [220].

The software setup for the simulation of SM processes[2] is summarised in Table 6.1. Except for the $t\bar{t}t$ and $t\bar{t}t\bar{t}$ processes, which use the NNPDF3.1 PDF set [236], all

[1] The five-flavour scheme considers PDFs for all quarks except for top-quarks [237].
[2] Explanations of the different SM processes can be found in Chapter 8.

Process	Event generating program (GEN)	GEN PDF accuracy	PS	PS tune	Total cross-section accuracy
$t\bar{t}$ [252]	PowHeg-Box v2 [218, 221, 222, 257]	NLO	Pythia 8 [235]	A14	NNLO + NNLL[258–264]
Single top quark	PowHeg-Box v1 & v2 [265–267]	NLO	Pythia 8	A14	NNLO + NNLL [268–271]
$t\bar{t}+V$ [272]	MadGraph5_aMC@NLO v2.3.3 [220]	NLO	Pythia 8	A14	NLO [273]
V+jets [274]	Sherpa 2.2.1 [215, 226, 275–278]	NNLO	Sherpa	Sherpa	NNLO [279, 280]
VV [281]	Sherpa 2.2.1 & 2.2.2	NNLO	Sherpa	Sherpa	NLO
Triboson [281]	Sherpa 2.2.2	NNLO	Sherpa	Sherpa	NLO
tZ, $tWZ(\to \ell\ell)$	MadGraph5_aMC@NLO v2.3.3	NLO	Pythia 8	A14	NLO
$tWZ(\to \nu\nu)$	MadGraph5_aMC@NLO v2.6.7	NLO	Pythia 8	A14	NLO
$t\bar{t}+h$ [255]	PowHeg-Box v2 [282]	NLO	Pythia 8	A14	NLO
$t\bar{t}t$, $t\bar{t}t\bar{t}$	MadGraph5_aMC@NLO v2.2.2	NLO	Pythia 8	A14	NLO [220, 283]

Table 6.1: Software setup used to generate simulated events of SM processes. "GEN" abbreviates the program generating the matrix element and the hard-scatter events, while "PS" abbreviates the program used for parton showering, hadronisation and the underlying event simulation. A single "V" indicates a Z- or W-boson. All PDFs used by the GENs are provided by the NNPDF collaboration [236]. If given without a reference, the total cross-section of a process is taken directly from the program simulating the hard-scatter event.

programs simulating the hard-scatter event use the NNPDF3.0 PDF set [236]. For all SM samples, parton showering, hadronisation and underlying event simulation are carried out either by Pythia 8 [235] or by Sherpa [226]. The A14 tune [241] is utilised for all samples for which Pythia is used for the parton showering, hadronisation and underlying event simulation. For these samples the LO NNPDF2.3 [240] set of PDFs is input to Pythia. For the samples generated with Sherpa, the Sherpa parton showering [216, 247–250], employing the NNPDF3.0 PDF set [236] and the standard tuning are used. Decays of b- and c-hadrons are simulated with EvtGen [242] for samples not generated with Sherpa. The total cross-sections of the SM processes are either obtained from the program calculating the matrix element or from another program as indicated by the references in Table 6.1.

As the tW process, i.e. the associated production of a top-quark and a W-boson, is simulated at NLO, it interferes with the $t\bar{t}$ process [251]. Doubly resonant diagrams, which can be regarded as LO $t\bar{t}$ Feynman diagrams where one of the top-quarks (on-shell or virtual) decays into a W-boson and a b-quark, cause interference. To avoid these interferences, two procedures, the diagram removal [251] and diagram subtraction [251, 252] procedures are used, with diagram removal being the nominal choice. In the diagram removal procedure, the interfering diagrams are removed from the tW amplitudes. In the diagram subtraction procedure, the tW cross-section is modified to account locally for the interference. Neither procedure gives an accurate prediction of the tW process cross-section. Rather, the predictions from the two procedures appear to bracket the data in tW enriched regions, as is discussed in Section 10.1.3. In the analysis presented in this thesis, the tW prediction is corrected to obtain a more accurate prediction. In addition, samples are generated for both the diagram removal and diagram subtraction and differences are accounted for as a systematic uncertainty as described in Section 10.3. A diagram removal scheme is also employed for the tWZ process [252–255], removing interference with the $t\bar{t}+Z$ process.

Multiple proton-proton interactions can occur per bunch crossing in addition to the hard-scatter. Energy deposits from these pile-up interactions are added to all simulated events in the detector simulation step. The additional interactions are simulated with Pythia 8.186 [234, 235]. The NNPDF2.3 PDF set [240] accurate to LO is input to Pythia together with the A3 set of tuned parameters [256] for the generation of pile-up events.

Chapter 7

Particle reconstruction

Hadrons and charged leptons traversing the ATLAS detector induce signals in the sensitive detector volume. Compound physics objects, such as charged particle tracks, electrons, muons, τ-leptons, jets, and missing transverse momentum, are reconstructed by combining signals from individual sub-detectors using specialised algorithms.

The sub-detectors that are used to reconstruct the different objects are shown in Figure 7.1. Trajectories of charged particles (tracks) are reconstructed with the

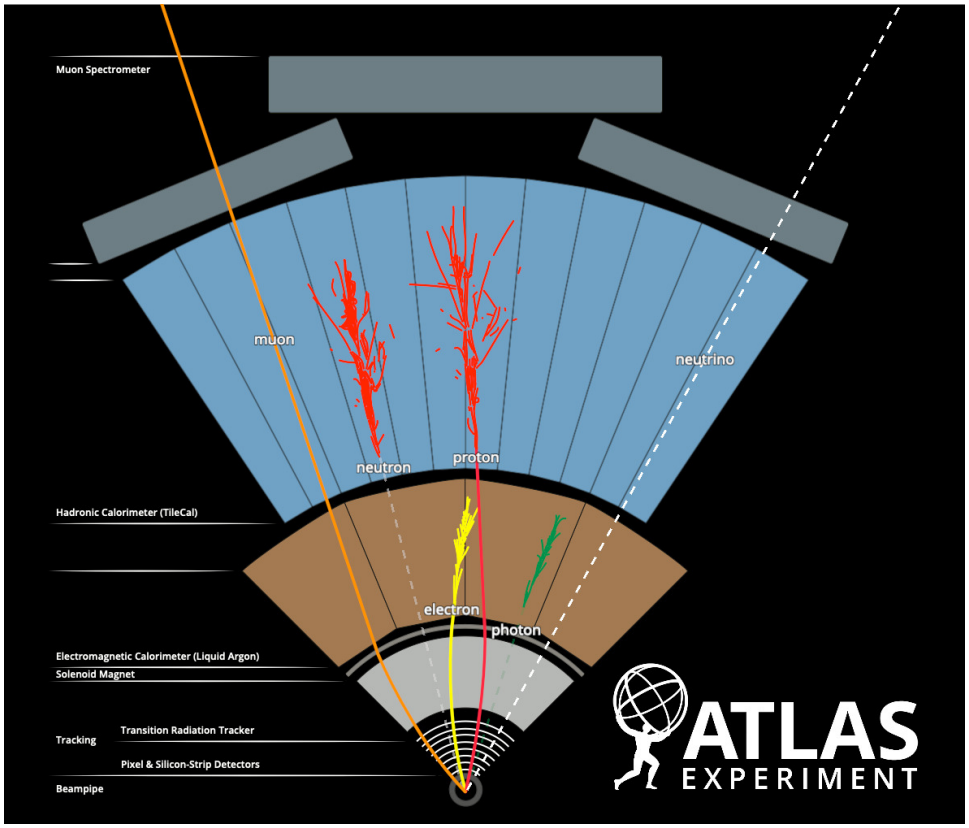

Figure 7.1: Energy deposits by different particles in the ATLAS detector. Copyright: CERN.

inner detector (ID) [284]. Muons are typically reconstructed with measurements provided by the ID and the muon system [285]. Electrons are identified by a track

in the ID and energy deposits in the electromagnetic calorimeter (ECAL) [286]. Photons are reconstructed from energy deposits in the ECAL which do not have associated tracks.

Jets, i.e. hadron sprays resulting from the hadronisation of quarks and gluons, yield multiple tracks in the ID and energy deposits in the calorimeters. In the ATLAS detector, jets are reconstructed as a whole rather than reconstructing the individual hadrons.

Besides the described objects, multiple others are used in the analysis presented in this thesis. Jets containing b-hadrons (b-jets) are identified by exploiting properties of b-hadron decays [203]. Jets covering a large angular area (large-radius jets [287]) may contain the decay products of hadronically decaying high-p_{T} W-bosons. Using W-tagging techniques [288], such large-radius jets can be distinguished from large-radius jets formed by other particles, as detailed in Section 7.4.5. Finally, weakly interacting particles, such as neutrinos or DM particles, yield missing transverse momentum ($E_{\mathrm{T}}^{\mathrm{miss}}$, see Section 5.2.1) in an event [201]. The $E_{\mathrm{T}}^{\mathrm{miss}}$ is calculated by using all reconstructed objects as described in Section 7.5.

Different objects reconstructed in an event can use the information from the same energy deposits. To avoid having two different objects reconstructed from the same energy deposits, a dedicated overlap removal procedure is used. Furthermore, in accordance with the objects expected from the 2HDM+a model signal, only a selection of objects is used for the search for DM particles presented in this thesis. The overlap removal and object selection criteria are described in Section 7.6.

7.1 Track and vertex reconstruction

Tracks are an ingredient to most of the objects reconstructed with the ATLAS detector. Tracks are reconstructed by using the ATLAS ID [284]. The building blocks of tracks are hits.

In the inside-out track finding procedure, tracks are seeded by groups of three hits from the IBL, pixel detector and SCT [289]. These seeds are extended into track candidates using hits from other layers of the ID, excluding the TRT, with the help of a Kalman filter [290]. Track candidates may share hits. To resolve these ambiguities, a quality score is assigned to each track candidate. The score is based on the number of ID layers with a hit, a track fit χ^2 and the momentum of a track candidate, as detailed in References [284, 289]. Shared hits are removed from the track candidates with a lower score. The track candidates with removed hits are refit, scored and enter the ambiguity resolution procedure again. Track candidates failing certain quality criteria, including the requirements $p_{\mathrm{T}} > 400\,\mathrm{MeV}$ and $|\eta| < 2.5$, are rejected by the ambiguity resolution. Using hits in the TRT, the final track candidates are extended and a track fit is performed.

Though there may be multiple proton-proton interactions per bunch-crossing, there is typically at most one, the hard-scatter, yielding the interaction of interest. To identify the proton-proton interaction of interest, the vertices of the proton-proton interactions in an event are reconstructed [291–294]. The vertex reconstruction is based on reconstructed tracks compatible with originating from the luminous region and fulfilling certain quality criteria. By finding peaks in the distribution of these tracks along the z-axis, seed vertices are constructed. For each seed vertex, an exact vertex position is then calculated using a vertex fitting algorithm [295].

In the analysis presented in this thesis, events must contain at least one reconstructed vertex with which at least two tracks with a $p_{\mathrm{T}} > 500\,\mathrm{MeV}$ are compatible. If an event contains multiple vertices, the primary vertex is selected by the largest squared sum of track momenta $\sum p_{\mathrm{T}}^2$.

7.2 Electrons

Electrons are reconstructed by matching energy deposits in the calorimeter to tracks [286]. The reconstruction of electrons consists of four steps, which are discussed in more detail below: first energy deposits in the ECAL are combined into EM-topo clusters, then tracks are matched to these clusters and superclusters are formed. Finally, electrons are defined from the superclusters.

The EM-topo clusters are built from proto-clusters [286, 296]. Proto-clusters are seeded by ECAL and HCAL cells which fulfil

$$|\zeta_{\text{cell}}^{\text{EM}}| = \left| \frac{E_{\text{cell}}^{\text{EM}}}{\sigma_{\text{noise,cell}}^{\text{EM}}} \right| \geq 4.$$

The energy $E_{\text{cell}}^{\text{EM}}$ deposited in a calorimeter cell is calibrated to the EM scale, i.e. in such a way that the energy of electromagnetic showers is correctly measured[1]. The noise $\sigma_{\text{noise,cell}}^{\text{EM}}$ per calorimeter cell accounts for electronic noise and noise due to energy deposits from particles emerging from pile-up interactions. The proto-clusters made of the seeds are extended by adding all neighbouring calorimeter cells. In the next step, the neighbouring cells of all collected cells with $|\zeta_{\text{cell}}^{\text{EM}}| \geq 2$ are added to the cluster as well. This step is repeated iteratively, until no new cells are added to the proto cluster [296].

Proto-clusters are built from ECAL and HCAL cells, but only ECAL cells are of relevance for the electron reconstruction [286]. The HCAL cells are, however, used to remove clusters originating from pile-up interactions. The resulting, ECAL cell only proto-clusters are referred to as EM-topo clusters.

EM-topo clusters are matched to tracks in the next step [286]. Electrons can loose a significant fraction of their energy compared to other charged particles when traversing the ID. To ensure an efficient electron reconstruction, additional tracks with more loose quality criteria compared to the standard tracks are reconstructed. If the conditions $|\eta_{\text{track}} - \eta_{\text{cluster}}| < 0.05$ and $-0.10 < q(\phi_{\text{track}} - \phi_{\text{cluster}}) < 0.05$ with q the charge of the track are fulfilled, a track is matched to a cluster. Multiple tracks may be matched to an EM topo-cluster. Tracks matched to a cluster are scored according to their hits in the ID and the ΔR between the tracks and the cluster. The highest scored track matched to an EM topo-cluster is used in the further steps of the electron reconstruction.

Superclusters are built next from the EM topo-clusters [286]. Seed clusters to construct the electron superclusters are selected by requiring $E_{\text{T}} = \sqrt{m^2 + p_{\text{T}}^2} \geq 1\,\text{GeV}$ and a matched track fulfilling certain quality criteria. The superclusters defined by the seeds are extended by adding EM topo-clusters within $\Delta\eta \times \Delta\phi = 0.075 \times 0.125$ and, if the seed and the adjacent cluster share the matched track, within $\Delta\eta \times \Delta\phi = 0.125 \times 0.3$. Tracks are matched to the supercluster using the same procedure as for EM-topo clusters and ambiguities with the photon reconstruction are resolved. The remaining track-matched superclusters define the reconstructed electrons. A four-momentum vector is assigned to a reconstructed electron by using the η and ϕ from the highest ranked matched track, the energy from the calorimeter energy clusters and assuming that the invariant mass equals the electron mass [297].

The energy of electrons reconstructed in data is subsequently calibrated according to the energy of reconstructed electrons in the simulation [286, 298]. This is

[1] The calorimeters of the ATLAS detector are non-compensating [296]. That means that electromagnetic and hadronic showers initiated by particles of the same energy yield different signals in the calorimeters. When using clusters calibrated to the EM scale, the energy of electromagnetic showers is accurately measured [286]. When using local hadronic cell weighting (LCW) calibrated clusters, see Section 7.4.4, the energy of both types of showers is, making up for the non-compensating nature of the ATLAS calorimeters.

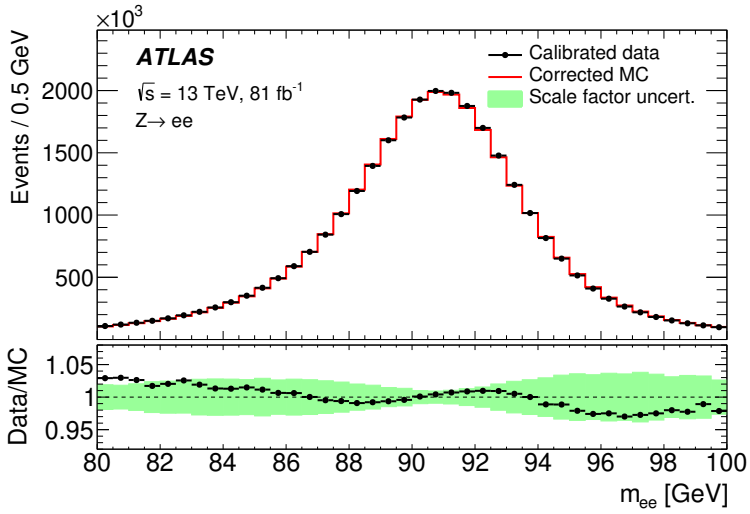

Figure 7.2: Good agreement between data and simulation is observed in the invariant mass of the two reconstructed electrons in selected $Z \to ee$ events after the calibration of energy scale and resolution [286]. The total number of events in the simulation has been normalised to the total number of data events.

referred to as energy scale calibration. In addition, the energy resolution of electrons found in data is used to calibrate the one found in simulation. $Z \to ee$ events are used to derive the energy scale and resolution calibration correction factors. The invariant mass of the two electrons in data and the simulation after the energy calibration is shown for $Z \to ee$ events in Figure 7.2. Good agreement between data and simulation is observed.

Electrons can originate from the hard-scatter interaction or immediate subsequent decays, e.g. of W-bosons, Z-bosons [297]. Such electrons are called prompt electrons. Non-prompt electrons emerge from the decay of hadrons and photons [286] and are typically not of interest in physics analyses. Furthermore, reconstructed electrons can originate from energy deposits of other particles, e.g. hadrons. Such "fake electrons" are also not of interest for physics analyses. The electron identification procedure aims at reducing the fraction of non-prompt and fake electrons. It is based on a likelihood function and employs various properties of the track, the energy deposits in the calorimeter and the matching of track and cluster. Three identification working points are defined: `Tight`, `Medium` and `Loose`. The average efficiency of a prompt electron to pass the identification working point conditions are 80 %, 88 % and 93 %, respectively. With increasing efficiency, the fraction of non-prompt and fake electrons passing the working point conditions increases.

Additional activity close to a reconstructed electron is more likely to be found for non-prompt and fake electrons than for prompt electrons [286]. To further increase the fraction of prompt electrons, calorimeter- and track-based isolation criteria on the activity in the vicinity of an electron are defined. The calorimeter-based isolation variable sums up all the energy deposits in a cone of size $\Delta R = 0.2$ around the electron cluster barycentre. Energy contributions from the electron are removed and other effects, e.g. energy contributions from pile-up interactions, are accounted for. The track-based isolation variable sums the transverse momentum of all tracks not matched to an electron in cone with a size depending on the electron p_{T}. The cone size is p_{T} dependent to not penalise prompt electrons produced in the decay of a heavy particle, which can lead to close-by particles. Multiple isolation working

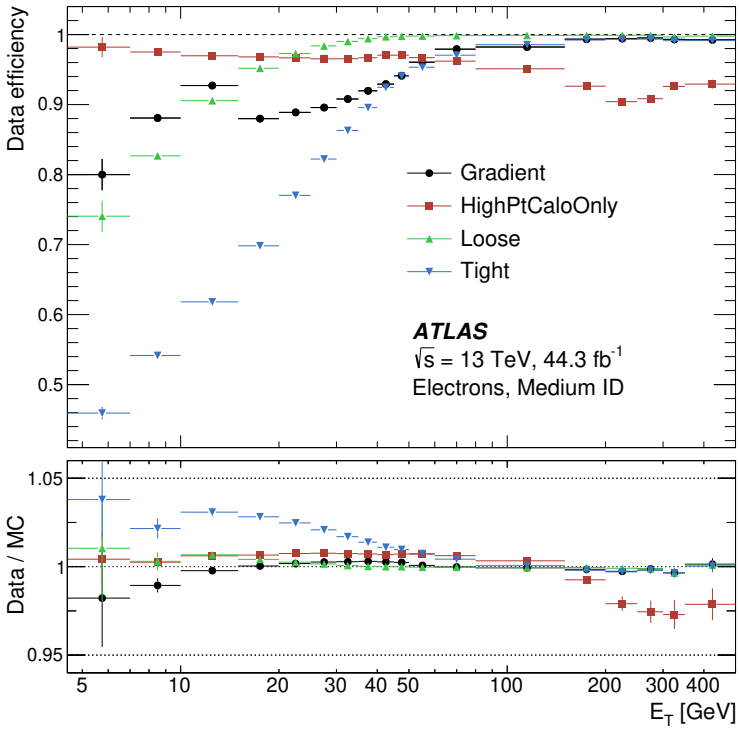

Figure 7.3: Prompt electron isolation efficiency for the different isolation working points in measured $Z \to ee$ events [286]. The `Gradient` isolation working point is described in Reference [286]. Selected electrons must satisfy the conditions of the `Medium` identification working point. The ratio of the efficiency in data and simulation is shown in the bottom panel.

points are defined based on the calorimeter- and track-based isolation variables. In the analysis presented in this thesis, the `Loose`, `Tight` and `HighPtCaloOnly` working points are of relevance. Requirements on the calorimeter- and track-based isolation variables are placed in the former two working points, while requirements on the calorimeter-based isolation variable are placed in the latter. The `HighPtCaloOnly` working point has the strongest suppression of electrons that are not prompt at high-E_{T}. The efficiency of a prompt electron to pass the requirements of the different isolation working points is shown in Figure 7.3 as a function of E_{T}.

Using $Z \to ee$ and $J/\Psi \to ee$ events, the efficiencies to reconstruct, identify and isolate a prompt electron are determined both in data and in simulation [297]. A sample with a high purity of such events can be obtained by requiring the invariant mass of the reconstructed electron-positron pair to be compatible with the decaying particle. The so-called tag-and-probe method is then used to measure the different efficiencies. One of the electrons, the tag, is required to pass the most tight requirement, while the requirement on the other electron, the probe, is varied to measure the efficiency. The reconstruction, identification and isolation efficiencies measured in data and simulation are compared. Multiplicative factors to correct the efficiencies in the simulation are derived.

7.3 Muons

Muons can traverse the entire ATLAS detector without being absorbed. They are reconstructed using tracks reconstructed in the ID and in the muon system, potentially supplemented by calorimeter information [285]. Tracks in the muon system are constructed by first identifying track segments in the individual muon system chambers. These segments are then combined into a track, accounting for the bending in the magnetic field and using a χ^2 fit.

Five different methods are used to reconstruct muons in the ATLAS experiment [285]:

- Combined (CB) muons are reconstructed by combining muon system and ID tracks. Most CB muons are reconstructed with a full ID track in the ID coverage $|\eta| < 2.5$. CB muons outside of this range are reconstructed by matching muon system tracks to ID track segments.

- ID tracks are extrapolated to the muon system and required to be compatible with at least three hits in the muon system for Inside-Out combined (IO) muons. A refined track fit is made accounting for the muon system hits. Similarly, Segment Tagged (ST) muons are defined by an ID track matched to at least one track segment in the muon system. Both IO and ST muons allow reconstructing low energetic muons and muons traversing detector areas with little muon system coverage [299].

- Calorimeter Tagged (CT) muons combine ID tracks with energy deposits in the calorimeter. CT muons are used in particular to reconstruct muons at low $|\eta| < 0.1$, where there is no coverage by the muon system due to service trays [299].

- Muon-spectrometer Extrapolated (ME) muons extrapolate muon system tracks back to the interaction point without the requirement of matching to an ID track. By using ME muons the muon reconstruction abilities can be extended to high η areas ($2.5 < |\eta| < 2.7$) where there is little ID coverage.

Similar to electrons, an identification selection is used for muons to increase the fraction of prompt muons over those originating from hadron decays [299]. The identification selection makes use of the number of hits in the ID and the muon system, measures resulting from the track fit, and differences between properties derived from the ID and muon system tracks [285]. Different working points, `Loose`, `Medium`, `Tight`, are defined, each with different average prompt muon efficiencies. For what concerns this thesis, only the `Medium` working point is used. For $|\eta| < 2.5$, muons identified with the `Medium` working point are either CB or IO muons, while they are CB or ME muons at higher $|\eta|$. Requirements on the difference of the ratio of charge to momentum determined with ID and muon system tracks, as well as the number of hits in the muon system are made, as detailed in Reference [285].

Muons from hadron decays are additionally suppressed by placing isolation requirements [285]. Calorimeter- and track-based isolation variables are defined. The sum of all energy deposits in a cone of size $\Delta R = 0.2$ around the extrapolated muon track defines the calorimeter-based isolation variable. Energy deposits from the muon are subtracted and contributions from pile-up interactions are corrected for. The total momentum of all tracks in a cone around the muon track in the ID, except for the track of the muon, defines the track-based isolation variable. For what concerns this thesis, the cone size depends on the muon p_{T}. Multiple isolation working points are defined with the two isolation variables. In this thesis, the `Loose` isolation working point is used, which employs both the calorimeter- and track-based isolation variables.

Using $Z \to \mu\mu$ and $J/\Psi \to \mu\mu$ events, the muon momenta in simulation are corrected to the ones obtained from data [299]. Also using $Z \to \mu\mu$ and $J/\Psi \to \mu\mu$ events, multiplicative correction factors are obtained to correct the reconstruction, identification and isolation efficiencies of the simulation to data. These correction factors are derived with the help of the tag-and-probe method and others, as discussed in Reference [285].

7.4 Jets

Jets are collimated sprays of colour-less hadrons, initiated by individual quarks and gluons due to the confinement in QCD. These jets are reconstructed in the ATLAS experiment using information from the ID and the calorimeters.

7.4.1 Definition of jets

Being interested in the underlying dynamics of the fundamental particles, it is desirable in the jet reconstruction to construct an object that reflects the dynamics of the initial quark or gluon, e.g. in the direction and momentum. In addition, a jet reconstruction algorithm must allow for the reliable comparison of theory (forming jets at particle level for example) and experiment [300]. To this extent it is crucial that a jet reconstruction algorithm is insensitive to soft (low momentum) and collinear (low angle) QCD emissions, in other words, that it is infrared and collinear safe.

The anti-k_t algorithm [300] satisfies these requirements. It takes a list of "entities" as input and forms jets from these entities. Different lists of entities are used throughout this thesis, as described below. For each entity i in the list of entities, the anti-k_t algorithm calculates the distances d_{ij} to all other entities and the distance d_{iB} between entity i and the beam:

$$\begin{aligned} d_{ij} &= \min\left(p_{\mathrm{T},i}^{2p}, p_{\mathrm{T},j}^{2p}\right)\frac{\Delta(i,j)^2}{R^2}, \\ d_{iB} &= p_{\mathrm{T},i}^{2p}. \end{aligned} \tag{7.1}$$

In the equation, $p_{\mathrm{T},i}$ and $p_{\mathrm{T},j}$ are the transverse momenta of entities i and j, $\Delta(i,j)^2 = (y_i - y_j)^2 + (\phi_i - \phi_j)^2$ with y_i and y_j the rapidities and ϕ_i and ϕ_j the azimuth angles of entities i and j. Moreover, R is the so-called distance parameter, which controls the size of the jets. The fixed parameter p is set to -1 in the anti-k_t algorithm. After the calculation of the d_{ij} and d_{iB}, the anti-k_t algorithm finds the minimum of the d_{ij} and d_{iB}. If the minimum is one of the d_{ij}, the four momenta of entities i and j are added and the summed entity replaces entities i and j in the list of entities. If instead d_{iB} is found to be the minimum, entity i is regarded as a jet and erased from the list. The procedure continues as long as entities remain in the list.

Because of the inverse dependence on the p_{T}, soft entities are combined with the hardest close-by momentum entities before soft entities are combined [300].

In the simplest case, jets formed by the anti-k_t algorithm have a conical shape, with a relatively high momentum entity i in the center surrounded by lower momentum entities [300]. If there are, however, multiple relatively hard entities i and j within $\Delta(i,j) \leq 2R$, the shape and substructure (i.e. the spatial distribution of hard entities) of a jet can be very different, as illustrated in Figure 7.4a. If the two hard entities are found within $R < \Delta(i,j) \leq 2R$, the anti-k_t algorithm forms two jets. Depending on the transverse momenta of the two hard entities $p_{\mathrm{T},i}$ and $p_{\mathrm{T},j}$, one of these jets can be cone-shaped (green jet in Figure 7.4a) for example while the other is partially cone-shaped (pink jet). If two relatively hard entities are found

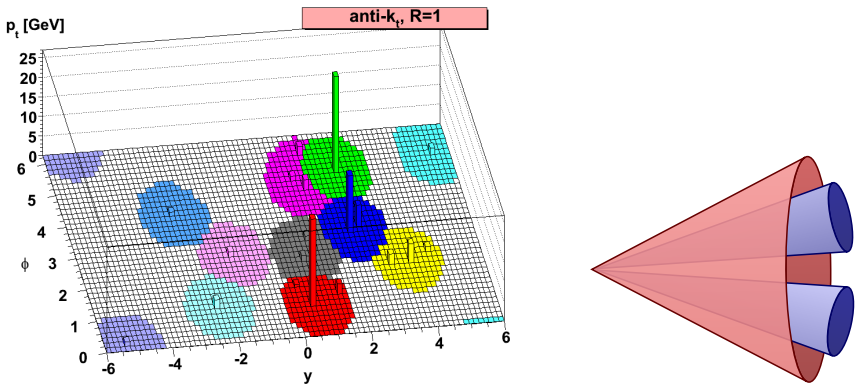

(a) (b)

Figure 7.4: (a) The shapes and the substructure of jets formed with the anti-k_t algorithm are shown in the $\phi - y$ plane [300]. The area covered by a jet is coloured. The z-axis indicates the momentum of the constituting entities. The inputs used for the anti-k_t algorithm are obtained from an event simulated with Herwig [301] and additional soft particles. (b) Substructure of a jet formed by two hard entities of similar p_{T}. Modified from Reference [302].

within $\Delta(i,j) < R$, one jet is formed by the anti-k_t algorithm. The shape and substructure depends on the momenta of the two hard entities. If their momenta are similar for example, the jet is made of two cones (with a radius lower than R) around the hard entities, contained in a larger cone around the jet barycentre. This situation is illustrated in Figure 7.4b.

Three types of jets are defined with the anti-k_t algorithm in the analysis presented in this thesis: small-radius jets with $R = 0.4$, large-radius jets with $R = 1.0$ and adaptive-radius reclustered jets with a variable R, as explained in the following subsections.

7.4.2 Small-radius jets

Particle-flow

Particle-flow objects [303, 304] are the basic ingredient for the formation of small-radius jets. They are constituted of tracks and calorimeter energy clusters.

The calorimeter energy clusters used to define particle-flow objects correspond to the proto-clusters [296] introduced for the electron reconstruction in Section 7.2 [303]. The energies measured in the ECAL and HCAL cells used to form these clusters are calibrated to the EM scale, correctly measuring the energy of electromagnetic showers. By calculating a weighted mean of the cluster cells, ϕ and η coordinates, as well as an energy is assigned to a cluster [296]. It is thereby assumed that the cluster points to the origin of the coordinate system in the detector [305]. A four-momentum vector is calculated by interpreting a cluster as a particle of zero mass [296]. Assuming that all proto-clusters originate from particles produced in the primary vertex, an origin correction is performed [304], modifying the momentum such that it points to the primary vertex [305].

Small-radius jets can be defined using these proto-clusters [304]. Until the end of run-II, these EM topo jets have been the standard small-radius jets in the ATLAS experiment. As the energy resolution of the calorimeters decreases with the deposited energy, the energy resolution of EM topo jets also decreases with the jet

energy [303]. Because the ID has a very precise momentum resolution for low momentum tracks, combining calorimeter and ID information helps to improve the jet energy resolution at low energies. Simultaneously, the usage of ID information increases the directional precision of the jet axis and allows reducing the impact of energy deposits from pile-up interactions on jets. The usage of particle-flow objects, which are made up of tracks and calorimeter energy clusters, thus allows defining jets with an improved resolution of the energy and jet direction as well as less dependence on the number of pile-up interactions compared to EM topo jets [304].

The tracks defined as particle-flow objects must conform to certain stricter quality criteria compared to the default tracks [303, 304]. To not double count energy contributions from particles depositing energy in the ID and in the calorimeters, a dedicated energy subtraction procedure is performed. Energy is subtracted from calorimeter energy clusters that can be associated to a track. Firstly, the selected tracks are matched to calorimeter energy clusters. For each track, the uncertainty accounting angular distance $\Delta R' = \sqrt{\left(\frac{\Delta\phi}{\sigma_\phi}\right)^2 + \left(\frac{\Delta\eta}{\sigma_\eta}\right)^2}$ to each cluster is calculated. The symbols σ_ϕ and σ_η denote the standard deviation of the cluster cells in ϕ and η with respect to the cluster barycentre. The cluster with the smallest $\Delta R'$ below $\Delta R' = 1.64$ is matched to a track.

For each track matched to a cluster, the expected energy deposited by a particle producing the track in the calorimeter is evaluated next using simulated events [303]. Energy deposited in the calorimeter by a particle producing a track can yield more than one cluster. If the energy in the calorimeter energy cluster matched to a track is significantly below the expected deposited energy, all clusters within $\Delta R = 0.2$ of the track are matched to it.

Energy is subtracted from the calorimeter energy clusters according to the expected deposited energy after the track-to-cluster matching [303]. Furthermore, remaining energy deposits which are found to be compatible with shower fluctuations are subtracted from the matched clusters. The final particle-flow objects are those selected tracks which are compatible with the primary vertex ("particle-flow tracks") and the energy subtracted calorimeter energy clusters.

Small-radius jet formation and calibration

The particle-flow objects are input into the anti-k_t algorithm [300, 306] with $R = 0.4$ to define the small-radius jets. These jets are subsequently calibrated in a multi-step procedure [304].

The energy of a reconstructed jet is corrected at first in the calibration process to match the energy of a reconstructed jet at particle level [304]. This is referred to as jet energy scale (JES) calibration and consists of four steps.

Particles produced in pile-up proton-proton interactions deposit energy in the detector and can modify the kinematics of a small-radius jet [304]. Such contributions are subtracted in the first step of the JES calibration. Using reconstructed jets at particle level obtained from simulated di-jet events, the four-momentum vectors of the jets are subsequently corrected [304].

Numerous effects are corrected for in the global sequential calibration (GSC) step of the JES calibration [304]. Among them are dependencies on the particle initiating a jet, shower fluctuations and showers not captured completely by the HCAL and leaking into the muon system. The corrections applied by the GSC are evaluated using simulated di-jet events.

Additional correction factors are derived for jets in data to mitigate remaining discrepancies to jets in the simulation [304]. These in-situ JES calibration factors are evaluated by studying events where jets are produced in association with other well-calibrated objects, such as electrons, photons, muons or previously calibrated

jets in $Z(\to \ell\ell) + \text{jet}$, $\gamma + \text{jet}$ and multi-jet events. Using the momentum balance, factors to correct the energy of jets reconstructed in data are derived. Systematic uncertainties associated with these correction factors arise from the modelling of the simulation and the reference objects for example.

The jet energy resolution (JER) of jets in simulation is also calibrated [304]. The JER depends on the noise induced by electronics, on energy deposits from pile-up interactions, on the stochastic nature of energy deposits and on other effects. The calibration corrects the JER of simulated events to the JER measured in data. The correction factors are derived using di-jet events and applied to the simulation by smearing the energy distribution. Systematic uncertainties on the JER are derived in this calibration process.

Jet Vertex Tagger

Jets not from the hard-scatter, but from pile-up interactions are not of interest in the analysis presented in this thesis. The fraction of jets from pile-up interactions is reduced by using the multivariate jet vertex tagger (JVT) algorithm [307]. Apart from the jet p_{T}, tracks associated to a jet are used by the JVT. The tracks can be associated to different proton-proton vertices. This is exploited to discriminate jets from the primary vertex from other jets.

The JVT is only used for jets within $|\eta| < 2.5$. For forward jets, the forward jet vertex tagger (fJVT) is used [308, 309].

The efficiencies of jets originating from the primary vertex and passing requirements on the outputs of the JVT and fJVT are measured in data and simulation [307, 309]. They are determined by selecting $Z \to \mu\mu + \text{jets}$ events and employing a tag-and-probe method. Factors to correct for the discrepancies in the efficiency measured in data and simulation are derived. Simulated events are corrected by these factors in the analysis presented in this thesis.

7.4.3 *b*-tagging

Hadrons containing b-quarks (b-hadrons) have a comparably long lifetime of about 1.5 ps [25] resulting in decay lengths of $O(\text{mm})$ inside of the ATLAS detector [203]. For example, a b-hadron with a $p_{\mathrm{T}} = 50\,\text{GeV}$ has a mean flight path of $\langle l \rangle = \beta\gamma c\tau \simeq 5\,\text{mm}$. b-hadrons can be found in jets initiated by b-quarks (b-jets) and allow identifying (b-tagging) and distinguishing these jets from jets initiated by c-hadrons (c-jets) and all other jets (light-flavour-jets). The b-tagging exploits the relatively long decay lengths of the b-hadrons and other properties, such as the decay chain. Detector quantities used to identify b-jets include the longitudinal and transversal impact parameters d_0 and z_0 of tracks associated to a b-jet and reconstructed secondary and tertiary vertices from b-hadron and subsequent decays, as illustrated in Figure 7.5.

Multiple low-level algorithms have been developed to identify distinct features of b-jets. High-level algorithms use the outputs of multiple low-level algorithms and allow increasing the b-jet discrimination power compared to the low-level algorithms. The low-level algorithms relevant in this thesis are described in the following.

- Transverse impact parameter significances of tracks associated to a jet are used by the IP2D and IP3D algorithms [203, 311]. The IP2D only considers the significance of d_0, while IP3D also considers the significance of z_0. In both algorithms, probabilities of a track being compatible with a b-jet, a c-jet and a light-flavour-jet are evaluated. Ratios of these probabilities are formed per track and multiplied for all tracks. The logarithm of the resulting likelihood ratio is employed in the high-level algorithms.

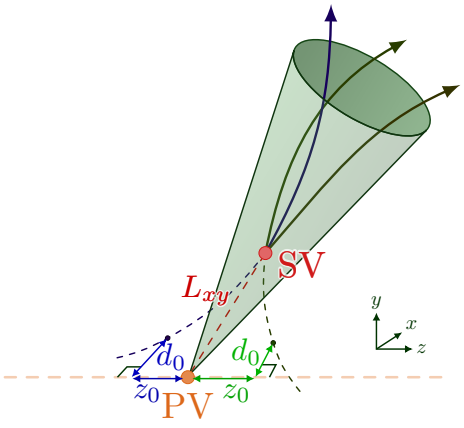

Figure 7.5: Illustration of transverse (d_0) and longitudinal (z_0) impact parameters of tracks associated to a b-jet. In addition the distance L_{xy} between the primary (PV) and secondary vertex (SV) is shown [310].

- The IP2D and IP3D algorithms do not account for correlations between the different tracks [312]. The recurrent neural network algorithm RNNIP additionally accounts for correlations between tracks. It uses the same inputs as the IP3D algorithm per track as well as the momentum fraction of a track relative to the total jet momentum and the ΔR between the jet-axis and a track.

- The SV1 algorithm [313] reconstructs secondary vertices from tracks associated to a jet. It outputs several quantities which are used to identify b-jets in the high-level algorithms, among them [203]: the invariant mass of the four-momentum sum of all vertex-matched tracks and the distance between the secondary vertex and the primary vertex.

- The JetFitter algorithm [314] reconstructs multiple decay vertices in a jet and attempts to reconstruct the decay chain of a b-hadron. It outputs multiple properties per reconstructed vertex such as the number of tracks associated, the invariant mass of the sum of these tracks and the mean significance of the decay length [203]. These quantities are used by the high-level algorithms.

The discussed low-level algorithms are combined into high level algorithms to increase the discrimination power of identifying b-jets. The high-level DL1r algorithm [203, 311, 312, 315] is the standard algorithm in the ATLAS experiment and is used in this thesis. DL1r combines the low-level algorithms discussed above in a deep neural network. For each input jet, DL1r outputs three probabilities, according to how compatible a jet is with a b-jet (p_b), a c-jet (p_c) and a light-flavour-jet (p_l). Following discriminant is then constructed from these probabilities to identify b-jets:

$$D_{\mathrm{DL1r}} = \ln\left(\frac{p_b}{f_c \cdot p_c + (1 - f_c) \cdot p_l}\right).$$

In the equation, f_c is the fraction of events containing c-jets in the background sample (sample containing no b-jets) used for the training of the neural network. A value of $f_c = 1.8\,\%$ was found to be optimal [203, 315]. D_{DL1r} is also referred to as b-tagging score.

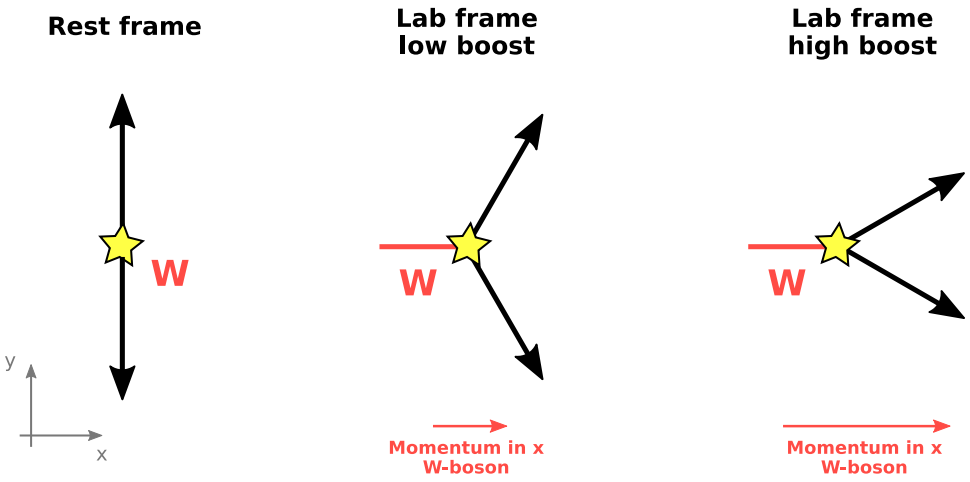

Figure 7.6: The decay products of the W-boson are back-to-back in the rest frame and become more and more collimated as the W-boson momentum along the x-axis increases in the laboratory frame.

Multiple b-tagging working points have been developed, defining a jet as b-tagged depending on the b-tagging score [203]. In the analysis presented in this thesis the working points which have an average efficiency of b-tagging a b-jet of 85 % and 77 %, respectively, are used. These working points are defined using simulated $t\bar{t}$ events [315]. For the 77 % working point, 20 % of the c-jets and less than 1 % of the light-flavour-jets are misidenitified (mis-tagged) as b-jets, as determined in $t\bar{t}$ events.

The b-tagging and mis-tag efficiencies are measured in data and in simulation. The b-tagging efficiency [203] and c-jet mis-tag efficiency [316] are measured in $t\bar{t}$ events, where $W \to cs$ decays are used in the latter case. Light jet mis-tag efficiencies are measured for example by inverting the requirements on some of the variables from the low-level algorithms to obtain a sample enriched in light jets, as detailed in Reference [317]. Due to imperfections of the detector simulation, there are discrepancies between the efficiencies in data and simulation. Correction factors to be applied to the simulation are derived for that reason.

7.4.4 Large-radius jets

As the momentum of a W-boson momentum increases, its decay products become more and more collimated, as is illustrated in Figure 7.6. Hadronically decaying W-bosons with a relatively high p_{T} yield collimated decay products than can be reconstructed in anti-k_t jets with large radius parameters, in so-called large-radius jets [287, 318]. This technique is used in the analysis presented in this thesis. The large-radius jets are defined by inputting calorimeter energy clusters calibrated with the local hadronic cell weighting (LCW) scheme into the anti-k_t algorithm [300, 306] with $R = 1.0$.

The calorimeter energy clusters used for the large-radius jets are constructed like the proto-clusters described in the electron reconstruction in Section 7.2 [318]. These clusters are calibrated according to the LCW scheme, which allows for the mitigation of the non-compensating response of the calorimeter [296]. That means it compensates for the fact that for two particles of the same energy producing an electromagnetic and a hadronic shower, respectively, the measured energy in the calorimeters is different. In addition, the LCW scheme corrects for energy deposits that are not included into a cluster by the clustering algorithm and energy losses

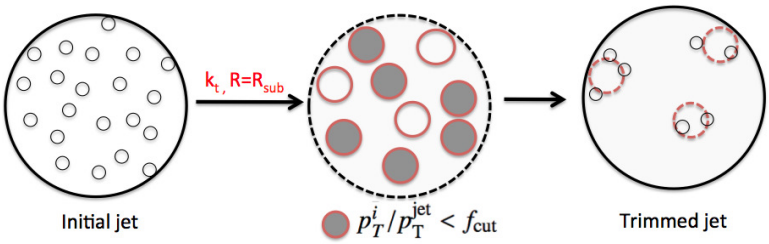

Figure 7.7: Illustration of the trimming procedure [320].

in insensitive materials.

To each cluster, a probability $\mathcal{P}$ whether the cluster was produced by an electromagnetic shower is assigned at first. Cell-by-cell correction factors are then applied as a function of $\mathcal{P}$. As changing the energy per cell, the LCW calibration modifies the cluster barycentre and direction. Coordinates and momenta are recalculated for the LCW calibrated clusters and their direction is corrected to point to the primary vertex, as done for the clusters employed for constructing small-radius jets (Section 7.4.2).

The large-radius jets constructed from the LCW clusters are trimmed to remove low energy contributions from pile-up interactions and other sources [318–320]. The trimming helps to improve the mass resolution of a large-radius jet and produces a clean substructure (energy distribution within the large-radius jet). These two features are relevant in the further usage of the large-radius jets discussed in Section 7.4.5. In the trimming procedure illustrated in Figure 7.7 the original list of entities that was used to define the large-radius jet is input into the k_{T} algorithm [321] to form subjets. The k_{T} algorithm is equal to the anti-k_t algorithm, but uses $p = +1$ in Equation (7.1) [300]. The radius parameter is set to $R_{\mathrm{sub}} = 0.2$. The subjets with a momentum fraction relative to the total jet momentum $p_{\mathrm{T}}^{\mathrm{sub}}/p_{\mathrm{T}}^{\mathrm{tot}}$ of below $f_{\mathrm{cut}} = 0.05$ are removed. Using the remaining entities, the energy and four-momentum are calculated for the trimmed large-radius jet. The parameters $R_{\mathrm{sub}} = 0.2$ and $f_{\mathrm{cut}} = 0.05$ have been found to be optimal in the studies presented in Reference [322].

A mass m_{jet} is assigned to each trimmed jet according to the four-momentum squared. To improve the mass resolution for high-p_{T} large-radius jets, an additional mass m_{TA} [323], based on tracks associated to a jet, is calculated. Tracks are associated to a large-radius jet by using a technique called ghost-association [320, 324, 325]: a pseudo-particle is generated for each reconstructed track which has the same coordinates and direction as the track[2], but an infinitesimal momentum. These pseudo-particles are input into the anti-k_t algorithm together with the calorimeter energy clusters. As the pseudo-particles are very soft, they do not change the resulting jets. A track is associated to a jet if the corresponding pseudo-particle is clustered into the jet. Compared to associating tracks to jets by their angular distance ΔR, which assumes that jets are cone-shaped, ghost-association has the advantage of being independent of irregular jet shapes and boundaries [320]. The mass m_{TA} is defined from the associated tracks by

$$m_{\mathrm{TA}} = \frac{p_{\mathrm{T}}^{\mathrm{jet}}}{p_{\mathrm{T}}^{\mathrm{track}}} m_{\mathrm{track}},$$

with $p_{\mathrm{T}}^{\mathrm{jet}}$ the transverse momentum of the large-radius jet, $p_{\mathrm{T}}^{\mathrm{track}}$ the transverse

[2]The coordinates and direction are determined at the perigee point, the point of closest approach of a track to the z-axis. This gives track coordinates and a direction that have not been diverted away from the corresponding jet in the magnetic field of the ID.

momenta of a trimmed anti-k_t jet of radius $R = 1.0$ formed from the tracks associated to the jet and m_{track} the mass of this track jet. The bare track jet mass m_{track} would only account for the charged particles within the jet and not correctly resemble the jet mass. It is corrected by the ratio of $p_{\text{T}}^{\text{jet}}$ and $p_{\text{T}}^{\text{track}}$ in m_{TA} for that reason.

To further improve the mass resolution, a combined mass is defined from the weighted average of m_{jet} and m_{TA} [318]

$$m_{\text{comb}} \coloneqq a \cdot m_{\text{jet}} + b \cdot m_{\text{TA}}.$$

The weights a and b satisfy $a + b = 1$ and are derived from the resolutions of m_{jet} and m_{TA}, ensuring that the mass resolution of m_{comb} always improves compared to m_{jet} and m_{TA}. In this thesis, m_{comb} is used to determine the mass of large-radius jets.

The energy and the mass (m_{jet}) of the trimmed large-radius jets are calibrated in data and simulation to equal those values found at particle level in simulated di-jet events [318]. This is referred to as JES and jet mass scale (JMS) calibration. The JES is corrected at first, also correcting η. Subsequently the JMS is calibrated. The JMS calibration is important for large-radius jets, as the mass is an important quantity to identify large-radius jets from W-boson decays, as discussed in the next section.

In-situ calibrations to account for the imperfect detector simulation are derived for the JES, the JER, the JMS and the jet mass resolution (JMR) of a large-radius jet [318, 326]. The mass calibration is performed for m_{jet} and m_{TA}, subsequently also calibrating m_{comb}.

Firstly, the JES is calibrated and factors to correct the data are derived [318]. The calibration methods used are similar to the ones used for small-radius jets and require the large-radius jet to recoil against a well-calibrated object. $Z \to \ell\ell$+jet, γ+jet as well as events where multiple small-radius jets recoil from a large-radius jet are used. An η-intercalibration to calibrate forward jets ($|\eta| > 0.8$) is performed using di-jet events.

The JER is calibrated in-situ using di-jet events [318]. Due to the good agreement between data and simulation, no correction factors are derived, but the difference is instead treated as an uncertainty in addition to the remaining JER calibration uncertainties.

After correcting the JES in data, the JMS and JMR are calibrated in-situ [318, 326]. This is done by measuring the masses of high-p_{T}, hadronically decaying W-bosons and top-quarks in $t\bar{t}$ events where the decay products of each of the two particles are reconstructed within one large-radius jet. In addition, ratios of quantities derived from a large-radius jet and its corresponding jet formed from associated tracks are used to calibrate the JMS, as detailed in References [318, 320]. For the JMS, factors to correct the data, as well as systematic uncertainties are derived. Similar to the JER, good agreement of the JMR measured in data and simulation is observed and no correction factors for the JMR are defined. Systematic uncertainties are however derived during the JMR calibration.

7.4.5 W-tagging

The decay products of a hadronically decaying, high-p_{T} W-boson can be reconstructed in a large-radius jet and such a large-radius jet is called a W-boson jet [288]. W-boson jets have characteristic features which allow distinguishing them from large-radius jets seeded by other particles. Examples of other particles reconstructed in large-radius jets are the decay products of individual and multiple quarks or gluons as well as other hadronically decaying heavy particles, such as top-quarks,

Z-bosons, Higgs-bosons, etc. The process of identifying a large-radius jet originating from a W-boson decay is called W-tagging. Following features are used for W-tagging large-radius jets in this thesis:

- **Mass**: Capturing the entire W-boson decay, W-boson jets are expected to have a mass m_{comb} compatible with the W-boson mass.
- **Substructure**: W-boson jets contain the hadrons resulting from the hadronisation of two quarks. Subsequently, a substructure within the large-radius W-boson jet of two cones with relatively high-p_{T} entities is expected (see e.g. Figure 7.4b). This substructure is denoted as two prong.
- **Associated tracks**: Large-radius jets initiated by gluons of high energy have a larger number N_{trk} of associated tracks before trimming than W-boson jets [327]. This feature is used to suppress large-radius jets not containing a hadronic W-boson decay.

For the substructure, the D_2 variable [288, 328, 329] is used. It exploits correlations among the entities forming a large-radius jet and is defined as [329]

$$D_2 := \frac{e_3}{(e_2)^3},$$

with

$$e_3 := \frac{1}{p_{\text{T,jet}}^3} \sum_{i<j<k\leq n} p_{\text{T}}^i p_{\text{T}}^j p_{\text{T}}^k \Delta R_{ij} \Delta R_{jk} \Delta R_{ki},$$
$$e_2 := \frac{1}{p_{\text{T,jet}}^2} \sum_{i<j\leq n} p_{\text{T}}^i p_{\text{T}}^j \Delta R_{ij}.$$

In the equation, i, j, k denote jet entities, n is the total number of jet entities, p_{T}^i is the transverse momentum of entity i and ΔR_{ij} the angular distance between entities i and j. For jets compatible with a two prong substructure, D_2 takes comparably low values roughly below one, while the values of D_2 are higher for substructures with a different number of spatially separated hard entities. Compared to the multitude of other substructure variables, see e.g. Reference [288], D_2 was found to show the best performance regarding W-tagging large-radius jets in Reference [322].

The W-tagging algorithm used in this thesis makes use of the combined mass m_{comb}, D_2 and N_{trk} [288, 330]. It is optimised using a $W' \to WZ \to qqqq$ sample and two working points with different efficiencies of W-tagging W-boson jets are defined. In this thesis, the 50 % efficiency working point is used. The efficiency of W-tagging a large-radius jet seeded by quarks and gluons (mis-tag efficiency) is found to be between 0.05 %–2 % in multijet events for this working point.

To correct for the imperfect detector simulation, the W-boson jet and mis-tag efficiencies are derived in data and simulation and factors to correct the simulation are determined [330]. The W-boson jet efficiency is evaluated in $t\bar{t}$ events, while the mis-tag efficiency is in γ+jets and multijet events. Systematic uncertainties on the efficiencies are derived, considering uncertainties due to the modelling of the simulation and the reconstructed objects used in the evaluation of the efficiencies.

7.4.6 Adaptive-radius reclustered jets

The decay products of a hadronically decaying, relatively low-p_{T} W-boson may not be sufficiently collimated to be reconstructed in a large-radius jet. A reconstruction algorithm using an adaptive jet radius is employed [21, 331, 332] to reconstruct such W-bosons inside of one jet. The algorithm utilises the $R = 0.4$ small-radius jets in

an event and forms larger radius jets from them using the anti-k_t algorithm [300, 306].

Initially, all small-radius jets in an event are input into the anti-k_t algorithm with a radius parameter of $R_0 = 3.0$. For each of these reclustered jets, the radius according to the transverse momentum of the reclustered jet and the W-boson mass m_W is calculated:

$$R(p_{\mathrm{T}}) = \frac{2m_W}{p_{\mathrm{T}}}. \tag{7.2}$$

The validity of this relationship can be observed e.g. in Figure 8.1a in Section 8.2. If $R(p_{\mathrm{T}})$ is smaller than R_0 by some constant, then the small-radius jets within a reclustered jet are input into the anti-k_t algorithm again with a decreased radius parameter R_1. The procedure is repeated iteratively until the radius parameter R_i in iteration i is close to the average expected radius $R(p_{\mathrm{T}})$.

Only one reclustered jet candidate is employed per event. If multiple candidate jets emerge from the algorithm, the one with an invariant mass closest to the W-boson mass is selected.

7.5 Missing transverse momentum

Missing transverse momentum is an observable sensitive to particles not leaving a signature in the active detector material, such as neutrinos and BSM particles. As the beams collide head-on in the z-axis of the ATLAS detector, the momenta of all produced particles in the transversal plane must sum to zero [201]. The missing transverse momentum vector $\vec{p}_{\mathrm{T}}^{\,\mathrm{miss}}$ is defined as the negative vectorial sum of all reconstructed and calibrated muons μ, electrons e, small-radius jets j and a soft-term:

$$-\vec{p}_{\mathrm{T}}^{\,\mathrm{miss}} \coloneqq \sum_{\mu} \vec{p}_{\mathrm{T}}^{\,\mu} + \sum_{e} \vec{p}_{\mathrm{T}}^{\,e} + \sum_{j} \vec{p}_{\mathrm{T}}^{\,j} + \vec{p}_{\mathrm{T}}^{\,\mathrm{soft}}.$$

The soft-term accumulates contributions to the total transverse momentum in an event stemming from other sources than the reconstructed particles. It is defined as the sum of the $\vec{p}_{\mathrm{T}}$ of all particle-flow tracks compatible with primary vertex and unassociated to any of the reconstructed objects.

In the analysis presented in this thesis, the magnitude $E_{\mathrm{T}}^{\mathrm{miss}}$ of the $\vec{p}_{\mathrm{T}}^{\,\mathrm{miss}}$ and its azimuth ϕ_{miss} are commonly used. Reconstructed particles whose momentum is poorly reconstructed can artificially increase the measured $E_{\mathrm{T}}^{\mathrm{miss}}$ ("fake $E_{\mathrm{T}}^{\mathrm{miss}}$"). Techniques to suppress events with large fake $E_{\mathrm{T}}^{\mathrm{miss}}$ contributions are discussed in Chapter 9.

7.6 Quality selection criteria

Not all reconstructed particles and objects are used in the analysis presented in Chapter 8. The selection of objects employed is discussed in this section.

For each type of object, two quality criteria are defined, referred to as "baseline" and "signal", with the latter being a subset of the former. The baseline objects are used to calculate the $E_{\mathrm{T}}^{\mathrm{miss}}$ and to resolve ambiguities with other objects. Signal objects are used to define the signal enhanced phase space regions in the analysis.

Baseline electrons must satisfy the `Loose` identification working point conditions, have a minimum p_{T} of 4.5 GeV and $|\eta| < 2.47$. To suppress electrons from pile-up interactions, the impact parameter $|z_0 \cdot \sin\theta|$ must be below 0.5 mm. Signal electrons must fulfil the conditions of the `Medium` identification working point and

to have a $p_{\mathrm{T}} > 20\,\mathrm{GeV}$. For transverse momenta below 200 GeV, the `Loose` isolation working point utilising both track and calorimeter information must be passed by signal electrons. Signal electrons of higher p_{T} must be isolated according to the `HighPtCaloOnly` working point using only calorimeter information. To suppress electrons from pile-up interactions, the transverse impact parameter significance is required to be $|{}^{d_0}/_{\sigma_{d_0}}| < 5$ for signal electrons.

Muons are categorised as baseline, if they have a $p_{\mathrm{T}} > 4\,\mathrm{GeV}$, an $|\eta| < 2.7$, a $|z_0 \cdot \sin\theta| < 0.5\,\mathrm{mm}$ and pass the `Medium` identification working point conditions. To reject muons from hadron decays and pile-up interactions, signal muons must additionally satisfy the `Loose` isolation working point and $|{}^{d_0}/_{\sigma_{d_0}}| < 3$, respectively. The p_{T} of signal muons must be greater than 20 GeV. Events containing cosmic or poorly reconstructed muons are rejected.

Baseline jets are required to fulfil $p_{\mathrm{T}} > 20\,\mathrm{GeV}$ and $|\eta| < 4.5$. The JVT and fJVT are used to suppress jets from pile-up interactions. The JVT is only applied to jets with a $p_{\mathrm{T}} < 60\,\mathrm{GeV}$ and $|\eta| < 2.4$, while the fJVT is only applied to jets with an $|\eta| > 2.5$ and a $p_{\mathrm{T}} < 50\,\mathrm{GeV}$. Signal jets must be within $|\eta| < 2.5$ and have a $p_{\mathrm{T}} > 30\,\mathrm{GeV}$. Jets are b-tagged with the `DL1r` tagger with a b-jet efficiency of 85 % (baseline) and 77 % (signal). Baseline b-tagged jets must have a $p_{\mathrm{T}} > 30\,\mathrm{GeV}$ and an $|\eta| < 2.5$.

Trimmed large-radius jets must fulfil $200\,\mathrm{GeV} < p_{\mathrm{T}} < 2.5\,\mathrm{TeV}$ and have a mass in the range $40\,\mathrm{GeV} < m_{\mathrm{comb}} < 600\,\mathrm{GeV}$. Large-radius jets with an $|\eta| > 2.0$ are discarded.

Ambiguities of reconstructed objects with overlapping tracks or calorimeter energy clusters are resolved in a hierarchical procedure using the baseline definitions. Electrons which share a track with a muon are removed. Non-b-tagged jets within $\Delta R = 0.2$ of an electron are discarded. To reject electrons emerging from a hadron decay, their angular distance to the remaining jets must be greater than $\Delta R_{\mathrm{slide}} = \min(0.4, 0.04 + {}^{10\,\mathrm{GeV}}/_{p_{\mathrm{T}}^{\ell}})$ with p_{T}^{ℓ} the p_{T} of the electron. A muon is favoured over a jet if it is ghost associated (see Section 7.4.4) to the jet and the latter contains less than three tracks. Similarly to electrons, muons within $\Delta R_{\mathrm{slide}}$ of the remaining jets are removed. Finally, large-radius jets which contain an electron or muon are discarded.

All object selection criteria are summarised in Table 7.1.

Electrons		
	Baseline	*Signal*
p_{T} [GeV]	≥ 4.5	≥ 20
$\lvert\eta\rvert$	< 2.47	
Identification working point	`Loose`	`Medium`
Isolation working point	–	`Loose` if $p_{\mathrm{T}} < 200\,\mathrm{GeV}$ else `HighPtCaloOnly`
Longitudinal impact parameter	$\lvert z_0 \cdot \sin\theta\rvert < 0.5\,\mathrm{mm}$	
Transversal impact parameter	–	$\lvert d_0/\sigma_{d_0}\rvert < 5$

Muons		
	Baseline	*Signal*
p_{T} [GeV]	≥ 4	≥ 20
$\lvert\eta\rvert$	< 2.7	
Identification working point	`Medium`	
Isolation working point	–	`Loose`
Longitudinal impact parameter	$\lvert z_0 \cdot \sin\theta\rvert < 0.5\,\mathrm{mm}$	
Transversal impact parameter	–	$\lvert d_0/\sigma_{d_0}\rvert < 3$

Small-radius jets & b-tagging		
	Baseline jets	*Signal jets*
p_{T} [GeV]	≥ 20	≥ 30
$\lvert\eta\rvert$	< 4.5	< 2.5
JVT	If $p_{\mathrm{T}} < 60\,\mathrm{GeV}$, $\lvert\eta\rvert < 2.4$	
fJVT	If $\lvert\eta\rvert > 2.5$, $p_{\mathrm{T}} < 50\,\mathrm{GeV}$	
b-tagged jets	*Baseline*	*Signal*
p_{T} [GeV]	≥ 30	
$\lvert\eta\rvert$	< 2.5	
Tagger	DL1r	
Working point	85 % efficiency	77 % efficiency

Large-radius jets & W-tagging	
p_{T} [GeV]	$200\,\mathrm{GeV} < p_{\mathrm{T}} < 2.5\,\mathrm{TeV}$
m_{comb} [GeV]	$40\,\mathrm{GeV} < m_{\mathrm{comb}} < 600\,\mathrm{GeV}$
$\lvert\eta\rvert$	< 2.0
Trimming parameters	$R_{\mathrm{sub}} = 0.2$, $f_{\mathrm{cut}} = 0.05$
W-tagging working point	50 % efficiency

Overlap removal	
Remove	*If*
Electron	Shares a track with a muon
Non-b-tagged jet	Within $\Delta R = 0.2$ of an electron
Electron	Within $\Delta R_{\mathrm{slide}}$ of a jet
Jet	Muon ghost associated and < 3 tracks
Muon	Within $\Delta R_{\mathrm{slide}}$ of a jet
Large-radius jet	Contains an electron or muon

Table 7.1: Summary of the object selection criteria. Objects are removed by the overlap removal in the given order from top to bottom.

Chapter 8

Searching for dark matter in association with a top-quark and a W-boson

The tW+DM signature is described by the associated production of dark matter (DM) particles, a top-quark and a W-boson. As was discussed in Section 4.2, the tW+DM signature is a key signature to test the 2HDM+a model, due to its large cross-section. A search for DM particles in this signature is presented in the following chapters. The search results have been published in Reference [22]. The data and triggers used, properties of the signal, the SM background processes, the strategy of the search and the statistical analysis are presented in this chapter.

8.1 Dataset and triggering

The presented analysis uses the full run-II dataset obtained at a centre-of-mass energy of 13 TeV between 2015 and 2018 with the ATLAS detector. Only data of high quality [200] is used in the analysis. The integrated luminosity of the resulting dataset corresponds to $139\,\text{fb}^{-1}$ with an uncertainty of 1.7 % [197], as determined with the primary luminosity measuring detector LUCID-2 [198].

Events selected in the search must pass the $E_{\text{T}}^{\text{miss}}$ [213, 333] or the single lepton triggers [334–336]. For events with a $E_{\text{T}}^{\text{miss}} \geq 250\,\text{GeV}$, the $E_{\text{T}}^{\text{miss}}$ trigger has an efficiency of 99 % of firing on such events [333]. The single lepton triggers are sensitive to events with at least one reconstructed electron or muon passing certain conditions on the momentum, identification and isolation. The minimum p_{T} threshold of the single lepton triggers used in this thesis are 20 GeV (muons) and 24 GeV (electrons) for the data collected in 2015 [334] and 26 GeV (electrons and muons) for the data collected from 2016-2018 [335, 336].

8.2 Signal characterisation

The Feynman diagrams with the largest cross-section of the tW+DM signature are shown in Figures 4.1e and 4.1f. Due to its short lifetime, the top-quark decays before hadronising. In more than 99 % of the cases the top-quark decays into a W-boson and a b-quark [25]. Hence, two W-bosons can be found in the tW+DM final state. Each of these W-bosons decays either into two quarks or into a charged lepton and a corresponding neutrino. Therefore, signal events contain either zero,

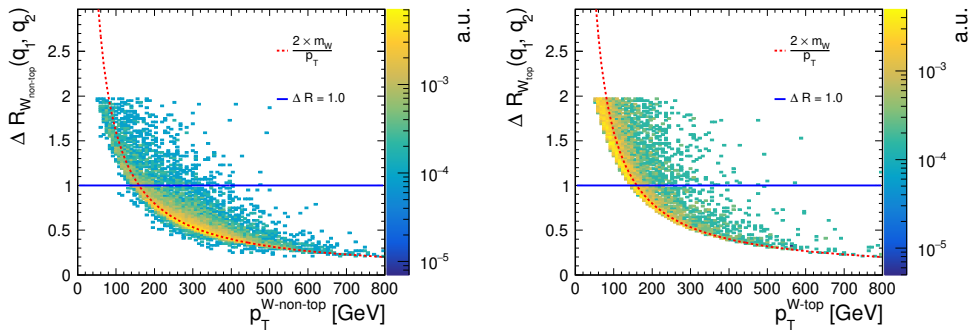

(a) (b)

Figure 8.1: Distribution of the angular distance $R_W(q_1, q_2)$ between the two quarks from a hadronically decaying W-boson versus the boson's p_T at particle level. The distribution in (a) considers W-bosons from the $H^\pm$-boson decay (Figure 4.1e) and from the $b \to Wt$ vertex (Figure 4.1f), while in (b) W-bosons that originate from the top-quark decay are considered. Both distributions are normalised to unity. The signal sample used for the distributions is generated with the 2HDM+a model parameters $m_a = 250\,\mathrm{GeV}$, $m_{H^\pm} = 800\,\mathrm{GeV}$, $\tan\beta = 1$ and $\sin\theta = 0.7$.

one or two reconstructed leptons[1] (electrons, muons). Three analysis channels are defined accordingly, denoted as the 0L, 1L and 2L channel, respectively, selecting events with the corresponding number of reconstructed leptons. This thesis mainly focusses on the 1L channel. The 0L channel is introduced alongside with the 1L channel for completeness, as the 1L and 0L channels are developed to be statistically combined. Results from the statistical combination of the 1L and 0L channels are shown in Chapter 11. The 2L channel from Reference [21] is also combined with the 1L and 0L channels and results from the combination are presented in Chapter 12. The technical implementation of a statistical combination is discussed in Section 8.5.

Since at least one W-boson decays into quarks in the 1L and 0L channels, several $R = 0.4$ small-radius jets can be found in signal events, with their number being greater in the 0L than in the 1L channel, due to the additional hadronic W-boson decay. In both channels the signal contains at least one small-radius jet from the hadronisation of the b-quark from the top-quark decay. Furthermore, due to the DM particles escaping the detector without interacting, signal events are characterised by large $E_\mathrm{T}^\mathrm{miss}$ (see e.g. Section 3.5.3).

The W-boson emerging from the decay of the $H^\pm$-boson is, depending on the 2HDM+a model parameters, likely to have a relatively high p_T. The W-boson from the $b \to Wt$ vertex in the a-boson diagram may also be highly energetic. Such high-p_T W-bosons can be reconstructed in a large-radius jets ($R = 1.0$) if decaying into quarks. The large-radius jet can be identified with the help of W-tagging (see Section 7.4.5). The W-bosons from the top-quark decays are less likely to have a high p_T.

To assess the probability of reconstructing hadronic W-boson decays in an $R = 1.0$ large-radius jet, the angular distance $R_W(q_1, q_2)$ between the two quarks of the W-boson decays is studied at particle level for a benchmark signal with $m_a = 250\,\mathrm{GeV}$, $m_{H^\pm} = 800\,\mathrm{GeV}$, $\tan\beta = 1$ and $\sin\theta = 0.7$. For this benchmark signal, $R_W(q_1, q_2)$ is shown in Figure 8.1a as a function of the W-boson p_T for W-bosons that are not from a top-quark decay. The production of these W-bosons is driven

[1] Events where at least one $W \to \tau\nu_\tau$ and an isolated electron or muon is produced in the τ-lepton decay are included in this categorisation.

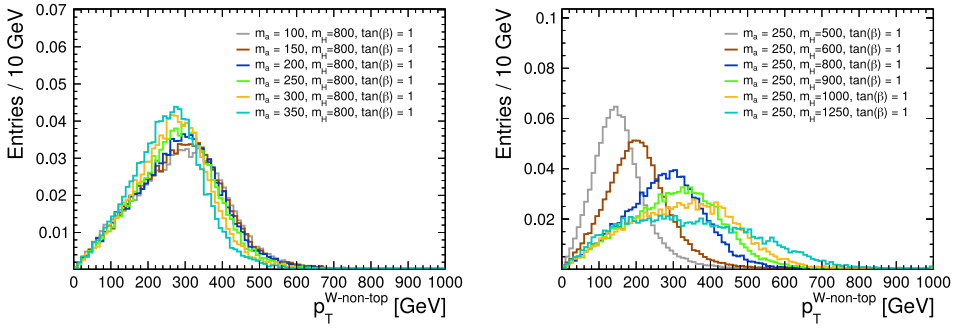

(a) (b)

Figure 8.2: Transverse momentum distribution at particle level for W-bosons that do not originate from a top-quark decay in the signal. The distributions are shown for multiple values of (a) m_a and (b) $m_{H^\pm}$. All distributions are normalised to unity. Unless indicated otherwise, the signal samples are generated with the 2HDM+a model parameters $m_a = 250\,\text{GeV}$, $m_{H^\pm} = 800\,\text{GeV}$, $\tan\beta = 1$ and $\sin\theta = 0.7$.

by decays of the $H^\pm$-boson for the benchmark signal, as the Feynman diagram involving the $H^\pm$-boson decay dominates the cross-section for the model parameters. The color coding in Figure 8.1a indicates the relative fraction of events in a given range of the $R_W(q_1, q_2)$ and the W-boson p_T. A correlation between the transverse momentum of the W-boson and the quark separation is observed, which is well described by the ratio of the W-boson mass and p_T: $R_W(q_1, q_2)(p_\text{T}) \simeq \frac{2m_W}{p_\text{T}}$. This correlation is observed independently of the 2HDM+a model parameters. For a W-boson p_T greater than 160 GeV, the angular quark distance is most likely below 1.0. For such quark distances, the W-boson decay can be reconstructed in a large-radius jet with radius parameter $R = 1.0$, which can potentially be W-tagged. Most events of the benchmark signal have a transverse momentum of the hadronically decaying W-boson from the $H^\pm$-boson decay or the $b \to Wt$ vertex above 160 GeV and can therefore be reconstructed in a large-radius jet.

The probability of reconstructing a hadronically decaying W-boson from the $H^\pm$-boson decay or the $b \to Wt$ vertex in a large-radius jet as a function of the 2HDM+a model parameters is studied. Due to the correlation of the $R_W(q_1, q_2)$ and the W-boson p_T, it is sufficient to examine the latter quantity. Since the selected $R = 1.0$ large-radius jets must have a $p_\text{T} > 200\,\text{GeV}$ in this search (Section 7.6), only hadronically decaying W-bosons with a transverse momentum greater than 200 GeV are considered as reconstructable in an $R = 1.0$ large-radius jet. Particle level distributions of the p_T of the W-boson that is not from the top-quark are shown for multiple values of m_a in Figure 8.2a, of $m_{H^\pm}$ in Figure 8.2b and of $\tan\beta$ in Figure 4.3a. The model parameters that are not varied are set to the parameters of the benchmark signal $m_a = 250\,\text{GeV}$, $m_{H^\pm} = 800\,\text{GeV}$, $\tan\beta = 1$ and $\sin\theta = 0.7$. All of the shown distributions are normalised to unity.

As can be seen in Figure 8.2a, the transverse momentum distribution of the W-boson slightly shifts towards lower p_T as m_a increases from 100 GeV to 350 GeV. This is due to the decreasing mass difference between the $H^\pm$- and a-boson[2], which leaves less energy to the W-boson. As the mass difference is still well above the W-boson mass for all probed values of m_a, the change in p_T is not very large. The p_T is most likely above 200 GeV for all values of m_a for the studied value of $m_{H^\pm}$.

[2]The diagram involving the $H^\pm$-boson dominates the total cross-section for $m_{H^\pm} = 800\,\text{GeV}$.

As a function of $m_{H^\pm}$, the transverse momentum of the W-boson from the $H^\pm$-boson or from the $b \to Wt$ vertex is most likely below 200 GeV for $m_{H^\pm} = 500\,\text{GeV}$. Hadronic decays are unlikely to be reconstructed within an $R = 1.0$ large-radius jet for such a signal. The relatively low p_T of the W-boson is due to mass difference between the $H^\pm$- and the a-boson ($m_a = 250\,\text{GeV}$), leaving little energy for the momentum of the W-boson. For values of $m_{H^\pm} \geq 600\,\text{GeV}$ the majority of the W-bosons from the $H^\pm$-boson or the $b \to Wt$ vertex are expected to have a $p_\text{T} > 200\,\text{GeV}$. The most probable transverse momentum of the W-boson increases as $m_{H^\pm}$ increases until $m_{H^\pm} \simeq 1000\,\text{GeV}$. This can be explained by the dominance of the $H^\pm$-boson diagram in this regime and that with increasing $m_{H^\pm}$, the mass difference to the a-boson increases and more energy is available for the momentum of the W-boson from the $H^\pm$-boson decay. For greater values of $m_{H^\pm} \gtrsim 1000\,\text{GeV}$, the a-radiation Feynman diagram (Figure 4.1f) starts to dominate the tW+DM cross-section as discussed in Section 4.2.1. The W-boson in the $b \to Wt$ vertex of the a-radiation diagram does not emerge from the decay of a heavy particle and has a lower transverse momentum than the W-boson from the $H^\pm$-boson decay. For that reason, the most probable transverse momentum of the W-boson decreases for $m_{H^\pm} > 1000\,\text{GeV}$. However, the fraction of events with a W-boson p_T above 200 GeV does not change significantly compared to lower values of $m_{H^\pm}$. The W-boson from the $b \to Wt$ vertex is also likely to have a relatively high p_T and contributes to the hadronically decaying W-bosons that can be reconstructed in a large-radius jet.

No significant differences of the W-boson's p_T distributions are observed in Figure 4.3a on page 32, where $\tan\beta$ is altered. In conclusion, if the 2HDM+a model is realised with $m_{H^\pm} \geq 600\,\text{GeV}$, most signal events contain a W-boson from the $H^\pm$-boson or the $b \to Wt$ vertex which has a transverse momentum greater than 200 GeV. This W-boson can potentially be reconstructed in an $R = 1.0$ large-radius jet if decaying hadronically. The transverse momentum of the W-boson decreases slightly as m_a increases and is roughly independent of $\tan\beta$.

On the other hand, the W-boson from the top-quark is unlikely to be reconstructed in a large-radius jet. This can be seen in Figure 8.1b, which shows the distribution of simulated signal events in $R_W(q_1, q_2)$ versus the W-boson p_T for hadronically decaying W-bosons from the top-quark. The same benchmark 2HDM+a model parameters as above are used to generate the signal. The correlation between the $R_W(q_1, q_2)$ and the W-boson p_T is described well again by $R_W(q_1, q_2)(p_\text{T}) \simeq \frac{2m_W}{p_\text{T}}$. More than 80 % of the events have an angular quark separation $R_W(q_1, q_2) > 1.0$. The relative fraction of events peaks at a p_T of roughly 70 GeV and smoothly decreases with increasing W-boson p_T. No large differences in the p_T distribution of the W-boson from the top-quark decay are observed for the different 2HDM+a model parameters, as shown exemplarily in Figure 4.3b on page 32 for variations of $m_{H^\pm}$. Therefore, reconstructing hadronically decaying W-bosons from the top-quark in a large-radius jet ($R = 1.0$) is unlikely. This feature of the signal is used in the 1L channel as discussed in Section 9.1.

8.3 Standard Model background

Background to the search for the tW+DM signal arises from multiple SM processes. Simulated samples, produced as described in Section 6.7, are utilised to study the background composition and reduction techniques. The background composition is found to be different among the 1L and 0L analysis channels.

Large contributions to the background are from the production of a top-quark pair ($t\bar{t}$). Each of the top-quarks most likely decays into a b-quark and a W-boson. As the W-bosons can decay into quarks or leptons, the $t\bar{t}$ final state is characterised

by zero, one or two charged leptons, denoted respectively as hadronic, semi-leptonic and di-leptonic $t\bar{t}$ decays.

The most dominant background processes in the 1L channel are $t\bar{t}$, the associated production of a W-boson and jets (W+jets) and the associated production of a top-quark pair and a Z-boson ($t\bar{t}+Z$). Semi-leptonic $t\bar{t}$ decays have a similar event topology to the signal in the 1L channel, see the Feynman diagrams in Figures 8.3a and 8.3b. They can, however, be reduced to a negligible fraction exploiting kinematic features of this background process compared to the signal, as discussed in Section 9.1. Di-leptonic $t\bar{t}$ decays represent the largest SM background in the 1L channel. Such events contribute to the background, if one of the two charged leptons is a hadronically decaying τ-lepton, escapes detection or if an electron or muon in the final is misidentified as a jet. An example Feynman diagram of a di-leptonic $t\bar{t}$ decay contributing to the background is shown in Figure 8.3c, where a charged lepton escapes detection. Furthermore, the $t\bar{t}+Z$ process is one of the most dominant SM backgrounds in the 1L channel. This is due to its similarity with the signal topology if the Z-boson decays into neutrinos and the W-boson from one of the top-quarks decays into leptons as shown in Figure 8.3e. Another sizeable background process in the 1L channel is W+jets. Events where the W-boson decays into leptons contribute significantly to the SM background. A corresponding Feynman diagram is shown in Figure 8.3d. The SM production of single top quarks is another sizeable background process in the 1L channel, dominated by the associated production of a top-quark and a W-boson (tW). A Feynman diagram of this background process is shown in Figure 8.3f. In this diagram both W-bosons in the final state, one being from the decay of the top-quark, decay into leptons. One of the charged leptons escapes detection. Less significant background contributions stem from the associated production of two vector bosons (VV) and other rare processes, such as the associated production of three top-quarks or three vector bosons. The background reduction strategy for the 1L channel is the subject of Section 9.1.

In the 0L channel, the most dominant background processes are $t\bar{t}$, W+jets and the associated production of a Z-boson and jets (Z+jets). Semi-leptonic $t\bar{t}$ decays constitute a large fraction of the SM background in the 0L channel. They contribute to the background if the charged lepton is a hadronically decaying τ-lepton, escapes detection or if an electron or muon is misidentified as a jet. The similarity of the final states of the signal and this $t\bar{t}$ background can be seen from the Feynman diagrams in Figures 8.4a and 8.4b. The W+jets process with the W-boson decaying into leptons $\ell\nu$ contributes to the background by the same means as semi-leptonic $t\bar{t}$ decays do, e.g. if the charged lepton ℓ escapes detection. An example Feynman diagram is shown in Figure 8.4c. The Z+jets process also largely contributes to the background in the 0L channel. If the Z-boson decays to neutrinos, the experimental signature of the Z+jets process is similar to the signal with large $E_{\mathrm{T}}^{\mathrm{miss}}$ from the Z-boson decay and multiple jets in the final state, see Figure 8.4d. A background in the 0L channel is the production of multiple jets, e.g. from QCD interactions or hadronic $t\bar{t}$ decays. A Feynman diagram of a hadronic $t\bar{t}$ decay is shown in Figure 8.4e. This multi-jet background, not characterised by large genuine $E_{\mathrm{T}}^{\mathrm{miss}}$, is only relevant if large $E_{\mathrm{T}}^{\mathrm{miss}}$ originates from the mismeasurement of jets. Using this property, it can be reduced to a negligible fraction. The SM production of single top quarks, dominated by tW, as well as the VV, $t\bar{t}+Z$ and other SM processes are minor backgrounds in the 0L channel. As an example, a VV Feynman diagram is shown in Figure 8.4f. The reduction of the different background processes for the 0L channel is discussed in Section 9.2.

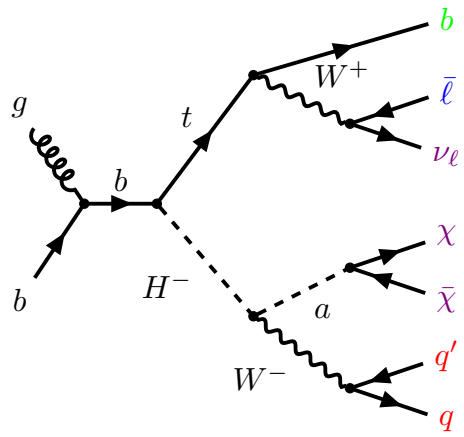

(a) 1L signal

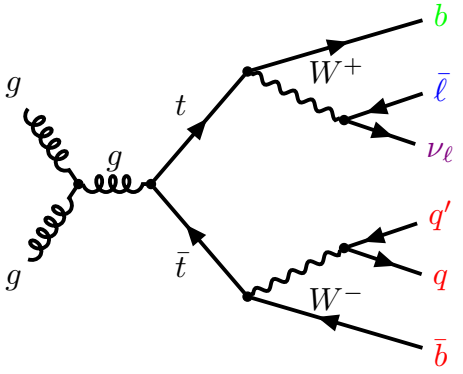

(b) Semi-leptonic $t\bar{t}$ decay

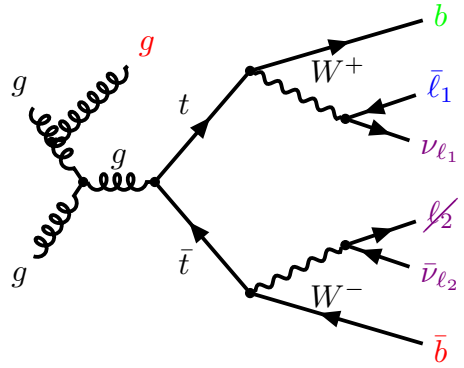

(c) Di-leptonic $t\bar{t}$ decay

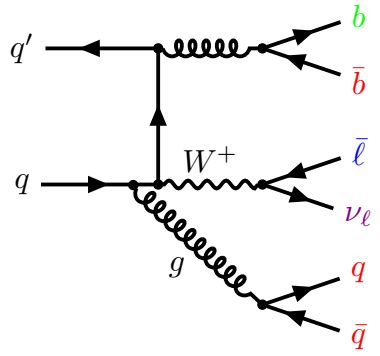

(d) W+jets

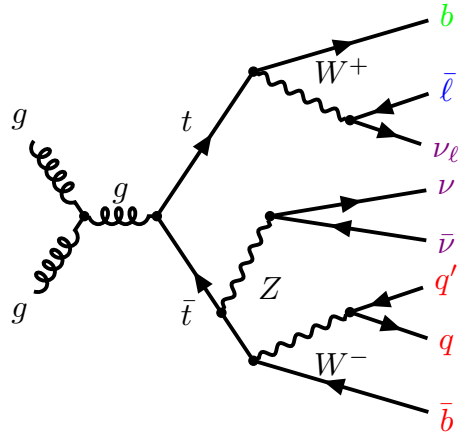

(e) $t\bar{t} + Z$

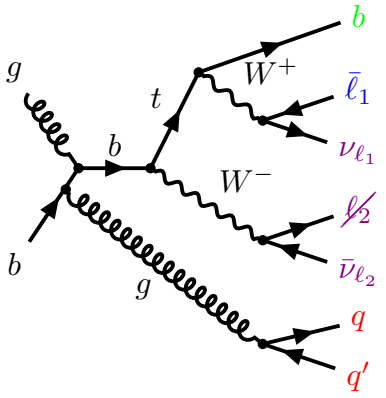

(f) Single top quark (tW)

Figure 8.3: Examples of Feynman diagrams of background processes in the 1L channel. A crossed-out charged lepton indicates that it escapes detection. The similarity of the final states of the SM processes to the signal is highlighted by different colours: a b-quark (green), a charged lepton (blue), particles that escape detection (violet) and additional quarks and gluons (red).

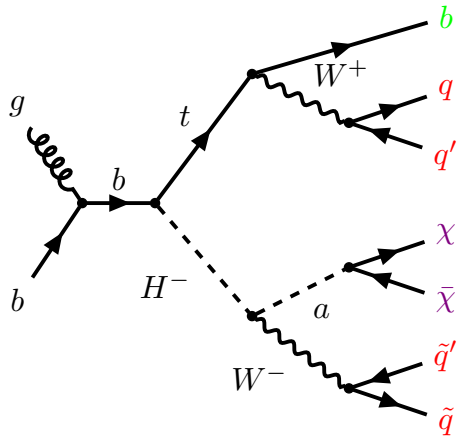

(a) 0L signal

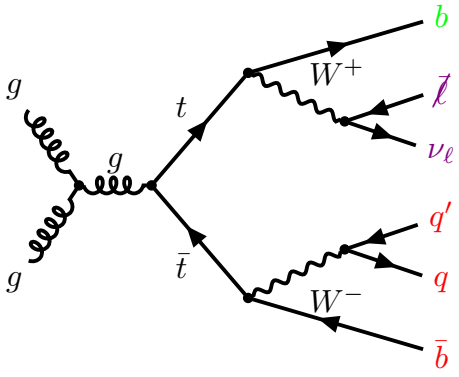

(b) Semi-leptonic $t\bar{t}$ decay

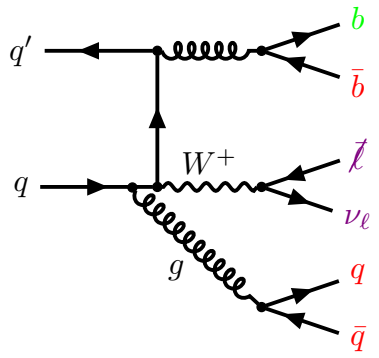

(c) W+jets

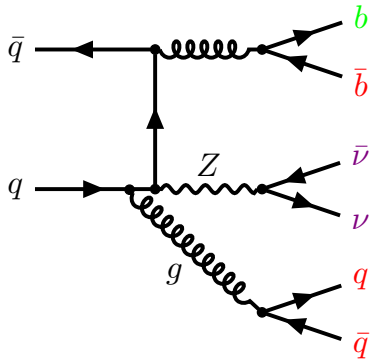

(d) Z+jets

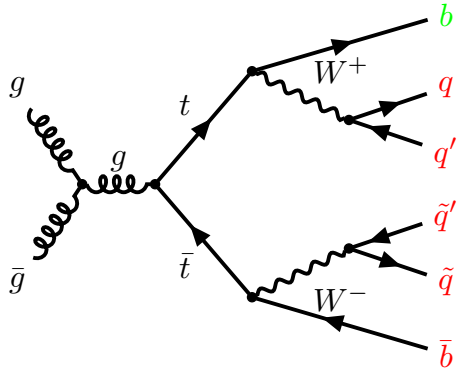

(e) Hadronic $t\bar{t}$ decay

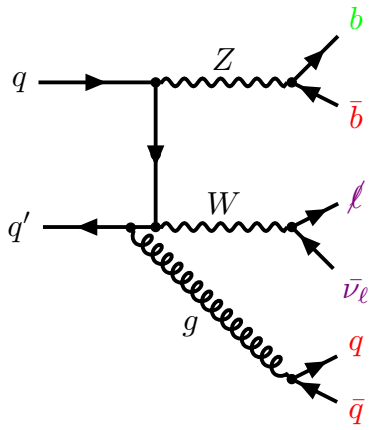

(f) VV

Figure 8.4: Examples of Feynman diagrams of background processes in the 0L channel. A crossed-out charged lepton indicates that it escapes detection. The similarity of the final states of the SM processes to the signal is highlighted by different colours: a b-quark (green), particles that escape detection (violet) and additional quarks (red).

8.4 Analysis strategy

This thesis presents a search for DM particles in the tW+DM signature. The work is published in Reference [22] and uses the search published in Reference [21] as supporting previous result. The search follows a particular strategy: phase space regions enriched in the signal (signal regions (SRs)) are defined for the 1L and 0L channels with the help of simulated signal and background events. Constraints on dedicated variables exploiting kinematic features of the signal are used for the regions' definitions, as discussed in Chapter 9. Due to the correlation of the variables, an optimisation procedure is employed, to achieve the ideal separation of signal and background in terms of a figure of merit.

Different distributions of the $E_{\mathrm{T}}^{\mathrm{miss}}$ are expected for varying differences of the 2HDM+a model parameters $m_{H^{\pm}}$ and m_a, which define the DM momentum spectrum. To increase the sensitivity towards a multitude of signals with differing model parameters, the SRs of the 1L and 0L channels are divided into multiple $E_{\mathrm{T}}^{\mathrm{miss}}$ bins, which are then statistically combined.

To achieve an accurate description of the SM background, dedicated regions of phase space (control regions (CRs)) are utilised. Normalisation parameters, as discussed in Section 8.5 below, are defined for each of the background processes $t\bar{t}$, Z+jets, W+jets, $t\bar{t}+Z$ and single top quark. These parameters are derived with the help of the CRs in a semi-data-driven manner. The $t\bar{t}$ background is dominated by di-leptonic decays in the 1L channel and by semi-leptonic decays in the 0L channel. Dedicated normalisation parameters and CRs are defined to estimate the $t\bar{t}$ contribution as accurately as possible in the two channels. Common normalisation parameters and CRs are used for all other background processes. The definition of the CRs utilises simulated signal and background events. They are designed such that the purity of the target process is high, while the contribution from signal events is negligible. The phase spaces of the CRs must be non-overlapping with the SRs' ones, yet close. The CRs employed in this search are detailed in Section 10.1.

The background predictions estimated with the help of the CRs are verified using dedicated validation regions (VRs). For each of the dominant background processes in the 0L channel, one VR is defined and likewise in the 1L channel. In the presented search, the phase spaces of VRs must be non-overlapping with the phase spaces of all SRs and CRs, while being closer to the SRs' phase spaces than the phase spaces of the CRs. A VR is designed to be enriched in the SM processes it is meant to verify and to contain a low fraction of signal events. The VRs used in this search are described in Section 10.2.

Once the background estimation has been verified in the VRs, the expected SM background yields in the SRs are estimated and compared to data. Upper limits on the number of BSM physics signal events are set for a generic BSM physics signal by performing multiple hypothesis tests. Furthermore, exclusion limits on the normalisation of 2HDM+a model signals are derived. These limits give rise to exclusion limits on the 2HDM+a model parameters. More details on these steps of the statistical analysis are given in the following section.

8.5 Statistical analysis

The estimation of the normalisation parameters of the SM background processes is based on the maximisation of a likelihood function [26]. The hypothesis tests that are performed in the statistical analysis use the ratio of maximised likelihood functions. A likelihood function quantifies the agreement between the data and a prediction in a set of phase space regions. The data is assumed to be Poisson distributed. The agreement of the data with the prediction is implemented as con-

ditional probability in the likelihood function. The prediction is given by the sum of the expected signal and the SM background yields, which are scaled by normalisation parameters μ_{sig} and μ_j for each SM background process j, respectively. These normalisation parameters are allowed to float freely. Systematic uncertainties impacting the number of predicted events are implemented as nuisance parameters θ_k in the likelihood and assumed to be Gaussian or Poisson distributed. That means that the nuisance parameters cannot float freely, but are constrained by additional Gaussian or Poisson terms. Poisson terms are only used for the uncertainties related to the limited number of simulated events and Gaussian terms otherwise.

Conditional probabilities are multiplied for each region of phase space to be included in the background determination or hypothesis testing. The resulting likelihood function takes the form [26]:

$$\mathcal{L}(\boldsymbol{N}, \mu_{\text{sig}}, \boldsymbol{\theta}) = \prod_{i \in \text{ regions}} P(N_i | \mu_{\text{sig}} s_i(\boldsymbol{\theta}) + \sum_j \mu_j b_{i,j}(\boldsymbol{\theta})) \cdot \mathcal{C}(\boldsymbol{\theta}), \tag{8.1}$$

with N_i the observed data count in each analysis region i and $\boldsymbol{N}$ the vector of counts, $\boldsymbol{\theta}$ the set of systematic uncertainty nuisance parameters θ_k, s_i the signal prediction in analysis region i, $b_{i,j}$ the prediction of background process j in region i, $\mathcal{C}$ describing the Gaussian or Poisson terms constraining the θ_k. The Poisson probability density function is denoted by P.

For uncertainties constrained by a Gaussian term, the Gaussian is assumed to have a central value of zero and a width of one [26, 337]. For nuisance parameter values of plus or minus one, alternative signal and SM predictions are used to evaluate the change in the yield in each region. Interpolation functions are employed to estimate the impact of a nuisance parameter α on the yields for values of α other than zero or plus or minus one.

The negative logarithm of the likelihood in Equation (8.1) is minimised to determine the normalisation parameters of the SM background processes and in all hypothesis tests. This corresponds to maximising the likelihood, but is computationally more advantageous. In the following, the SM background normalisation parameters will be included in the set of nuisance parameters $\boldsymbol{\theta}$ for convenience.

8.5.1 Hypothesis testing

Hypothesis tests are used to quantify the agreement of the data with the background prediction and to derive exclusion limits on the normalisation of BSM physics signals. In the former case, a background-only hypothesis test is conducted, in the latter case a signal-plus-background hypothesis test is. Different test statistics are used for the two types of hypothesis tests, both based on the profile likelihood ratio $\lambda(\mu_{\text{sig}}, \boldsymbol{N})$ [338]

$$\lambda(\mu_{\text{sig}}, \boldsymbol{N}) \coloneqq -2 \ln \left(\frac{\mathcal{L}(\boldsymbol{N}, \mu_{\text{sig}}, \tilde{\boldsymbol{\theta}})}{\mathcal{L}(\boldsymbol{N}, \widehat{\mu_{\text{sig}}}, \widehat{\boldsymbol{\theta}})} \right).$$

In this equation $\tilde{\boldsymbol{\theta}}$ denotes the set of nuisance parameters for which the likelihood is maximal given a fixed μ_{sig}. The likelihood is globally maximised for the parameters $\widehat{\mu_{\text{sig}}}$ and $\widehat{\boldsymbol{\theta}}$. The function λ is close to zero if the data agrees well with the signal-plus-background prediction for the fixed normalisation parameter μ_{sig}, and larger otherwise.

Based on λ, test statistics $q(\boldsymbol{N})$ are defined to test the background-only hypothesis or the signal-plus-background hypotheses. A low value of $q(\boldsymbol{N})$ indicates good agreement of the data with the tested hypothesis, while a high value of q

indicates bad agreement. For a given test-statistic q, the p-value is calculated:

$$p_q(\boldsymbol{N}, \xi) = \int_{q(\boldsymbol{N})}^{\infty} f(q, \xi)\, \mathrm{d}q.$$

The p-value depends on the probability density function (PDF) $f(q, \xi)$ of q under the assumption that the data follows the signal-plus-background hypothesis with the signal normalisation parameter ξ. The PDF $f(q, \xi)$ is calculated in this thesis by exploiting that $f(q, \xi)$ can be approximated by an asymptotic formula made up of a transformed, non-central χ^2 distribution for event counts above roughly five [338].

When testing the background-only hypothesis, following test statistic is used [338]:

$$q_{\mathrm{bkg}}(\boldsymbol{N}) \coloneqq \begin{cases} \lambda(0, \boldsymbol{N}), & \widehat{\mu_{\mathrm{sig}}} \geq 0, \\ 0 & \widehat{\mu_{\mathrm{sig}}} < 0. \end{cases}$$

The background-only hypothesis is rejected, if $p_{q_{\mathrm{bkg}}}(\boldsymbol{N}, \xi = 0) < 0.05$.

To test the signal-plus-background hypothesis, as done when deriving model-independent and model-dependent exclusion limits, following test-statistic is used [338]

$$q_{\mathrm{s+b}}(\mu_{\mathrm{sig}}, \boldsymbol{N}) \coloneqq \begin{cases} -2\ln(\frac{\mathcal{L}(\boldsymbol{N}, \mu_{\mathrm{sig}}, \tilde{\boldsymbol{\theta}})}{\mathcal{L}(\boldsymbol{N}, \widehat{\mu_{\mathrm{sig}}}, \widehat{\boldsymbol{\theta}})}), & 0 \leq \widehat{\mu_{\mathrm{sig}}} \leq \mu_{\mathrm{sig}}, \\ -2\ln(\frac{\mathcal{L}(\boldsymbol{N}, \mu_{\mathrm{sig}}, \tilde{\boldsymbol{\theta}})}{\mathcal{L}(\boldsymbol{N}, 0, \tilde{\boldsymbol{\theta}}(0))}), & \widehat{\mu_{\mathrm{sig}}} < 0, \\ 0, & \mu_{\mathrm{sig}} < \widehat{\mu_{\mathrm{sig}}}. \end{cases}$$

Model-independent and model-dependent exclusion limits on the signal normalisation parameter are derived using the $\mathrm{CL_s}$ [339–342]:

$$\mathrm{CL_s}(\mu_{\mathrm{sig}}, \boldsymbol{N}) \coloneqq \frac{\mathrm{CL_{s+b}}}{\mathrm{CL_b}} \coloneqq \frac{p_{q_{\mathrm{s+b}}}(\mu_{\mathrm{sig}}, \boldsymbol{N}, \xi = \mu_{\mathrm{sig}})}{p_{q_{\mathrm{s+b}}}(\mu_{\mathrm{sig}}, \boldsymbol{N}, \xi = 0)}.$$

Exclusion limits on μ_{sig} are calculated, by solving the equation $\mathrm{CL_s}(\mu_{\mathrm{sig}}, \boldsymbol{N}) = 0.05$ for μ_{sig}. If the upper exclusion limit on μ_{sig} is below one, the signal is deemed as excluded at 95 % CL. Using the $\mathrm{CL_s}$ instead of the p-value to set exclusion limits has the advantage of being more robust against underfluctuations of the data [340].

8.5.2 Expected exclusion limits

Besides deriving the exclusion limits on the signal normalisation parameter of a BSM physics model using the data ("observed limits"), limits are derived to quantify the expected sensitivity under the assumption of the background-only hypothesis [343]. These expected limits are evaluated by replacing the data by the expected number of background events in all of the phase space regions. This dataset is referred to as the Asimov dataset [338]. In what concerns this thesis, the expected number of simulated events is estimated using the background normalisation and nuisance parameters obtained from maximising the likelihood accounting for all regions included in the exclusion limit setting[3], assuming the absence of signal. In that way both the observed and expected limits make use of the best possible background estimate, though the expected limit does indirectly depend on the observed number of events [26]. Systematic uncertainties on the expected limits are derived using the asymptotic formulas presented in Reference [338] and with the refined procedure detailed in Reference [344].

[3]Note that this may include SRs and CRs.

8.5.3 Benefit of statistically combining signal regions

In the simplest case of hypothesis testing, the product of probabilities in the likelihood in Equation (8.1) runs over one SR and the relevant CRs. If statistically combining multiple SRs, the product runs over all of these SRs and the corresponding CRs. The SRs that are to be combined must have phase spaces that do not overlap in this thesis.

The advantage of combining multiple SRs is illustrated by following example [345]. Assume there are two SRs disfavouring a signal, but both not excluding the signal. Both maximum likelihoods employing the individual SRs will then be low. In the simplest case, statistically combining these SRs results in multiplying these maximum likelihoods and hence an even lower combined maximum likelihood. This lower value of the combined likelihood results in a greater value of the test statistic, in turn a lower p-value and a higher chance of excluding the signal. In general, the outcome of a combination is difficult to predict though, as it depends e.g. on the background normalisation factors resulting from the maximisation of the combined likelihood, the PDF of the test statistic and on the $\mathrm{CL_b}$.

An additional reason why statistical combinations are beneficial is that different SRs may be sensitive to different model parameters [345]. The combination of the individual SRs then allows obtaining the most stringent exclusion limits on the model parameters.

When referring to the statistical combination of multiple analysis channels in this thesis, the likelihood becomes a product of the SRs and the CRs of the analysis channels. To maximise the impact of the 1L channel, the signal and control regions are designed to have non-overlapping phase spaces with the regions of the 0L channel. This allows combining the two channels easily.

8.5.4 Statistical analysis procedure

The statistical analysis of the presented search utilises the `HistFitter v0.66.0` framework [26]. The procedure of the statistical analysis in the presented search is the following.

Background-only fit First a background-only fit is carried out, deriving the normalisation and nuisance parameters in the CRs. The product of regions in the likelihood runs over the CRs, but not the SRs in the background-only fit. The normalisation parameters of the SM processes and all nuisance parameters are fit simultaneously. The absence of signal is assumed ($\mu_{\mathrm{sig}} = 0$). Using the normalisation and nuisance parameters obtained from the background-only fit, SM yields in the VRs and SRs are estimated. The yields predicted in the VRs are compared to the data to test the validity of the background estimation. Subsequently, the data and the predicted yields are compared in the SRs and the compatibility of the data with the SM prediction is evaluated.

The yield and uncertainty estimation in the VRs and SRs can be illustrated through the transfer factor method [26]: let $N_{\mathrm{MC}}^{\mathrm{CR}}$ and $N_{\mathrm{MC}}^{\mathrm{other}}$ be the simulated yields for some background process B in a CR dominated by B and some other phase space region, respectively. Denote by μ_B the normalisation parameter of B. Given the observation of $N_{\mathrm{obs}}^{\mathrm{CR}}$ events in the CR, the expected yield $N_{\mathrm{exp}}^{\mathrm{other}}$ of process B in a VR or SR can be estimated by

$$N_{\mathrm{exp}}^{\mathrm{other}} = N_{\mathrm{obs}}^{\mathrm{CR}} \cdot \frac{N_{\mathrm{MC}}^{\mathrm{other}}}{N_{\mathrm{MC}}^{\mathrm{CR}}} = \mu_B N_{\mathrm{MC}}^{\mathrm{other}}. \tag{8.2}$$

The transfer factor is defined as $N_{\mathrm{MC}}^{\mathrm{other}}/N_{\mathrm{MC}}^{\mathrm{CR}}$ and related to μ_B by Equation (8.2). Using the transfer factor method, uncertainties propagated to $N_{\mathrm{exp}}^{\mathrm{other}}$ may cancel

by the ratio in the transfer factor if the uncertainties impact the simulated yields in the two regions similarly.

This behaviour is emulated in the statistical analysis in the presented search by defining a set of normalisation regions. The sum of the total predicted SM events in these normalisation regions is kept constant. For each source of systematic uncertainty two scaling factors are defined. They are given by the ratio of the sum of the nominal yields and the sum of the $\pm 1\sigma$ yields in the normalisation regions, respectively. The $\pm 1\sigma$ predictions in all regions are multiplied with the respective factors and additional nuisance parameters related to the scaling factors are added to the likelihood. The fit is then performed with these modified uncertainties. The use of normalisation regions avoids the double counting of uncertainties when extrapolating from the CRs to the VRs and SRs. Using normalisation regions also makes it beneficial to define the CRs kinematically close to the SRs as is illustrated by the transfer factor: if large extrapolation between regions is avoided and the systematic uncertainties in the SRs and CRs can be kept as similar as possible, they will cancel in the ratio.

In this thesis, the normalisation regions and scaling factors are defined per SM process. For all processes other than $t\bar{t}$, the normalisation regions are given by all CRs. For the $t\bar{t}$ prediction used in the 1L channel, the normalisation regions are given by the 1L channel $t\bar{t}$ CR, as well as the W+jets, $t\bar{t}+Z$ and single top CRs. In the 0L channel, the normalisation regions of the $t\bar{t}$ prediction are defined as the 0L channel $t\bar{t}$ CR and the Z+jets CR.

Model-independent hypothesis tests Following the background-only fit, model-independent hypothesis tests are performed. In each test a generic BSM physics signal and the background prediction are fit in dedicated SRs described in Chapter 9. Instead of using the $E_{\mathrm{T}}^{\mathrm{miss}}$-binned SRs, the SRs used in the model-independent hypothesis tests place different requirements on the minimum $E_{\mathrm{T}}^{\mathrm{miss}}$. One SR is considered per test. The background predictions input into the fits are extrapolated from the CRs using the results of the background-only fit. Firstly, model-independent upper limits on the cross-section of BSM physics signals are derived for each dedicated SR. Secondly, the compatibility of the data with the SM predictions is quantified using a background-only hypothesis test. Generic BSM physics signal statements can only be made if no assumptions on the kinematic distributions of the signal are made. That is the reason why SRs with requirements on the minimum $E_{\mathrm{T}}^{\mathrm{miss}}$ are used instead of binned SRs for the model-independent hypothesis tests. In the latter case assumptions on the distribution of the signal in the different bins would have to be made, while not in the former case. The cross-section of a hypothetical BSM physics signal is varied in the tests via the signal normalisation parameter.

Deriving exclusion limits In the next step, exclusion limits on the parameters of the 2HDM+a model are set. For a variety of simulated 2HDM+a model signals, 95 % CL exclusion limits on the signal normalisation parameter are derived. All SRs (binned in $E_{\mathrm{T}}^{\mathrm{miss}}$) and CRs are included in the likelihood used for the fitting. From the excluded signals, exclusion limits on the 2HDM+a model parameters are obtained.

Chapter 9

Signal regions

Dedicated variables that exploit kinematic features of the signal are employed to define the signal enriched SRs of the search. As these variables are correlated, a dedicated procedure is used to optimise the number of signal events compared to the number of background events in terms of a figure of merit. The optimisation is based on simulated signal and background events.

The discovery significance Z [346, 347] is used as figure of merit for the optimisation. Given the prediction of s signal events and $b \pm \sigma$ background events, with σ the uncertainty on b, as well as setting $n = s + b$, this discovery significance is defined as:

$$Z = \zeta\sqrt{2\left(n\ln\left[\frac{n(b+\sigma^2)}{b^2+n\sigma^2}\right] - \frac{b^2}{\sigma^2}\ln\left[1+\frac{\sigma^2(n-b)}{b(b+\sigma^2)}\right]\right)}, \quad \zeta = \begin{cases} +1, n \geq b, \\ -1, n < b. \end{cases} \tag{9.1}$$

The discovery significance Z is an approximation of the significance obtained from a maximum likelihood based background-only hypothesis test, assuming that n and b are Poisson distributed. This approximation was found to accurately describe the exact significance for $n \gtrsim 4$ and to slightly overestimate it for lower n [347]. In the conventions of particle physics, if the signal were realised in nature (and $n = s + b$ would equal the data), a Z of three would indicate evidence for the existence of the signal and a Z of five would be considered as the discovery of the signal. For the analysis presented in the following, the aim is to maximise Z.

The discovery significance accounts for the statistical nature of event counts as well as for systematic uncertainties of the background prediction (σ). Because calculating all systematic uncertainties in the optimisation procedure is computationally expensive, a constant uncertainty of 20 % on the background is assumed. This value of uncertainty is found to be typical in other DM particle searches in similar phase spaces [21, 348].

The optimisation procedure is as follows. A rough, manual optimisation is performed at first. To further enhance the discovery significance, the random grid search (RGS) algorithm [349] is employed consecutively. The RGS algorithm varies the constraints on the variables randomly and calculates Z for those combinations of constraints for which the signal yield is non-zero. It returns the variable constraints giving the maximum Z. The choice of using the RGS algorithm over the multitude of others (see e.g. Refs. [350, 351]) is motivated by its simplicity and computational inexpensiveness.

The SRs of the 1L and 0L channel are introduced in the following. Main focus is on the 1L channel. To set the context for the statistical combination, the relevant information of the 0L channel detailed in Reference [22] is also given.

9.1 The 1L channel

9.1.1 Anatomy of the signal

There are two W-bosons in the tW+DM signature. One is from the top-quark decay. The other is either from the decay of the $H^{\pm}$-boson in the resonant diagram Figure 4.1e or from the $b \to Wt$ vertex in the a-boson radiation diagram Figure 4.1f. In the 1L channel, one of the two W-bosons in an event decays into leptons, while the other W-boson decays into quarks. Correspondingly, signal events contain one electron or muon, high $E_{\mathrm{T}}^{\mathrm{miss}}$ from the DM particles and the neutrino and at least two small-radius jets. Of these two jets, one is from the b-quark of the top-quark decay and at least one originates from the hadronically decaying W-boson.

Preselection criteria are imposed in the 1L channel in accordance with the signal characteristics and for a coarse background suppression:

- Events are selected if they pass the triggers sensitive to high $E_{\mathrm{T}}^{\mathrm{miss}}$ in an event.
- The reconstructed $E_{\mathrm{T}}^{\mathrm{miss}}$ in an event must be greater than 250 GeV.
- The number $N^{\ell,b}$ of baseline and $N^{\ell,s}$ of signal electrons or muons must equal one. The reconstructed lepton in an event must have a transverse momentum p_{T}^{l1} greater than 30 GeV.
- Selected events are required to contain at least two small-radius jets, that is $N^{j} \geq 2$. The transverse momenta of the two leading-p_{T} jets must be $p_{\mathrm{T}}^{j1} \geq 50\,\mathrm{GeV}$ and $p_{\mathrm{T}}^{j2} \geq 30\,\mathrm{GeV}$.
- Of these small-radius jets, at least one must be b-tagged ($N^{b} \geq 1$). For the p_{T} of the two leading-p_{T} b-jets, $p_{\mathrm{T}}^{b1} \geq 50\,\mathrm{GeV}$ and $p_{\mathrm{T}}^{b2} < 50\,\mathrm{GeV}$ is required[1].
- If large contributions to the $E_{\mathrm{T}}^{\mathrm{miss}}$ stem from a mismeasured jet, the direction of the $\vec{p}_{\mathrm{T}}$ of the jet and of the $\vec{p}_{\mathrm{T}}^{\,\mathrm{miss}}$ may be similar. The fraction of events with large $E_{\mathrm{T}}^{\mathrm{miss}}$ from the mismeasurement of jets is reduced by requiring the minimum azimuth angular difference $\Delta\phi_{\mathrm{min},1-4}$ between the four leading-p_{T} small-radius jets and the $\vec{p}_{\mathrm{T}}^{\,\mathrm{miss}}$ to be greater than 0.5.
- The contribution of background events containing electrons or muons produced in hadron decays ("non-prompt leptons"), as well as objects misidenitified as electrons or muons ("fake leptons") is reduced by employing a transverse mass variable. Denoting by $\vec{p}_{\mathrm{T}}^{\,l}$ the transverse momentum vector of the reconstructed lepton in an event, it is defined as

$$m_{\mathrm{T}}^{\mathrm{lep}} \coloneqq m_T(\vec{p}_{\mathrm{T}}^{\,\mathrm{miss}}, \vec{p}_{\mathrm{T}}^{\,l}) = \sqrt{2|\vec{p}_{\mathrm{T}}^{\,\mathrm{miss}}| \cdot |\vec{p}_{\mathrm{T}}^{\,l}| \left(1 - \cos\Delta\phi(\vec{p}_{\mathrm{T}}^{\,\mathrm{miss}}, \vec{p}_{\mathrm{T}}^{\,l})\right)}. \quad (9.2)$$

  Events with non-prompt and fake leptons are suppressed by requiring $m_{\mathrm{T}}^{\mathrm{lep}} \geq 30\,\mathrm{GeV}$ [352]. The $m_{\mathrm{T}}^{\mathrm{lep}}$ variable is also used to suppress background events with W-bosons decaying into an electron or muon and a neutrino, see Section 9.1.2.

The phase space region defined by these preselection criteria is denoted by $\mathrm{Pre}_{\mathrm{1L}}$. All analysis regions requiring the presence of one electron or muon are a subset of the $\mathrm{Pre}_{\mathrm{1L}}$ in the following. The significance Z of signals generated with different 2HDM+a model parameters is below 0.1. Further optimisation is carried out to construct SRs with an increased Z. The dominant background contributions in the $\mathrm{Pre}_{\mathrm{1L}}$ are semi- and di-leptonic $t\bar{t}$ decays and the W+jets process. The design of

[1] Events with one b-jet are also accepted by the criterion on the second leading-p_{T} b-jet.

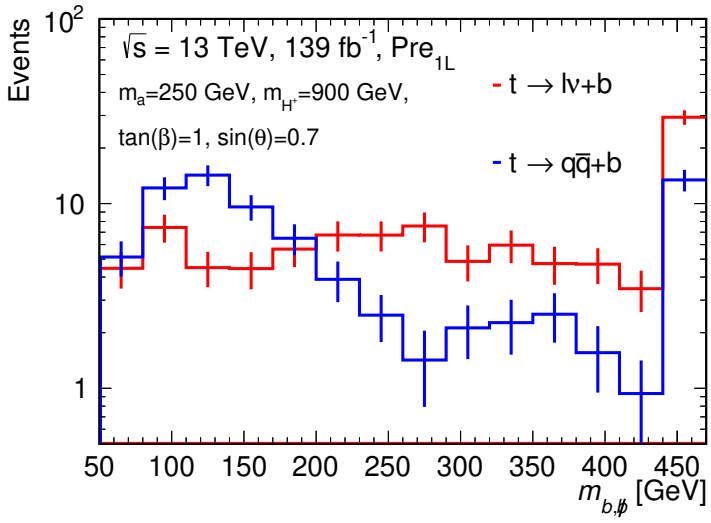

Figure 9.1: Simulated signal events in which the W-boson from the top-quark decays hadronically (blue) are dominantly distributed at $m_{b,\not{p}}$ below roughly the top-quark mass, while events in which the W-boson decays leptonically (red) are distributed more uniformly. Events shown in the figure must fulfil the $\text{Pre}_{1\text{L}}$ criteria. The signal sample used for the plot has the 2HDM+a model parameters $m_a = 250\,\text{GeV}$, $m_{H^\pm} = 900\,\text{GeV}$, $\tan\beta = 1$, $\sin\theta = 0.7$. The shown uncertainties are due to the limited number of simulated events. Events beyond the range of the x-axis are added to the rightmost bin.

the 1L channel SRs in this thesis builds on ideas of References [21, 179, 353] and complements them by utilising W-tagging.

In the 1L channel, one of the W-bosons in the signal decays into leptons and the other into quarks. As was discussed in Section 8.2, the hadronically decaying W-boson from the $H^\pm$-boson decay or the $b \to Wt$ vertex is likely to be reconstructed in an $R = 1.0$ large-radius jet, which can be W-tagged. On the other hand, the hadronically decaying W-boson from the top-quark is unlikely to be reconstructed in a large-radius jet. Two different SRs are defined in the 1L channel, exploiting these different properties. The $\text{SR}_{1\text{L}}^{\text{LepTop}}$ selects events where the W-boson from the top-quark decays into leptons and the W-boson from the $H^\pm$-boson or the $b \to Wt$ vertex decays into quarks. Conversely, the $\text{SR}_{1\text{L}}^{\text{HadTop}}$ selects events where the W-boson from the top-quark decays into quarks and the W-boson from the $H^\pm$-boson or the $b \to Wt$ vertex decays into leptons.

The two regions are defined with the help of the invariant mass $m_{b,\not{p}}$ of the system made up of the leading-p_T b-jet and the leading-p_T small-radius jet that does not pass the b-tagging requirements [179]. If both of these jets are from the top-quark decay, the top-quark mass bounds their invariant mass $m_{b,\not{p}}$, as shown in Figure 9.1. Otherwise, $m_{b,\not{p}}$ is more uniformly distributed, as can be seen in the same figure. To guarantee a good separation between events with a leptonic and hadronic top-quark decay, events in the $\text{SR}_{1\text{L}}^{\text{LepTop}}$ are required to fulfil $m_{b,\not{p}} \geq 200\,\text{GeV}$, while events are selected in the $\text{SR}_{1\text{L}}^{\text{HadTop}}$ if $m_{b,\not{p}}$ is $< 200\,\text{GeV}$. These requirements also make the phase spaces of the $\text{SR}_{1\text{L}}^{\text{LepTop}}$ and $\text{SR}_{1\text{L}}^{\text{HadTop}}$ non-overlapping such that the two regions can be statistically combined.

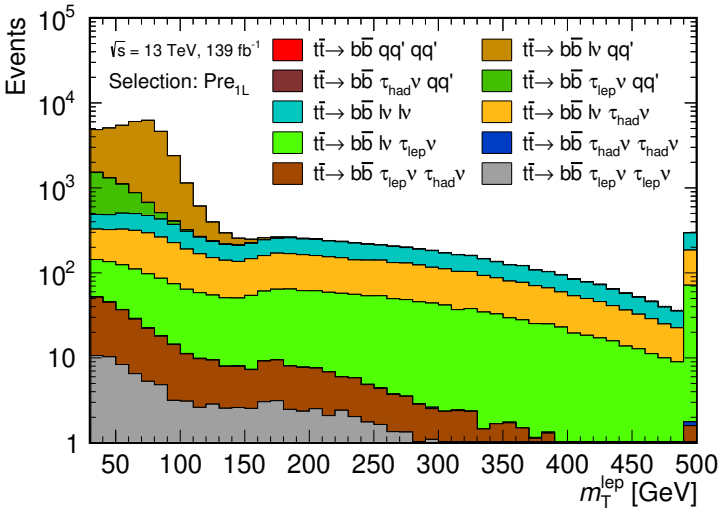

Figure 9.2: Distribution of simulated $t\bar{t}$ events in the $m_{\mathrm{T}}^{\mathrm{lep}}$ variable, categorised into the different decay channels. Shown events must pass the $\mathrm{Pre}_{1\mathrm{L}}$ selection criteria. If an electron or muon is found in the final state of a top-quark decay, it is labelled by an "lν". Top-quark decays yielding τ-leptons are labelled by "$\tau\nu$" and leptonic and hadronic decays of the τ-leptons are indicated. Final states of the top-quark decay consisting of quarks only are are indicated by "qq′". Events beyond the range of the x-axis are added to the rightmost bin.

9.1.2 Common variables for background suppression

To suppress a large fraction of the SM background, dominated by semi- and di-leptonic $t\bar{t}$ decays and W+jets events, two variables are used in both the $\mathrm{SR}_{1\mathrm{L}}^{\mathrm{LepTop}}$ and the $\mathrm{SR}_{1\mathrm{L}}^{\mathrm{HadTop}}$.

Transverse mass ($m_{\mathrm{T}}^{\mathrm{lep}}$)

Leptonically decaying W-bosons are reconstructed in the SM background with the help of the transverse mass $m_{\mathrm{T}}^{\mathrm{lep}}$ (Eq. 9.2). The variable utilises the transverse momentum vector of the electron or muon in an event and the $\vec{p}_{\mathrm{T}}^{\,\mathrm{miss}}$. Background events from semi-leptonic $t\bar{t}$ decays and from the W+jets process are suppressed by using $m_{\mathrm{T}}^{\mathrm{lep}}$.

Figure 9.2 shows the $m_{\mathrm{T}}^{\mathrm{lep}}$ distribution in the $\mathrm{Pre}_{1\mathrm{L}}$ region of the $t\bar{t}$ background, separated into the $t\bar{t}$ decay channels. Semi-leptonic decays (see Section 8.3) constitute the dominant fraction of $t\bar{t}$ decays for $m_{\mathrm{T}}^{\mathrm{lep}}$ below 130 GeV and become negligible for $m_{\mathrm{T}}^{\mathrm{lep}} \geq 180$ GeV.

The $m_{\mathrm{T}}^{\mathrm{lep}}$ distribution of all SM background processes and four signals generated with different 2HDM+a model parameter assumptions is shown in Figure 9.3 for the $\mathrm{Pre}_{1\mathrm{L}}$ region. Most of the background processes, in particular the $t\bar{t}$ and W+jets ones, peak at values of $m_{\mathrm{T}}^{\mathrm{lep}}$ close to the W-boson mass and drop significantly for higher values of $m_{\mathrm{T}}^{\mathrm{lep}}$. Due to the $E_{\mathrm{T}}^{\mathrm{miss}}$ from the DM particles, the $m_{\mathrm{T}}^{\mathrm{lep}}$ distribution is relatively flat for the signals.

Events selected in the $\mathrm{SR}_{1\mathrm{L}}^{\mathrm{LepTop}}$ are required to fulfil $m_{\mathrm{T}}^{\mathrm{lep}} \geq 130$ GeV. This condition reduces the semi-leptonic $t\bar{t}$ background significantly. Di-leptonic $t\bar{t}$ decays (see Section 8.3) then dominate the SM background. In the $\mathrm{SR}_{1\mathrm{L}}^{\mathrm{HadTop}}$, a constraint

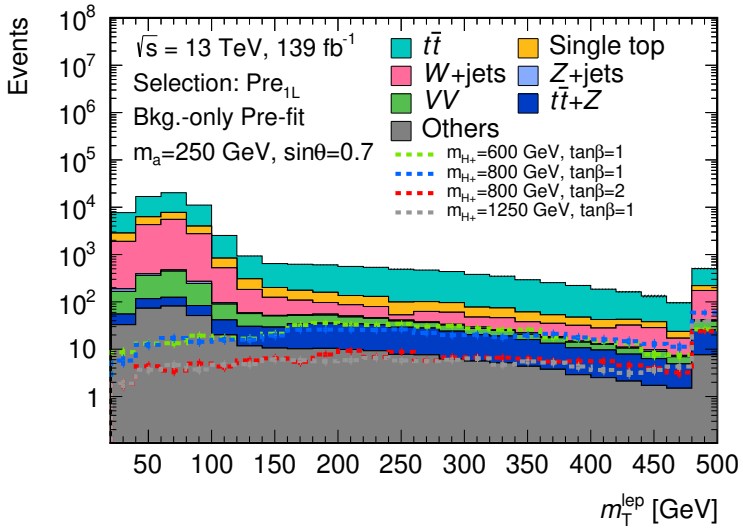

Figure 9.3: Distribution of simulated events in the $\text{Pre}_{1\text{L}}$ region for the $m_{\text{T}}^{\text{lep}}$ variable. Background events are indicated by filled bars, which are stacked, while signal events for different 2HDM+a model parameters are indicated by coloured, dashed lines. Only statistical uncertainties are shown. The normalisation of the simulated background samples has not been corrected by the background-only fit. "Others" contains contributions from the $t\bar{t}+h$, $t\bar{t}+W$, tZ and tWZ processes. Events beyond the range of the x-axis are added to the rightmost bin.

of $m_{\text{T}}^{\text{lep}} \geq 200\,\text{GeV}$ is placed, rendering the contribution of semi-leptonic $t\bar{t}$ decays to the background negligible. Both conditions have been determined using the SR optimisation procedure described before. The impact of these requirements on the significance Z is discussed below, when presenting the remaining variables employed for the background suppression in the $\text{SR}_{1\text{L}}^{\text{LepTop}}$ and the $\text{SR}_{1\text{L}}^{\text{HadTop}}$.

Assymmetric stransverse mass (am_{T2})

After imposing the $m_{\text{T}}^{\text{lep}}$ requirements, the $t\bar{t}$ background is dominated by di-leptonic decays. These events pass the $\text{Pre}_{1\text{L}}$ selection criteria, if one of the charged leptons in the decays is

- an electron or muon, which is misidentified as a jet or escapes the detector acceptance,
- a τ-lepton decaying into a neutrino and hadrons,
- a τ-lepton decaying into neutrinos and a lighter charged lepton, which is misidenitified or not reconstructed.

The neutrinos and the electron or muon escaping the detector acceptance contribute to the $E_{\text{T}}^{\text{miss}}$. Events from the $t\bar{t}$ background with an escaping charged lepton are suppressed using a dedicated variable called am_{T2} [354, 355], which is based on the m_{T2} variable [356, 357].

The stransverse mass m_{T2} [356, 357] is designed to reconstruct the mass of two equal-mass particles produced in an event. It assumes that both of these particles p_1 and p_2 decay into an electron or a muon and at least one undetected particle. The total $\vec{p}_{\text{T}}^{\,\text{miss}}$ is constituted of the transverse momentum vectors of these undetected particles. The components of the $\vec{p}_{\text{T}}^{\,\text{miss}}$ stemming from each of the mother particles,

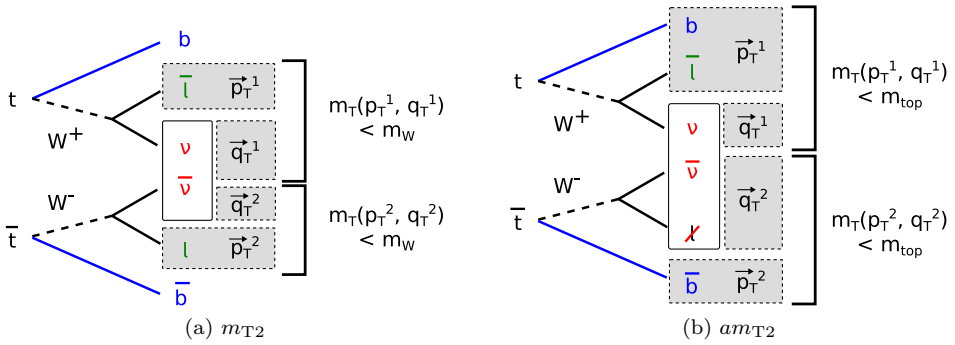

(a) m_{T2} (b) am_{T2}

Figure 9.4: Illustration of (a) the reconstruction of a lower bound on the W-boson mass by the m_{T2} variable in di-leptonic $t\bar{t}$ decays with two identified leptons in the event and (b) the reconstruction of a lower bound on the top-quark mass by the am_{T2} variable in di-leptonic $t\bar{t}$ decays where one charged lepton escapes the detector acceptance.

denoted by $\vec{q}_{\mathrm{T}}^{\,1}$ and $\vec{q}_{\mathrm{T}}^{\,2}$, cannot be measured individually. The idea of the m_{T2} is to decompose the $\vec{p}_{\mathrm{T}}^{\,\mathrm{miss}}$ into two vector candidates for the $\vec{q}_{\mathrm{T}}^{\,i}$ such that a mass bounded by the mass of the two particles can be reconstructed. This is illustrated in Figure 9.4a for di-leptonic $t\bar{t}$ decays. With $\vec{p}_{\mathrm{T}}^{\,\ell 1}$ and $\vec{p}_{\mathrm{T}}^{\,\ell 2}$ being the transverse momentum vectors of the two reconstructed leptons, m_{T2} is defined as

$$m_{\mathrm{T2}}(\vec{p}_{\mathrm{T}}^{\,\ell 1}, \vec{p}_{\mathrm{T}}^{\,\ell 2}, \vec{p}_{\mathrm{T}}^{\,\mathrm{miss}}) := \min_{\vec{q}_{\mathrm{T}}^{\,1}+\vec{q}_{\mathrm{T}}^{\,2}=\vec{p}_{\mathrm{T}}^{\,\mathrm{miss}}} \left[\max\left(m_{\mathrm{T}}(\vec{p}_{\mathrm{T}}^{\,\ell 1}, \vec{q}_{\mathrm{T}}^{\,1}), m_{\mathrm{T}}(\vec{p}_{\mathrm{T}}^{\,\ell 2}, \vec{q}_{\mathrm{T}}^{\,2})\right)\right]. \quad (9.3)$$

All decompositions of the $\vec{p}_{\mathrm{T}}^{\,\mathrm{miss}}$ are probed in the minimisation. For events from di-leptonic $t\bar{t}$ decays an event yield cut-off is observed in the m_{T2} at around the W-boson mass. This is shown in Figure 9.5 in an event selection requiring two reconstructed leptons. No such cut-off is apparent in the tW+DM signal also shown in the figure. This is due to additional $E_{\mathrm{T}}^{\mathrm{miss}}$ from the DM particles in addition to the $E_{\mathrm{T}}^{\mathrm{miss}}$ from the neutrinos from the W-boson decays. The m_{T2} variable is used to define the 2L channel SR presented in Section 12.1.

In the 1L channel, a modified version of the m_{T2} variable is used, the asymmetric stransverse mass am_{T2} [354, 355]. Di-leptonic $t\bar{t}$ decay events where a charged lepton escapes the geometric detector acceptance are suppressed with the help of the variable. The visible objects of these $t\bar{t}$ decays are two b-jets and the electron or muon in the event, as sketched in Figure 9.4b. The m_{T2} calculation is modified as follows. The two transverse momenta of the reconstructed leptons are replaced by the transverse momenta of the two small-radius jets with the highest output value of the multivariate b-tagging algorithm (b-tagging score). The $\vec{p}_{\mathrm{T}}$ of the electron or muon is added to the $\vec{p}_{\mathrm{T}}$ of one of the jets. Due to the ambiguity of the jet-lepton pairing, the m_{T2} is calculated for both jet-lepton combinations and the am_{T2} is defined as the maximum of the two:

$$am_{\mathrm{T2}} := \max\left[m_{\mathrm{T2}}(\vec{p}_{\mathrm{T}}^{\,j1} + \vec{p}_{\mathrm{T}}^{\,\ell}, \vec{p}_{\mathrm{T}}^{\,j2}, \vec{p}_{\mathrm{T}}^{\,\mathrm{miss}}), m_{\mathrm{T2}}(\vec{p}_{\mathrm{T}}^{\,j1}, \vec{p}_{\mathrm{T}}^{\,j2} + \vec{p}_{\mathrm{T}}^{\,\ell}, \vec{p}_{\mathrm{T}}^{\,\mathrm{miss}})\right].$$

Di-leptonic $t\bar{t}$ decays exhibit a steep drop of events at the top-quark mass in the am_{T2}, as shown in Figure 9.6 in the $\mathrm{Pre}_{\mathrm{1L}}$ region, where the constraint $m_{\mathrm{T}}^{\mathrm{lep}} \geq 130\,\mathrm{GeV}$ has been added to suppress semi-leptonic $t\bar{t}$ decays. Signal events on the other hand, as shown in the same figure, do not feature such a drop, due to the additional $E_{\mathrm{T}}^{\mathrm{miss}}$ from the DM particles.

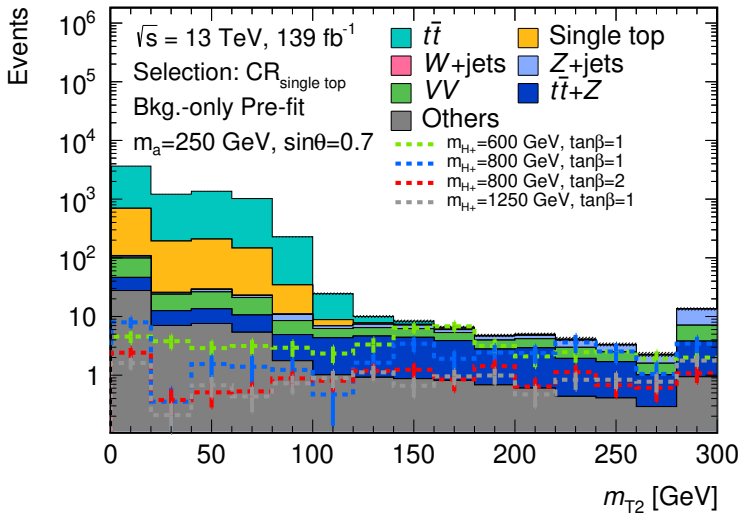

Figure 9.5: Distribution of simulated events in the m_{T2} variable for the $\mathrm{CR}_{\text{single top}}$ (Table 10.3) without any requirements on the m_{T2}, $\min_l m_{bl}$ and m^t_{bl}. This phase space region selects events with exactly two reconstructed leptons and high $E_{\mathrm{T}}^{\mathrm{miss}}$. The variables $\min_l m_{bl}$ and m^t_{bl} as well as the CR are introduced in Section 10.1.3. Background events are indicated by filled bars, which are stacked, while signal events for different 2HDM+a model parameters are indicated by coloured, dashed lines. Only statistical uncertainties are shown. The normalisation of the simulated background samples has not been corrected by the background-only fit. "Others" contains contributions from the $t\bar{t}+h$, $t\bar{t}+W$, tZ and tWZ processes. Events beyond the range of the x-axis are added to the rightmost bin.

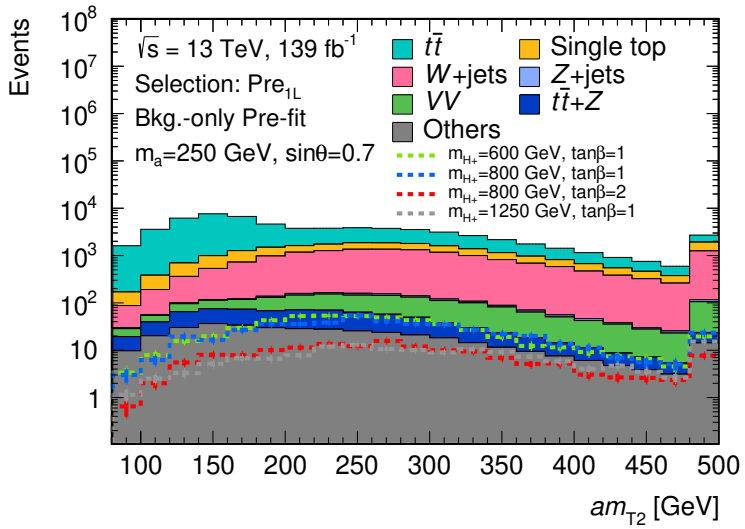

Figure 9.6: Distribution of simulated events for the am_{T2} variable in the $\mathrm{Pre}_{\mathrm{1L}}$ region with the additional constrain $m_{\mathrm{T}}^{\mathrm{lep}} \geq 130\,\mathrm{GeV}$ to suppress semi-leptonic $t\bar{t}$ decay events. Background events are indicated by filled bars, which are stacked, while signal events for different 2HDM+a model parameters are indicated by coloured, dashed lines. Only statistical uncertainties are shown. The normalisation of the simulated background samples has not been corrected by the background-only fit. "Others" contains contributions from the $t\bar{t}+h$, $t\bar{t}+W$, tZ and tWZ processes. Events beyond the range of the x-axis are added to the rightmost bin.

In the $\mathrm{SR}_{\mathrm{1L}}^{\mathrm{LepTop}}$ and $\mathrm{SR}_{\mathrm{1L}}^{\mathrm{HadTop}}$, events are selected if $am_{\mathrm{T2}} \geq 180\,\mathrm{GeV}$. This condition strongly suppresses di-leptonic $t\bar{t}$ decay background events. The impact on the significance Z is discussed below.

9.1.3 Variables for background suppression in the $\mathrm{SR}_{\mathrm{1L}}^{\mathrm{LepTop}}$

The $\mathrm{SR}_{\mathrm{1L}}^{\mathrm{LepTop}}$ is designed to select signal events with a leptonically decaying W-boson from the top-quark decay and a hadronically decaying W-boson from the decay of the $H^{\pm}$-boson or the $b \to Wt$ vertex. Constraints on four variables are used in addition to the preselection and $m_{b,\not{p}}$ requirements to define the $\mathrm{SR}_{\mathrm{1L}}^{\mathrm{LepTop}}$.

Tranverse mass ($m_{\mathrm{T}}^{\mathrm{lep}}$)

The $m_{\mathrm{T}}^{\mathrm{lep}}$ variable is used in the $\mathrm{SR}_{\mathrm{1L}}^{\mathrm{LepTop}}$ to suppress background events from semi-leptonic $t\bar{t}$ decays. The distribution of the $m_{\mathrm{T}}^{\mathrm{lep}}$ in the $\mathrm{SR}_{\mathrm{1L}}^{\mathrm{LepTop}}$ is shown in Figure 9.7a for the SM background processes and for multiple signals generated with different 2HDM+a model parameters for illustration. The SR constraint on the $m_{\mathrm{T}}^{\mathrm{lep}}$ has been removed in this figure and is indicated by an arrow. The bottom panel of Figure 9.7a shows the significance Z. For each signal prediction and bin, Z is calculated using the cumulative yield towards greater $m_{\mathrm{T}}^{\mathrm{lep}}$. That is, the signal yield s entering the significance calculation in bin i is given by $s = \sum_{j \geq i} s_j$, with s_j the signal yield in bin j and likewise for the background. In this way the impact on the discovery significance Z of placing a lower bound on the variable $m_{\mathrm{T}}^{\mathrm{lep}}$ at bin i becomes visible. This significance calculated with cumulative yields and referred to as inclusive significance, is employed throughout this chapter unless indicated

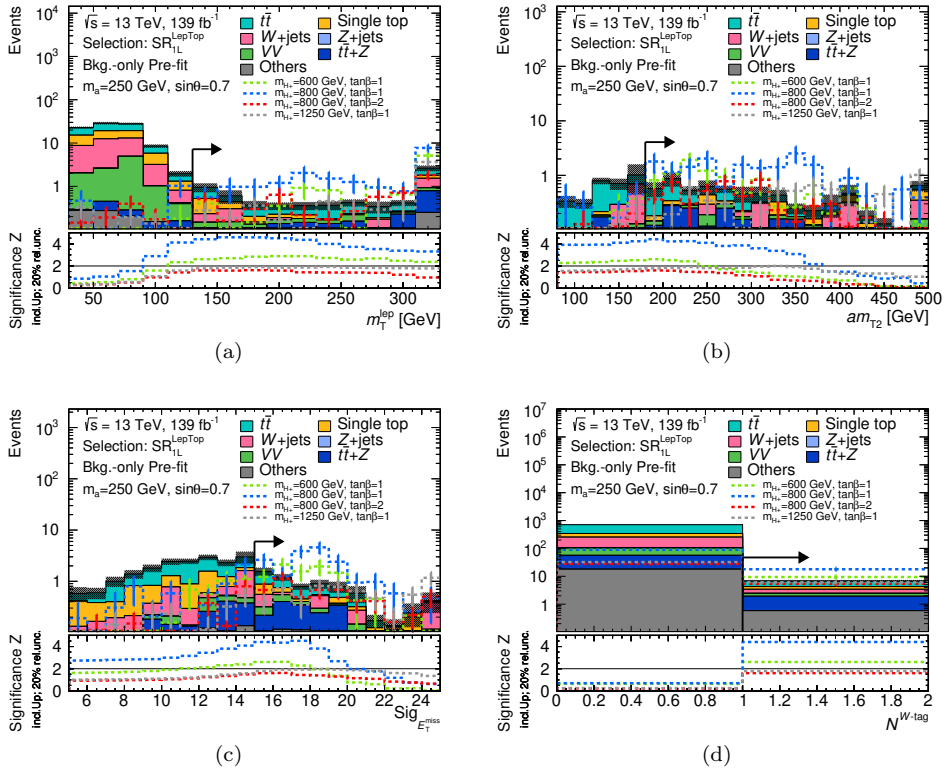

Figure 9.7: Distribution of simulated events as a function of different variables in the $\mathrm{SR}_{1\mathrm{L}}^{\mathrm{LepTop}}$ without a requirement on the shown variable. Background events are indicated by filled bars, which are stacked, while signal events for different 2HDM+a model parameters are indicated by coloured, dashed lines. The variables are (a) $m_{\mathrm{T}}^{\mathrm{lep}}$, (b) am_{T2}, (c) $\mathrm{Sig}_{E_{\mathrm{T}}^{\mathrm{miss}}}$, (d) $N^{W-\mathrm{tag}}$. The significance is calculated per bin with Equation (9.1) using cumulative yields towards greater values for all variables. The arrow indicates the direction and position of the requirement in the SR. Only statistical uncertainties are shown. The normalisation of the simulated background samples has not been corrected by the background-only fit. "Others" contains contributions from the $t\bar{t}+h$, $t\bar{t}+W$, tZ and tWZ processes. Events beyond the range of the x-axis are added to the rightmost bin.

otherwise. As the different signals have their maximum in the inclusive significance at different values of the $m_{\mathrm{T}}^{\mathrm{lep}}$, the constraint on the $m_{\mathrm{T}}^{\mathrm{lep}}$ must not be too high to not reduce the inclusive discovery significance for certain signals, in particular for the shown one with $m_{H^{\pm}} = 800\,\mathrm{GeV}$ and $\tan\beta = 2$. Requiring $m_{\mathrm{T}}^{\mathrm{lep}} \geq 130\,\mathrm{GeV}$ is found to be optimal to increase the discovery significance of all shown signals without reducing Z for one of them.

Assymmetric stransvere mass (am_{T2})

To reduce the fraction of di-leptonic $t\bar{t}$ background events, am_{T2} is employed. The am_{T2} distribution in the $\mathrm{SR}_{1\mathrm{L}}^{\mathrm{LepTop}}$ without any constraints on the am_{T2} is shown in Figure 9.7b. The bottom panel shows the significance Z, calculated per bin using cumulative yields towards greater am_{T2}, to study the impact of placing a constraint on the variable. Requiring $am_{\mathrm{T2}} \geq 180\,\mathrm{GeV}$ maximises the inclusive significance for three of the shown signals and represents the optimal SR condition.

Missing transverse momentum significance ($\mathrm{Sig}_{E_\mathrm{T}^\mathrm{miss}}$)

To further suppress background events with large $E_\mathrm{T}^\mathrm{miss} = |\vec{p}_\mathrm{T}^\,\mathrm{miss}|$ from mismeasurements, as opposed to signal events with large $E_\mathrm{T}^\mathrm{miss}$ due to particles escaping the detector without interacting, the object-based $E_\mathrm{T}^\mathrm{miss}$-significance $\mathrm{Sig}_{E_\mathrm{T}^\mathrm{miss}}$ [358] is used. It is defined as:

$$\mathrm{Sig}_{E_\mathrm{T}^\mathrm{miss}} = \frac{|\vec{p}_\mathrm{T}^\,\mathrm{miss}|}{\sqrt{\sigma_\mathrm{L}^2(1-\rho_\mathrm{LT}^2)}}, \tag{9.4}$$

where σ_L is the resolution component of the $\vec{p}_\mathrm{T}^\,\mathrm{miss}$ parallel to the direction of the $\vec{p}_\mathrm{T}^\,\mathrm{miss}$ vector, and ρ_LT is the correlation between the parallel and perpendicular resolution components. The significance expression is derived from a hypothesis test based on a log-likelihood, testing how likely the $E_\mathrm{T}^\mathrm{miss}$ is consistent with a mismeasurement. A low value of the $\mathrm{Sig}_{E_\mathrm{T}^\mathrm{miss}}$ corresponds to a high probability of the $E_\mathrm{T}^\mathrm{miss}$ stemming from mismeasurements and vice versa.

The distribution of the $\mathrm{Sig}_{E_\mathrm{T}^\mathrm{miss}}$ in the $\mathrm{SR}_\mathrm{1L}^\mathrm{LepTop}$ without any requirements on the $\mathrm{Sig}_{E_\mathrm{T}^\mathrm{miss}}$ is shown in Figure 9.7c. Signal events are dominantly distributed at relatively high values of the $\mathrm{Sig}_{E_\mathrm{T}^\mathrm{miss}}$, due to the large genuine $E_\mathrm{T}^\mathrm{miss}$. Background processes which have a $E_\mathrm{T}^\mathrm{miss}$ more compatible with originating from a mismeasurement, such as $t\bar{t}$, are distributed at lower values of the $\mathrm{Sig}_{E_\mathrm{T}^\mathrm{miss}}$. The inclusive significance is close to its peak for three of the four shown signals for the constraint $\mathrm{Sig}_{E_\mathrm{T}^\mathrm{miss}} \geq 15$. For the remaining signal, the maximum Z is reached at a higher constraint on the $\mathrm{Sig}_{E_\mathrm{T}^\mathrm{miss}}$. Selected events in the $\mathrm{SR}_\mathrm{1L}^\mathrm{LepTop}$ must fulfil $\mathrm{Sig}_{E_\mathrm{T}^\mathrm{miss}} \geq 15$.

The number of W-tagged large-radius jets ($N^{W-\mathrm{tag}}$)

The $\mathrm{SR}_\mathrm{1L}^\mathrm{LepTop}$ is intended to select signal events with a hadronically decaying W-boson from the $H^\pm$-boson or the $b \to Wt$ vertex. As was discussed in Section 8.2, the W-boson from the $H^\pm$-boson decay or the $b \to Wt$ vertex is likely to have a relatively high p_T and to be reconstructed in an $R = 1.0$ large-radius jet if decaying hadronically. This large-radius jet can be W-tagged. The distribution of W-tagged jets ($N^{W-\mathrm{tag}}$) is shown in Figure 9.7d in the $\mathrm{SR}_\mathrm{1L}^\mathrm{LepTop}$, without any constraint on the $N^{W-\mathrm{tag}}$. When requiring at least one W-tagged jet, the background is reduced by two orders of magnitude, while the signal is reduced by roughly a factor four. The inclusive significance Z increases by a factor of 4–10. Requiring at least one W-tagged jet maximises the inclusive discovery significance in the $N^{W-\mathrm{tag}}$ variable for the signals shown in Figure 9.7d. Events with at least one W-tagged jet are selected in the $\mathrm{SR}_\mathrm{1L}^\mathrm{LepTop}$.

The reduction of the background by two orders of magnitude when requiring $N^{W-\mathrm{tag}} \geq 1$ can be explained by the small fraction of hadronically decaying high-p_T W-bosons in most of the background processes:

- $\boldsymbol{V}$**+jets**: In the selected phase space requiring the presence of one electron or muon, the W+jets and Z+jets background processes are both characterised by the absence of hadronically decaying W-bosons.
- $\boldsymbol{t\bar{t}}$**, single top-quark**, $\boldsymbol{VV}$: In the Pre_1L, which the $\mathrm{SR}_\mathrm{1L}^\mathrm{LepTop}$ is based on, the major backgrounds containing hadronically decaying high-p_T W-bosons are semi-leptonic $t\bar{t}$ decays, single top-quark (dominated by the associated production of a top-quark and a W-boson) and VV processes. Requiring $m_\mathrm{T}^\mathrm{lep} \geq 130\,\mathrm{GeV}$ reduces the number of background events from these processes containing hadronically decaying W-bosons to a small fraction. For example, the fraction of semi-leptonic $t\bar{t}$ decays to the total $t\bar{t}$ background is reduced to below 5 % (see Figure 9.2).

	$\mathrm{SR}_{\mathrm{1L}}^{\mathrm{LepTop}}$	$\mathrm{SR}_{\mathrm{1L}}^{\mathrm{HadTop}}$
Trigger	$E_{\mathrm{T}}^{\mathrm{miss}}$	$E_{\mathrm{T}}^{\mathrm{miss}}$
$E_{\mathrm{T}}^{\mathrm{miss}}$ [GeV]	≥ 250	≥ 250
$\mathrm{Sig}_{E_{\mathrm{T}}^{\mathrm{miss}}}$	≥ 15	–
$\Delta\phi_{\mathrm{min},1-4}$ [rad]	≥ 0.5	≥ 0.5
$N^{\ell,b}$,$N^{\ell,s}$	$= 1$	$= 1$
p_{T}^{l1} [GeV]	≥ 30	≥ 30
N^{j}	≥ 2	≥ 3
p_{T}^{j1} [GeV]	≥ 50	≥ 50
p_{T}^{j2} [GeV]	≥ 30	≥ 30
p_{T}^{j3} [GeV]	–	≥ 30
N^{b}	≥ 1	≥ 1
p_{T}^{b1} [GeV]	≥ 50	≥ 50
p_{T}^{b2} [GeV]	< 50	< 50
$m_{b,\not{b}}$ [GeV]	≥ 200	< 200
$m_{\mathrm{T}}^{\mathrm{lep}}$ [GeV]	≥ 130	≥ 200
am_{T2} [GeV]	≥ 180	≥ 180
$N^{W-\mathrm{tag}}$	≥ 1	–
m_{W}^{recl} [GeV]	–	≥ 60

Table 9.1: Selection criteria of the 1L channel SRs.

- $\boldsymbol{t\bar{t}+Z}$: The background process containing the largest fraction of events with hadronically decaying, high-p_{T} W-bosons is the $t\bar{t}+Z$ process with the top-quark pair decaying semi-leptonically and the Z-boson decaying to neutrinos. The additional $E_{\mathrm{T}}^{\mathrm{miss}}$ from the neutrinos prevents that such background events are suppressed by the $m_{\mathrm{T}}^{\mathrm{lep}}$ requirement. If the hadronically decaying W-boson from one of the top-quarks has a high p_{T}, it is likely to be reconstructed in a large-radius jet. This large-radius jet is W-tagged with an efficiency of 50 % as determined by the W-tagging working point (see Section 7.4.5). Compared to the other discussed background processes, the $t\bar{t}+Z$ process is only reduced by roughly one order of magnitude when requiring $N^{W-\mathrm{tag}} \geq 1$. It represents the second largest background process in the $\mathrm{SR}_{\mathrm{1L}}^{\mathrm{LepTop}}$.

Summarising, as the $m_{\mathrm{T}}^{\mathrm{lep}}$ requirement strongly reduces the fraction of hadronically decaying W-bosons in multiple background processes, the background is suppressed by two orders of magnitude when requiring $N^{W-\mathrm{tag}} \geq 1$. It is only the $t\bar{t}+Z$ process that contains a relatively large fraction of high-p_{T}, hadronically decaying W-bosons and is enhanced with respect to the other background processes by the W-tagging requirement.

The selection criteria of the $\mathrm{SR}_{\mathrm{1L}}^{\mathrm{LepTop}}$ are summarised in Table 9.1. Less than 10 background events N_b are predicted by the simulation. To not increase the statistical uncertainties, conservatively assuming the absence of signal events, i.e. that the number of data events $N_{\mathrm{data}} \simeq N_b$, no binned distribution of the SR is used for the statistical analysis.

9.1.4 Variables for background suppression in the $\mathrm{SR}_{\mathrm{1L}}^{\mathrm{HadTop}}$

The $\mathrm{SR}_{\mathrm{1L}}^{\mathrm{LepTop}}$ discussed just above, requiring at least one W-tagged large-radius jet, is specialised to select signal events with a high-p_{T}, hadronically decaying W-boson from the $H^{\pm}$-boson decay or the $b \to Wt$ vertex. As was shown in Figure 8.2b, the expected fraction of such events differs depending on the assumed 2HDM+a model parameters. The $\mathrm{SR}_{\mathrm{1L}}^{\mathrm{LepTop}}$ can thus be regarded as dedicated towards signals which yield a large fraction of high-p_{T} W-bosons. The $\mathrm{SR}_{\mathrm{1L}}^{\mathrm{HadTop}}$, discussed in this subsection, is designed to select events with a hadronically decaying W-boson from the top-quark. The W-boson from the top-quark is less likely to have a high-p_{T}, relatively independent of the 2HDM+a model parameters, see Figure 4.3b. The optimisation strategy of the $\mathrm{SR}_{\mathrm{1L}}^{\mathrm{HadTop}}$ is chosen to be complementary to the $\mathrm{SR}_{\mathrm{1L}}^{\mathrm{LepTop}}$. Rather than specialising on signals with a high fraction of high-p_{T} W-bosons, the $\mathrm{SR}_{\mathrm{1L}}^{\mathrm{HadTop}}$ is designed to cover a broad range of 2HDM+a model signals. As the momentum of the DM particles depends on the masses of the $H^{\pm}$-boson and the a-boson, it is advantageous to divide the $E_{\mathrm{T}}^{\mathrm{miss}}$ distribution into multiple bins in the statistical analysis to be sensitive to a broad range of signals. To ensure that multiple bins can be defined with the statistical uncertainty being a negligible source of uncertainty, the optimisation does, apart from maximising the significance Z, consider the total number of selected background events. The number of background events is conservatively regarded as a proxy for the number of data events. The balance between the maximisation of Z and a high number of background events is implemented in the optimisation procedure by requiring a minimum number of background events in the RGS algorithm. The definition of the $\mathrm{SR}_{\mathrm{1L}}^{\mathrm{HadTop}}$ makes use of four variables in addition to the $\mathrm{Pre}_{\mathrm{1L}}$ and $m_{b,\not{p}} < 200\,\mathrm{GeV}$ requirements.

Tranverse mass ($m_{\mathrm{T}}^{\mathrm{lep}}$)

Background events from semi-leptonic $t\bar{t}$ decays are suppressed in the $\mathrm{SR}_{\mathrm{1L}}^{\mathrm{HadTop}}$ using the $m_{\mathrm{T}}^{\mathrm{lep}}$ variable. Figure 9.8a shows the $m_{\mathrm{T}}^{\mathrm{lep}}$ distribution in the $\mathrm{SR}_{\mathrm{1L}}^{\mathrm{HadTop}}$, without any requirements on the $m_{\mathrm{T}}^{\mathrm{lep}}$. The bottom panel of Figure 9.8a shows the significance Z, employing cumulative yields towards higher $m_{\mathrm{T}}^{\mathrm{lep}}$. The inclusive significance increases for the shown signals as a function of $m_{\mathrm{T}}^{\mathrm{lep}}$ until high values of $m_{\mathrm{T}}^{\mathrm{lep}}$. For one of the signals, Z becomes roughly constant for values of $m_{\mathrm{T}}^{\mathrm{lep}}$ greater than 160 GeV. Balancing the increase in Z and the number of selected events, events in the $\mathrm{SR}_{\mathrm{1L}}^{\mathrm{HadTop}}$ are selected, if $m_{\mathrm{T}}^{\mathrm{lep}} \geq 200\,\mathrm{GeV}$.

Assymmetric stransvere mass (am_{T2})

The am_{T2} variable is used to reduce background events from di-leptonic $t\bar{t}$ decays. Figure 9.8b shows the am_{T2} distribution in the $\mathrm{SR}_{\mathrm{1L}}^{\mathrm{HadTop}}$ without any requirement on the am_{T2}. The inclusive significance Z increases for all shown signals as the condition on am_{T2} is tightened, until $am_{\mathrm{T2}} \simeq 270\,\mathrm{GeV}$. As a trade-off between the increase in Z and the number of background events, events selected in the $\mathrm{SR}_{\mathrm{1L}}^{\mathrm{HadTop}}$ are required to fulfil $am_{\mathrm{T2}} \geq 180\,\mathrm{GeV}$.

Number of small-radius jets (N^j)

The significance Z in the $\mathrm{SR}_{\mathrm{1L}}^{\mathrm{HadTop}}$ is further increased by selecting events with three or more $R = 0.4$ small-radius jets. Figure 9.8c shows the distribution of signal and background events in the number N^j of small-radius jets in the $\mathrm{SR}_{\mathrm{1L}}^{\mathrm{HadTop}}$ without any condition on the N^j. While the background distribution is smoothly falling, the signals peak at $N^j = 3$ in agreement with the signal characteristics in the 1L

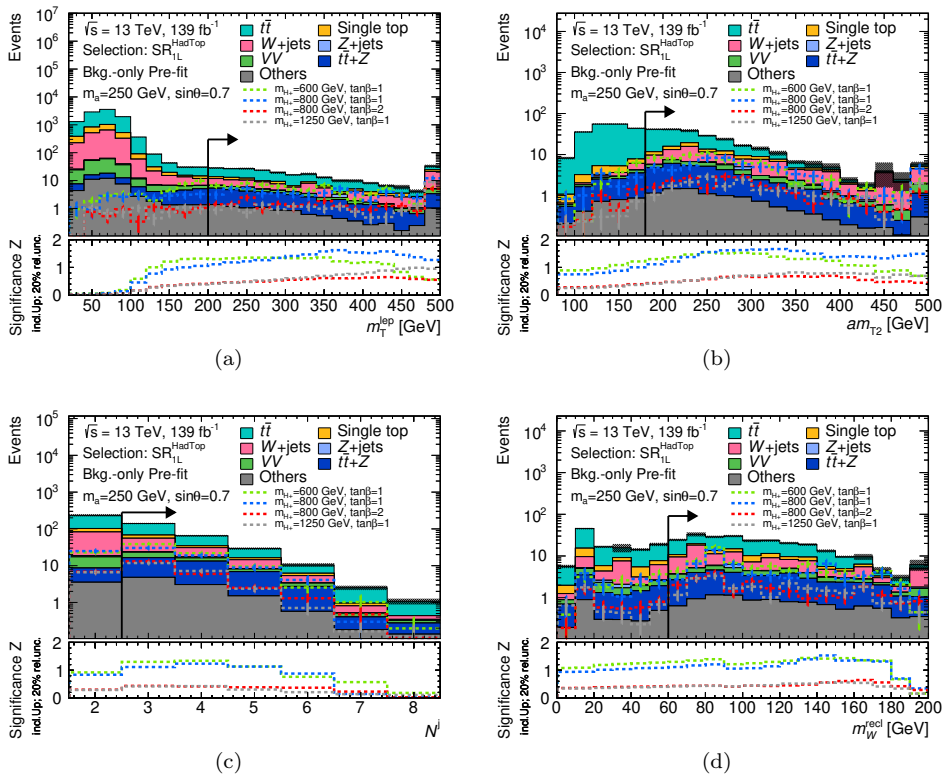

Figure 9.8: Distribution of simulated events as a function of different variables in the $\mathrm{SR}_{1\mathrm{L}}^{\mathrm{HadTop}}$ without a requirement on the shown variable. Background events are indicated by filled bars, which are stacked, while signal events for different 2HDM+a model parameters are indicated by coloured, dashed lines. The variables are (a) $m_{\mathrm{T}}^{\mathrm{lep}}$, (b) am_{T2}, (c) N^j, (d) m_W^{recl}. The significance is calculated per bin with Equation (9.1) using cumulative yields towards greater values for all variables. The arrow indicates the direction and position of the requirement in the SR. Only statistical uncertainties are shown. The normalisation of the simulated background samples has not been corrected by the background-only fit. "Others" contains contributions from the $t\bar{t}+h$, $t\bar{t}+W$, tZ and tWZ processes. Events beyond the range of the x-axis are added to the rightmost bin.

channel (one b-jet and two jets from the W-boson decay). The inclusive significance Z increases when selecting events with at least three small-radius jets. For tighter requirements on N^j, the increase in Z is small. In the interest of retaining a high number of background events, the selection requirement on N^j in the $\mathrm{SR}_{1\mathrm{L}}^{\mathrm{HadTop}}$ is found to be $N^j \geq 3$ with the optimisation algorithm.

Reclustered jet mass (m_W^{recl})

The $\mathrm{SR}_{1\mathrm{L}}^{\mathrm{HadTop}}$ is intended to select signal events with a hadronically decaying W-boson from the top-quark. The W-bosons from the top-quark decay are unlikely to have a high-p_{T} (see Section 8.2). Their decay products are therefore much more rarely reconstructed in an $R = 1.0$ large-radius jet which is W-tagged compared to the W-bosons from the $H^{\pm}$-boson decay or the $b \to Wt$ vertex.

To reconstruct a high fraction of hadronically decaying W-bosons in the events selected by the $\mathrm{SR}_{1\mathrm{L}}^{\mathrm{HadTop}}$, the jet reconstruction algorithm with an adaptive jet

radius parameter introduced in Section 7.4.6 [21, 331, 332] is utilised. The algorithm clusters $R = 0.4$ small-radius jets into jets with a larger radius parameter. It returns at most one reclustered jet candidate per event compatible with a hadronic W-boson decay. The distribution of events as a function of the invariant mass m_W^{recl} of this reclustered jet in the $\text{SR}_{\text{1L}}^{\text{HadTop}}$ without any constraints on the m_W^{recl} is shown in Figure 9.8d. While there is a well visible peak in the signals at the W-boson mass, the distribution of the background is more smooth, though also peaking around the W-boson mass. This more smooth distribution is due to the suppression of hadronically decaying W-bosons by the $m_{\text{T}}^{\text{lep}}$ variable in multiple background processes.

The inclusive significance Z, increases as a function of the m_W^{recl} for the shown signals until $m_W^{\text{recl}} = 90\,\text{GeV}$. Balancing Z against the number of background events in the $\text{SR}_{\text{1L}}^{\text{HadTop}}$, events selected by the $\text{SR}_{\text{1L}}^{\text{HadTop}}$ must contain a reclustered jet with an invariant mass m_W^{recl} greater than 60 GeV.

Binning of the $\text{SR}_{\text{1L}}^{\text{HadTop}}$

The selection requirements of the $\text{SR}_{\text{1L}}^{\text{HadTop}}$ are summarised in Table 9.1. Depending on the 2HDM+a model parameters, in particular $m_{H^\pm}$ and m_a, the DM particle momentum can vary significantly, yielding diverse $E_{\text{T}}^{\text{miss}}$ spectra. Different requirements on the $E_{\text{T}}^{\text{miss}}$ may therefore be beneficial to be the most sensitive to signals with differing model parameters. An approach would be to define one SR per set of model parameters. These SRs could have overlapping $E_{\text{T}}^{\text{miss}}$ requirements though and could therefore not be statistically combined in a straight-forward manner. In addition, the specialised regions would not be sensitive to signals which have other $E_{\text{T}}^{\text{miss}}$ characteristics than the signals used to define them. Circumventing the discussed caveats of specialised SRs, the $E_{\text{T}}^{\text{miss}}$ distribution of the $\text{SR}_{\text{1L}}^{\text{HadTop}}$ is divided into multiple bins. Each bin is treated as individual SR in the likelihood and these SRs are statistically combined. This approach accounts for the different $E_{\text{T}}^{\text{miss}}$ distributions of the signals, while potentially enhancing the sensitivity to a signal by the statistical combination of the $E_{\text{T}}^{\text{miss}}$ bins. The bin boundaries of the SRs are defined by trading the statistical uncertainty off against $E_{\text{T}}^{\text{miss}}$ intervals in which the background is low and the signal is high for multiple model parameters. An equidistant binning with the bin boundaries $[250, 300]$ GeV, $[300, 350]$ GeV, $[350, 400]$ GeV, $[400, 450]$ GeV and $> 450\,\text{GeV}$ is used in this thesis in the $\text{SR}_{\text{1L}}^{\text{HadTop}}$. The bins are denoted as $\text{SR}_{\text{1L}}^{\text{HadTop Bin 1}}$ to $\text{SR}_{\text{1L}}^{\text{HadTop Bin 5}}$. Signal and background distributions in the $E_{\text{T}}^{\text{miss}}$ bins in the $\text{SR}_{\text{1L}}^{\text{HadTop}}$ are shown in Figure 9.9. The bottom panel shows the significance Z calculated per bin using the yields in that bin. The four shown signals peak in Z in three different bins, indicating the benefit of dividing the SR into the chosen bins.

Five SRs for the model-independent hypothesis tests are defined from the $\text{SR}_{\text{1L}}^{\text{HadTop}}$, by selecting events with $E_{\text{T}}^{\text{miss}} \geq 250\,\text{GeV}$, $E_{\text{T}}^{\text{miss}} \geq 300\,\text{GeV}$, $E_{\text{T}}^{\text{miss}} \geq 350\,\text{GeV}$, $E_{\text{T}}^{\text{miss}} \geq 400\,\text{GeV}$ and $E_{\text{T}}^{\text{miss}} \geq 450\,\text{GeV}$.

9.2 The 0L channel

9.2.1 Preselection criteria

Events in the 0L channel are preselected in compliance with the properties of the signal. The phase space region defined by the preselection criteria is denoted by Pre_{0L}. Preselected events must pass the $E_{\text{T}}^{\text{miss}}$ trigger, have a $E_{\text{T}}^{\text{miss}} \geq 250\,\text{GeV}$ and zero baseline and signal electrons or muons. They must contain at least four small-radius jets with transverse momenta of the four leading-p_{T} jets of $p_{\text{T}}^{j1} \geq 100\,\text{GeV}$,

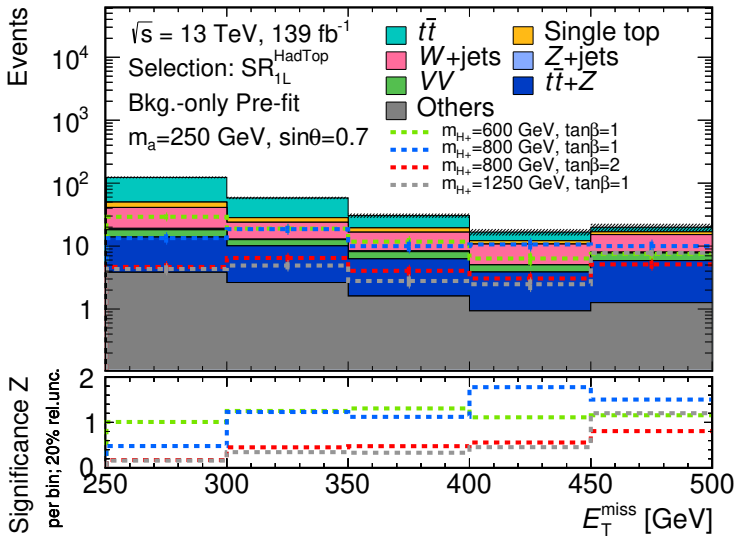

Figure 9.9: $E_{\mathrm{T}}^{\mathrm{miss}}$ distribution in the $\mathrm{SR}_{\mathrm{1L}}^{\mathrm{HadTop}}$. Background events are indicated by filled bars, which are stacked, while signal events for different 2HDM+a model parameters are indicated by coloured, dashed lines. The significance is calculated per bin with Equation (9.1) using the yields in that bin. Only statistical uncertainties are shown. The normalisation of the simulated background samples has not been corrected by the background-only fit. "Others" contains contributions from the $t\bar{t}+h$, $t\bar{t}+W$, tZ and tWZ processes. Events beyond the range of the x-axis are added to the rightmost bin.

$p_{\mathrm{T}}^{j2} \geq 60\,\mathrm{GeV}$, $p_{\mathrm{T}}^{j3} \geq 60\,\mathrm{GeV}$ and $p_{\mathrm{T}}^{j4} \geq 40\,\mathrm{GeV}$. Events entering the $\mathrm{Pre}_{\mathrm{0L}}$ must contain at least one b-jet. For the p_{T} of the two leading-p_{T} b-jets, $p_{\mathrm{T}}^{b1} \geq 50\,\mathrm{GeV}$ and $p_{\mathrm{T}}^{b2} < 50\,\mathrm{GeV}$ is required[2]. The fraction of events with large $E_{\mathrm{T}}^{\mathrm{miss}}$ from the mismeasurement of jets, such as events with multiple QCD jets or hadronic $t\bar{t}$ decays, is decreased by requiring $\Delta\phi_{\mathrm{min},1-4} \geq 0.9$. This requirement reduces the multijet and hadronic $t\bar{t}$ background to a negligible fraction. All event selections which require zero reconstructed leptons must fulfil these preselection criteria in the following. The dominant backgrounds in the $\mathrm{Pre}_{\mathrm{0L}}$ are semi-leptonic $t\bar{t}$, Z+jets and W+jets. Further optimisation is performed to increase the sensitivity towards 2HDM+a model tW+DM signals.

9.2.2 Signal region definition

Dedicated variables are used to further suppress background events while retaining a large fraction of the signal events.

Missing transverse momentum significance ($\mathrm{Sig}_{E_{\mathrm{T}}^{\mathrm{miss}}}$)

Background events with large $E_{\mathrm{T}}^{\mathrm{miss}}$ from mismeasurement are suppressed by using the $\mathrm{Sig}_{E_{\mathrm{T}}^{\mathrm{miss}}}$ variable introduced in Section 9.1.3. Figure 9.10a shows the distribution of the $\mathrm{Sig}_{E_{\mathrm{T}}^{\mathrm{miss}}}$ in the $\mathrm{SR}_{\mathrm{0L}}$ without any requirement on the $\mathrm{Sig}_{E_{\mathrm{T}}^{\mathrm{miss}}}$ for the SM background and four signals. The condition $\mathrm{Sig}_{E_{\mathrm{T}}^{\mathrm{miss}}} \geq 14$ is found to be the optimal in the $\mathrm{SR}_{\mathrm{0L}}$.

[2]As in the 1L channel, the p_{T} condition on the second leading-p_{T} b-jet does not veto events containing exactly one b-jet.

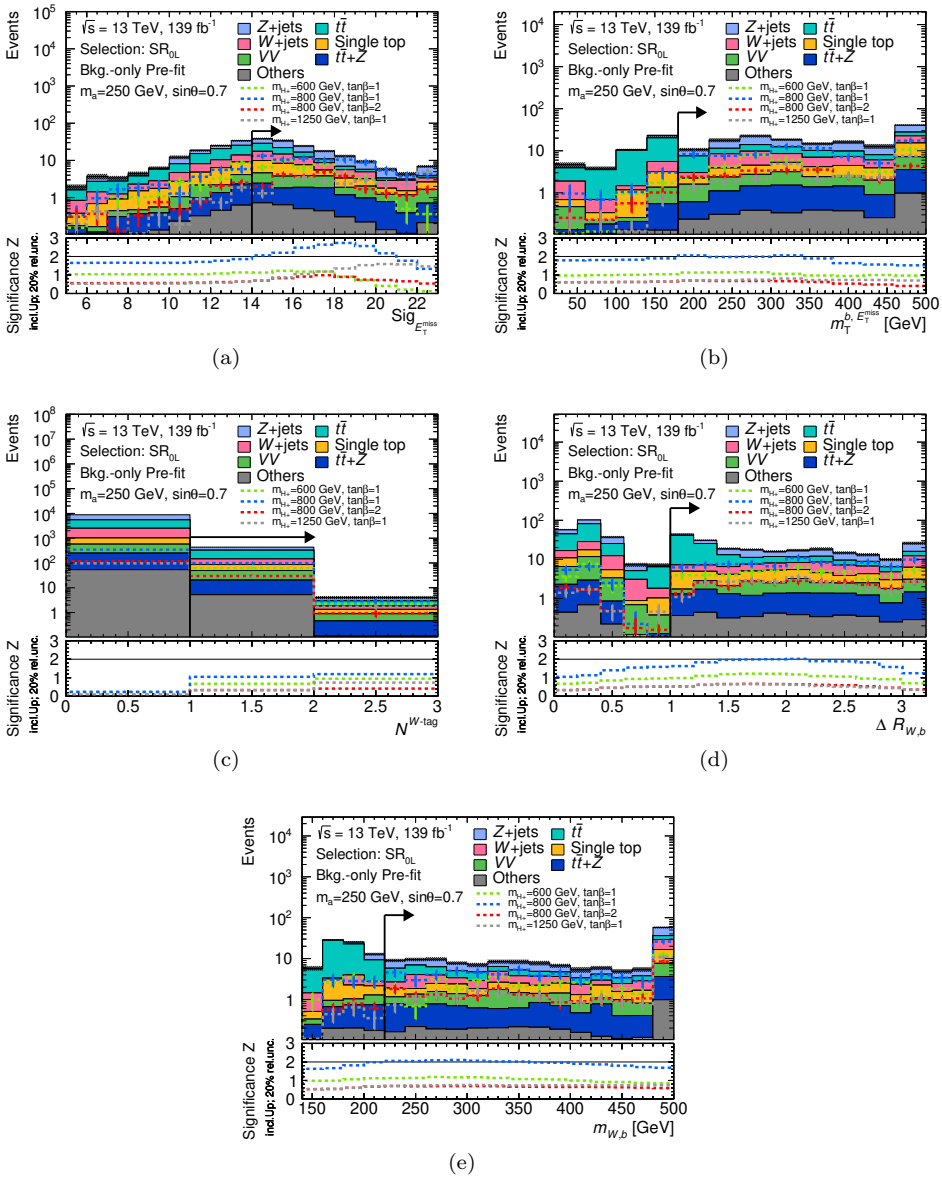

(a) (b) (c) (d) (e)

Figure 9.10: Distributions of simulated events as a function of different variables in the SR_{0L} without a requirement on the shown variable. Background events are indicated by filled bars, which are stacked, while signal events for different 2HDM+a model parameters are indicated by coloured, dashed lines. The variables are (a) $\mathrm{Sig}_{E_\mathrm{T}^\mathrm{miss}}$, (b) $m_\mathrm{T}^{b,E_\mathrm{T}^\mathrm{miss}}$, (c) $N^{W-\mathrm{tag}}$, (d) $\Delta R_{W,b}$ and (e) $m_{W,b}$. In (c) and (d) no constraints on both the $\Delta R_{W,b}$ and the $m_{W,b}$ variables are placed. The lower panel shows the significance Z calculated per bin with Equation (9.1), using cumulative yields towards greater values for all variables. The arrow indicates the direction and position of the requirement in the SR. Only statistical uncertainties are shown. The normalisation of the simulated background samples has not been corrected by the background-only fit. "Others" contains contributions from the $t\bar{t}+h$, $t\bar{t}+W$, tZ and tWZ processes. Events beyond the range of the x-axis are added to the rightmost bin.

Transverse mass of b-jet and $E_{\mathrm{T}}^{\mathrm{miss}}$ ($m_{\mathrm{T}}^{b,E_{\mathrm{T}}^{\mathrm{miss}}}$)

The $t\bar{t}$ background in the 0L channel is mainly constituted of semi-leptonic decays, where the electron or muon in the final state escapes the detection or is misidentified as a jet; or the charged lepton is a hadronically decaying τ-lepton. The neutrino(s) and the electron or muon escaping the detector acceptance contribute to the $E_{\mathrm{T}}^{\mathrm{miss}}$. To suppress events stemming from this background, the transverse mass between the $E_{\mathrm{T}}^{\mathrm{miss}}$ and the leading-p_{T} b-jet with transverse momentum vectors $\vec{p}_{\mathrm{T}}^{\,\mathrm{miss}}$ and $\vec{p}_{\mathrm{T}}^{\,b1}$, respectively, is employed [359]:

$$m_{\mathrm{T}}^{b,E_{\mathrm{T}}^{\mathrm{miss}}} \coloneqq m_T(\vec{p}_{\mathrm{T}}^{\,\mathrm{miss}}, \vec{p}_{\mathrm{T}}^{\,b1}) \coloneqq \sqrt{2|\vec{p}_{\mathrm{T}}^{\,\mathrm{miss}}| \cdot |\vec{p}_{\mathrm{T}}^{\,b1}| \left(1 - \cos\Delta\phi(\vec{p}_{\mathrm{T}}^{\,\mathrm{miss}}, \vec{p}_{\mathrm{T}}^{\,b1})\right)}.$$

If the leading-p_{T} b-jet in a semi-leptonic $t\bar{t}$ decay event originates from the same top-quark as the neutrino(s) and the potentially escaping electron or muon does, $m_{\mathrm{T}}^{b,E_{\mathrm{T}}^{\mathrm{miss}}}$ is bounded by the top-quark mass.

The distribution of the $m_{\mathrm{T}}^{b,E_{\mathrm{T}}^{\mathrm{miss}}}$ in the SR, without constraints on the $m_{\mathrm{T}}^{b,E_{\mathrm{T}}^{\mathrm{miss}}}$, is shown in Figure 9.10b. A strong decrease of $t\bar{t}$ background events as of roughly the top-quark mass (m_{top}) is visible. This is not the case in the signal, due to the contributions to the $\vec{p}_{\mathrm{T}}^{\,\mathrm{miss}}$ from the DM particles. Only a small fraction of the signal events is found at $m_{\mathrm{T}}^{b,E_{\mathrm{T}}^{\mathrm{miss}}} < m_{\mathrm{top}}$. In the $\mathrm{SR}_{\mathrm{0L}}$, $m_{\mathrm{T}}^{b,E_{\mathrm{T}}^{\mathrm{miss}}}$ is required to be greater than or equal to 180 GeV.

W-tagging and related variables

For $H^{\pm}$-boson masses above approximately 600 GeV the signal in the 0L channel is, in the majority of events, expected to contain a hadronically decaying, high-p_{T} W-boson, which can be reconstructed in an $R = 1.0$ large-radius jet and W-tagged (see Section 8.2). Figure 9.10c shows the distribution of the number of W-tagged large-radius jets $N^{W-\mathrm{tag}}$ in the SR without any constraint on the variable and other variables related to W-tagged jets (see below). While the total background yield is reduced by a factor 20 if requiring at least one W-tagged large-radius jet, the signal yields are reduced by only a factor 4–6. Events containing at least one W-tagged large-radius jet ($N^{W-\mathrm{tag}} \geq 1$) are selected in the 0L channel SR.

To further reduce the $t\bar{t}$ background, correlations between the leading-p_{T} W-tagged jet and the leading-p_{T} b-tagged jet are exploited. The $t\bar{t}$ background is dominantly constituted of semi-leptonic decays. If the top-quark decaying entirely into quarks has a high p_{T}, it may, as a whole, be reconstructed in a large-radius jet. This large-radius jet may, falsely, be W-tagged. As ambiguities between small-radius and large-radius jets are not resolved in the object reconstruction and selection procedure, this W-tagged large-radius jet overlaps with the b-jet from the same top-quark. As the W-tagged jet in the signal mainly originates from the $H^{\pm}$-boson decay and the $b \to Wt$ vertex, such an overlap is more rare in the signal than in the $t\bar{t}$ background.

The overlap is measured by the angular distance $\Delta R_{W,b}$ between the leading-p_{T} W-tagged jet and the leading-p_{T} b-jet. Due to the radius parameter $R = 1.0$ of the large-radius jets, any overlap between the leading-p_{T} W-tagged jet and the leading-p_{T} b-jet is removed if $\Delta R_{W,b} \geq 1.0$. The $\Delta R_{W,b}$ distribution for the SM background processes and for four illustrative signals is shown in Figure 9.10d in the $\mathrm{SR}_{\mathrm{0L}}$ without any requirements on the $\Delta R_{W,b}$ and the $m_{W,b}$ (introduced below), due to correlations of the two. The majority of background events, dominated by the $t\bar{t}$ process, is found at $\Delta R_{W,b} < 1.0$, while only a small fraction of the signal is. The condition $\Delta R_{W,b} \geq 1.0$ is required in the $\mathrm{SR}_{\mathrm{0L}}$.

The leading-p_{T} W-tagged jet and the leading-p_{T} b-jet of the $t\bar{t}$ background events fulfilling $\Delta R_{W,b} \geq 1$ most likely both originate from the decay of the same

top-quark. This is due to the constraint on the $m_{\mathrm{T}}^{b,E_{\mathrm{T}}^{\mathrm{miss}}}$ variable, which removes events where the b-jet originates from the leptonically decaying W-boson. In the signal, the leading-p_{T} W-tagged jet does mostly not originate from the top-quark. The invariant mass of the leading-p_{T} W-tagged jet and the leading-p_{T} b-tagged jet, $m_{W,b}$, is thus expected to be more likely bounded from above by the top-quark mass in the $t\bar{t}$ background than in the signal. Figure 9.10e shows the distribution of the $m_{W,b}$ in the $\mathrm{SR}_{\mathrm{0L}}$ without any requirements on the $m_{W,b}$. Events from the $t\bar{t}$ background are found dominantly at $m_{W,b} < 220\,\mathrm{GeV}$, while only a small fraction of the signal events is. The condition $m_{W,b} \geq 220\,\mathrm{GeV}$ is placed in the SR.

Binning of the $\mathrm{SR}_{\mathrm{0L}}$

The selection criteria of the $\mathrm{SR}_{\mathrm{0L}}$ are summarised in Table 9.2. To enhance the sensitivity to signals with diverse $E_{\mathrm{T}}^{\mathrm{miss}}$ spectra, a binning in $E_{\mathrm{T}}^{\mathrm{miss}}$ is pursued in the 0L channel SR with the bins $[250, 330]$ GeV, $[330, 400]$ GeV, $[400, 500]$ GeV, $[500, 600]$ GeV and $> 600\,\mathrm{GeV}$, denoted as $\mathrm{SR}_{\mathrm{0L}}^{\mathrm{Bin}\ 1}$ to $\mathrm{SR}_{\mathrm{0L}}^{\mathrm{Bin}\ 5}$. The resulting $E_{\mathrm{T}}^{\mathrm{miss}}$ distribution in the $\mathrm{SR}_{\mathrm{0L}}$ is shown in Figure 9.11.

Five SRs for the model-independent hypothesis tests are defined based on the $\mathrm{SR}_{\mathrm{0L}}$, selecting events with $E_{\mathrm{T}}^{\mathrm{miss}} \geq 250\,\mathrm{GeV}$, $E_{\mathrm{T}}^{\mathrm{miss}} \geq 330\,\mathrm{GeV}$, $E_{\mathrm{T}}^{\mathrm{miss}} \geq 400\,\mathrm{GeV}$, $E_{\mathrm{T}}^{\mathrm{miss}} \geq 500\,\mathrm{GeV}$ and $E_{\mathrm{T}}^{\mathrm{miss}} \geq 600\,\mathrm{GeV}$, respectively.

	$\mathrm{SR}_{\mathrm{0L}}$
Trigger	$E_{\mathrm{T}}^{\mathrm{miss}}$
$E_{\mathrm{T}}^{\mathrm{miss}}$ [GeV]	≥ 250
$\mathrm{Sig}_{E_{\mathrm{T}}^{\mathrm{miss}}}$	≥ 14
$\Delta\phi_{\mathrm{min},1-4}$ [rad]	≥ 0.9
$N^{\ell,b}$,$N^{\ell,s}$	$= 0$
N^{j}	≥ 4
p_{T}^{j1} [GeV]	≥ 100
p_{T}^{j2} [GeV]	≥ 60
p_{T}^{j3} [GeV]	≥ 60
p_{T}^{j4} [GeV]	≥ 40
N^{b}	≥ 1
p_{T}^{b1} [GeV]	≥ 50
p_{T}^{b2} [GeV]	< 50
$m_{\mathrm{T}}^{b,E_{\mathrm{T}}^{\mathrm{miss}}}$ [GeV]	≥ 180
$N^{W-\mathrm{tag}}$	≥ 1
$\Delta R_{W,b}$	≥ 1.0
$m_{W,b}$ [GeV]	≥ 220

Table 9.2: Selection criteria of the 0L channel SRs.

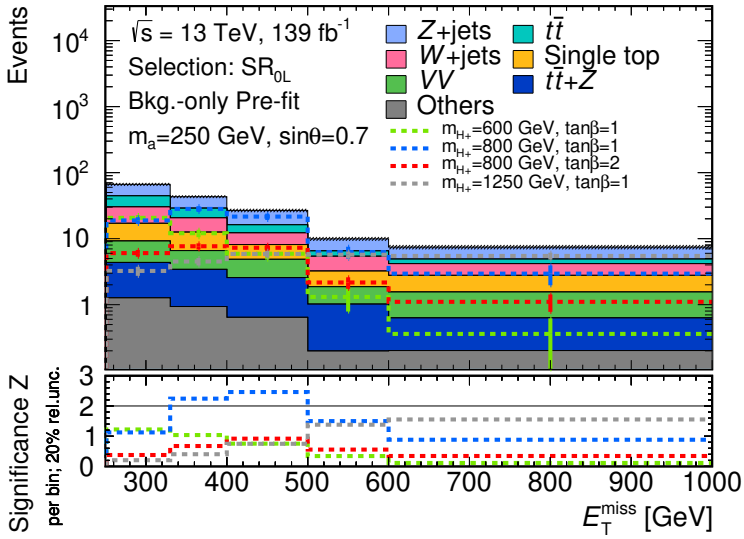

Figure 9.11: $E_{\mathrm{T}}^{\mathrm{miss}}$ distribution in the $\mathrm{SR}_{0\mathrm{L}}$. Background events are indicated by filled bars, which are stacked, while signal events for different 2HDM+a model parameters are indicated by coloured, dashed lines. The lower panel shows the significance Z calculated per bin with Equation (9.1), using the yields in that bin. Only statistical uncertainties are shown. The normalisation of the simulated background samples has not been corrected by the background-only fit. "Others" contains contributions from the $t\bar{t}+h$, $t\bar{t}+W$, tZ and tWZ processes. Events beyond the range of the x-axis are added to the rightmost bin.

Chapter 10

Background estimation and systematic uncertainties

10.1 Control regions

To determine the normalisation of the dominant SM background processes, CRs are used. CRs are defined for each of the major SM background processes in the SRs. These are $t\bar{t}$ and $t\bar{t}+Z$ in the $\mathrm{SR}_{\mathrm{1L}}^{\mathrm{LepTop}}$, $t\bar{t}$ and W+jets in the $\mathrm{SR}_{\mathrm{1L}}^{\mathrm{HadTop}}$ and Z+jets, W+jets and $t\bar{t}$ in the $\mathrm{SR}_{\mathrm{0L}}$. For the $t\bar{t}$ process, events are mainly constituted of di-leptonic decays in the 1L SRs and of semi-leptonic decays in the $\mathrm{SR}_{\mathrm{0L}}$ as discussed in Section 8.3. Two separate CRs are employed to constrain the $t\bar{t}$ background in the 1L and 0L channel. When combining the two channels, both CRs are included in the likelihood and different normalisation parameters are used for the $t\bar{t}$ background in the 1L and 0L channel regions. The normalisations of the remaining background processes are, regardless of which channel they are dominant in, determined using the same control regions in the 1L and 0L channels to facilitate the combination of the two channels.

To ensure an independent estimation of the background normalisation, the phase spaces of CRs must be non-overlapping with the SRs' ones. At the same time, the phase space of a CR should be close to the phase spaces of the SRs. The fraction of events of the SM process that is constrained by the CR should be high in the CR. Furthermore, the region should have a sufficient number of events to estimate the normalisation reliably. To prevent a bias on the signal due to the background determination, signal events must have a low or negligible contribution in the CRs.

That the CRs are non-overlapping with the SRs and yet kinematically close is illustrated in Figure 10.1. The phase space coverage of the CRs, SRs and VRs (see Section 10.2) is shown in the figure in multiple variables. These variables are the transverse mass $m_{\mathrm{T}}^{\mathrm{lep}}$ and the invariant mass of the leading-p_{T} b-jet and leading-p_{T} non-b-tagged jet $m_{b,j}$, see Section 9.1, in the 1L channel regions. In the 0L channel regions, these variables are the number of reconstructed leptons N^{l} and the number of W-tagged large-radius jets $N^{W-\mathrm{tag}}$.

10.1.1 $t\bar{t}$ control regions

In both 1L channel SRs, the SM background is dominated by di-leptonic $t\bar{t}$ decays, where one of the charged leptons escapes detection, is a hadronically decaying τ-lepton or the electron or muon in an event is reconstructed as a jet. A CR is defined to determine the normalisation of this background process. Di-leptonic $t\bar{t}$ decay events most likely have a value of the am_{T2} below the top-quark mass. The

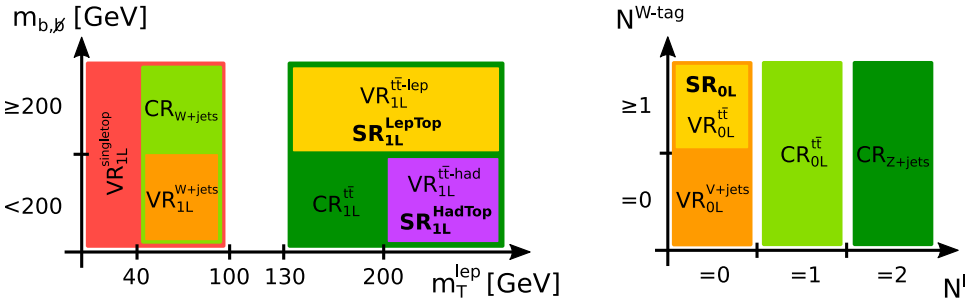

Figure 10.1: The phase spaces covered by the CRs and VRs are non-overlapping and kinematically close to the phase spaces of the SRs. This is shown exemplarily for the requirements on the transverse mass $m_{\mathrm{T}}^{\mathrm{lep}}$ and invariant mass $m_{b,\not{p}}$ of the leading-p_{T} b-jet and the leading-p_{T} non-b-tagged jet (see Section 9.1) in the 1L channel regions on the left. On the right hand side the 0L channel regions and the constraints of these regions on the number of reconstructed leptons N^l and the number of W-tagged large-radius jets $N^{W-\mathrm{tag}}$ are shown.

reverse requirement $am_{\mathrm{T2}} < 180\,\mathrm{GeV}$ with respect to the 1L channel SRs is therefore imposed, increasing the di-leptonic $t\bar{t}$ purity. Furthermore, $t\bar{t}$ events are expected to contain two highly energetic b-jets. For that reason, the p_{T} of the subleading b-jet is also reverted with respect to the 1L channel SRs and required to be $> 50\,\mathrm{GeV}$. This condition also increases the $t\bar{t}$ purity. To make the phase space of the CR, denoted by $\mathrm{CR}_{\mathrm{1L}}^{t\bar{t}}$, as close as possible to the phase spaces of both SRs, no constraints on the number of W-tagged jets $N^{W-\mathrm{tag}}$, the reclustered jet mass m_W^{recl} and on the $\mathrm{Sig}_{E_{\mathrm{T}}^{\mathrm{miss}}}$ are placed. This also increases the number of events as well as the $t\bar{t}$ fraction in the CR. Furthermore, events must comply with the least strict condition of the SRs on the $m_{\mathrm{T}}^{\mathrm{lep}}$, that is $m_{\mathrm{T}}^{\mathrm{lep}} > 130\,\mathrm{GeV}$, to ensure that the CR is kinematically close to both SRs. The purity of the $t\bar{t}$ process in the $\mathrm{CR}_{\mathrm{1L}}^{t\bar{t}}$ is above 94 % in simulation prior to the background-only fit and the ratio of signal to background is below 2.3 %. For the $t\bar{t}$ prediction in the 1L channel, a normalisation parameter of $\mu_{1L}^{t\bar{t}} = 0.92 \pm 0.06$ is obtained from the background-only fit, which agrees with the SM prediction of $\mu_{1L}^{t\bar{t}} = 1$ within two standard deviations. The deviation of the parameter from one can be related to modelling inaccuracies of the top-quark kinematics in the simulated $t\bar{t}$ samples [360]. The data and the background prediction obtained from the background-only fit are compared in Figure 10.2 in the $E_{\mathrm{T}}^{\mathrm{miss}}$ distribution in the $\mathrm{CR}_{\mathrm{1L}}^{t\bar{t}}$. No significant deviations are observed.

One of the three largest contributions to the SM background in the $\mathrm{SR}_{\mathrm{0L}}$ stems from semi-leptonic $t\bar{t}$ decays. This background is constrained in the $\mathrm{CR}_{\mathrm{0L}}^{t\bar{t}}$. A high purity of semi-leptonic $t\bar{t}$ events is achieved by selecting events with exactly one electron or muon and $m_{\mathrm{T}}^{\mathrm{lep}} < 130\,\mathrm{GeV}$. Requiring low am_{T2} in the CR guarantees that the phase spaces of the CR and the 1L channel SRs and other CRs do not overlap. The purity of $t\bar{t}$ events in the $\mathrm{CR}_{\mathrm{0L}}^{t\bar{t}}$ is greater than 80 % prior to the background-only fit and the ratio of the signal yield to the total predicted SM background is below 1.2 % for all studied 2HDM+a model signals. The normalisation parameter obtained from the background-only fit for the $t\bar{t}$ background in the 0L channel is $\mu_{0L}^{t\bar{t}} = 1.00 \pm 0.12$, which agrees with one very well. Good agreement between the data and post-fit background prediction is observed in the $E_{\mathrm{T}}^{\mathrm{miss}}$ distribution in Figure 10.3.

The selection criteria employed in the $t\bar{t}$ CRs are summarised in Table 10.1. Table 10.2 shows the observed data and the predicted yields prior to the background-only fit and corrected by the fit in the CRs.

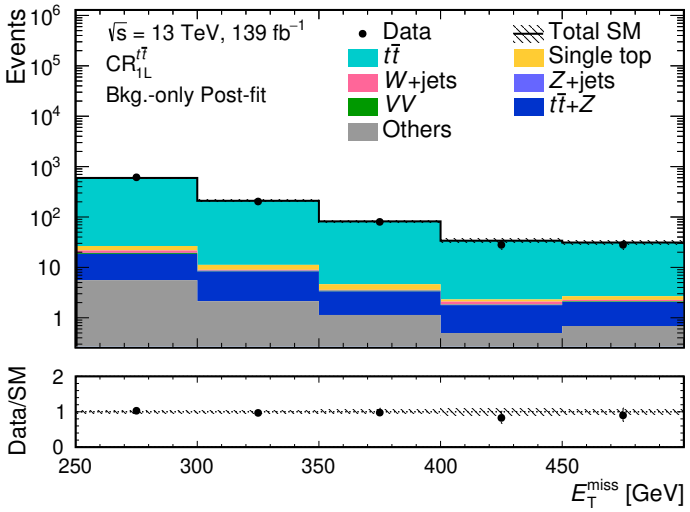

Figure 10.2: Distribution of the data and the SM background processes as a function of the $E_{\mathrm{T}}^{\mathrm{miss}}$ in the $\mathrm{CR}^{t\bar{t}}_{1\mathrm{L}}$. The hashed uncertainty band includes all systematic uncertainty sources described in Section 10.3. The post-fit normalisation parameters of the SM processes and the post-fit systematic uncertainties obtained from the background-only fit described in Section 8.4 are used in the figure. Events beyond the range of the x-axis are added to the rightmost bin. The bottom panel shows the ratio of the data and the sum of all SM predictions in each bin. "Others" contains contributions from the triboson, tWZ, tZ, $t\bar{t}+W$, $t\bar{t}+h$, $t\bar{t}t$ and $t\bar{t}t\bar{t}$ processes.

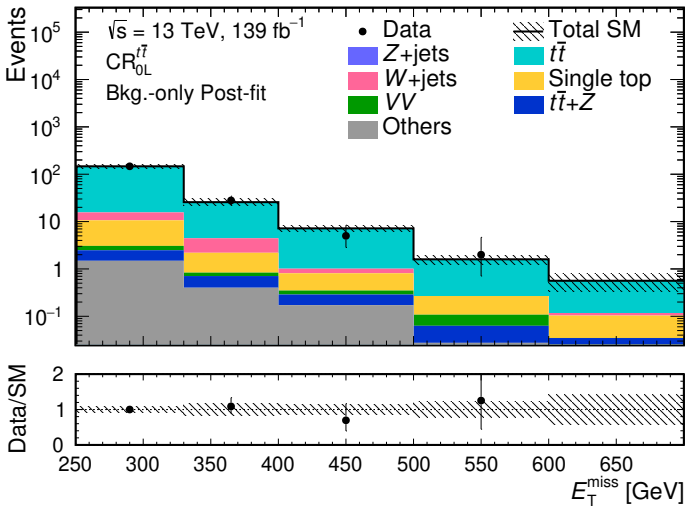

Figure 10.3: Distribution of the data and the SM background processes as a function of the $E_{\mathrm{T}}^{\mathrm{miss}}$ in the $\mathrm{CR}^{t\bar{t}}_{0\mathrm{L}}$. The hashed uncertainty band includes all systematic uncertainty sources described in Section 10.3. The normalisation and nuisance parameters obtained from the background-only fit described in Section 8.4 are used for the SM predictions in the figure. Events beyond the range of the x-axis are added to the rightmost bin. The bottom panel shows the ratio of the data and the sum of all SM predictions in each bin. "Others" contains contributions from the triboson, tWZ, tZ, $t\bar{t}+W$, $t\bar{t}+h$, $t\bar{t}t$ and $t\bar{t}t\bar{t}$ processes.

	$\mathrm{CR}^{t\bar{t}}_{0\mathrm{L}}$	$\mathrm{CR}^{t\bar{t}}_{1\mathrm{L}}$
Trigger	$E_{\mathrm{T}}^{\mathrm{miss}}$	$E_{\mathrm{T}}^{\mathrm{miss}}$
$E_{\mathrm{T}}^{\mathrm{miss}}$ [GeV]	≥ 250	≥ 250
$\Delta\phi_{\mathrm{min},1-4}$ [rad]	≥ 0.5	≥ 0.5
$N^{\ell,b}$,$N^{\ell,s}$	$= 1$	$= 1$
p_{T}^{l1} [GeV]	≥ 30	≥ 30
N^{j}	≥ 4	≥ 3
p_{T}^{j1} [GeV]	≥ 100	≥ 50
p_{T}^{j2} [GeV]	≥ 60	≥ 30
p_{T}^{j3} [GeV]	≥ 60	≥ 30
p_{T}^{j4} [GeV]	≥ 40	–
N^{b}	≥ 1	≥ 1
p_{T}^{b1} [GeV]	≥ 50	≥ 50
p_{T}^{b2} [GeV]	< 50	≥ 50
$m_{\mathrm{T}}^{\mathrm{lep}}$ [GeV]	< 130	≥ 130
am_{T2} [GeV]	< 180	< 180
$N^{W-\mathrm{tag}}$	≥ 1	–
$\Delta R_{W,b}$	≥ 1.0	–
$m_{W,b}$ [GeV]	≥ 220	–

Table 10.1: Selection criteria of the $t\bar{t}$ CRs.

		$\mathrm{CR}^{t\bar{t}}_{0\mathrm{L}}$	$\mathrm{CR}^{t\bar{t}}_{1\mathrm{L}}$
	Data	182	952
Post-fit	Total SM	182 ± 14	950 ± 40
	$t\bar{t}$	160 ± 18	900 ± 40
	Z+jets	$0.04^{+0.09}_{-0.04}$	0.18 ± 0.09
	W+jets	7 ± 3	3.1 ± 0.7
	$t\bar{t} + Z$	$1.5^{+1.7}_{-1.5}$	24 ± 12
	Single top	10^{+11}_{-10}	9^{+13}_{-9}
	VV	0.8 ± 0.7	1.2 ± 0.4
	Others	2.1 ± 0.4	10.0 ± 0.9
Pre-fit	Total SM	194.65	1036.57
	$t\bar{t}$	160.95	981.04
	Z+jets	0.04	0.18
	W+jets	6.91	2.91
	$t\bar{t} + Z$	1.24	20.35
	Single top	22.57	20.87
	VV	0.82	1.19
	Others	2.11	10.03

Table 10.2: Data and predicted yields in the CRs targeting the $t\bar{t}$ process prior to the background-only fit ("pre-fit") and using the normalisation and uncertainties as derived by the background-only fit ("post-fit"). The uncertainties include all systematic uncertainty sources described in Section 10.3. "Others" contains contributions from the triboson, tWZ, tZ, $t\bar{t} + W$, $t\bar{t} + h$, $t\bar{t}t$ and $t\bar{t}t\bar{t}$ processes.

10.1.2 Vector-boson plus jets control regions

The W+jets process is among the three most dominant background processes in all SRs of the 1L and 0L channels. As requiring the presence of at least one b-tagged jet in these SRs, the W+jets background is dominated by events with heavy flavour jets. Constructing a CR that is highly pure in W+jets events is challenging as the $t\bar{t}$ cross-section is relatively high compared to the W+jets cross-section in the phase spaces of the search. The normalisation of the W+jets process is determined in the $\mathrm{CR_{W+jets}}$, which is kinematically close to the $\mathrm{SR_{1L}^{HadTop}}$ where W+jets is the second largest background process. Events with a W-boson decaying into leptons are selected by requiring $m_{\mathrm{T}}^{\mathrm{lep}}$ to be compatible with the W-boson mass. This increases the W+jets purity. A large number of events from the $t\bar{t}$ process also enter in this low $m_{\mathrm{T}}^{\mathrm{lep}}$ region and require a dedicated suppression to ensure a high W+jets purity. They are suppressed by selecting events with high am_{T2}. Furthermore, requiring $\mathrm{Sig}_{E_{\mathrm{T}}^{\mathrm{miss}}} \geq 15$ is found to suppress $t\bar{t}$ events, while increasing the purity of the W+jets process. In the phase space region selecting events with one reconstructed lepton, one leptonically decaying W-boson is expected in the W+jets process. Due to the absence of hadronically decaying W-bosons in the W+jets process in this phase space, events with exactly zero W-tagged large-radius jets and an $m_W^{\mathrm{recl}} < 60\,\mathrm{GeV}$ are selected. This increases the fraction of W+jets events in the CR. The W+jets purity of the $\mathrm{CR_{W+jets}}$ is greater than 60 % prior to the background-only fit with a ratio of signal to background below 0.5 %. The background-only fit yields a W+jets normalisation parameter of $\mu_{W+\mathrm{jets}} = 1.08 \pm 0.09$, which is consistent with the SM prediction of $\mu_{W+\mathrm{jets}} = 1$. The data and background prediction corrected by the background-only fit are compared in Figure 10.4 in the $E_{\mathrm{T}}^{\mathrm{miss}}$ distribution in the $\mathrm{CR_{W+jets}}$. No significant deviations within the uncertainties are observed.

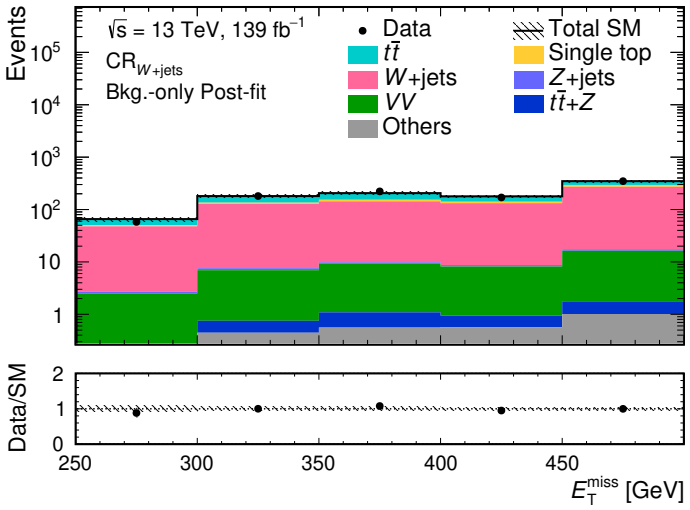

Figure 10.4: Distribution of the data and the SM background processes as a function of the $E_{\mathrm{T}}^{\mathrm{miss}}$ in the $\mathrm{CR_{W+jets}}$. The hashed uncertainty band includes all systematic uncertainty sources described in Section 10.3. The post-fit normalisation of the SM processes and the post-fit systematic uncertainties obtained from the background-only fit described in Section 8.4 are used in the figure. Events beyond the range of the x-axis are added to the rightmost bin. The bottom panel shows the ratio of the data and the sum of all SM predictions in each bin. "Others" contains contributions from the triboson, tWZ, tZ, $t\bar{t}+W$, $t\bar{t}+h$, $t\bar{t}t$ and $t\bar{t}t\bar{t}$ processes.

The largest background process in the SR_{0L} is Z+jets, with the Z-boson decaying into neutrinos. Its normalisation is determined in the CR_{Z+jets}. The CR_{Z+jets} selects events with two reconstructed leptons. They must have an opposite sign (OS) charge, the same flavour (SF) and an invariant mass $m_{\ell\ell}$ compatible with the Z-boson mass. The phase space of the CR_{Z+jets} is designed to be as close as possible to the one of the SR_{0L}. To imitate the impact of the E_T^{miss} related variables employed in the SR_{0L}, the two reconstructed leptons in the CR_{Z+jets} are regarded to be neutrinos. A modified variant of the $\vec{p}_T^{\,miss}$ is defined by summing the transverse momentum vectors of the leptons and $\vec{p}_T^{\,miss}$. The E_T^{miss} related variables are recalculated with this modified $\vec{p}_T^{\,miss}$ and denoted by $E_{T,\ell\ell}^{miss}$, $Sig_{E_{T,\ell\ell}^{miss}}$, $\Delta\phi_{min,1-4,\ell\ell}$ and $m_T^{b,E_{T,\ell\ell}^{miss}}$. Conditions very similar to the ones in the SR_{0L} are imposed on these modified E_T^{miss} variables in the Z+jets CR. The genuine E_T^{miss} in this CR is required to be below 120 GeV to increase the Z+jets purity as Z+jets events have little genuine E_T^{miss} in the $Z \to \ell\bar{\ell}$ final state. Furthermore the requirement on the E_T^{miss} suppresses signal events. The CR_{Z+jets} has a Z+jets purity above 85 % and a ratio of signal to background below 1 % prior to the background-only fit. The Z+jets normalisation parameter given by the background-only fit is $\mu_{Z+jets} = 0.99 \pm 0.07$ and agrees with the SM predicted value of one. Good agreement between the data and the SM prediction corrected by the background-only fit is observed in the CR_{Z+jets} as shown in Figure 10.5 in the $E_{T,\ell\ell}^{miss}$ variable.

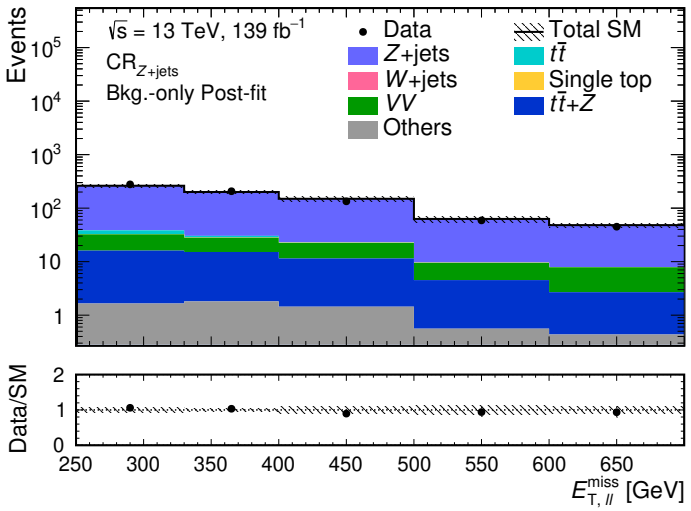

Figure 10.5: Distribution of the data and the SM background processes as a function of the $E_{T,\ell\ell}^{miss}$ in the CR_{Z+jets}. The hashed uncertainty band includes all systematic uncertainty sources described in Section 10.3. The post-fit normalisation of the SM processes and the post-fit systematic uncertainties obtained from the background-only fit described in Section 8.4 are used in the figure. Events beyond the range of the x-axis are added to the rightmost bin. The bottom panel shows the ratio of the data and the sum of all SM predictions in each bin. "Others" contains contributions from the triboson, tWZ, tZ, $t\bar{t}+W$, $t\bar{t}+h$, $t\bar{t}t$ and $t\bar{t}t\bar{t}$ processes.

Table 10.3 summarises the selection criteria employed in the CR_{Z+jets} and the CR_{W+jets}. The observed number of events and the predicted number of SM events prior to the background-only fit and resulting from the fit are shown for the two CRs in Table 10.4.

	CR_{Z+jets}	CR_{W+jets}	$CR_{t\bar{t}+Z}$	$CR_{single\ top}$
Trigger	Single lepton	E_T^{miss}	Single lepton	E_T^{miss}
E_T^{miss} [GeV]	≤ 120	≥ 250	–	≥ 250
$E_{T,\ell\ell}^{miss}$ [GeV]	≥ 250	–	≥ 140	–
$Sig_{E_T^{miss}}$	–	≥ 15	–	–
$Sig_{E_{T,\ell\ell}^{miss}}$	≥ 14	–	–	–
$\Delta\phi_{min,1-4}$ [rad]	–	≥ 0.5	–	≥ 0.5
$\Delta\phi_{min,1-4,\ell\ell}$ [rad]	≥ 0.5	–	–	–
$N^{\ell,b}$,$N^{\ell,s}$	$= 2$	$= 1$	$= 3$	$= 2$
p_T^{l1} [GeV]	≥ 30	≥ 30	≥ 30	≥ 25
p_T^{l2} [GeV]	≥ 20	–	≥ 20	≥ 20
p_T^{l3} [GeV]	–	–	≥ 20	–
$m_{\ell\ell}$ [GeV]	$\in [81, 101]$	–	$\in [71, 111]$	$> 40, \notin [71, 111]$
N^j	≥ 4	≥ 3	≥ 3	≥ 1
p_T^{j1} [GeV]	≥ 100	≥ 50	≥ 30	≥ 50
p_T^{j2} [GeV]	≥ 60	≥ 30	≥ 30	–
p_T^{j3} [GeV]	≥ 60	≥ 30	≥ 30	–
p_T^{j4} [GeV]	≥ 40	–	–	–
N^b	≥ 1	≥ 1	≥ 2	≥ 1
p_T^{b1} [GeV]	≥ 50	≥ 50	≥ 30	≥ 50
p_T^{b2} [GeV]	< 50	< 50	≥ 30	–
$m_T^{b,E_{T,\ell\ell}^{miss}}$ [GeV]	≥ 180	–	–	–
m_T^{lep} [GeV]	–	$\in [40, 100]$	–	≥ 30
am_{T2} [GeV]	–	≥ 180	–	–
m_{T2} [GeV]	–	–	–	≤ 100
$\min_l m_{bl}$ [GeV]	–	–	–	≥ 170
m_{bl}^t [GeV]	–	–	–	≥ 150
N^{W-tag}	–	$= 0$	–	–
m_W^{recl} [GeV]	–	< 60	–	–

Table 10.3: Selection criteria of the common CRs. The transverse momentum vectors of the selected SF-OS lepton pair are added to the $\vec{p}_T^{\,miss}$ for the $E_{T,\ell\ell}^{miss}$, $Sig_{E_{T,\ell\ell}^{miss}}$, $\Delta\phi_{min,1-4,\ell\ell}$ and $m_T^{b,E_{T,\ell\ell}^{miss}}$ variables.

		CR_{Z+jets}	CR_{W+jets}	$CR_{t\bar{t}+Z}$	$CR_{single\ top}$
	Data	723	979	234	397
Post-fit	Total SM	720 ± 30	980 ± 40	234 ± 16	400 ± 20
	$t\bar{t}$	9 ± 4	200 ± 30	7 ± 7	170 ± 40
	Z+jets	610 ± 30	2.9 ± 0.8	2.6 ± 1.2	2.0 ± 0.6
	W+jets	0	680 ± 60	0	1.3 ± 0.7
	$t\bar{t} + Z$	44 ± 9	2.1 ± 1.9	173 ± 19	3^{+4}_{-4}
	Single top	$0.2^{+0.5}_{-0.3}$	50 ± 40	$0.07^{+0.14}_{-0.07}$	170 ± 50
	VV	50 ± 6	39 ± 6	14 ± 3	39 ± 4
	Others	5.9 ± 0.6	2.7 ± 0.3	38 ± 4	10.9 ± 1.1
Pre-fit	Total SM	725.99	1017.40	208.39	638.64
	$t\bar{t}$	8.54	221.84	7.56	185.75
	Z+jets	623.24	2.99	2.63	2.00
	W+jets	0.00	626.94	0.00	1.20
	$t\bar{t} + Z$	37.34	1.78	146.69	2.65
	Single top	0.54	122.57	0.17	397.21
	VV	50.44	38.61	13.62	38.93
	Others	5.90	2.66	37.72	10.88

Table 10.4: Data and predicted yields in the common CRs prior to the background-only fit ("pre-fit") and using the normalisation and uncertainties as derived by the background-only fit ("post-fit"). The uncertainties include all systematic uncertainty sources described in Section 10.3. "Others" contains contributions from the triboson, tWZ, tZ, $t\bar{t} + W$, $t\bar{t} + h$, $t\bar{t}t$ and $t\bar{t}t\bar{t}$ processes.

10.1.3 $t\bar{t} + Z$ and single top quark control regions

The second largest background process in the SR^{LepTop}_{1L} is $t\bar{t} + Z$, with the Z-boson decaying into neutrinos. As in the CR_{Z+jets}, the normalisation of the $t\bar{t}+Z$ process is determined in a phase space region where the Z-boson decays into charged leptons. By regarding the charged leptons to be neutrinos, the impact of the constraints on E^{miss}_T related variables on $t\bar{t} + Z$ events is imitated. The used CR was first introduced in Reference [361] and is denoted by $CR_{t\bar{t}+Z}$. It selects events with three reconstructed leptons, at least three small-radius jets and at least two b-jets. Two of the three reconstructed leptons in an event are required to form an SF-OS pair compatible with a Z-boson decay. If an event contains multiple such lepton pairs, the one with an invariant mass closest to the Z-boson mass is selected. The selected charged lepton pair is regarded to be a pair of neutrinos and the $E^{miss}_{T,\ell\ell}$ is calculated as in the CR_{Z+jets}. Events in the $CR_{t\bar{t}+Z}$ must have an $E^{miss}_{T,\ell\ell}$ greater than 140 GeV. The purity of the $t\bar{t} + Z$ process is greater than 69 % in the $CR_{t\bar{t}+Z}$ prior to the background-only fit and the ratio of signal to background is below 1 %. Events containing fake and non-prompt leptons constitute less than 10 % of the events in the $CR_{t\bar{t}+Z}$, as was estimated using the simulation. This fraction of events is in good agreement with what was determined in Reference [361] in the $CR_{t\bar{t}+Z}$. The normalisation parameter obtained from the background-only fit for the $t\bar{t} + Z$ background process is $\mu_{t\bar{t}+Z} = 1.18 \pm 0.19$, which agrees with the SM prediction of one. The normalisation parameter obtained is compatible with the one from a recent $t\bar{t} + Z$ cross-section measurement in a similar phase space

region[1] [362]. The distribution of the data and the SM prediction resulting from the background-only fit are shown in Figure 10.6 for the $E_{\mathrm{T},\ell\ell}^{\mathrm{miss}}$ variable in the $\mathrm{CR}_{\mathrm{t\bar{t}+Z}}$. No significant deviations between the two are observed.

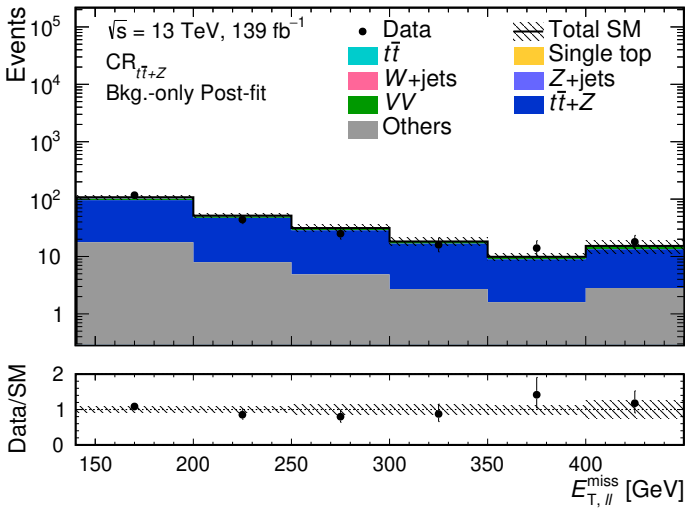

Figure 10.6: Distribution of the data and the SM background processes as a function of the $E_{\mathrm{T},\ell\ell}^{\mathrm{miss}}$ in the $\mathrm{CR}_{\mathrm{t\bar{t}+Z}}$. The hashed uncertainty band includes all systematic uncertainty sources described in Section 10.3. The post-fit normalisation of the SM processes and the post-fit systematic uncertainties obtained from the background-only fit described in Section 8.4 are used in the figure. Events beyond the range of the x-axis are added to the rightmost bin. The bottom panel shows the ratio of the data and the sum of all SM predictions in each bin. "Others" contains contributions from the triboson, tWZ, tZ, $t\bar{t}+W$, $t\bar{t}+h$, $t\bar{t}t$ and $t\bar{t}t\bar{t}$ processes.

Due to the large uncertainties related to the modelling of the single top quark process (see the discussion below and Section 10.3), the normalisation of the single top quark process is derived in a CR. As the single top quark background is dominated by the associated production of a top-quark and a W-boson (tW), the $\mathrm{CR}_{\text{single top}}$ is designed to select events compatible with the tW decay topology. Events with exactly two reconstructed leptons (i.e. ee, $\mu\mu$ or $e\mu$), high $E_{\mathrm{T}}^{\mathrm{miss}}$ and at least one small-radius jet, of which at least one is b-tagged, are selected. The two reconstructed leptons must be of opposite sign. Events with two reconstructed leptons of same flavour are rejected if their invariant mass $m_{\ell\ell}$ is compatible with the Z-boson mass to suppress the Z+jets events. The fraction of tW events in the $\mathrm{CR}_{\text{single top}}$ is increased by using the m_{T2} variable introduced in Section 9.1.2 and requiring $m_{\mathrm{T2}} < 100\,\mathrm{GeV}$ (see Figure 9.5).

To enhance the fraction of events from the single top quark process and to suppress events from di-leptonic $t\bar{t}$ decays, the $\min_l m_{bl}$ and m_{bl}^t variables [21] are employed in the $\mathrm{CR}_{\text{single top}}$. The minimum of the invariant masses of each of the two reconstructed leptons in an event and the leading-p_{T} b-jet define the $\min_l m_{bl}$ variable:

$$\min_l m_{bl} \coloneqq \min_l m_{b1,l}.$$

The distribution of signal and background events in the $\min_l m_{bl}$ variable in the

[1]The main difference in the event selection criteria is the absence of the $E_{\mathrm{T},\ell\ell}^{\mathrm{miss}}$ constraint in the measurement.

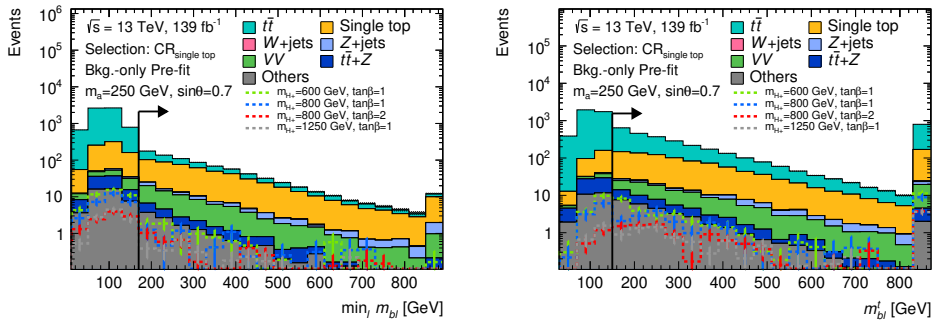

(a) (b)

Figure 10.7: Distribution of signal and background events in the (a) $\min_l m_{bl}$ and (b) m^t_{bl} variables in the $\mathrm{CR}_{\text{single top}}$ without any requirements on the m_{T2}, $\min_l m_{bl}$ and m^t_{bl}. The arrow indicates the direction and position of the requirement in the CR. Only statistical uncertainties are shown. The normalisation of the simulated background samples has not been corrected by the background-only fit. "Others" contains contributions from the $t\bar{t}+h$, $t\bar{t}+W$, tZ and tWZ processes. Events beyond the range of the x-axis are added to the rightmost bin.

$\mathrm{CR}_{\text{single top}}$ without any requirements on the m_{T2}, $\min_l m_{bl}$ and m^t_{bl} is shown in Figure 10.7a. Events from the $t\bar{t}$ process have a kinematic endpoint in $\min_l m_{bl}$ at roughly the top-quark mass. Events selected in the $\mathrm{CR}_{\text{single top}}$ must fulfil $\min_l m_{bl} \geq 170\,\mathrm{GeV}$.

The suppression of $t\bar{t}$ events is complemented by the m^t_{bl} variable [363]. In events with at least two small-radius jets, it is defined as

$$m^t_{bl} \coloneqq \min\left[\max(m_{b1,l1}, m_{b2,l2}), \max(m_{b1,l2}, m_{b2,l1})\right],$$

where $m_{bi,lj}$ indicates the invariant mass of jet i and reconstructed lepton j. The jets are sorted in descending order by the output value of the multivariate b-tagging algorithm (b-tagging score), while the electrons and muons are sorted by their transverse momenta. The distribution of signal and background events in the m^t_{bl} variable in the $\mathrm{CR}_{\text{single top}}$ without any requirements on the m_{T2}, $\min_l m_{bl}$ and m^t_{bl} is shown in Figure 10.7b. For $t\bar{t}$ events, m^t_{bl} has a kinematic endpoint around the top-quark mass. This is exploited to discriminate $t\bar{t}$ and single top quark events in the $\mathrm{CR}_{\text{single top}}$ by requiring $m^t_{bl} \geq 150\,\mathrm{GeV}$.

The purity of single top quark events is $\simeq 62\,\%$ in the $\mathrm{CR}_{\text{single top}}$ prior to the background-only fit, while the ratio of signal to background is below $1.5\,\%$. A normalisation parameter of $\mu_{\text{single top}} = 0.43 \pm 0.13$ is obtained from the background-only fit. The large deviation of $\mu_{\text{single top}}$ from the SM prediction of one is due to the treatment of the interference of the tW and $t\bar{t}$ processes. The nominal interference treatment procedure, diagram removal [251] is compared to the diagram subtraction procedure [251] in the $\mathrm{CR}_{\text{single top}}$. While the SM prediction employing the nominal diagram removal procedure exceeds the data, the data is found to exceed the SM prediction if using diagram subtraction. The single top quark normalisation can therefore be estimated irrespective of the interference removal procedure of tW and $t\bar{t}$ with the $\mathrm{CR}_{\text{single top}}$. The deviations between the diagram removal and diagram subtraction predictions and the observed $\mu_{\text{single top}} = 0.43 \pm 0.13$ show how challenging an accurate modelling of the tW process is.

Figure 10.8 shows the $E_{\mathrm{T}}^{\mathrm{miss}}$ distribution in the $\mathrm{CR}_{\text{single top}}$ for the data and the SM processes. The SM prediction has been corrected using the results from the

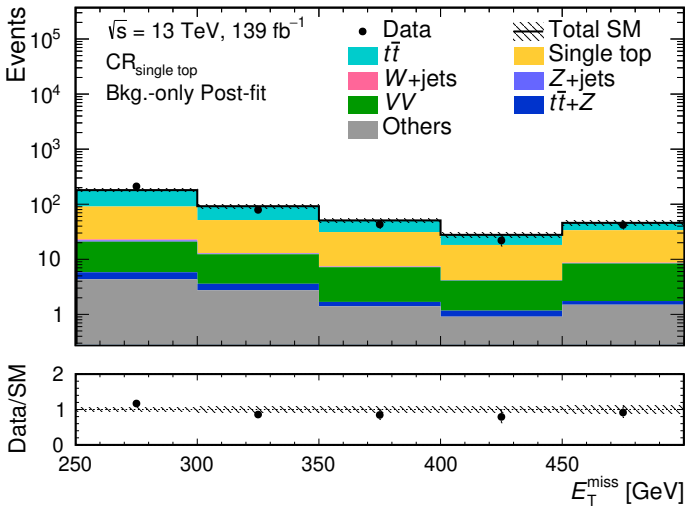

Figure 10.8: Distribution of the data and the SM background processes as a function of the $E_{\mathrm{T}}^{\mathrm{miss}}$ in the $\mathrm{CR}_{\text{single top}}$. The hashed uncertainty band includes all systematic uncertainty sources described in Section 10.3. The post-fit normalisation of the SM processes and the post-fit systematic uncertainties obtained from the background-only fit described in Section 8.4 are used in the figure. Events beyond the range of the x-axis are added to the rightmost bin. The bottom panel shows the ratio of the data and the sum of all SM predictions in each bin. "Others" contains contributions from the triboson, tWZ, tZ, $t\bar{t}+W$, $t\bar{t}+h$, $t\bar{t}t$ and $t\bar{t}t\bar{t}$ processes.

background-only fit. Good agreement between the data and the SM prediction is observed.

The selection criteria of the $\mathrm{CR}_{\mathrm{t\bar{t}+Z}}$ and the $\mathrm{CR}_{\text{single top}}$ are summarised in Table 10.3. Observed and predicted event numbers for the $\mathrm{CR}_{\mathrm{t\bar{t}+Z}}$ and the $\mathrm{CR}_{\text{single top}}$ can be found in Table 10.4.

10.2 Validation regions

The background normalisation parameters obtained with the CRs are validated by using dedicated validation regions (VRs). For each of the dominant background processes in the different SRs a VR is defined.

To be an independent measure of the quality of the background estimation, a VR must have a non-overlapping phase space with the SRs and CRs. At the same time, the phase space of a VR should be as close as possible to the phase spaces of the SRs it is meant to validate the background estimation of. The fraction of events of the estimated SM process to be verified should be as large as possible, while the signal yield in a VR should be small.

That the phase spaces of the VRs employed in this analysis are non-overlapping, yet kinematically close to the ones of the SRs is shown schematically in Figure 10.1.

10.2.1 Validation regions for the 1L channel

The $t\bar{t}$ prediction in the 1L channel is verified in two VRs. The phase space of the $\mathrm{VR}_{\mathrm{1L}}^{t\bar{t}-\mathrm{lep}}$ is kinematically close to the one of the $\mathrm{SR}_{\mathrm{1L}}^{\mathrm{LepTop}}$, while the $\mathrm{VR}_{\mathrm{1L}}^{t\bar{t}-\mathrm{had}}$'s phase space is kinematically close to the $\mathrm{SR}_{\mathrm{1L}}^{\mathrm{HadTop}}$. In both regions it is exploited

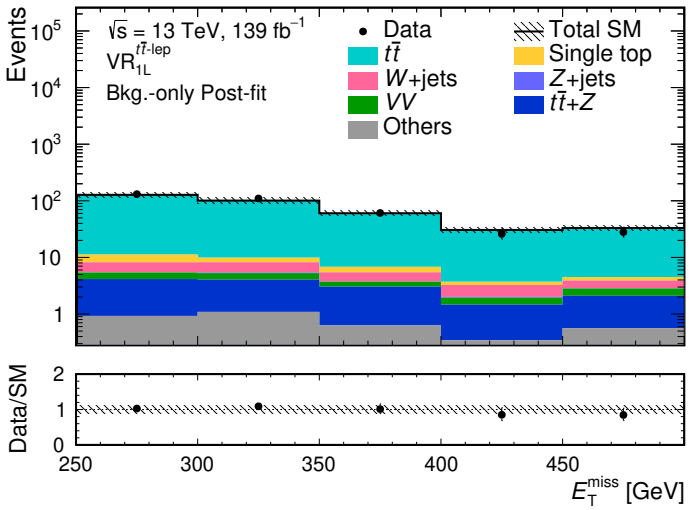

Figure 10.9: Distribution of the data and the SM background processes as a function of the $E_{\mathrm{T}}^{\mathrm{miss}}$ in the $\mathrm{VR}_{\mathrm{1L}}^{t\bar{t}-\mathrm{lep}}$. The hashed uncertainty band includes all systematic uncertainty sources described in Section 10.3. The post-fit normalisation of the SM processes and the post-fit systematic uncertainties obtained from the background-only fit described in Section 8.4 are used in the figure. Events beyond the range of the x-axis are added to the rightmost bin. The bottom panel shows the ratio of the data and the sum of all SM predictions in each bin. "Others" contains contributions from the triboson, tWZ, tZ, $t\bar{t}+W$, $t\bar{t}+h$, $t\bar{t}t$ and $t\bar{t}t\bar{t}$ processes.

that the dominant di-leptonic $t\bar{t}$ component in the 1L SRs takes low values of the am_{T2}. For that reason, the am_{T2} requirement is inverted with respect to the SRs in these two VRs. This increases the purity of di-leptonic $t\bar{t}$ decays in the regions. No constraints on the number of W-tagged jets and the reclustered jet mass m_W^{recl} are placed in the two regions, increasing the statistics. Prior to the background-only fit, the purity of the $t\bar{t}$ process in the two VRs is greater than 88 % and the ratio of signal to background is below 7.2 %. The $E_{\mathrm{T}}^{\mathrm{miss}}$ distributions of the data and the SM predictions corrected using the background-only fit results in the $\mathrm{VR}_{\mathrm{1L}}^{t\bar{t}-\mathrm{lep}}$ and $\mathrm{VR}_{\mathrm{1L}}^{t\bar{t}-\mathrm{had}}$ regions are shown in Figures 10.9 and 10.10, respectively. Good agreement between the data and the corrected SM prediction is observed in both regions.

In the 1L channel, the W+jets prediction is validated in the $\mathrm{VR}_{\mathrm{1L}}^{W+\mathrm{jets}}$. As W+jets is the second largest SM background in the $\mathrm{SR}_{\mathrm{1L}}^{\mathrm{HadTop}}$, the phase space of the $\mathrm{VR}_{\mathrm{1L}}^{W+\mathrm{jets}}$ is designed to be close to the one of the $\mathrm{SR}_{\mathrm{1L}}^{\mathrm{HadTop}}$. Events with leptonically decaying W-bosons are selected by requiring $m_{\mathrm{T}}^{\mathrm{lep}}$ to be compatible with the W-boson mass. This enhances the fraction of W+jets events and ensures non-overlapping phase spaces of the VR and the SRs. By retaining the $\mathrm{SR}_{\mathrm{1L}}^{\mathrm{HadTop}}$ constraint on the m_W^{recl}, overlap of the phase spaces of the $\mathrm{VR}_{\mathrm{1L}}^{W+\mathrm{jets}}$ and the $\mathrm{CR}_{\mathrm{W+jets}}$ are avoided. By requiring selected events to fulfil $\mathrm{Sig}_{E_{\mathrm{T}}^{\mathrm{miss}}} \geq 15$, the fraction of W+jets events is further increased. The purity of W+jets events prior to the background-only fit is roughly 26 % in the $\mathrm{VR}_{\mathrm{1L}}^{W+\mathrm{jets}}$. The most dominant other SM processes are $t\bar{t}$ (60 %) and single top quark (11 %). The $\mathrm{VR}_{\mathrm{1L}}^{W+\mathrm{jets}}$ therefore verifies the prediction of the three processes all together. A signal to background ratio below 0.6 % is found in the VR. The $E_{\mathrm{T}}^{\mathrm{miss}}$ distributions of the data and the SM prediction corrected by the background-only fit are shown in Figure 10.11. No

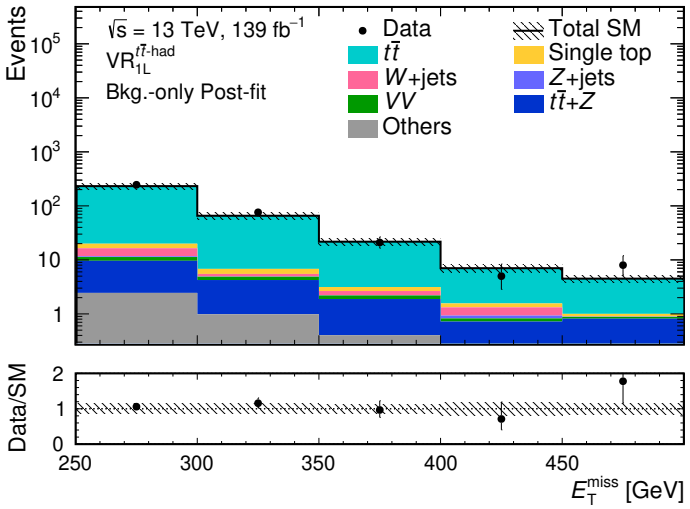

Figure 10.10: Distribution of the data and the SM background processes as a function of the $E_{\mathrm{T}}^{\mathrm{miss}}$ in the $\mathrm{VR}_{1\mathrm{L}}^{t\bar{t}-\mathrm{had}}$. The hashed uncertainty band includes all systematic uncertainty sources described in Section 10.3. The post-fit normalisation of the SM processes and the post-fit systematic uncertainties obtained from the background-only fit described in Section 8.4 are used in the figure. Events beyond the range of the x-axis are added to the rightmost bin. The bottom panel shows the ratio of the data and the sum of all SM predictions in each bin. "Others" contains contributions from the triboson, tWZ, tZ, $t\bar{t}+W$, $t\bar{t}+h$, $t\bar{t}t$ and $t\bar{t}t\bar{t}$ processes.

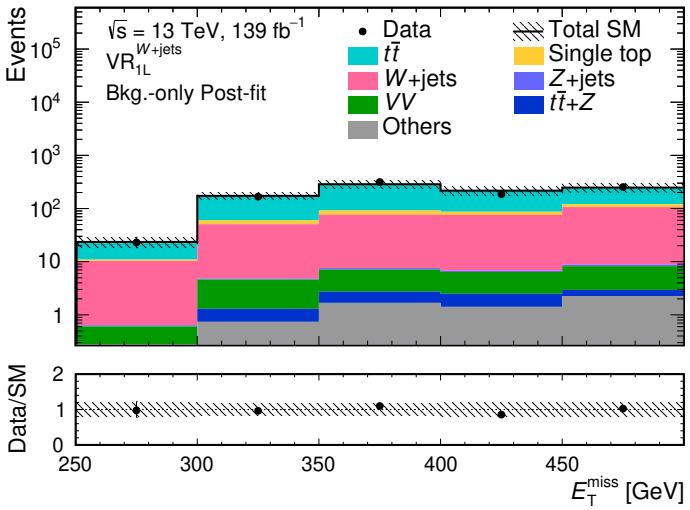

Figure 10.11: Distribution of the data and the SM background processes as a function of the $E_{\mathrm{T}}^{\mathrm{miss}}$ in the $\mathrm{VR}_{1\mathrm{L}}^{W+\mathrm{jets}}$. The hashed uncertainty band includes all systematic uncertainty sources described in Section 10.3. The post-fit normalisation of the SM processes and the post-fit systematic uncertainties obtained from the background-only fit described in Section 8.4 are used in the figure. Events beyond the range of the x-axis are added to the rightmost bin. The bottom panel shows the ratio of the data and the sum of all SM predictions in each bin. "Others" contains contributions from the triboson, tWZ, tZ, $t\bar{t}+W$, $t\bar{t}+h$, $t\bar{t}t$ and $t\bar{t}t\bar{t}$ processes.

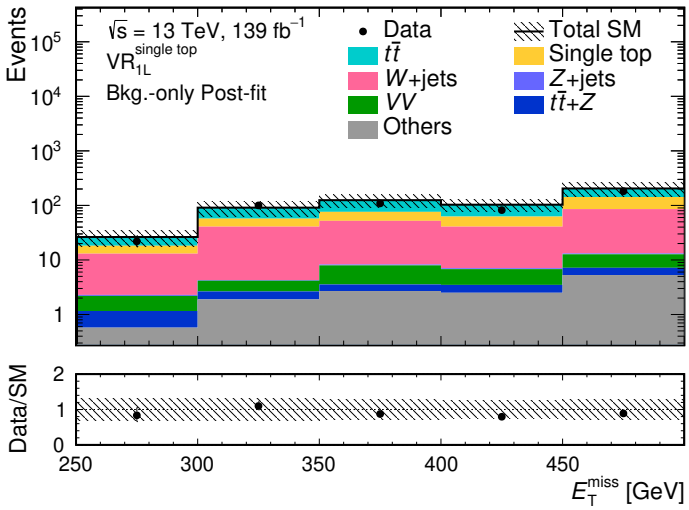

Figure 10.12: Distribution of the data and the SM background processes as a function of the $E_{\mathrm{T}}^{\mathrm{miss}}$ in the $\mathrm{VR}_{\mathrm{1L}}^{\text{single top}}$. The hashed uncertainty band includes all systematic uncertainty sources described in Section 10.3. The post-fit normalisation of the SM processes and the post-fit systematic uncertainties obtained from the background-only fit described in Section 8.4 are used in the figure. Events beyond the range of the x-axis are added to the rightmost bin. The bottom panel shows the ratio of the data and the sum of all SM predictions in each bin. "Others" contains contributions from the triboson, tWZ, tZ, $t\bar{t}+W$, $t\bar{t}+h$, $t\bar{t}t$ and $t\bar{t}t\bar{t}$ processes.

significant deviations between the data and the prediction are observed.

The $\mathrm{VR}_{\mathrm{1L}}^{\text{single top}}$ is defined to verify the single top quark prediction. The phase space of the $\mathrm{VR}_{\mathrm{1L}}^{\text{single top}}$ is kinematically close to the $\mathrm{SR}_{\mathrm{1L}}^{\mathrm{HadTop}}$. Events with leptonically decaying W-bosons are selected by placing the constraint $m_{\mathrm{T}}^{\mathrm{lep}} \leq 100\,\mathrm{GeV}$. This increases the number of events from the single top quark process. Furthermore, the purity of single top quark events is found to increase by selecting events with two b-jets, with the second leading-p_{T} b-jet having a p_{T} greater than 50 GeV. These conditions on the $m_{\mathrm{T}}^{\mathrm{lep}}$ and the second b-jet lead to a large number of $t\bar{t}$ events entering the region. The $\mathrm{SR}_{\mathrm{1L}}^{\mathrm{HadTop}}$ requirements on the $\mathrm{Sig}_{E_{\mathrm{T}}^{\mathrm{miss}}}$ and the am_{T2} are also imposed in this VR and reduce the fraction of events from the $t\bar{t}$ process. To increase the number of events and to make the region closer to both 1L SRs, the requirements on the $m_{b,\ell}$ and the m_W^{recl} are removed with respect to the $\mathrm{SR}_{\mathrm{1L}}^{\mathrm{HadTop}}$. The resulting region has a single top quark process purity of above 40 % prior to the background-only fit and a ratio of signal to background below 1.3 %. Figure 10.12 shows the distributions of the data and the SM predictions as estimated with the background-only fit in the $E_{\mathrm{T}}^{\mathrm{miss}}$ variable in the $\mathrm{VR}_{\mathrm{1L}}^{\text{single top}}$. The data and the SM prediction agree well within the uncertainties. This confirms the validity of the normalisation parameter of the single top quark process, which was found to be $\mu_{\text{single top}} = 0.43 \pm 0.13$ and hence incompatible with one.

Also employing the $\mathrm{CR}_{\mathrm{t\bar{t}+Z}}$, data and $t\bar{t}+Z$ prediction were observed to agree well in Reference [361]. For that reason, a VR verifying the $t\bar{t}+Z$ background is not designed.

The selection requirements of all 1L channel VRs are summarised in Table 10.5. The number of observed events and the number of expected SM events predicted by simulation and corrected by the background-only fit are shown in Table 10.6.

	$\text{VR}_{\text{1L}}^{t\bar{t}-\text{lep}}$	$\text{VR}_{\text{1L}}^{t\bar{t}-\text{had}}$	$\text{VR}_{\text{1L}}^{W+\text{jets}}$	$\text{VR}_{\text{1L}}^{\text{single top}}$
Trigger	$E_{\text{T}}^{\text{miss}}$	$E_{\text{T}}^{\text{miss}}$	$E_{\text{T}}^{\text{miss}}$	$E_{\text{T}}^{\text{miss}}$
$E_{\text{T}}^{\text{miss}}$ [GeV]	≥ 250	≥ 250	≥ 250	≥ 250
$\text{Sig}_{E_{\text{T}}^{\text{miss}}}$	≥ 15	–	≥ 15	≥ 15
$\Delta\phi_{\text{min},1-4}$ [rad]	≥ 0.5	≥ 0.5	≥ 0.5	≥ 0.5
$N^{\ell,b}$,$N^{\ell,s}$	$= 1$	$= 1$	$= 1$	$= 1$
p_{T}^{l1} [GeV]	≥ 30	≥ 30	≥ 30	≥ 30
N^{j}	≥ 2	≥ 3	≥ 3	≥ 3
p_{T}^{j1} [GeV]	≥ 50	≥ 50	≥ 50	≥ 50
p_{T}^{j2} [GeV]	≥ 30	≥ 30	≥ 30	≥ 30
p_{T}^{j3} [GeV]	–	≥ 30	≥ 30	≥ 30
N^{b}	≥ 1	≥ 1	≥ 1	≥ 2
p_{T}^{b1} [GeV]	≥ 50	≥ 50	≥ 50	≥ 50
p_{T}^{b2} GeV	< 50	< 50	< 50	≥ 50
$m_{b,\not{p}}$ [GeV]	≥ 200	< 200	< 200	–
$m_{\text{T}}^{\text{lep}}$ [GeV]	≥ 130	≥ 200	$\in [40, 100]$	≤ 100
am_{T2} [GeV]	< 180	< 180	≥ 180	≥ 180
m_{W}^{recl} [GeV]	–	–	≥ 60	–

Table 10.5: Selection criteria of the VRs of the 1L channel.

		$\text{VR}_{\text{1L}}^{t\bar{t}-\text{lep}}$	$\text{VR}_{\text{1L}}^{t\bar{t}-\text{had}}$	$\text{VR}_{\text{1L}}^{W+\text{jets}}$	$\text{VR}_{\text{1L}}^{\text{single top}}$
	Observed	356	356	945	495
Post-fit	Total SM	350 ± 40	330 ± 50	950 ± 170	550 ± 160
	$t\bar{t}$	320 ± 40	300 ± 50	580 ± 110	190 ± 40
	Z+jets	$0.3^{+0.3}_{-0.3}$	$0.5^{+1.8}_{-0.5}$	1.6 ± 0.7	1.2 ± 0.6
	W+jets	10 ± 3	6 ± 5	290 ± 100	200 ± 150
	$t\bar{t} + Z$	11 ± 8	13 ± 4	3 ± 4	5 ± 5
	Single top	7^{+13}_{-8}	6^{+10}_{-6}	50^{+100}_{-50}	120 ± 40
	VV	4.4 ± 0.5	2.8 ± 0.4	17 ± 3	16 ± 3
	Others	3.6 ± 0.4	4.3 ± 0.4	6.2 ± 0.7	13.0 ± 1.6
Pre-fit	Total SM	386.27	361.29	1042.90	718.05
	$t\bar{t}$	342.93	323.71	627.58	209.25
	Z+jets	0.26	0.48	1.63	1.25
	W+jets	8.89	5.76	270.25	183.11
	$t\bar{t} + Z$	9.54	11.02	2.90	4.31
	Single top	16.70	13.24	117.00	291.39
	VV	4.40	2.80	17.34	15.77
	Others	3.56	4.29	6.20	12.96

Table 10.6: Data and predicted yields in the 1L channel VRs prior to the background-only fit ("pre-fit") and using the normalisation and uncertainties as derived by the background-only fit ("post-fit"). The uncertainties include all systematic uncertainty sources described in Section 10.3. "Others" contains contributions from the triboson, tWZ, tZ, $t\bar{t} + W$, $t\bar{t} + h$, $t\bar{t}t$ and $t\bar{t}t\bar{t}$ processes.

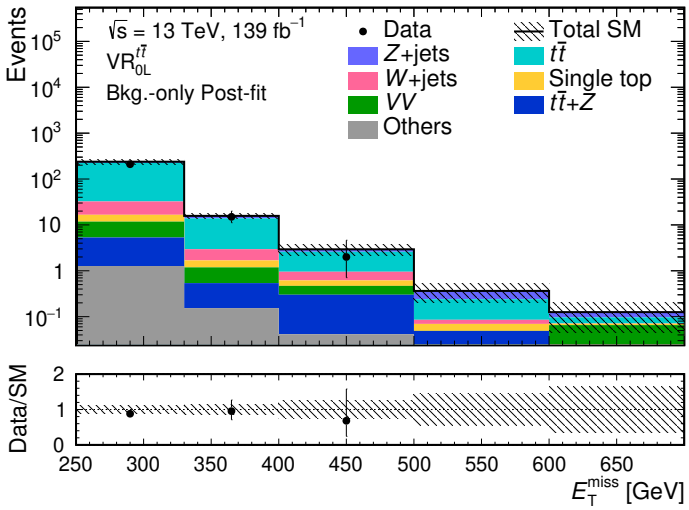

Figure 10.13: Distribution of the data and the SM background processes as a function of the $E_{\mathrm{T}}^{\mathrm{miss}}$ in the $\mathrm{VR}_{0\mathrm{L}}^{t\bar{t}}$. The hashed uncertainty band includes all systematic uncertainty sources described in Section 10.3. The post-fit normalisation of the SM processes and the post-fit systematic uncertainties obtained from the background-only fit described in Section 8.4 are used in the figure. Events beyond the range of the x-axis are added to the rightmost bin. The bottom panel shows the ratio of the data and the sum of all SM predictions in each bin. "Others" contains contributions from the triboson, tWZ, tZ, $t\bar{t}+W$, $t\bar{t}+h$, $t\bar{t}t$ and $t\bar{t}t\bar{t}$ processes.

10.2.2 Validation regions for the 0L channel

Two VRs are defined for the 0L channel. Both select events with zero electrons or muons. The $\mathrm{VR}_{0\mathrm{L}}^{t\bar{t}}$ is used to verify the $t\bar{t}$ prediction. By removing the $\Delta R_{W,b}$ and reversing the $m_{W,b}$ constraint with respect to the $\mathrm{SR}_{0\mathrm{L}}$, the fraction of $t\bar{t}$ events is increased. The $t\bar{t}$ purity is further enriched by selecting events with $10 \leq \mathrm{Sig}_{E_{\mathrm{T}}^{\mathrm{miss}}} \leq 14$. The purity of $t\bar{t}$ events prior to the background-only fit is 71 % in the $\mathrm{VR}_{0\mathrm{L}}^{t\bar{t}}$ and the ratio of signal to background $< 6.5\,\%$. The $E_{\mathrm{T}}^{\mathrm{miss}}$ distributions of the data and the predicted SM events corrected by the background-only fit in the $\mathrm{VR}_{0\mathrm{L}}^{t\bar{t}}$ are shown in Figure 10.13. Good agreement between the data and the SM prediction is observed, verifying the $t\bar{t}$ estimation.

The estimation of the Z+jets and W+jets predictions in the 0L channel is verified in the $\mathrm{VR}_{0\mathrm{L}}^{V+\mathrm{jets}}$. With respect to the $\mathrm{SR}_{0\mathrm{L}}$, the conditions on the $m_{W,b}$, $N^{W-\mathrm{tag}}$ and $\Delta R_{W,b}$ variables are removed, loosened and reversed, respectively[2]. The fraction of W+jets and Z+jets events in the VR is further enriched by using the angular separation $\Delta R_{j_1,j_2}$ between the two leading-p_{T} jets and the minimum $\Delta\phi$ between the $E_{\mathrm{T}}^{\mathrm{miss}}$ and all reconstructed jets. The purity of the W+jets process in the $\mathrm{VR}_{0\mathrm{L}}^{V+\mathrm{jets}}$ is 18 %, while the Z+jets purity is 48 % prior to the background-only fit. The ratio of signal to background is below 9.1 % in the $\mathrm{VR}_{0\mathrm{L}}^{V+\mathrm{jets}}$. Figure 10.14 shows the $E_{\mathrm{T}}^{\mathrm{miss}}$ distribution of the data and the predicted SM events corrected by the background-only fit in the $\mathrm{VR}_{0\mathrm{L}}^{V+\mathrm{jets}}$. No significant deviations of the data and the corrected SM prediction are observed.

The selection criteria of the 0L VRs are summarised in Table 10.7. Table 10.8 shows the number of events observed in the data and predicted by the SM prior to

[2]This $\Delta R_{W,b}$ condition does not veto events with zero W-tagged large-radius jets.

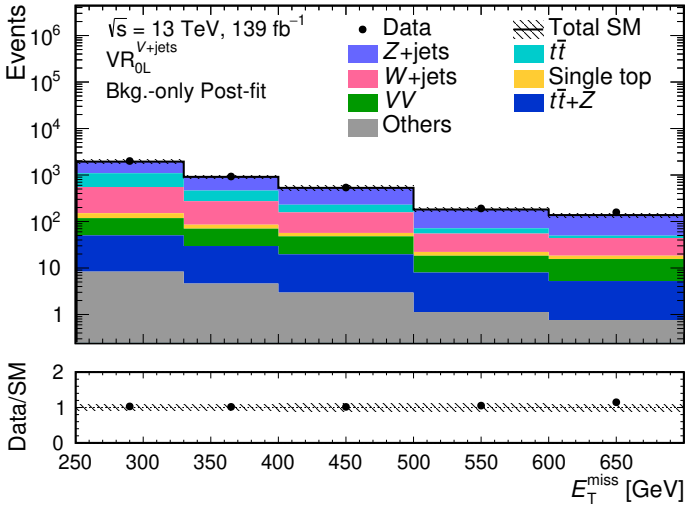

Figure 10.14: Distribution of the data and the SM background processes as a function of the $E_{\mathrm{T}}^{\mathrm{miss}}$ in the $\mathrm{VR}_{0\mathrm{L}}^{V+\mathrm{jets}}$. The hashed uncertainty band includes all systematic uncertainty sources described in Section 10.3. The post-fit normalisation of the SM processes and the post-fit systematic uncertainties obtained from the background-only fit described in Section 8.4 are used in the figure. Events beyond the range of the x-axis are added to the rightmost bin. The bottom panel shows the ratio of the data and the sum of all SM predictions in each bin. "Others" contains contributions from the triboson, tWZ, tZ, $t\bar{t}+W$, $t\bar{t}+h$, $t\bar{t}t$ and $t\bar{t}t\bar{t}$ processes.

the background-only fit and corrected using the results of the fit for both VRs.

Figure 10.15 shows the number of observed and predicted SM events corrected by the combined background-only fit for all CRs and VRs of the 1L and 0L channels. The significance of the discrepancy between the data and the SM prediction, calculated with Equation (9.1) is shown in the bottom panel. In the equation, n is set equal to the data and $b \pm \sigma$ to the total background prediction and its uncertainty. No deviations beyond one standard deviation between the data and the SM prediction are observed. The background predictions are hence verified. Perfect agreement between the data and the predictions can be reported for the CRs, since the number of normalisation parameters equals the number of constraining regions.

10.3 Systematic uncertainties

Systematic uncertainties from multiple sources are accounted for in the presented tW+DM search. Experimental uncertainties are all those uncertainties that arise from the reconstruction, identification, isolation and calibration of objects, as well as uncertainties due to the luminosity precision and number of simultaneous proton-proton interactions in a bunch crossing. Uncertainties related to the generation of simulated BSM signal and SM events are referred to as modelling uncertainties. The uncertainties are implemented in the likelihood function as Poisson or Gaussian constrained nuisance parameters as described in Section 8.5.

Figure 10.16 shows the relative impact on the bins of the 1L and 0L channel SRs of: the total systematic uncertainty and of the sources of the systematic uncertainty, grouped into four categories and added up per category. The systematic uncertainty sources are discussed in more detail below. A more detailed breakdown of the

	$\text{VR}_{\text{0L}}^{t\bar{t}}$	$\text{VR}_{\text{0L}}^{V+\text{jets}}$
Trigger	$E_{\text{T}}^{\text{miss}}$	$E_{\text{T}}^{\text{miss}}$
$E_{\text{T}}^{\text{miss}}$ [GeV]	≥ 250	≥ 250
$\text{Sig}_{E_{\text{T}}^{\text{miss}}}$	$\in [10, 14]$	≥ 14
$\Delta\phi_{\text{min},1-4}$ [rad]	≥ 0.9	≥ 0.5
$N^{\ell,b}$,$N^{\ell,s}$	$= 0$	$= 0$
N^{j}	≥ 4	≥ 4
p_{T}^{j1} [GeV]	≥ 100	≥ 100
p_{T}^{j2} [GeV]	≥ 60	≥ 60
p_{T}^{j3} [GeV]	≥ 60	≥ 60
p_{T}^{j4} [GeV]	≥ 40	≥ 40
N^{b}	≥ 1	≥ 1
p_{T}^{b1} [GeV]	≥ 50	≥ 50
p_{T}^{b2} [GeV]	< 50	< 50
$m_{\text{T}}^{b,E_{\text{T}}^{\text{miss}}}$ [GeV]	≥ 180	≥ 180
$\Delta R_{j_1,j_2}$	–	≥ 1.2
$\Delta\phi_{\text{min,all}}$	–	≥ 1.2
$N^{W-\text{tag}}$	≥ 1	≥ 0
$\Delta R_{W,b}$	–	< 1.0
$m_{W,b}$ [GeV]	< 220	–

Table 10.7: Selection criteria of the VRs of the 0L channel.

		$\text{VR}_{\text{0L}}^{t\bar{t}}$	$\text{VR}_{\text{0L}}^{V+\text{jets}}$
	Observed	227	3817
Post-fit	Total SM	260 ± 30	3700 ± 400
	$t\bar{t}$	200 ± 30	800 ± 300
	Z+jets	17 ± 4	1800 ± 300
	W+jets	17 ± 5	750 ± 80
	$t\bar{t} + Z$	4.7 ± 1.6	100 ± 50
	Single top	6^{+6}_{-6}	60 ± 60
	VV	7.4 ± 1.7	157 ± 11
	Others	1.5 ± 0.4	17.9 ± 1.8
Pre-fit	Total SM	263.87	3747.79
	$t\bar{t}$	205.04	827.96
	Z+jets	16.94	1821.12
	W+jets	16.17	694.10
	$t\bar{t} + Z$	4.01	80.70
	Single top	12.87	148.75
	VV	7.36	157.30
	Others	1.47	17.85

Table 10.8: Data and predicted yields in the 0L channel VRs prior to the background-only fit ("pre-fit") and using the normalisation and uncertainties as derived by the background-only fit ("post-fit"). The uncertainties include all systematic uncertainty sources described in Section 10.3. "Others" contains contributions from the triboson, tWZ, tZ, $t\bar{t} + W$, $t\bar{t} + h$, $t\bar{t}t$ and $t\bar{t}t\bar{t}$ processes.

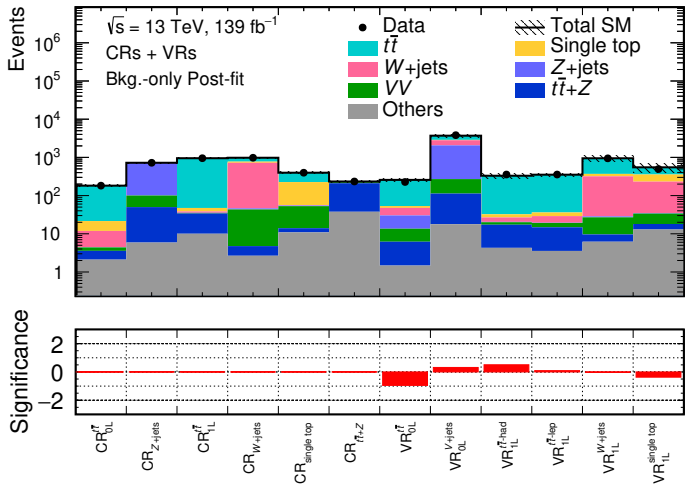

Figure 10.15: Number of events in the CRs and VRs observed in the data and predicted by the SM corrected by the background-only fit. The bottom panel shows the significance of the deviation between data and prediction, calculated with Equation (9.1). In this equation, n is set equal to the data yield and $b \pm \sigma$ are the total SM prediction yield and (post-fit) systematic uncertainty, respectively. The systematic uncertainties are calculated as described in Section 10.3. "Others" contains contributions from the triboson, tWZ, tZ, $t\bar{t}+W$, $t\bar{t}+h$, $t\bar{t}t\bar{t}$ and $t\bar{t}t\bar{t}$ processes.

impact of the systematic uncertainties is given in Table 10.9 for the 1L channel SRs and in Table 10.10 for the $\mathrm{SR_{0L}}$. All of these uncertainties are obtained from the background-only fit using a likelihood combining the signal regions of the 1L and 0L channels.

The statistical uncertainty of the data is found to be comparable to the total systematic uncertainty for the $\mathrm{SR_{1L}^{LepTop}}$, the three lowest $E_{\mathrm{T}}^{\mathrm{miss}}$ bins of the $\mathrm{SR_{1L}^{HadTop}}$, as well as the three lowest $E_{\mathrm{T}}^{\mathrm{miss}}$ bins of the $\mathrm{SR_{0L}}$. In the two highest $E_{\mathrm{T}}^{\mathrm{miss}}$ bins of the $\mathrm{SR_{1L}^{HadTop}}$, the total systematic uncertainty exceeds the statistical uncertainty of the data. For the two highest $E_{\mathrm{T}}^{\mathrm{miss}}$ bins of the $\mathrm{SR_{0L}}$, the statistical uncertainty of the data exceeds the total systematic uncertainty.

10.3.1 Experimental uncertainties

The sources of experimental uncertainties considered in this analysis, as well as their impact on the SM predictions are described in the following. The impact on the signal is described in Section 10.3.3. All experimental uncertainty sources are correlated between the different regions and bins for the 1L and 0L channels, as well as between the SM processes and the signal.

Small-radius jet uncertainties

Uncertainties on the JES of small-radius ($R = 0.4$) jets stem from the calibration procedure [304]. Dominant contributions are from the modelling of pile-up interactions, uncertainties related to the flavour of a jet (i.e. what sort of particle a jet originates from) as well as the in-situ calibration. In total, there are 125 nuisance parameters contributing to the JES uncertainties. Since considering such a large number of nuisance parameters is computationally expensive, some of the uncer-

	Uncertainty of channel	SR_{1L}^{HadTop} Bin 1	Bin 2	Bin 3	Bin 4	Bin 5	SR_{1L}^{LepTop}
	Total post-fit SM prediction	116.06	55.25	29.04	16.56	20.16	6.42
	Total post-fit syst. uncert.	10.9%	14.7%	14.6%	35.2%	41.8%	36.2%
Experimental	Small-radius JES	3.6%	5.2%	2.7%	9.6%	3.1%	18.1%
	Small-radius JER	3.6%	3.8%	5.6%	23.9%	11.2%	3.8%
	JVT	$\leq 0.1\%$	$\leq 0.1\%$	$\leq 0.1\%$	0.2%	0.2%	$\leq 0.1\%$
	b-tagging	1.3%	1.1%	1.3%	0.8%	1.3%	1.0%
	Large-radius JES	$\leq 0.1\%$	$\leq 0.1\%$	$\leq 0.1\%$	$\leq 0.1\%$	$\leq 0.1\%$	1.9%
	Large-radius JER	0.9%	1.6%	0.9%	0.7%	0.8%	4.9%
	Large-radius JMS	0.4%	0.5%	1.0%	$\leq 0.1\%$	0.7%	1.0%
	Large-radius JMR	0.5%	0.8%	0.3%	0.6%	0.8%	0.2%
	W-tagging	2.0%	1.8%	3.5%	2.1%	2.1%	10.1%
	Electron	1.8%	1.1%	1.7%	2.1%	2.0%	12.0%
	Muon	0.6%	0.2%	$\leq 0.1\%$	0.3%	0.3%	0.5%
	$E_{\mathrm{T}}^{\mathrm{miss}}$ soft-term	0.3%	1.0%	1.1%	4.2%	3.0%	11.7%
	Lumi. and pile-up	1.1%	1.0%	0.8%	0.6%	0.5%	0.9%
Theoretical	$t\bar{t}$ modelling	7.0%	10.3%	5.5%	5.5%	5.5%	19.3%
	Z+jets modelling	0.8%	$\leq 0.1\%$	$\leq 0.1\%$	$\leq 0.1\%$	$\leq 0.1\%$	$\leq 0.1\%$
	W+jets modelling	5.9%	7.6%	4.2%	17.8%	36.3%	1.1%
	single top quark modelling	2.5%	2.2%	4.5%	6.4%	2.5%	9.7%
	$t\bar{t} + Z$ modelling	1.4%	1.4%	6.8%	6.6%	3.3%	7.2%
Other	Simulation statistics	3.3%	4.1%	7.2%	11.6%	13.4%	8.0%
	Background normalisation	3.2%	3.4%	3.8%	4.4%	5.4%	4.1%

Table 10.9: The table shows the total number of predicted SM events, the total systematic uncertainty and the individual contributions to the systematic uncertainty in the bins of the SR_{1L}^{HadTop} and in the SR_{1L}^{LepTop}. Systematic uncertainty components may be correlated and not sum to the total uncertainty. Percentages indicate the size of an uncertainty relative to the total predicted SM yield in a bin. The predicted yields and systematic uncertainties shown are obtained from the background-only fit using the likelihood combining the regions of the 1L and 0L channels.

	Uncertainty of channel	SR$_{0L}$ Bin 1	Bin 2	Bin 3	Bin 4	Bin 5
	Total post-fit SM prediction	63.93	40.81	25.39	9.55	7.03
	Total post-fit syst. Uncert.	12.9%	15.2%	17.0%	21.3%	24.5%
Experimental	Small-radius JES	3.7%	3.3%	3.1%	5.6%	4.5%
	Small-radius JER	5.9%	3.6%	8.6%	6.3%	7.7%
	JVT	0.2%	0.2%	$\leq 0.1\%$	0.3%	0.5%
	b-tagging	0.6%	0.7%	0.6%	0.7%	1.2%
	Large-radius JES	0.5%	1.0%	0.9%	1.6%	1.1%
	Large-radius JER	1.4%	2.9%	4.7%	6.9%	7.9%
	Large-radius JMS	0.7%	0.7%	0.7%	2.3%	2.3%
	Large-radius JMR	0.9%	0.4%	$\leq 0.1\%$	1.4%	2.1%
	W-tagging	6.9%	7.1%	7.6%	8.0%	9.1%
	Electron	1.2%	1.1%	1.0%	1.3%	2.2%
	Muon	0.3%	0.4%	0.4%	0.4%	0.3%
	$E_{\mathrm{T}}^{\mathrm{miss}}$ soft-term	1.4%	3.2%	0.4%	3.6%	1.6%
	Lumi. and pile-up	0.6%	0.5%	0.5%	0.4%	0.5%
Theoretical	$t\bar{t}$ modelling	2.2%	7.0%	3.8%	3.4%	6.6%
	Z+jets modelling	4.4%	3.8%	5.3%	3.3%	3.8%
	W+jets modelling	1.3%	1.7%	1.2%	1.7%	1.9%
	single top quark modelling	2.4%	6.5%	3.7%	8.1%	15.4%
	$t\bar{t} + Z$ modelling	0.7%	1.5%	1.9%	10.6%	4.6%
Other	Simulation statistics	5.0%	4.7%	5.9%	6.4%	7.4%
	Background normalisation	4.0%	4.1%	4.2%	4.2%	3.9%

Table 10.10: The table shows the total number of predicted SM events, the total systematic uncertainty and the individual contributions to the systematic uncertainty in the bins of the SR$_{0L}$. Systematic uncertainty components may be correlated and not sum to the total uncertainty. Percentages indicate the size of an uncertainty relative to the total predicted SM yield in a bin. The predicted yields and systematic uncertainties shown are obtained from the background-only fit using the likelihood combining the regions of the 1L and 0L channels.

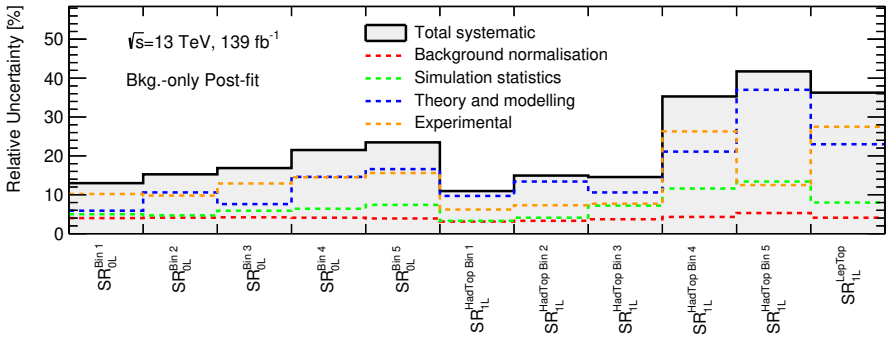

Figure 10.16: The total systematic uncertainty relative to the total SM prediction (solid black) in all SRs and their bins. The dashed lines indicate the size of the normalisation, simulation statistical, modelling and experimental uncertainties. As these systematic uncertainty components may be correlated, their quadratic sum may not agree with the square of the total systematic uncertainty. The systematic uncertainties shown are obtained from the background-only fit using the likelihood combining the 1L and 0L channels.

tainty components have been combined, such that the total number of nuisance parameters is reduced. Such a reduced set of JES nuisance parameters is employed in this analysis.

Small-radius jets are furthermore affected by JER calibration uncertainties [304]. They dominantly originate from propagated JES uncertainties, the modelling of SM processes and non-closure differences between quantities measured in or with the help of data and estimated from the simulation. As for the JES, a reduced set of nuisance parameters is employed for the JER.

The small-radius jet JES and JER uncertainties constitute one of the largest experimental uncertainties on the SM background in all SRs and their bins. They range between 3.1 %–23.9 %.

Additional uncertainties due to the multiplicative factors employed to correct the JVT efficiency derived from the simulation to the one derived from the data [307] are considered for small-radius jets. Their impact on the SM prediction is found to be negligible.

b-tagging uncertainties

The *b*-tagging efficiency and mistag rates derived in simulation are calibrated to match the values found in data [203]. The uncertainties resulting from this procedure account for an uncertainty on the SM processes of 0.6 %–1.3 % throughout the SRs, making their impact on the result minor.

Large-radius jet and *W*-tagging uncertainties

As for the small-radius jets, uncertainties from the JES and JER calibration are accounted for for the large-radius ($R = 1.0$) jets [318]. Similarly, uncertainties from the calibration of the mass scale (JMS) and mass resolution (JMR) are taken into consideration [326]. A reduced set of nuisance parameters is employed for the large-radius jet JES uncertainties, while all available nuisance parameters are for the JER, JMS and JMR uncertainties.

The large-radius jet JES, JMS and JMR uncertainties play a minor role in the $\mathrm{SR}_{1\mathrm{L}}^{\mathrm{LepTop}}$ and the $\mathrm{SR}_{0\mathrm{L}}$, where their value is below 2.3 % relative to the total SM

prediction. Uncertainties related to the JER calibration of large-radius jets are more sizeable and are 4.9 % in the $\mathrm{SR}_{1\mathrm{L}}^{\mathrm{LepTop}}$ and between 1.4 %–7.9 % in the $\mathrm{SR}_{0\mathrm{L}}$, where they increase with the $E_{\mathrm{T}}^{\mathrm{miss}}$. All large-radius jet uncertainties are below 1.6 % in the $\mathrm{SR}_{1\mathrm{L}}^{\mathrm{HadTop}}$, where no requirements on large-radius jets are made. The uncertainties are non-zero due to events containing at least one reconstructed large-radius jet in this region.

Uncertainties from the correction of the W-tagging efficiency and mistag rate derived in simulation to the one measured in the data are further accounted for in this analysis [330]. These calibration uncertainties are dominated by uncertainties from the modelling of the SM processes and statistical uncertainties. In the $\mathrm{SR}_{1\mathrm{L}}^{\mathrm{LepTop}}$ and $\mathrm{SR}_{0\mathrm{L}}$, the W-tagging uncertainties represent the largest source of experimental uncertainty, ranging between 6.9 % and 10.1 % and increasing with the $E_{\mathrm{T}}^{\mathrm{miss}}$ in the $\mathrm{SR}_{0\mathrm{L}}$.

Lepton reconstruction uncertainties

The trigger, reconstruction, identification and isolation efficiency calibrations deduced for electrons and muons result in multiple sources of uncertainties [285, 286, 299]. Furthermore, uncertainties related to electrons and muons stem from the calibration of the energy scale and resolution. In the $\mathrm{SR}_{1\mathrm{L}}^{\mathrm{HadTop}}$ and the $\mathrm{SR}_{0\mathrm{L}}$, the impact of electron and muon uncertainties on the SM background is found to be below 2.2 % and thus of minor relevance. In the $\mathrm{SR}_{1\mathrm{L}}^{\mathrm{LepTop}}$, electron uncertainties are one of the most sizeable experimental uncertainties with a value of 12 % relative to the total SM prediction.

$\boldsymbol{E_{\mathrm{T}}^{\mathrm{miss}}}$ uncertainties

The $E_{\mathrm{T}}^{\mathrm{miss}}$ is calculated as the negative sum of the transverse momentum of all reconstructed objects in an event and a soft term, accounting for particle-flow objects not associated to any of the reconstructed objects, see Section 7.5. While the uncertainties on the reconstructed objects are accounted for by inputting modified objects into the $E_{\mathrm{T}}^{\mathrm{miss}}$ calculation, dedicated uncertainties are evaluated for the soft term [201]. The uncertainties related to the soft term of the $E_{\mathrm{T}}^{\mathrm{miss}}$ have a minor impact in the $\mathrm{SR}_{0\mathrm{L}}$ and the $\mathrm{SR}_{1\mathrm{L}}^{\mathrm{HadTop}}$ where they range between 0.3 %–4.2 %. They are one of the major experimental uncertainty sources in the $\mathrm{SR}_{1\mathrm{L}}^{\mathrm{LepTop}}$ with an uncertainty of 11.7 %.

Luminosity and pile-up uncertainties

Further sources of experimental uncertainties arise from the measurement of the integrated luminosity and the correction of the number of pile-up interactions to data in simulated events. The uncertainty on the integrated luminosity is 1.7 % [197, 198] for the data collected between 2015 and 2018 and accounted for as an uncertainty of the normalisation of all SM processes that are not constrained in a CR [337]. The impact of the luminosity and pile-up uncertainties on the final result is minor, being close to or below one percent of the total SM prediction in all SRs and $E_{\mathrm{T}}^{\mathrm{miss}}$ bins.

10.3.2 Modelling uncertainties

As shown in Table 10.9, the modelling uncertainties are among the major uncertainties in each bin of the $\mathrm{SR}_{1\mathrm{L}}^{\mathrm{HadTop}}$ and in the $\mathrm{SR}_{1\mathrm{L}}^{\mathrm{LepTop}}$. Uncertainties related to the modelling of the $t\bar{t}$ process are the largest source of systematic uncertainty in the two lowest $E_{\mathrm{T}}^{\mathrm{miss}}$ bins of the $\mathrm{SR}_{1\mathrm{L}}^{\mathrm{HadTop}}$, ranging between 7.0 %–10.3 %. In

the two highest $E_{\mathrm{T}}^{\mathrm{miss}}$ bins, the W+jets modelling uncertainties become the major modelling uncertainty with values of 17.8 %–36.3 %. The systematic uncertainties in the $\mathrm{SR}_{\mathrm{1L}}^{\mathrm{LepTop}}$ are dominated by the $t\bar{t}$ modelling uncertainties (19.3 %) with significant contributions from the single top quark (9.7 %) and $t\bar{t}+Z$ (7.2 %) modelling uncertainties. Uncertainties due to the modelling of the $t\bar{t}$, single top and Z+jets processes have a large impact on the SM prediction in the three first bins of the $\mathrm{SR}_{\mathrm{0L}}$ (2.2 %–7 %). In the remaining two bins, the $t\bar{t}+Z$ and single top modelling uncertainties are the largest sources of systematic uncertainty (4.6 %–15.4 %).

The sources of the modelling uncertainties are described in the following.

Renormalisation and factorisation scale

The SM predictions are a function of the renormalisation (μ_R) and factorisation scales (μ_F, see Section 2.5). To derive the uncertainties on the SM predictions due to their dependence on μ_R and μ_F, the scales are halved and doubled with respect to their nominal values.

Initial and finite state radiation

Uncertainties on the modelling of the ISR and FSR in the $t\bar{t}$ and single top processes are estimated by varying the value of the strong coupling constant used in the simulation of extra radiations in the parton showering. This is implemented by varying the renormalisation scale used for the FSR modelling and by changing the α_{S} value through the A14 eigentune set [241] used for the parton showering with Pythia 8. For the $t\bar{t}+Z$ process, ISR uncertainties are similarly estimated.

Event generation

Uncertainties are derived to estimate the impact of using the programs described in Section 6.7 for generating the hard-scatter event and performing the parton showering, hadronisation and underlying event simulation. For the $t\bar{t}$ and single top-quark processes, uncertainties due to the use of the hard-scatter generator are estimated by employing samples generated with MadGraph5_aMC@NLO [220] interfaced to Pythia 8 [235], instead of the nominal PowHeg-Box interfaced to Pythia 8. Uncertainties due to the parton showering, hadronisation and underlying event simulation are estimated by using samples produced by interfacing the nominal PowHeg-Box matrix element generator into the Herwig 7 [224, 225] parton showering program instead of the nominal Pythia 8. The H7UE parameter tune [225] is input into the Herwig 7 program.

Similar uncertainties are derived for the $t\bar{t}+Z$ process by employing samples generated with Sherpa 2.2.1 [226] at NLO accuracy and samples generated with MadGraph5_aMC@NLO [220] interfaced to Herwig 7 [224, 225] as compared to the nominal samples produced with MadGraph5_aMC@NLO and Pythia 8.

Additional modelling uncertainties

Uncertainties on the matching between the matrix element generator and parton showering of the Z+jets and W+jets processes are accounted for by altering the respective matching scale. Furthermore, uncertainties on the soft gluon resummation scale ("QSF") are evaluated by varying the scale up and down by a factor of four.

The interference of the associated production of a single top quark and a W-boson (tW) with the $t\bar{t}$ process is nominally treated by the diagram removal procedure [251]. An uncertainty is estimated for the use of this procedure. Alternative tW samples are generated using the diagram subtraction procedure [251]. Using these two procedures to model the tW process gives very different cross-sections, as

discussed in Section 10.1.3. The cross-section of the single top quark process, which is dominated by tW in this analysis, is however estimated independently of the interference procedure in the CRs. For that reason, only differences in the shapes of the two resulting distributions are considered as an uncertainty.

10.3.3 Signal uncertainties

The same sources of experimental uncertainties as described in Section 10.3.1 are considered for the signal predictions. These uncertainties range between 9 %–45 % throughout the $\mathrm{SR}_{\mathrm{1L}}^{\mathrm{HadTop}}$, $\mathrm{SR}_{\mathrm{1L}}^{\mathrm{LepTop}}$ and $\mathrm{SR}_{\mathrm{0L}}$ for the different signal samples. The small-radius jet JES and JER (2.5 %–39.1 %), as well as the W-tagging uncertainties (1.7 %–17.1 %) represent the largest sources of experimental uncertainty.

Uncertainties due to the renormalisation and factorisation scale are evaluated by varying the scales up and down by a factor of two with respect to the nominal value. Furthermore, modelling uncertainties concerning the parton showering, hadronisation and underlying event are estimated by varying parameters of the A14 tune [241]. The impact of the modelling uncertainties ranges between 3 %–24 % in the 1L channel SRs and 3 %–30 % in the $\mathrm{SR}_{\mathrm{0L}}$ for almost all of the different signal samples. Individual signal samples exhibit an uncertainty greater than 50 % in the highest $E_{\mathrm{T}}^{\mathrm{miss}}$ bins of the $\mathrm{SR}_{\mathrm{1L}}^{\mathrm{HadTop}}$ and the $\mathrm{SR}_{\mathrm{0L}}$.

The total systematic uncertainties of the signal ranges mostly between 10 %–45 %. Figures 10.17a and 10.17b show the size of the total systematic uncertainty as well as of the experimental, modelling and simulation statistical uncertainties for two example signal samples.

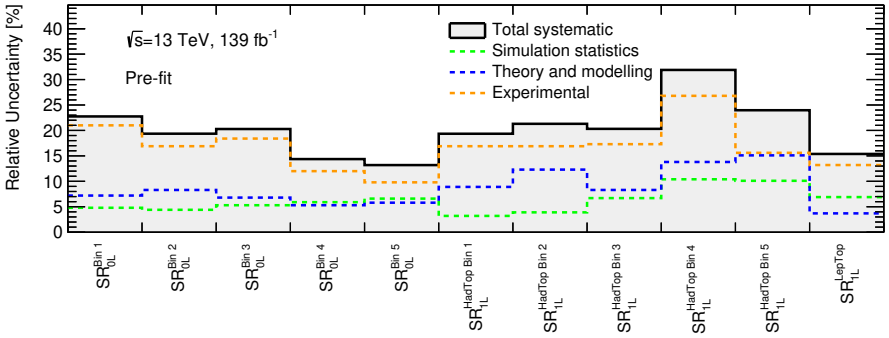

(a) $m_a = 250\,\text{GeV}$, $m_{H^\pm} = 1250\,\text{GeV}$, $\tan\beta = 1$, $\sin\theta = 0.7$

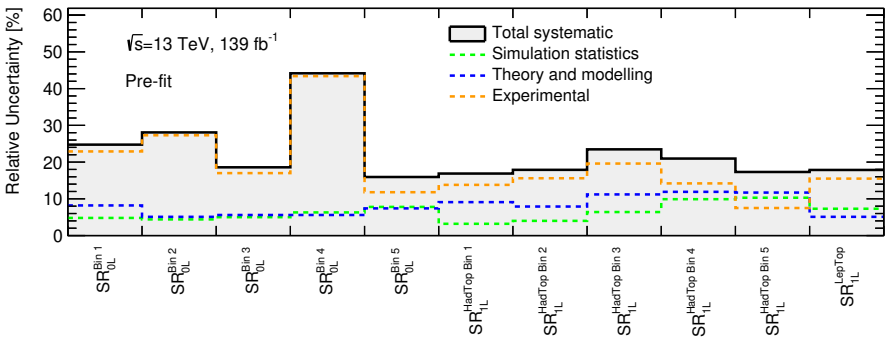

(b) $m_a = 300\,\text{GeV}$, $m_{H^\pm} = 1000\,\text{GeV}$, $\tan\beta = 1$, $\sin\theta = 0.35$

Figure 10.17: The total systematic uncertainty relative to the total signal prediction in all SRs and their bins (solid black). The signals are generated with the 2HDM+a model parameters (a) $m_a = 250\,\text{GeV}$, $m_{H^\pm} = 1250\,\text{GeV}$, $\tan\beta = 1$, $\sin\theta = 0.7$ and (b) $m_a = 300\,\text{GeV}$, $m_{H^\pm} = 1000\,\text{GeV}$, $\tan\beta = 1$, $\sin\theta = 0.35$. The dashed lines indicate the size of the simulation statistical, modelling and experimental uncertainties. As these systematic uncertainty components may be correlated, their quadratic sum may not agree with the square of the total systematic uncertainty. The systematic uncertainties shown are obtained prior to any fit.

Chapter 11

Results from the 1L and 0L channels

The results of the background-only fit and model-independent limits using the statistical combination of the 1L and 0L channels are presented in the following. Model-dependent exclusion limits on the 2HDM+a model parameters are shown for the combination of the 0L, 1L and 2L channels in Chapter 12.

11.1 Background-only fit

The normalisation parameters of the SM processes and the nuisance parameters are determined in a semi-data-driven way in the CRs in the background-only fit discussed in Section 8.5. The normalisation parameters and nuisance parameters are determined by maximising the combined likelihood. While the normalisation parameters of the Z+jets, W+jets, $t\bar{t}+Z$ and single top quark processes are determined across all CRs and used in the SRs of both channels, individual $t\bar{t}$ normalisation parameters are fit in selected regions for the 1L and 0L channel SRs. This is done to account for the different $t\bar{t}$ compositions in the SRs, which is dominated by dileptonic decays in the 1L and by semi-leptonic decays in the 0L channel. In the fit, the 0L channel $t\bar{t}$ normalisation parameter ($\mu_{0L}^{t\bar{t}}$) is used in the CRs which constrain the dominant SM background processes in the 0L SR, that is in the $\mathrm{CR}_{\mathrm{0L}}^{t\bar{t}}$ and in the $\mathrm{CR}_{\mathrm{Z+jets}}$. On the other hand, the 1L channel $t\bar{t}$ normalisation parameter is used in the $\mathrm{CR}_{\mathrm{1L}}^{t\bar{t}}$ and all other CRs in the fit. These CRs constrain background processes dominating in the 1L channel SRs. No signal is assumed to be present in the CRs in the background-only fit. Yields in the VRs and SRs are obtained by extrapolating from the CRs.

Good agreement between the data and the SM prediction was observed in the $E_{\mathrm{T}}^{\mathrm{miss}}$ and $E_{\mathrm{T},\ell\ell}^{\mathrm{miss}}$ distributions of the CRs and VRs using the yields and uncertainties obtained from the background-only fit, as discussed in Sections 10.1 and 10.2.

The observed and predicted event yields, both uncorrected ("pre-fit") and corrected ("post-fit") by the background-only fit, are reported for the $\mathrm{SR}_{\mathrm{1L}}^{\mathrm{LepTop}}$ in Table 11.1, for the $\mathrm{SR}_{\mathrm{1L}}^{\mathrm{HadTop}}$ in Table 11.2 and in Table 11.3 for the $\mathrm{SR}_{\mathrm{0L}}$. The quoted uncertainties account for all sources of systematic uncertainty described in Section 10.3. The observed data in the 1L and 0L channel SRs and the corresponding SM predictions corrected by the background-only fit are plotted in Figure 11.1. The agreement of the data and the prediction, quantified by the significance Z calculated with Equation (9.1) is given in the bottom panel. In the equation, n is set equal to the data yield and $b \pm \sigma$ are the total SM prediction yield and (post-fit)

		$\mathrm{SR}_{1\mathrm{L}}^{\mathrm{LepTop}}$
	Data	9
Post-fit	Total SM	6 ± 3
	$t\bar{t}$	2.3 ± 1.4
	Z+jets	0.010 ± 0.004
	W+jets	$1.0^{+1.6}_{-1.1}$
	$t\bar{t} + Z$	1.6 ± 0.7
	Single top	$0.4^{+0.7}_{-0.4}$
	VV	0.51 ± 0.09
	Others	0.62 ± 0.12
Pre-fit	Total SM	6.80
	$t\bar{t}$	2.48
	Z+jets	0.01
	W+jets	0.97
	$t\bar{t} + Z$	1.34
	Single top	0.87
	VV	0.51
	Others	0.62

Table 11.1: Data and predicted yields in the $\mathrm{SR}_{1\mathrm{L}}^{\mathrm{LepTop}}$ prior to the background-only fit ("pre-fit") and using the normalisation and uncertainties as derived by the background-only fit ("post-fit"). The uncertainties include all systematic uncertainty sources described in Section 10.3. "Others" contains contributions from the triboson, tWZ, tZ, $t\bar{t} + W$, $t\bar{t} + h$, $t\bar{t}t$ and $t\bar{t}t\bar{t}$ processes.

systematic uncertainty, respectively. Except for the fourth bin of the $\mathrm{SR}_{0\mathrm{L}}$, good agreement between the data and the post-fit SM prediction is observed and the significance of the deviations of data and SM prediction is below 1.5σ. In the fourth bin of the $\mathrm{SR}_{0\mathrm{L}}$, the SM prediction exceeds the data with a significance of more than 2.5 standard deviations. The disagreement is assumed to be due to a statistical fluctuation of the data, as the deviation between the data and the SM prediction is below 1σ in the remaining $E_{\mathrm{T}}^{\mathrm{miss}}$ bins of the $\mathrm{SR}_{0\mathrm{L}}$. It is worth noting that there is an excess of the data with a significance of roughly 1σ in the $\mathrm{SR}_{1\mathrm{L}}^{\mathrm{LepTop}}$. There is furthermore an excess of data in two out of the five bins of the $\mathrm{SR}_{1\mathrm{L}}^{\mathrm{HadTop}}$ with a significance of 1σ, though there are also deficits of the data in two bins.

Figure 11.2a and Figure 11.2b show the $N^{W-\mathrm{tag}}$ and $m_{b,\not{p}}$ distribution in the $\mathrm{SR}_{1\mathrm{L}}^{\mathrm{LepTop}}$ without a constraint on the respective variable shown and the SR condition being indicated by an arrow. In the $N^{W-\mathrm{tag}}$ distribution, the data is found to be consistent with the SM prediction corrected by the background-only fit. Data and SM prediction agree within uncertainties in the $m_{b,\not{p}}$, though no data is observed in several bins, which is in accordance with the low predicted yields.

The distribution of the data and the SM predictions corrected by the background-only fit in the $\mathrm{SR}_{1\mathrm{L}}^{\mathrm{HadTop}}$ in the $E_{\mathrm{T}}^{\mathrm{miss}}$ and the $m_{b,\not{p}}$ is shown in Figures 11.2c and 11.2d without the SR requirement on the variables. Within the statistical and systematic uncertainties, the data is consistent with the prediction.

The distribution of the data and the post-fit SM prediction is shown for the $E_{\mathrm{T}}^{\mathrm{miss}}$, $m_{\mathrm{T}}^{b,E_{\mathrm{T}}^{\mathrm{miss}}}$, $N^{W-\mathrm{tag}}$ and $m_{W,b}$ variables in the $\mathrm{SR}_{0\mathrm{L}}$ in Figures 11.3a-11.3d, without any requirement on the variable that is shown. For the $N^{W-\mathrm{tag}}$ variable Figure 11.3c, additionally no requirements on $m_{W,b}$ and $\Delta R_{W,b}$ are placed. The data

	SR_{1L}^{HadTop}	Bin 1	Bin 2	Bin 3	Bin 4	Bin 5
	Data	109	61	29	15	25
Post-fit	Total SM	116 ± 13	55 ± 9	29 ± 5	17 ± 6	20 ± 9
	$t\bar{t}$	68 ± 8	27 ± 6	10 ± 3	4.2 ± 1.2	2.9 ± 1.2
	Z+jets	$0.9^{+1.2}_{-1.0}$	0.22 ± 0.13	$0.3^{+0.3}_{-0.3}$	$0.04^{+0.09}_{-0.04}$	0.25 ± 0.08
	W+jets	24 ± 9	12 ± 6	9 ± 3	6 ± 6	8 ± 8
	$t\bar{t}+Z$	12 ± 4	9 ± 2	6 ± 3	3.5 ± 1.6	5.5 ± 1.8
	Single top	4 ± 4	1.9 ± 1.7	$1.2^{+1.6}_{-1.3}$	$0.6^{+1.2}_{-0.7}$	0.7 ± 0.6
	VV	4.2 ± 0.5	2.6 ± 0.4	1.9 ± 0.4	1.2 ± 0.3	1.9 ± 0.4
	Others	4.0 ± 0.4	2.7 ± 0.4	1.6 ± 0.2	0.97 ± 0.16	1.4 ± 0.3
Pre-fit	Total SM	123.36	57.95	30.04	16.75	19.93
	$t\bar{t}$	73.44	29.72	10.85	4.53	3.11
	Z+jets	0.95	0.23	0.25	0.04	0.25
	W+jets	21.87	10.81	7.96	5.72	7.15
	$t\bar{t}+Z$	10.09	7.45	4.66	2.94	4.62
	Single top	8.86	4.46	2.81	1.40	1.59
	VV	4.21	2.56	1.88	1.16	1.88
	Others	3.95	2.73	1.63	0.97	1.35

Table 11.2: Data and predicted yields in the E_T^{miss} bins of the SR_{1L}^{HadTop} prior to the background-only fit ("pre-fit") and using the normalisation and uncertainties as derived by the background-only fit ("post-fit"). The uncertainties include all systematic uncertainty sources described in Section 10.3. "Others" contains contributions from the triboson, tWZ, tZ, $t\bar{t}+W$, $t\bar{t}+h$, $t\bar{t}t$ and $t\bar{t}t\bar{t}$ processes.

	SR_{0L}	Bin 1	Bin 2	Bin 3	Bin 4	Bin 5
	Data	67	33	25	2	6
Post-fit	Total SM	64 ± 9	41 ± 7	25 ± 5	10 ± 3	7.0 ± 1.8
	$t\bar{t}$	14 ± 3	8 ± 4	3.9 ± 1.2	1.1 ± 0.6	0.7 ± 0.7
	Z+jets	22 ± 5	14 ± 3	10 ± 3	3.4 ± 0.9	2.5 ± 0.8
	W+jets	14 ± 4	8.8 ± 1.8	4.4 ± 1.3	2.4 ± 0.8	1.5 ± 0.3
	$t\bar{t}+Z$	3.6 ± 1.7	2.9 ± 1.1	2.3 ± 0.9	$1.0^{+1.1}_{-1.0}$	0.5 ± 0.4
	Single top	3 ± 3	3^{+4}_{-3}	1.4 ± 1.3	$0.6^{+0.8}_{-0.6}$	$0.5^{+1.2}_{-0.6}$
	VV	5.6 ± 1.2	3.2 ± 0.8	2.3 ± 0.8	0.9 ± 0.3	1.0 ± 0.4
	Others	1.3 ± 0.3	0.96 ± 0.17	0.66 ± 0.11	0.20 ± 0.04	0.20 ± 0.04
Pre-fit	Total SM	67.16	43.38	26.77	10.06	7.58
	$t\bar{t}$	14.31	8.35	3.95	1.10	0.72
	Z+jets	21.91	14.30	10.54	3.49	2.58
	W+jets	13.20	8.13	4.09	2.18	1.40
	$t\bar{t}+Z$	3.09	2.49	1.93	0.82	0.43
	Single top	7.75	5.95	3.28	1.36	1.22
	VV	5.60	3.21	2.33	0.92	1.02
	Others	1.29	0.96	0.66	0.20	0.20

Table 11.3: Data and predicted yields in the E_T^{miss} bins of the SR_{0L} prior to the background-only fit ("pre-fit") and using the normalisation and uncertainties as derived by the background-only fit ("post-fit"). The uncertainties include all systematic uncertainty sources described in Section 10.3. "Others" contains contributions from the triboson, tWZ, tZ, $t\bar{t}+W$, $t\bar{t}+h$, $t\bar{t}t$ and $t\bar{t}t\bar{t}$ processes.

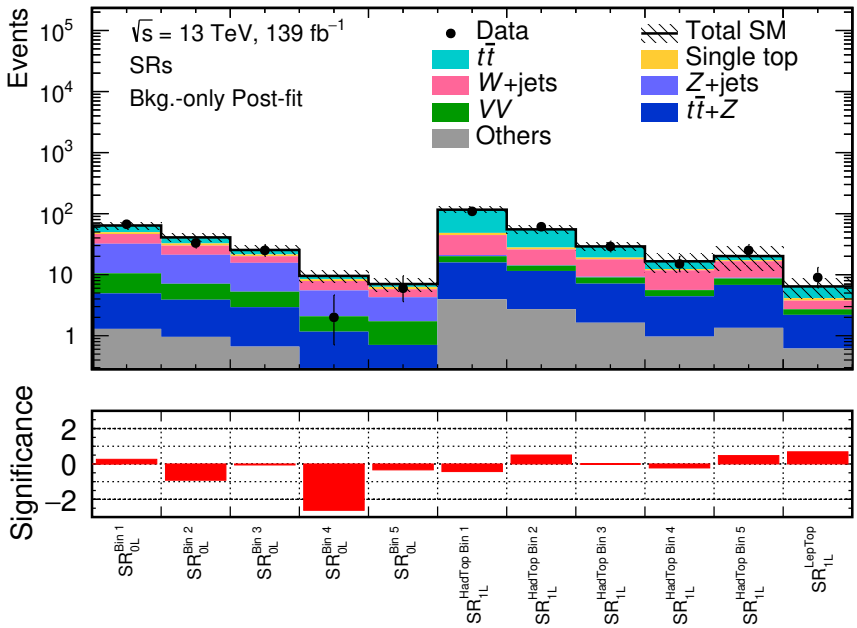

Figure 11.1: Number of events in the 1L and 0L channel SRs observed in the data and predicted by the SM corrected by the background-only fit. The bottom panel shows the significance of the deviation between data and prediction, calculated with Equation (9.1) [347]. In this equation, n is set equal to the data yield and $b \pm \sigma$ are the total SM prediction yield and (post-fit) systematic uncertainty, respectively. The systematic uncertainties are calculated as described in Section 10.3. "Others" contains contributions from the triboson, tWZ, tZ, $t\bar{t}+W$, $t\bar{t}+h$, $t\bar{t}t$ and $t\bar{t}t\bar{t}$ processes.

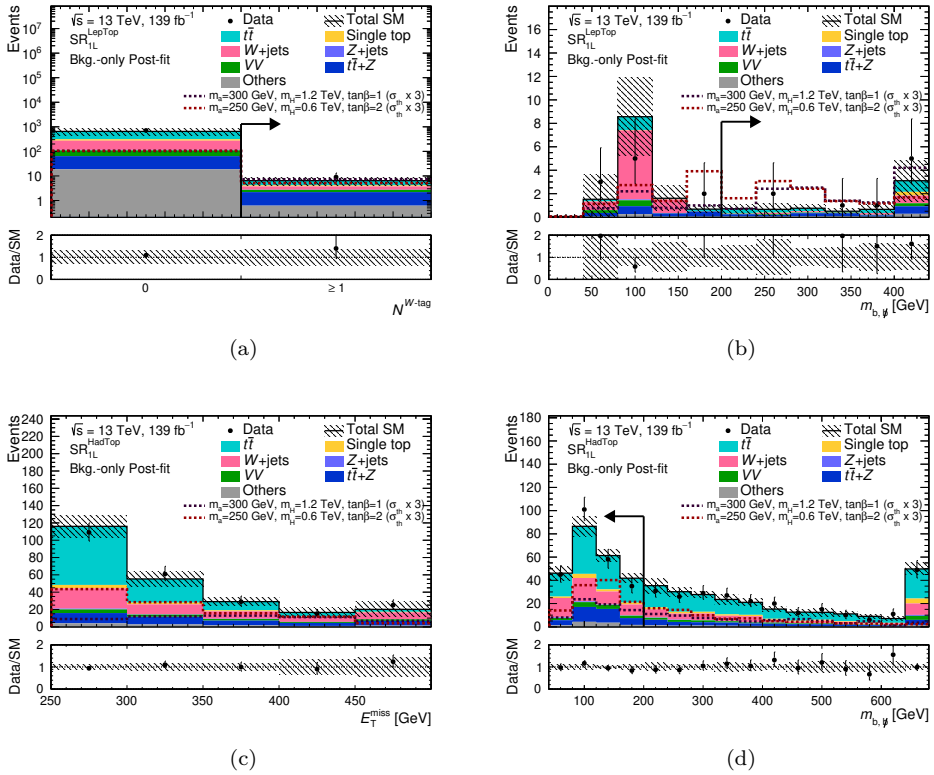

Figure 11.2: Distribution of the observed data and the post-fit SM prediction of multiple variables in the $\mathrm{SR}_{1\mathrm{L}}^{\mathrm{LepTop}}$ (a,b) and the $\mathrm{SR}_{1\mathrm{L}}^{\mathrm{HadTop}}$ (c,d) without a requirement on a shown variable. The variables are (a) $N^{W-\mathrm{tag}}$, (b) $m_{b,\ell\ell}$ in the $\mathrm{SR}_{1\mathrm{L}}^{\mathrm{LepTop}}$ and (c) $E_{\mathrm{T}}^{\mathrm{miss}}$ and (d) $m_{b,\ell\ell}$ in the $\mathrm{SR}_{1\mathrm{L}}^{\mathrm{HadTop}}$. The arrow indicates the direction and position of the requirement on a variable in the SR. All systematic uncertainties discussed in Section 10.3 are included in the uncertainty band of the SM prediction. The benchmark signals shown are generated with $\sin\theta = 0.7$. The signal cross-sections are multiplied by a factor of three to increase the visibility of the distributions. "Others" contains contributions from the triboson, tWZ, tZ, $t\bar{t}+W$, $t\bar{t}+h$, $t\bar{t}t$ and $t\bar{t}t\bar{t}$ processes. Events beyond the range of the x-axis are added to the rightmost bin.

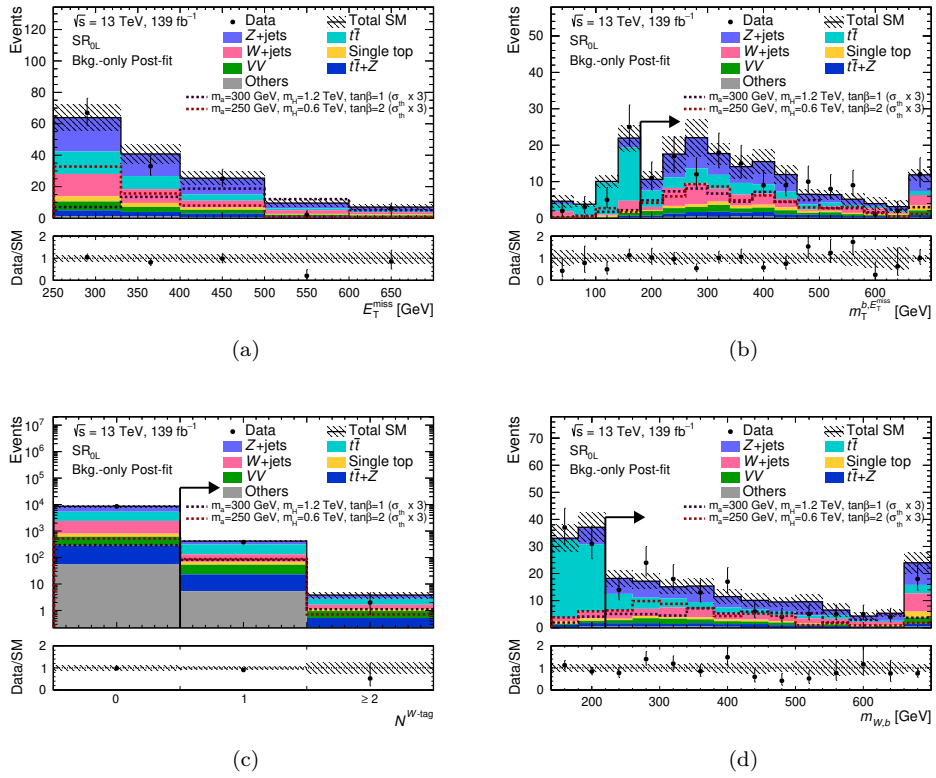

(a) (b)

(c) (d)

Figure 11.3: Distribution of the observed data and the post-fit SM prediction of multiple variables in the $\mathrm{SR_{0L}}$ without a requirement on a shown variable. The variables are (a) $E_{\mathrm{T}}^{\mathrm{miss}}$, (b) $m_{\mathrm{T}}^{b,E_{\mathrm{T}}^{\mathrm{miss}}}$, (c) $N^{W-\mathrm{tag}}$, (d) $m_{W,b}$. For the $N^{W-\mathrm{tag}}$ variable, no constraints on the $m_{W,b}$ and the $\Delta R_{W,b}$ are placed. The arrow indicates the direction and position of the requirement on a variable in the SR. All systematic uncertainties discussed in Section 10.3 are included in the uncertainty band of the SM prediction. The benchmark signals shown are generated with $\sin\theta = 0.7$. The signal cross-sections are multiplied by a factor of three to increase the visibility of the distributions. "Others" contains contributions from the triboson, tWZ, tZ, $t\bar{t}+W$, $t\bar{t}+h$, $t\bar{t}t$ and $t\bar{t}t\bar{t}$ processes. Events beyond the range of the x-axis are added to the rightmost bin.

and the prediction agree within uncertainties in the $m_{\mathrm{T}}^{b,E_{\mathrm{T}}^{\mathrm{miss}}}$ and $N^{W-\mathrm{tag}}$ variables. No large deviation between data and prediction are observed in the $E_{\mathrm{T}}^{\mathrm{miss}}$ variable, with the exception of the fourth bin, as discussed previously. The predicted number of events exceeds the observed yield with a significance greater than one standard deviation in one bin in the $m_{W,b}$ distribution. The disagreement is covered by two standard deviations however and no other disagreements $> 1\sigma$ are observed.

11.2 Model-independent hypothesis tests

Model-independent hypothesis tests are conducted by using the dedicated inclusive SRs described in Sections 9.1 and 9.2. The SM predictions input into the hypothesis testing are estimated in these inclusive SRs by using the background normalisation and nuisance parameters resulting from the background-only fit and extrapolating from the CRs to these regions. At first, hypothesis tests probing the signal-plus-background hypothesis are conducted with a generic signal, i.e. a signal that is not derived from a particular BSM model. Upper limits at 95 % CL on the visible cross-section[1] $\langle\epsilon\sigma\rangle_{\mathrm{obs}}^{95}$ and the number of BSM signal events are placed. The upper limits on the number of BSM signal events are calculated using the observed data (S_{obs}^{95}) and by using the Asimov data instead of the data (S_{exp}^{95}). Secondly, the agreement of the data with the SM prediction is probed. The agreement is quantified in terms of the $\mathrm{CL_b}$, which is the p-value calculated with the signal-plus-background test statistic assuming that the data follows the background-only hypothesis (see Section 8.5). In addition, a background-only hypothesis test is carried out and the discovery p-value $p(s = 0)$ is calculated. This p-value is capped at 0.5, since a one-sided profile likelihood test statistic is used. All conducted hypothesis tests use that the PDF of the test statistic can be approximated by an asymptotic formula [338].

The results are shown in Table 11.4. The 95 % CL upper limits on the visible BSM signal cross-sections range between 0.04 fb and 0.42 fb. The upper limit on the number of BSM signal events (S_{obs}^{95}) ranges between 5.4–29 in the regions derived from the $\mathrm{SR_{0L}}$, between 22–58 in the regions from the $\mathrm{SR_{1L}^{HadTop}}$ and is 10.2 in the $\mathrm{SR_{1L}^{LepTop}}$. In the regions derived from the $\mathrm{SR_{0L}}$ and the $\mathrm{SR_{1L}^{HadTop}}$, the limit on the number of BSM signal events decreases as the constraint on the $E_{\mathrm{T}}^{\mathrm{miss}}$ increases, except in the fourth inclusive $\mathrm{SR_{0L}}$ region ($E_{\mathrm{T}}^{\mathrm{miss}} \geq 500\,\mathrm{GeV}$). This region is characterised by a particularly large deficit of the data and for that reason the upper limit S_{obs}^{95} is below the one of the tightest region requiring $E_{\mathrm{T}}^{\mathrm{miss}} \geq 600\,\mathrm{GeV}$. In the inclusive $E_{\mathrm{T}}^{\mathrm{miss}}$ regions based on the $\mathrm{SR_{0L}}$, the central value of the S_{exp}^{95} is above the S_{obs}^{95}. This is because a deficit in the data improves the observed upper limit compared to the expected limit. This is opposite for an excess, as can be seen for the $\mathrm{SR_{1L}^{LepTop}}$ and most of the bins of the inclusive regions of the $\mathrm{SR_{1L}^{HadTop}}$, where small excesses of the data are observed.

The $\mathrm{CL_b}$ is well below 0.95 in all inclusive SRs. The comparably low value of the $\mathrm{CL_b}$ in the fourth inclusive $E_{\mathrm{T}}^{\mathrm{miss}}$ region ($E_{\mathrm{T}}^{\mathrm{miss}} \geq 500\,\mathrm{GeV}$) of the $\mathrm{SR_{0L}}$ is due to the large deficit of the data. The discovery p-value is between 0.24 and 0.5 in all regions. In conclusion, the background-only hypothesis cannot be rejected.

Model-dependent exclusion limits on the 2HDM+a model parameters are shown for the combination of the 0L, 1L and 2L channels in the next chapter.

[1] The visible cross-section is the cross-section observed with the ATLAS experiment without correcting for detector inefficiencies and the limited geometric acceptance.

Inclusive signal region	Obs.	SM. exp.	$\langle\epsilon\sigma\rangle^{95}_{\text{obs}}$[fb]	S^{95}_{obs}	S^{95}_{exp}	CL_{B}	$p(s=0)$ (Z)
SR_{0L} ($E_{\text{T}}^{\text{miss}} \geq 250\,\text{GeV}$)	133	147 ± 15	0.21	29	36^{+14}_{-10}	0.24	0.50 (0.00)
SR_{0L} ($E_{\text{T}}^{\text{miss}} \geq 330\,\text{GeV}$)	66	83 ± 9	0.11	15.5	24^{+10}_{-7}	0.09	0.50 (0.00)
SR_{0L} ($E_{\text{T}}^{\text{miss}} \geq 400\,\text{GeV}$)	33	42 ± 6	0.08	11.7	16^{+7}_{-5}	0.15	0.50 (0.00)
SR_{0L} ($E_{\text{T}}^{\text{miss}} \geq 500\,\text{GeV}$)	8	17 ± 3	0.04	5.4	10^{+5}_{-3}	0.03	0.50 (0.00)
SR_{0L} ($E_{\text{T}}^{\text{miss}} \geq 600\,\text{GeV}$)	6	7.0 ± 1.7	0.05	6.5	7^{+4}_{-3}	0.38	0.50 (0.00)
$\text{SR}^{\text{HadTop}}_{\text{1L}}$ ($E_{\text{T}}^{\text{miss}} \geq 250\,\text{GeV}$)	239	240 ± 30	0.42	58	60^{+30}_{-20}	0.53	0.47 (0.06)
$\text{SR}^{\text{HadTop}}_{\text{1L}}$ ($E_{\text{T}}^{\text{miss}} \geq 300\,\text{GeV}$)	130	121 ± 17	0.33	46.4	40^{+15}_{-11}	0.67	0.33 (0.44)
$\text{SR}^{\text{HadTop}}_{\text{1L}}$ ($E_{\text{T}}^{\text{miss}} \geq 350\,\text{GeV}$)	69	66 ± 9	0.19	26.3	24^{+10}_{-7}	0.60	0.39 (0.27)
$\text{SR}^{\text{HadTop}}_{\text{1L}}$ ($E_{\text{T}}^{\text{miss}} \geq 400\,\text{GeV}$)	40	37 ± 10	0.17	23.7	22^{+8}_{-6}	0.62	0.38 (0.30)
$\text{SR}^{\text{HadTop}}_{\text{1L}}$ ($E_{\text{T}}^{\text{miss}} \geq 450\,\text{GeV}$)	25	20 ± 9	0.16	22.0	19^{+7}_{-6}	0.69	0.30 (0.51)
$\text{SR}^{\text{LepTop}}_{\text{1L}}$	9	6 ± 3	0.07	10.2	8^{+4}_{-3}	0.74	0.24 (0.72)

Table 11.4: For each inclusive signal region, the number of observed data events as well as the number of predicted SM events as derived from the background-only fit is given. 95 % CL upper limits on the visible cross-section ($\langle\epsilon\sigma\rangle^{95}_{\text{obs}}$) of a generic BSM physics signal, as well as on the number of signal events are shown. The limits on the number of BSM signal events are calculated using the observed data (S^{95}_{obs}) and the Asimov data (S^{95}_{exp}). Furthermore, the agreement of the data with the SM prediction in terms of the CL_{b}, the discovery p-value ($p(s=0)$) and the significance Z of $p(s=0)$ are shown. The discovery p-value is capped at 0.5, due to the use of a one-sided profile likelihood test statistic. All upper limits, the CL_{b} and the p-value are derived using that the PDF of the test statistic can be approximated by an asymptotic formula [338].

Chapter 12

Combining the 0L, 1L and 2L channels and interpretation of results

The search for DM in the tW+DM signature is divided into the 0L, 1L and 2L channels. A SR for the 2L channel was introduced in Reference [21]. Its phase space does not overlap with the phase spaces of the 1L and 0L channels introduced in Sections 9.1 and 9.2. It was found to be particularly sensitive at low values of $m_{H^\pm}$. To obtain the best possible overall sensitivity, the 0L, 1L and 2L channels are statistically combined. The 2L channel is introduced in Section 12.1, the combination strategy is described in Section 12.2 and the resulting exclusion limits on the 2HDM+a model model parameters are shown in Section 12.3.

12.1 The 2L channel

The 2L SR selects events with exactly two reconstructed leptons and high $E_{\mathrm{T}}^{\mathrm{miss}}$ from the escaping DM particles [21]. The dominant SM backgrounds are di-leptonic $t\bar{t}$ decays and the $t\bar{t}+V$ process, with $V = Z, W$. The $t\bar{t}+V$ background is dominated by the $t\bar{t}+Z$ process ($Z \to \nu\nu$), which makes up roughly 80 % of the $t\bar{t}+V$ background [180]. Subdominant background contributions stem from the tWZ process with $Z \to \nu\nu$ and the VV process. The fraction of events containing non-prompt and fake electrons or muons is estimated in the 2L channel using the matrix method [21, 364, 365].

The di-leptonic $t\bar{t}$ background is suppressed in the $\mathrm{SR}_{\mathrm{2L}}$ using the m_{T2} variable [21]. This variable has a kinematic endpoint at the W-boson mass for such $t\bar{t}$ decays, see Section 9.1.2. Due to the presence of additional $E_{\mathrm{T}}^{\mathrm{miss}}$ from the DM particles, this is not the case for the signal and the signal is instead distributed flatly in m_{T2}. Leptonic top-quark decays are those where the W-boson decays into an electron or muon and a neutrino. To suppress background events not containing a leptonically decaying top-quark, the $\min_l m_{bl}$ variable, introduced in Section 10.1.3 is used. Furthermore, the m_{bl}^t variable, see Section 10.1.3, is employed to suppress background events from the $t\bar{t}$ and $t\bar{t}+V$ processes. In contrast to the signal, these processes are characterised by an additional top-quark. For events with two leptonically decaying top-quarks, m_{bl}^t has a kinematic endpoint at the top-quark mass. The requirements on these variables and the remaining event selection conditions in the $\mathrm{SR}_{\mathrm{2L}}$ are summarised in Table 12.1. Due to the low number of expected events in the $\mathrm{SR}_{\mathrm{2L}}$, the region is not divided into bins.

Variable	SR_{2L}	$CR_{2L}^{t\bar{t}}$	$CR_{2L}^{t\bar{t}+V}$
Trigger	di-lepton		di-lepton
N^{ℓ}	2 (OS)		3 (≥ 1 SF-OS pair)
$p_{\mathrm{T}}^{\ell 1}$ [GeV]	> 25		> 25
$p_{\mathrm{T}}^{\ell 2}$ [GeV]	> 20		> 20
$p_{\mathrm{T}}^{\ell 3}$ [GeV]	–		> 20
$m_{\ell\ell}$ [GeV]	$\geq 40, \notin [71, 111]$ if SF		$\in [71, 111]$
$E_{\mathrm{T}}^{\mathrm{miss}}$ [GeV]	> 200		–
$E_{\mathrm{T},\ell\ell}^{\mathrm{miss}}$ [GeV]	–		> 200
$\Delta\phi_{\mathrm{min},1-4}$ [rad]	> 1.1		–
N^{j}	≥ 1		≥ 3
N^{b-jet}	≥ 1		≥ 1 or ≥ 2
p_{T}^{b1} [GeV]	> 50		> 50
m_{T2} [GeV]	> 130	$\in [40, 80]$	–
m_{T2}^{ll} [GeV]	–	–	> 90
$\min_l m_{bl}$ [GeV]	< 170	< 170	–
$\min_l m_{bl}^{ll}$ [GeV]	–	–	< 170
m_{bl}^{t} [GeV]	> 150	< 150	–

Table 12.1: Selection requirements in the 2L channel SR, the $CR_{2L}^{t\bar{t}}$ and the $CR_{2L}^{t\bar{t}+V}$ [21].

The normalisation of the dominant background processes in the SR_{2L}, $t\bar{t}+V$ and $t\bar{t}$, are constrained using CRs [21]. The $t\bar{t}$ normalisation is determined in the $CR_{2L}^{t\bar{t}}$, which is kinematically very close to the SR_{2L}. To increase the purity of the $t\bar{t}$ process, events are selected in the $CR_{2L}^{t\bar{t}}$, if the m_{T2} is between 40 GeV and 80 GeV and the m_{bl}^{t} is below 150 GeV. The $t\bar{t}+V$ background is constrained in the $CR_{2L}^{t\bar{t}+V}$. Similarly to the CR to constrain the $t\bar{t}+Z$ background in the 1L and 0L channels, events with exactly three reconstructed leptons of which two form an SF-OS pair compatible with originating from a Z-boson decay are selected. This lepton pair is treated as invisible. Treating a lepton pair as invisible necessitates to define modifications of the m_{T2} and the $\min_l m_{bl}$ variables, denoted by m_{T2}^{ll} and $\min_l m_{bl}^{ll}$ and detailed in Reference [180]. The selection requirements of the $CR_{2L}^{t\bar{t}}$ and the $CR_{2L}^{t\bar{t}+V}$ are summarised in Table 12.1.

Due to the large contamination of events from the WZ process in the $CR_{2L}^{t\bar{t}+V}$, a dedicated CR is designed to constrain the normalisation of this process [21]. Furthermore, validation regions are defined to verify the background estimation of the $t\bar{t}$, $t\bar{t}+V$ and WZ processes. The details of these regions can be found in Reference [21]. Good agreement of the data and the SM prediction corrected by the background-only fit is observed in the 2L channel CRs and VRs.

Except for additional modelling uncertainties related to the tWZ process, the same sources of systematic uncertainties as described for the 1L and 0L channel in Section 10.3 are employed for the 2L channel [21]. The total systematic uncertainty in the SR_{2L} is 20.7 % [21, 180]. The dominant contributions to the systematic uncertainty stem from the small-radius jet JER and JES uncertainties (11.8 % and 9.4 %), uncertainties due to the normalisation of the $t\bar{t}+V$ background (10 %), uncertainties due to the limited number of simulated events (7.2 %) and modelling uncertainties of the single top quark and $t\bar{t}$ processes (4.5 % and 3.9 %) [180].

The number of events observed in the data and resulting from the background-

	SR_{2L}
Observed events	12
Fitted SM bkg events	5.9 ± 1.2
$t\bar{t}$	1.2 ± 0.9
Single top	$0.26^{+0.27}_{-0.26}$
W+jets	–
Z+jets	–
VV ($V = W, Z$)	0.5 ± 0.2
$t\bar{t} + V$ ($V = W, Z$)	2.9 ± 0.7
tWZ	0.8 ± 0.1
Others	0.16 ± 0.08

Table 12.2: Data and predicted yields in the SR_{2L} using the normalisation parameters and uncertainties as derived by the background-only fit ("post-fit") [21]. The uncertainties include all systematic uncertainty sources. "Others" contains contributions from the triboson, $t\bar{t} + h$, $t\bar{t}WW$ and $t\bar{t}t\bar{t}$ processes, as well as from events containing fake and non-prompt leptons.

only fit for the SM prediction are shown in Table 12.2 for the SR_{2L} [21]. The dominant SM process in the SR_{2L} is the $t\bar{t} + V$ process, which makes up roughly 50 % of the total SM background, followed by the $t\bar{t}$ (20 %), tWZ (14 %), VV (8 %) and other processes (< 3 %). Events with fake and non-prompt electrons or muons have a negligible contribution in the SR_{2L}. The normalisation parameters obtained for the $t\bar{t}$, $t\bar{t} + V$ and WZ processes are $\mu^{t\bar{t}}_{2L} = 1.00 \pm 0.03$, $\mu^{2L}_{t\bar{t}+V} = 0.80 \pm 0.16$ and $\mu^{2L}_{WZ} = 0.8 \pm 0.3$, respectively. An excess of the data with a significance of 1.92σ is observed.

12.2 Combination strategy

The SRs of the 0L, 1L and 2L channels have non-overlapping phase spaces and can thus be statistically combined. The $t\bar{t}+Z$ process makes up the largest contribution to the SM background in the SR_{2L} and the second largest in SR^{LepTop}_{1L}. The phase spaces of the $CR_{t\bar{t}+Z}$ employed by the 1L and 0L channel and of the 2L channel $CR^{t\bar{t}+V}_{2L}$ overlap, due to the similar event selection strategy, as can be seen from Tables 10.3 and 12.1. To have a consistent estimation of the $t\bar{t}+Z$ background, only the $CR_{t\bar{t}+Z}$ is used in the combination and the same $t\bar{t}+Z$ normalisation parameter is employed across all three channels. Results shown below in Section 12.3 for the individual 2L channel also employ the $CR_{t\bar{t}+Z}$ to estimate the normalisation of the $t\bar{t}+Z$ process. Since the fraction of VV events in the $CR_{t\bar{t}+Z}$ is small, the CR for the WZ process from the 2L channel is not included in the combined likelihood. The $t\bar{t}$ background in the 2L channel SR is estimated by using a dedicated normalisation parameter constrained in the $CR^{t\bar{t}}_{2L}$ in the combination of all three channels. By using the simulation, the predictions of the remaining background processes in the 2L channel regions are obtained.

The use of the 1L and 0L channel CR to determine the normalisation of the $t\bar{t}+Z$ process makes the $t\bar{t}+Z$ normalisation parameter increase from $\mu_{t\bar{t}+Z} = 0.80 \pm 0.16$ to $\mu_{t\bar{t}+Z} = 1.18 \pm 0.19$ in the 2L channel. Together with the corresponding removal of the CR of the WZ process from the likelihood, the total SM prediction in the SR_{2L} is increased by roughly 25 % in the combination of the three analysis channels. This increased yield agrees with the yield in Table 12.2 within 1.25 standard-deviations. The sensitivity of the SR_{2L} towards the 2HDM+a model was reassessed with the

increased yield by calculating expected exclusion limits. No significant changes were observed.

The only nuisance parameter that is correlated between the 2L channel and the two other channels is the one related to the signal modelling uncertainties. Due to the usage of different object definitions, object selection criteria and nuisance parameter reduction schemes, all other nuisance parameters are not correlated. The nuisance parameters related to the same systematic uncertainties are correlated between the 1L and 0L channels in the combination of all three channels. The combined likelihood is constructed with the `pyHF` software [27, 28].

12.3 2HDM+a model interpretation of the results

Model-dependent hypothesis tests detailed in Section 8.5 are used to set exclusion limits on the parameters of the 2HDM+a model. To perform the hypothesis tests, signal samples are generated for a multitude of 2HDM+a model parameters. Three planes of 2HDM+a model model parameters are probed. In the m_a-$m_{H^\pm}$ plane, $\tan\beta$ is fixed to one and the masses of the a- and $H^\pm$-bosons are varied between 100 GeV–600 GeV and 400 GeV–2000 GeV, respectively. In the two $m_{H^\pm}$-$\tan\beta$ planes, $m_{H^\pm}$ is varied between 300 GeV–2000 GeV and values of $\tan\beta$ from 0.3 to 30 are probed, while m_a equals either 150 GeV or 250 GeV. All three planes are studied for $\sin\theta = 0.7$ and $\sin\theta = 0.35$.

The tW+DM and $t\bar{t}$+DM final state are kinematically very similar. The analyses presented in this thesis are sensitive to both signatures. If the 2HDM+a model is a realistic model, contributions from both signatures have to be accounted for. For that reason, the signals input to the hypothesis testing are generated for the tW+DM final state and for the combination of tW+DM and $t\bar{t}$+DM final states. The $t\bar{t}$+DM samples are, as discussed in Section 6.7, produced for a simplified DM model [154, 155, 157, 158] and reweighted event-by-event [15, 173] to yield a 2HDM+a model prediction.

For each generated signal, model-dependent hypotheses tests are carried out, testing the signal-plus-background hypothesis, see Section 8.5. The value of the signal normalisation parameter μ_{sig}, where the CL_s of the hypothesis tests equals 0.05 gives the 95 % CL exclusion limit on the signal normalisation. Signals are declared as excluded, if the 95 % CL exclusion limit on μ_{sig} is below one. The exclusion limit is either derived using the data ("observed limit"), or by employing the Asimov data instead of the measured data ("expected limit"). All SRs and CRs are included in the likelihood used in the hypothesis test for the combination of all three channels. When deriving exclusion limits on μ_{sig} for the individual 0L, 1L and 2L channels, either only the $\text{SR}_{0\text{L}}$, the 1L channel SRs or the $\text{SR}_{2\text{L}}$ are included in the likelihood together with the respective CRs.

The excluded parameter space of the 2HDM+a model is shown in Figure 12.1 for $\sin\theta = 0.35$ and Figure 12.2 for $\sin\theta = 0.7$. Coloured, smoothened lines surround those parameter values for which the corresponding signals are excluded at 95 % CL. Different colours surround the excluded parameters obtained with the individual 0L (green), 1L (red) and 2L (yellow) channels, as well as their combination (blue). The model parameters excluded by observed exclusion limits at 95 % CL are indicated by solid lines and those excluded by expected limits by dashed lines. To obtain the excluded parameters shown in the left-hand columns in Figures 12.1 and 12.2, tW+DM signals are used. In the right-hand columns, tW+DM and $t\bar{t}$+DM signals are used.

For $\sin\theta = 0.35$ (Figure 12.1), values of m_a up to 300 GeV and $m_{H^\pm}$ between 450 GeV and 1250 GeV are excluded in the m_a-$m_{H^\pm}$ plane by the combination of all three channels for the tW+DM signal. In the $m_{H^\pm}$-$\tan\beta$ planes, values of $\tan\beta$

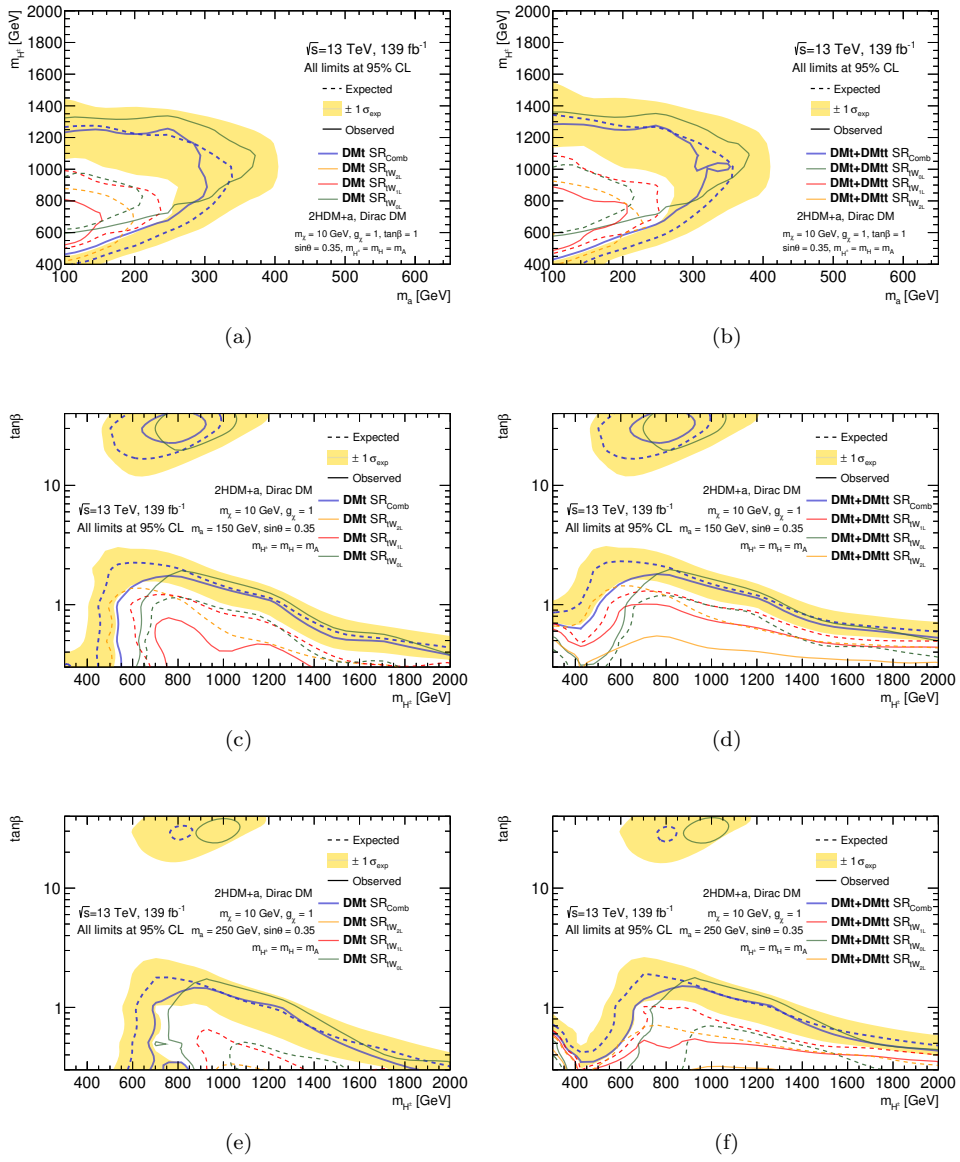

Figure 12.1: Excluded regions of 2HDM+a model parameters space in the m_a-$m_{H^\pm}$ plane (top), and the $m_{H^\pm}$-tan β planes with $m_a = 150\,\text{GeV}$ (middle) and $m_a = 250\,\text{GeV}$ (bottom) and a value of $\sin\theta = 0.35$ for all three planes. The results in the left column are obtained using tW+DM signals, while tW+DM and $t\bar{t}$+DM signals are used in the right column. The areas of parameter space excluded by the 0L, 1L and 2L channels are surrounded by green, red and yellow lines, respectively. The regions excluded by the combination of the three channels are indicated by blue lines. A point in parameter space is regarded as excluded, if the 95 % CL exclusion limit on the normalisation parameter of the corresponding signal is below one. The observed exclusion contours (solid lines) are derived using the data, while the expected exclusion contours (dashed lines) employ the Asimov data instead of the data (Section 8.5). The yellow band indicates the uncertainty on the expected exclusion contour of the combined result and accounts for systematic uncertainties of the signal and the SM predictions.

below two are excluded for masses of the $H^{\pm}$-boson from 550 GeV (700 GeV) to 2000 GeV and $m_a = 150$ GeV (250 GeV). Furthermore, for $m_a = 150$ GeV and $m_{H^{\pm}}$ in the range 650 GeV–950 GeV, values of $\tan\beta \simeq 20$–30 are excluded. The exclusion at low and at high values of $\tan\beta$, but not at intermediate values of $\tan\beta$ can be explained by the dependence of the tW+DM cross-section on $\tan\beta$ as shown in Figures 4.4a and 4.4b. The excluded parameter space is extended if also accounting for the $t\bar{t}$+DM signal. In the m_a-$m_{H^{\pm}}$ plane, the excluded region is increased by 100 GeV in $m_{H^{\pm}}$ and covers 400 GeV–1300 GeV. In the two $m_{H^{\pm}}$-$\tan\beta$ planes, the excluded area is extended to $H^{\pm}$-boson masses smaller than 600 GeV–700 GeV if accounting for the $t\bar{t}$+DM signal, where values of $\tan\beta$ up to 1.5 are excluded. Due to the linear dependence of the $t\bar{t}$+DM signal cross-section on $1/\tan\beta^2$ [15, 21, 173], the excluded parameters at high $\tan\beta$ do not change on the other hand.

By studying the expected exclusion contours, the sensitivity of the 0L, 1L and 2L channels to the 2HDM+a model is compared for $\sin\theta = 0.35$ in Figure 12.1. Except in the $m_{H^{\pm}}$-$\tan\beta$ plane with $m_a = 250$ GeV, the most sensitive channel at low values of $m_{H^{\pm}}$ up to $\simeq$ 600 GeV–800 GeV is the 2L channel. At higher values of $m_{H^{\pm}}$, the 1L channel becomes the most sensitive one. The sensitivity of the 1L and 0L channel becomes comparable in most of the parameter planes for $H^{\pm}$-boson masses beyond 800 GeV. The expected exclusion of the combination of the three channels excludes a wider range of parameter space than the individual channels in all planes. In the m_a-$m_{H^{\pm}}$ plane, the increase in the excluded values is up to 250 GeV in $m_{H^{\pm}}$ and 100 GeV in m_a. In the two $m_{H^{\pm}}$-$\tan\beta$ planes, the increase in $\tan\beta$ is up to one unit at low values of $\tan\beta$. At high values of $\tan\beta > 10$ an expected exclusion is only achieved when combining all three channels.

The observed exclusion contour of the combination of the 0L, 1L and 2L channels is dominated by the 0L channel for $m_{H^{\pm}} \gtrsim$ 800 GeV–900 GeV and at high values of $\tan\beta$. Due to the deficit of data in the 0L channel, a wider range of 2HDM+a model parameters is excluded by the observed contour than by the expected contour for the 0L channel. Conversely, the excess of data in the $\mathrm{SR}_{\mathrm{2L}}$ decreases the span of excluded parameters by the observed contour versus the expected contour. The excess of data in the $\mathrm{SR}_{\mathrm{2L}}$ is also the reason why no observed exclusion contour is visible for the 2L channel in Figures 12.1a, 12.1b, 12.1c and 12.1e.

Compared to $\sin\theta = 0.35$, the excluded range in all parameters is increased for $\sin\theta = 0.7$, as shown in Figure 12.2. This is due to the higher cross-section of the tW+DM signal at $\sin\theta = 0.7$ [179, 180]. Values up to 400 GeV in m_a and 400 GeV–1500 GeV in $m_{H^{\pm}}$ are excluded if accounting only for the tW+DM signal. In the $m_{H^{\pm}}$-$\tan\beta$ plane, values of $\tan\beta \lesssim 2.2$ are excluded in the $m_{H^{\pm}}$ range 300 GeV–2000 GeV (450 GeV–2000 GeV) assuming $m_a = 150$ GeV (250 GeV). For a-boson masses of 150 GeV (250 GeV) and masses of the $H^{\pm}$-boson in the range 500 GeV–850 GeV (800 GeV–950 GeV), high values of $\tan\beta \simeq 20$–30 ($\simeq$ 25–30) are excluded. As for $\sin\theta = 0.35$, accounting for the $t\bar{t}$+DM signal allows increasing the excluded area of parameter space. At high $m_{H^{\pm}}$, the excluded values of $m_{H^{\pm}}$ go beyond 2000 GeV, i.e. the exclusion is extended by more than 400 GeV if considering tW+DM and $t\bar{t}$+DM signals. This large extension of excluded parameters can be explained by the comparably high cross-section of the $t\bar{t}$+DM signal at $\sin\theta = 0.7$, low values of m_a and the considered $H^{\pm}$-boson masses. Compared to considering the tW+DM signal alone, the excluded range of parameters does not change significantly in the m_a-$m_{H^{\pm}}$ plane for $m_a > 350$ GeV when accounting for both the tW+DM and $t\bar{t}$+DM signals. In the $m_{H^{\pm}}$-$\tan\beta$ planes, the excluded parameter space remains similar at high values of $\tan\beta$ if including the $t\bar{t}$+DM signal. For $H^{\pm}$-boson masses smaller than 400 GeV (450 GeV), values of $\tan\beta$ between 1 and 2 (0.8 and 1) are additionally excluded for a-boson masses of 150 GeV (250 GeV) if accounting for the tW+DM and $t\bar{t}$+DM signals. The excluded value of $\tan\beta$ is increased by 0.2–0.3 at $m_{H^{\pm}} \simeq 2000$ GeV in both $m_{H^{\pm}}$-$\tan\beta$ planes.

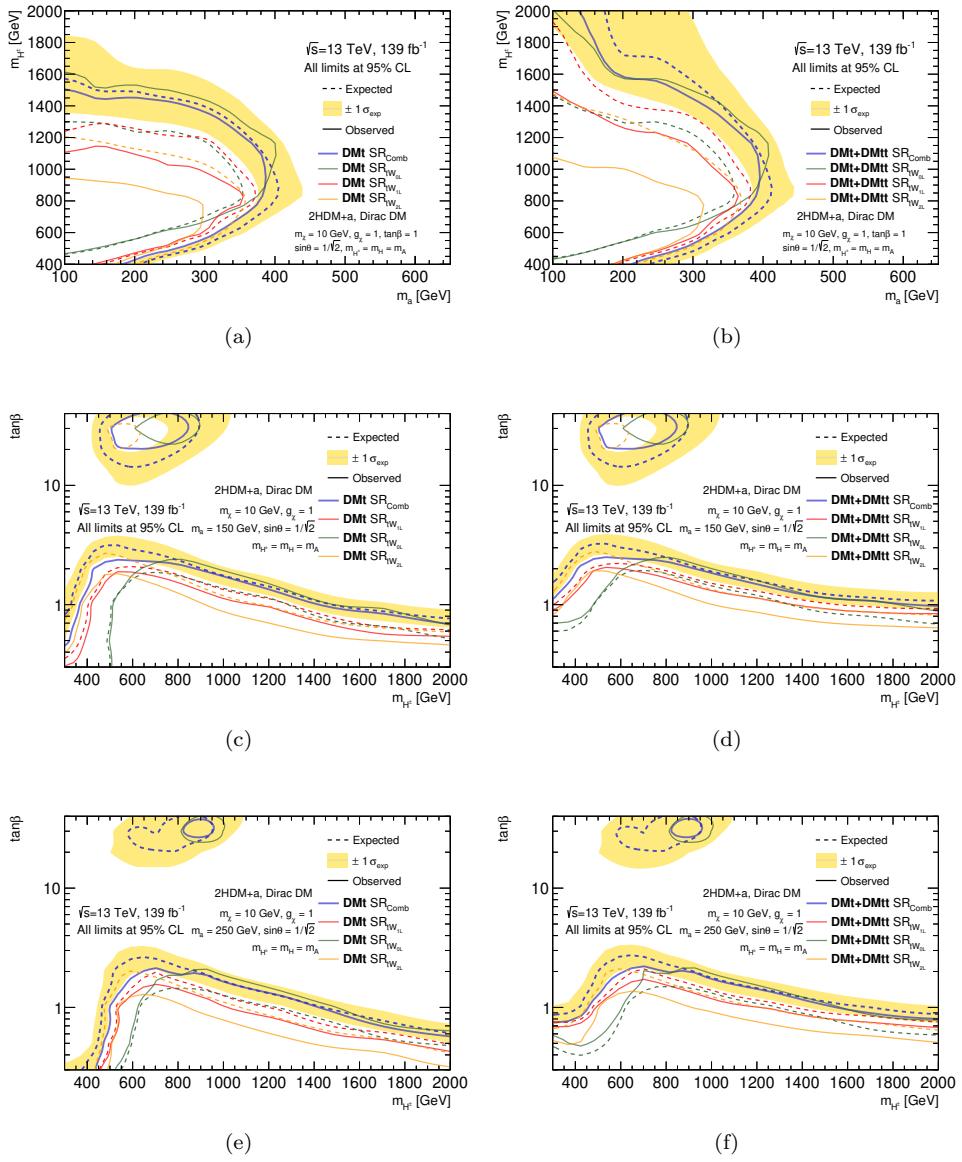

Figure 12.2: Excluded regions of 2HDM+a model parameters space in the m_a-$m_{H^\pm}$ plane (top), and the $m_{H^\pm}$-tan β planes with $m_a = 150\,\text{GeV}$ (middle) and $m_a = 250\,\text{GeV}$ (bottom) and a value of $\sin\theta = 0.7$ for all three planes. The results in the left column are obtained using tW+DM signals, while tW+DM and $t\bar{t}$+DM signals are used in the right column. The areas of parameter space excluded by the 0L, 1L and 2L channels are surrounded by green, red and yellow lines, respectively. The regions excluded by the combination of the three channels are indicated by blue lines. A point in parameter space is regarded as excluded, if the 95 % CL exclusion limit on the normalisation parameter of the corresponding signal is below one. The observed exclusion contours (solid lines) are derived using the data, while the expected exclusion contours (dashed lines) employ the Asimov data instead of the data (Section 8.5). The yellow band indicates the uncertainty on the expected exclusion contour of the combined result and accounts for systematic uncertainties of the signal and the SM predictions.

Similar to the studied parameter spaces with sin = 0.35, the 1L and 2L channels are the most sensitive channels for signals with low values of $m_{H^\pm}$ and $\sin\theta = 0.7$, as quantified with the expected exclusion contour. The 1L channel sensitivity becomes comparable to the 0L channel sensitivity at $m_{H^\pm} \gtrsim 800\,\text{GeV}$–$1000\,\text{GeV}$ considering the tW+DM signal only. If accounting for both the tW+DM and $t\bar{t}$+DM signals, the 1L channel becomes the most sensitive channel at high values of $m_{H^\pm}$ and low values of $\tan\beta < 3$. The strongest observed exclusion is given by the 0L channel for $m_{H^\pm} \gtrsim 600\,\text{GeV}$–$700\,\text{GeV}$, by the 1L channel for lower values of $m_{H^\pm}$ until $m_{H^\pm} \simeq 500\,\text{GeV}$–$600\,\text{GeV}$ and by the 2L channel for even lower $H^\pm$-boson masses.

12.4 Comparison to other searches

The 2HDM+a model parameters excluded with the search for DM particles in the tW+DM signature using the tW+DM and the $t\bar{t}$+DM signals are compared to the parameters excluded in other DM particle searches. Following searches are considered in the comparison:

- Searches for DM particles produced in association with a Higgs-boson (mono-Higgs signature). In the 2HDM+a model, the mono-Higgs signature is resonantly enhanced as discussed in Section 4.2. Searches with Higgs-boson decays into two b-quarks ($E_\text{T}^\text{miss} + h(b\bar{b})$) [17] and two photons ($E_\text{T}^\text{miss} + h(\gamma\gamma)$) [16] are included in the comparison.
- The mono-Z signature is also resonantly enhanced in the 2HDM+a model (see Section 4.2). The searches for DM particles produced in association with a Z-boson decaying into quarks ($E_\text{T}^\text{miss} + Z(q\bar{q})$) [366] and into two charged leptons ($E_\text{T}^\text{miss} + Z(ll)$) [19] are included in the comparison. Furthermore, the statistical combination of the $E_\text{T}^\text{miss}+h(b\bar{b})$ and the $E_\text{T}^\text{miss}+Z(ll)$ searches [367, 368] is.
- Finally, the tW+DM search results are compared to the results from a search for $H^\pm$-boson decays into a top-quark and a b-quark ($H^\pm tb$) [369] and searches for invisible Higgs-boson decays (h(inv)) [370].

The excluded areas of parameter space are compared in the m_a-$m_{H^\pm}$ plane with $\tan\beta = 1$ and the $m_{H^\pm}$-$\tan\beta$ plane with $m_a = 250\,\text{GeV}$. Figures 12.3a and 12.3b show the excluded parameter space regions of the different searches in the two planes for $\sin\theta = 0.35$ and Figures 12.4a and 12.4b for $\sin\theta = 0.7$. Excluded areas of parameter space are filled or enclosed by lines of different colours for the different searches. The decay-width of one of the Higgs-bosons exceeds 20 % of its mass in the hatched regions of parameter space.

Following features about the excluded parameter spaces are worth noting:

- In the m_a-$m_{H^\pm}$ plane, the $H^\pm tb$ and the h(inv) searches exclude respectively: values of $m_{H^\pm}$ almost independent of m_a, and values of m_a almost independent of $m_{H^\pm}$. The dominant Feynman diagram in the $H^\pm tb$ search features the production chain $gg \to tbH^\pm \to tbtb$ [369], while h(inv) searches mainly probe $gg \to h \to a\chi\bar{\chi} \to \chi\bar{\chi}\chi\bar{\chi}$ [15]. As these production chains only depend on the $H^\pm$-boson or the mediator, respectively, the excluded regions by the two searches primarily depend only on the according masses.
- For $\sin\theta = 0.7$, the excluded value of m_a by the two mono-Higgs searches $E_\text{T}^\text{miss} + h(b\bar{b})$ and $E_\text{T}^\text{miss} + h(\gamma\gamma)$ increases as a function of $m_{H^\pm}$ for $m_{H^\pm} > 800\,\text{GeV}$ and $m_{H^\pm} > 1200\,\text{GeV}$ in the m_a-$m_{H^\pm}$ plane (Figure 12.4a). This is due to the presence of two production diagrams with complementary cross-section dependencies [368]. The cross-section of the first diagram, featuring

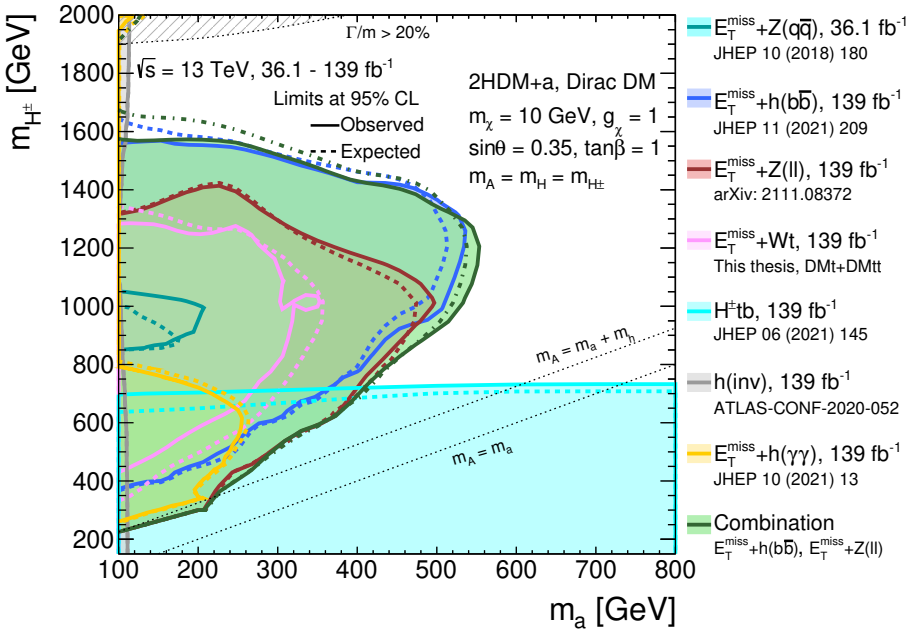

(a)

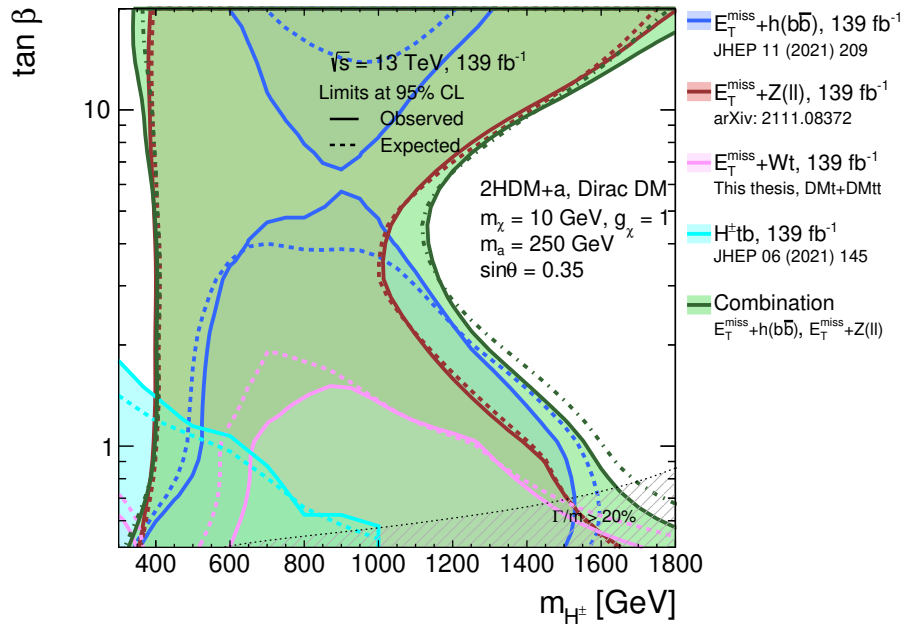

(b)

Figure 12.3: Excluded 2HDM+a model parameter spaces at 95 % CL (coloured areas) in (a) the m_a-$m_{H^\pm}$ plane with $\tan\beta = 1$ and (b) the $m_{H^\pm}$-$\tan\beta$ plane with $m_a = 250\,\text{GeV}$ and $\sin\theta = 0.35$ in both figures. Observed exclusion contours are shown by solid and expected exclusion contours by dashed lines. The hatched areas indicates parameter space regions where the decay width of one of the Higgs-bosons is larger than 20 % of its mass. The results shown from this thesis are derived using tW+DM and $t\bar{t}$+DM signals.

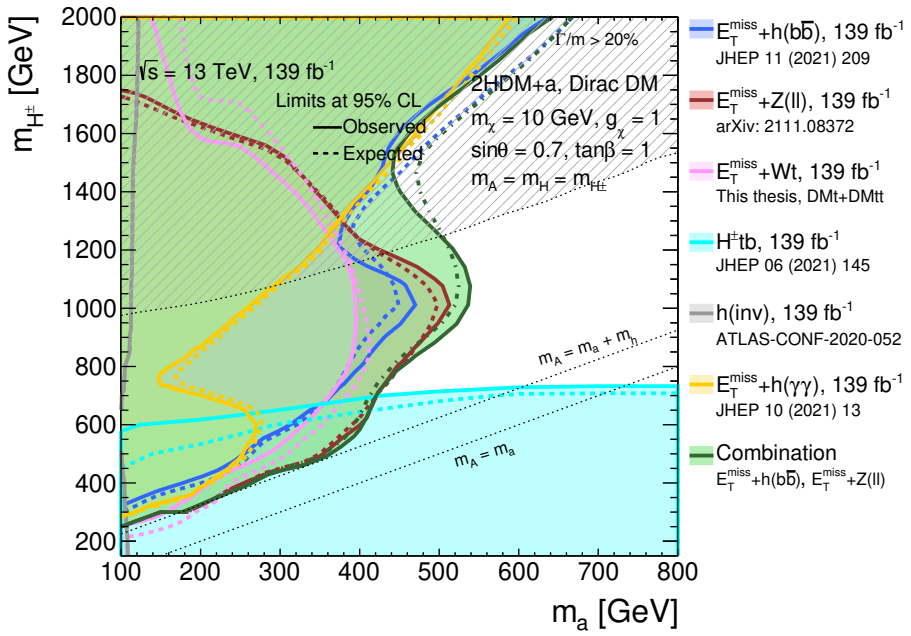

(a)

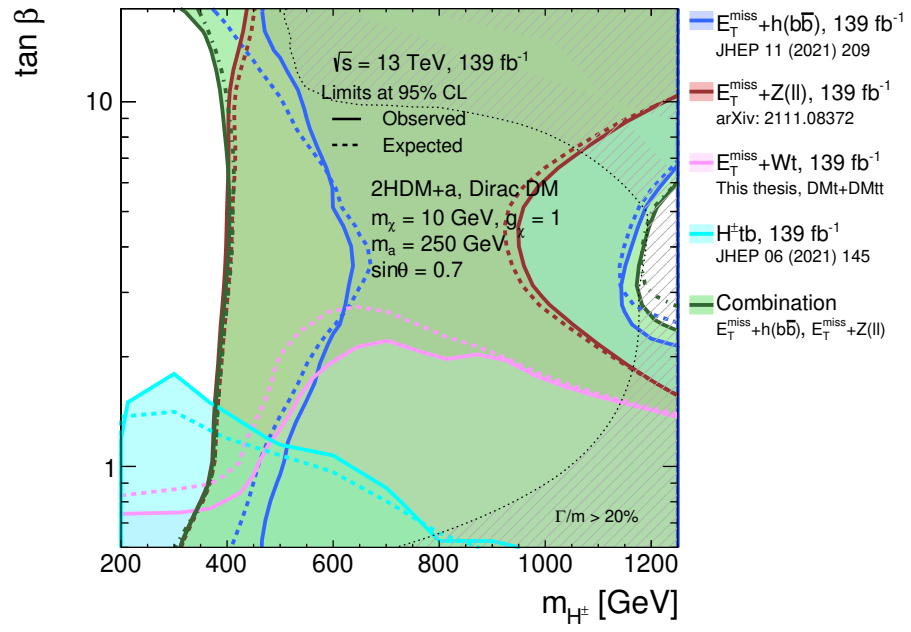

(b)

Figure 12.4: Excluded 2HDM+a model parameter spaces at 95 % CL (coloured areas) in (a) the m_a-$m_{H^\pm}$ plane with $\tan\beta = 1$ and (b) the $m_{H^\pm}$-$\tan\beta$ plane with $m_a = 250\,\text{GeV}$ and $\sin\theta = 0.7$ in both figures. Observed exclusion contours are shown by solid and expected exclusion contours by dashed lines. The hatched areas indicates parameter space regions where the decay width of one of the Higgs-bosons is larger than 20 % of its mass. The results shown from this thesis are derived using tW+DM and $t\bar{t}$+DM signals.

the resonant A-boson production and subsequent $A \to a(\to \chi\bar{\chi})h$ decay, decreases with incrementing m_A (which equals $m_{H^\pm}$ in the m_a-$m_{H^\pm}$ plane). On the other hand, the cross-section of the second diagram, featuring the production of an a-boson and the decay $a \to a(\to \chi\bar{\chi})h$, grows with m_A.

- In the $m_{H^\pm}$-$\tan\beta$ planes, the mono-Z and mono-Higgs searches exclude hourglass-shaped regions of parameter space. The particular shape is the result of gluon and b-quark induced production diagrams, which have inverse dependencies on $\tan\beta$ [19].

The parameter space exclusion is dominated among all planes and values of $\sin\theta$ by the combination of the mono-Higgs and mono-Z searches as well as the $H^\pm tb$ search. Nevertheless, the tW+DM search complements the other searches. In the $m_{H^\pm}$-$\tan\beta$ plane, the observed excluded area extends beyond the excluded area of the mono-Higgs and mono-Z combination at low $m_{H^\pm}$ for both values of $\sin\theta$. For $\sin\theta = 0.35$ and high values of $m_{H^\pm}$, the tW+DM search has the strongest observed exclusion on $\tan\beta$ of the mono-Higgs, mono-Z and tW+DM searches. In the $\sin\theta = 0.7$ m_a-$m_{H^\pm}$ plane, the observed excluded area of the tW+DM search is comparable to the area excluded by the mono-Higgs and the mono-Z searches and their combination at low values of $m_{H^\pm}$. At high values of $m_{H^\pm}$, the exclusion of parameters by the tW+DM search goes beyond the excluded values by the mono-Z search. Due to the complementarity of the different searches, a statistical combination of the mono-Higgs, mono-Z, tW+DM and $H^\pm tb$ searches could increase the excluded area in all planes.

Chapter 13

Summary and outlook

This thesis presented a search for DM particles in the tW+DM signature. The $\sqrt{s} = 13\,\text{TeV}$ data with an integrated luminosity of $139\,\text{fb}^{-1}$ recorded by the ATLAS detector at the LHC was analysed. Signal regions targeting a 2HDM+a model signal in the 0L, 1L and 2L channel were described, with special focus on the 1L channel. These SRs required high $E_{\text{T}}^{\text{miss}}$ due to the elusive nature of the DM particles and the presence of zero, one or two reconstructed leptons. Dedicated variables were used to suppress the dominant background contributions. For multiple 2HDM+a model parameters, high-p_{T}, hadronically decaying W-bosons are expected to be frequent in the signal in the 1L and 0L channel. Reconstructing these W-bosons in large-radius jets and identifying them by W-tagging was used to significantly increase the expected fraction of signal to background events.

The background contributions were estimated in dedicated CRs and verified in VRs. Good agreement between the SM prediction and the data was found after the background-only fit in the CRs and VRs. The SM prediction after the background-only fit and the data were also compared in the SRs. Good agreement of the prediction and the data was found with the significance of differences being within one standard deviation, except in the $\text{SR}_{0\text{L}}$ bin covering $500\,\text{GeV} < E_{\text{T}}^{\text{miss}} < 600\,\text{GeV}$, where the data was exceeded by the SM prediction by more than 2.5σ. Due to the good agreement otherwise in the $\text{SR}_{0\text{L}}$, this disagreement was considered to be due to a statistical fluctuation. In the 2L channel SR an excess of the data over the background with a significance of roughly 2σ was observed.

Model-independent upper limits on the number of events and the cross-section of a generic BSM signal were derived for the 1L and 0L channel. Subsequently, the 1L and 0L channel SRs were statistically combined with the SR of the 2L channel. To harmonise the $t\bar{t} + Z$ estimation, some of the CRs of the 2L channel were not included in the combined likelihood. Combining all three analysis channels, 95 % CL exclusion limits on the signal normalisation for signals generated for a multitude of 2HDM+a model parameters were used to exclude model parameters. Besides the tW+DM signal, the combination of the tW+DM signal and the $t\bar{t}$+DM signal was considered to set exclusion limits. The most stringent limits to date from searches for DM in the tW+DM signature were set.

For $\sin\theta = 0.35$, $H^{\pm}$-boson masses between 400 GeV–1300 GeV and a-boson masses below 350 GeV were excluded assuming $\tan\beta = 1$. Furthermore, values up to $\tan\beta = 2$ could be excluded for $m_{H^{\pm}}$ from 300 GeV–2000 GeV for a-boson masses of 150 GeV and 250 GeV. High values of $\tan\beta = 20$–30 could be excluded for values of $m_{H^{\pm}}$ between 650 GeV–950 GeV for $m_a = 150\,\text{GeV}$. For $\sin\theta = 0.7$, a wider region of model parameter space was excluded. For a value of $\tan\beta = 1$, the excluded parameter space ranged from $H^{\pm}$-boson masses below 400 GeV to beyond 2000 GeV and a-boson masses below 400 GeV. As a function of $\tan\beta$, the exclusion

was increased to values of $\tan\beta$ up to 2.2 for the probed $H^{\pm}$-boson masses between 300 GeV–2000 GeV. High values of $\tan\beta$ at around 25–30 could also be excluded for $m_a = 250\,\text{GeV}$.

The 2L channel was found to be the most sensitive channel at low values of $m_{H^{\pm}}$ up to values of $m_{H^{\pm}} \simeq 600\,\text{GeV}$–$800\,\text{GeV}$ independent of $\sin\theta$. At higher values of $m_{H^{\pm}}$, the 1L channel showed to be most sensitive up to $m_{H^{\pm}} \simeq 800\,\text{GeV}$–$1000\,\text{GeV}$, where the sensitivity of the 1L and 0L channels became comparable. At high values of $\tan\beta$, the 2L channel was found to be the most sensitive channel. The observed exclusion from the 0L channel dominated the combined observed exclusion at high $H^{\pm}$-boson masses and high values of $\tan\beta$.

Finally, the tW+DM search results were compared to results of 2HDM+a model searches exploring other signatures. While the excluded parameter space by the tW+DM search was always contained in the parameter space excluded by other searches, the results from the tW+DM search were found to be complementary. The tW+DM search was shown to be particularly strong at low and high values of $m_{H^{\pm}}$. Combining the tW+DM search with the mono-Higgs, mono-Z and $H^{\pm}tb$ searches may therefore be beneficial to increase the excluded parameter space of the 2HDM+a model.

One way to improve the sensitivity of the tW+DM search is to reduce the uncertainties. The dominant systematic uncertainties in the search were found to be due to the energy calibration of small-radius jets, the efficiency calibration of the W-tagging and the modelling of SM processes. Taking the exact values of the systematic uncertainties into account in the optimisation procedure of the SRs, rather than using a constant value, may be beneficial to reduce their impact. In addition, measurements of SM processes in the phase spaces of searches may help to reduce the modelling uncertainties. In contrast to what is suggested here, measurements of SM processes are currently most commonly performed in regions which are kinematically very different from the phase spaces of searches. First measurements of SM processes in phase spaces inspired by searches have recently been published [371, 372] with a strong involvement of the author in Reference [372]. Many other results are expected to come in the future.

In addition to potentially constraining the systematic uncertainties, these measurements will also benefit the search for DM particles by other means. To facilitate the testing of new models, the publication of model-independent results is important. Providing model-independent results that do not require the usage of a CPU intense and not easily accessible detector simulation will further simplify the testing of new SM extensions. Such results are, for example, the outcome of differential measurements. Using e.g. the `CONTUR` method [373, 374], measurement results allow for a straight-forward and fast testing of new DM models. Measurements in the phase spaces of searches - the latter being designed to be highly sensitive to BSM signals - may therefore considerably help to improve the current understanding of DM.

The statistical uncertainty of the data was found to be comparable or even higher than the total systematic uncertainty in the 0L channel SR and most of the bins of the $\text{SR}_{\text{1L}}^{\text{HadTop}}$ and in the $\text{SR}_{\text{1L}}^{\text{LepTop}}$ (Section 10.3). Searching for DM particles in the tW+DM signature will thus profit from the third run of the LHC which started in 2022, roughly doubling the amount of data until 2025. Towards the end of the decade, the High-Luminosity (HL) LHC [375] will start operating. The total integrated luminosity expected to be delivered by the HL-LHC is $4000\,\text{fb}^{-1}$. In agreement with the observation on the statistical uncertainty, recent studies [376] investigating the prospects of searching for DM in the tW+DM signature have shown that a large increase of the experimental sensitivity is expected with the data collected at the HL-LHC. Generally, the more than ten-fold increase of the data until the end of the HL-LHC will give new opportunities to probe the nature

of DM. The much larger dataset will allow investigating more rare processes and probing deviations from the SM prediction at yet unprecedented precision [376, 377]. Run-III and the HL-LHC may yield a spectacular new discovery or - at the very least - pin down the nature of DM even further. Unravelling the mysteries of DM remains exciting and many unknowns are yet to be discovered.

Bibliography

[1] Planck Collaboration. "Planck 2018 results. I. Overview and the cosmological legacy of Planck". In: *Astron. Astrophys.* 641 (2020), A1. DOI: 10.1051/0004-6361/201833880. arXiv: 1807.06205 [astro-ph.CO].

[2] K. Garrett and G. Duda. "Dark Matter: A Primer". In: *Adv. Astron.* 2011 (2011), p. 968283. DOI: 10.1155/2011/968283. arXiv: 1006.2483 [hep-ph].

[3] F. Zwicky. "Die Rotverschiebung von extragalaktischen Nebeln". In: *Helv. Phys. Acta* 6 (1933), pp. 110–127. DOI: 10.1007/s10714-008-0707-4.

[4] G. Bertone and D. Hooper. "History of dark matter". In: *Rev. Mod. Phys.* 90.4 (2018), p. 045002. DOI: 10.1103/RevModPhys.90.045002. arXiv: 1605.04909 [astro-ph.CO].

[5] F. Zwicky. "On the Masses of Nebulae and of Clusters of Nebulae". In: *Astrophys. J.* 86 (1937), pp. 217–246. DOI: 10.1086/143864.

[6] MACHO Collaboration. "The MACHO project: Microlensing results from 5.7 years of LMC observations". In: *Astrophys. J.* 542 (2000), pp. 281–307. DOI: 10.1086/309512. arXiv: astro-ph/0001272.

[7] EROS-2 Collaboration. "Limits on the Macho Content of the Galactic Halo from the EROS-2 Survey of the Magellanic Clouds". In: *Astron. Astrophys.* 469 (2007), pp. 387–404. DOI: 10.1051/0004-6361:20066017. arXiv: astro-ph/0607207.

[8] S. L. Glashow. "Partial Symmetries of Weak Interactions". In: *Nucl. Phys.* 22 (1961), pp. 579–588. DOI: 10.1016/0029-5582(61)90469-2.

[9] S. Weinberg. "A Model of Leptons". In: *Phys. Rev. Lett.* 19 (1967), pp. 1264–1266. DOI: 10.1103/PhysRevLett.19.1264.

[10] A. Salam. "Weak and Electromagnetic Interactions". In: *Conf. Proc. C* 680519 (1968), pp. 367–377. DOI: 10.1142/9789812795915_0034.

[11] G. 't Hooft and M. J. G. Veltman. "Regularization and Renormalization of Gauge Fields". In: *Nucl. Phys. B* 44 (1972), pp. 189–213. DOI: 10.1016/0550-3213(72)90279-9.

[12] J. Silk et al. *Particle Dark Matter: Observations, Models and Searches*. Ed. by G. Bertone. Cambridge: Cambridge Univ. Press, 2010. ISBN: 978-1-107-65392-4. DOI: 10.1017/CBO9780511770739.

[13] F. Kahlhoefer. "Review of LHC Dark Matter Searches". In: *Int. J. Mod. Phys. A* 32.13 (2017), p. 1730006. DOI: 10.1142/S0217751X1730006X. arXiv: 1702.02430 [hep-ph].

[14] M. Bauer, U. Haisch and F. Kahlhoefer. "Simplified dark matter models with two Higgs doublets: I. Pseudoscalar mediators". In: *JHEP* 05 (2017), p. 138. DOI: 10.1007/JHEP05(2017)138. arXiv: 1701.07427 [hep-ph].

[15] T. Abe et al. "LHC Dark Matter Working Group: Next-generation spin-0 dark matter models". In: *Phys. Dark Univ.* 27 (2020), p. 100351. DOI: 10.1016/j.dark.2019.100351. arXiv: 1810.09420 [hep-ex].

[16] ATLAS Collaboration. "Search for dark matter in events with missing transverse momentum and a Higgs boson decaying into two photons in pp collisions at $\sqrt{s} = 13$ TeV with the ATLAS detector". In: *JHEP* 10 (2021), p. 013. DOI: 10.1007/JHEP10(2021)013. arXiv: 2104.13240 [hep-ex].

[17] ATLAS Collaboration. "Search for dark matter produced in association with a Standard Model Higgs boson decaying into b-quarks using the full Run 2 dataset from the ATLAS detector". In: *JHEP* 11 (2021), p. 209. DOI: 10.1007/JHEP11(2021)209. arXiv: 2108.13391 [hep-ex].

[18] CMS Collaboration. "Search for dark matter produced in association with a Higgs boson decaying to a pair of bottom quarks in proton-proton collisions at $\sqrt{s} = 13\,\text{TeV}$". In: *Eur. Phys. J. C* 79.3 (2019), p. 280. DOI: 10.1140/epjc/s10052-019-6730-7. arXiv: 1811.06562 [hep-ex].

[19] ATLAS Collaboration. "Search for associated production of a Z boson with an invisibly decaying Higgs boson or dark matter candidates at s=13 TeV with the ATLAS detector". In: *Phys. Lett. B* 829 (2022), p. 137066. DOI: 10.1016/j.physletb.2022.137066. arXiv: 2111.08372 [hep-ex].

[20] CMS Collaboration. "Search for dark matter produced in association with a leptonically decaying Z boson in proton-proton collisions at $\sqrt{s} = 13$ TeV". In: *Eur. Phys. J. C* 81.1 (2021). [Erratum: Eur.Phys.J.C 81, 333 (2021)], p. 13. DOI: 10.1140/epjc/s10052-020-08739-5. arXiv: 2008.04735 [hep-ex].

[21] ATLAS Collaboration. "Search for dark matter produced in association with a single top quark in $\sqrt{s} = 13$ TeV *pp* collisions with the ATLAS detector". In: *Eur. Phys. J. C* 81 (2021), p. 860. DOI: 10.1140/epjc/s10052-021-09566-y. arXiv: 2011.09308 [hep-ex].

[22] ATLAS Collaboration. *Search for dark matter produced in association with a single top quark and an energetic W boson in $\sqrt{s} = 13$ TeV (pp) collisions with the ATLAS detector*. Tech. rep. ATLAS-CONF-2022-012. 2022. URL: https://cds.cern.ch/record/2805216.

[23] ATLAS Collaboration. "The ATLAS Experiment at the CERN Large Hadron Collider". In: *JINST* 3 (2008), S08003. DOI: 10.1088/1748-0221/3/08/S08003.

[24] L. Evans and P. Bryant. "LHC Machine". In: *JINST* 3 (2008), S08001. DOI: 10.1088/1748-0221/3/08/S08001.

[25] R. L. Workman and others (Particle Data Group). "Review of Particle Physics". In: *Prog. Theor. Exp. Phys.* 2022 (2022), p. 083C01. DOI: 10.1093/ptep/ptac097.

[26] M. Baak et al. "HistFitter software framework for statistical data analysis". In: *Eur. Phys. J. C* 75 (2015), p. 153. DOI: 10.1140/epjc/s10052-015-3327-7. arXiv: 1410.1280 [hep-ex].

[27] L. Heinrich, M. Feickert and G. Stark. *pyhf*. Version 0.6.3. DOI: 10.5281/zenodo.1169739. URL: https://github.com/scikit-hep/pyhf/releases/tag/v0.6.3.

[28] L. Heinrich et al. "pyhf: pure-Python implementation of HistFactory statistical models". In: *J. Open Source Softw.* 6.58 (2021), p. 2823. DOI: 10.21105/joss.02823. URL: https://doi.org/10.21105/joss.02823.

[29] *The Standard Model*. 2012. URL: https://cds.cern.ch/record/1997201 (visited on 8th Oct. 2022).

[30] Y. Nambu. "Quasiparticles and Gauge Invariance in the Theory of Superconductivity". In: *Phys. Rev.* 117 (1960), pp. 648–663. DOI: 10.1103/PhysRev.117.648.

[31] J. Goldstone. "Field Theories with Superconductor Solutions". In: *Nuovo Cim.* 19 (1961), pp. 154–164. DOI: 10.1007/BF02812722.

[32] P. W. Higgs. "Broken symmetries, massless particles and gauge fields". In: *Phys. Lett.* 12 (1964), pp. 132–133. DOI: 10.1016/0031-9163(64)91136-9.

[33] F. Englert and R. Brout. "Broken Symmetry and the Mass of Gauge Vector Mesons". In: *Phys. Rev. Lett.* 13 (1964), pp. 321–323. DOI: 10.1103/PhysRevLett.13.321.

[34] G. S. Guralnik, C. R. Hagen and T. W. B. Kibble. "Global Conservation Laws and Massless Particles". In: *Phys. Rev. Lett.* 13 (1964), pp. 585–587. DOI: 10.1103/PhysRevLett.13.585.

[35] M. Thomson. *Modern Particle Physics*. Cambridge: Cambridge University Press, 2013.

[36] Super-Kamiokande Collaboration. "Evidence for oscillation of atmospheric neutrinos". In: *Phys. Rev. Lett.* 81 (1998), pp. 1562–1567. DOI: 10.1103/PhysRevLett.81.1562. arXiv: hep-ex/9807003.

[37] C. Burgard. *The SM of particle physics, Copyright CC BY 2.5*. URL: https://www.texample.net/tikz/examples/model-physics/ (visited on 29th Jan. 2018).

[38] M. E. Peskin and D. V. Schroeder. *An Introduction to quantum field theory*. Reading, USA: Addison-Wesley, 1995. ISBN: 978-0-201-50397-5.

[39] C. S. Wu et al. "Experimental Test of Parity Conservation in β Decay". In: *Phys. Rev.* 105 (1957), pp. 1413–1414. DOI: 10.1103/PhysRev.105.1413.

[40] M. Goldhaber, L. Grodzins and A. W. Sunyar. "Helicity of Neutrinos". In: *Phys. Rev.* 109 (1958), pp. 1015–1017. DOI: 10.1103/PhysRev.109.1015.

[41] N. Cabibbo. "Unitary Symmetry and Leptonic Decays". In: *Phys. Rev. Lett.* 10 (1963), pp. 531–533. DOI: 10.1103/PhysRevLett.10.531.

[42] M. Kobayashi and T. Maskawa. "CP Violation in the Renormalizable Theory of Weak Interaction". In: *Prog. Theor. Phys.* 49 (1973), pp. 652–657. DOI: 10.1143/PTP.49.652.

[43] L. H. Ryder. *Quantum Field Theory*. 2nd ed. Cambridge University Press, 1996. ISBN: 978-0-521-47814-4. DOI: 10.1017/CBO9780511813900.

[44] J. Riebesell. *Mexican Hat*. URL: https://tikz.net/mexican-hat/ (visited on 10th May 2022).

[45] ATLAS Collaboration. "Observation of a new particle in the search for the Standard Model Higgs boson with the ATLAS detector at the LHC". In: *Phys. Lett. B* 716 (2012), pp. 1–29. DOI: 10.1016/j.physletb.2012.08.020. arXiv: 1207.7214 [hep-ex].

[46] CMS Collaboration. "Observation of a New Boson at a Mass of 125 GeV with the CMS Experiment at the LHC". In: *Phys. Lett. B* 716 (2012), pp. 30–61. DOI: 10.1016/j.physletb.2012.08.021. arXiv: 1207.7235 [hep-ex].

[47] M. Botje. *Lecture notes Particle Physics II, Quantum Chromo Dynamics*. Lecture notes. 2013. URL: https://www.nikhef.nl/~h24/qcdcourse/section-all.pdf (visited on 30th May 2022).

[48] B. Andersson et al. "Parton Fragmentation and String Dynamics". In: *Phys. Rept.* 97 (1983), pp. 31–145. DOI: 10.1016/0370-1573(83)90080-7.

[49] Belle Collaboration. "Observation of a resonance-like structure in the $\pi^{\pm}\psi'$ mass distribution in exclusive $B \to K\pi^{\pm}\psi'$ decays". In: *Phys. Rev. Lett.* 100 (2008), p. 142001. DOI: 10.1103/PhysRevLett.100.142001. arXiv: 0708.1790 [hep-ex].

[50] Belle Collaboration. "Experimental constraints on the spin and parity of the $Z(4430)^+$". In: *Phys. Rev. D* 88.7 (2013), p. 074026. DOI: 10.1103/PhysRevD.88.074026. arXiv: 1306.4894 [hep-ex].

[51] LHCb Collaboration. "Observation of the resonant character of the $Z(4430)^-$ state". In: *Phys. Rev. Lett.* 112.22 (2014), p. 222002. DOI: 10.1103/PhysRevLett.112.222002. arXiv: 1404.1903 [hep-ex].

[52] LHCb Collaboration. "Observation of $J/\psi p$ Resonances Consistent with Pentaquark States in $\Lambda_b^0 \to J/\psi K^- p$ Decays". In: *Phys. Rev. Lett.* 115 (2015), p. 072001. DOI: 10.1103/PhysRevLett.115.072001. arXiv: 1507.03414 [hep-ex].

[53] M. Steinhauser. "Leptonic contribution to the effective electromagnetic coupling constant up to three loops". In: *Phys. Lett. B* 429 (1998), pp. 158–161. DOI: 10.1016/S0370-2693(98)00503-6. arXiv: hep-ph/9803313.

[54] H. Flacher et al. "Revisiting the Global Electroweak Fit of the Standard Model and Beyond with Gfitter". In: *Eur. Phys. J. C* 60 (2009). [Erratum: Eur.Phys.J.C 71, 1718 (2011)], pp. 543–583. DOI: 10.1140/epjc/s10052-009-0966-6. arXiv: 0811.0009 [hep-ph].

[55] J. Haller et al. "Update of the global electroweak fit and constraints on two-Higgs-doublet models". In: *Eur. Phys. J. C* 78.8 (2018), p. 675. DOI: 10.1140/epjc/s10052-018-6131-3. arXiv: 1803.01853 [hep-ph].

[56] V. N. Gribov and L. N. Lipatov. "e+ e- pair annihilation and deep inelastic e p scattering in perturbation theory". In: *Sov. J. Nucl. Phys.* 15 (1972), pp. 675–684.

[57] V. N. Gribov and L. N. Lipatov. "Deep inelastic e p scattering in perturbation theory". In: *Sov. J. Nucl. Phys.* 15 (1972), pp. 438–450.

[58] L. N. Lipatov. "The parton model and perturbation theory". In: *Yad. Fiz.* 20 (1974), pp. 181–198.

[59] Y. L. Dokshitzer. "Calculation of the Structure Functions for Deep Inelastic Scattering and e+ e- Annihilation by Perturbation Theory in Quantum Chromodynamics." In: *Sov. Phys. JETP* 46 (1977), pp. 641–653.

[60] G. Altarelli and G. Parisi. "Asymptotic Freedom in Parton Language". In: *Nucl. Phys. B* 126 (1977), pp. 298–318. DOI: 10.1016/0550-3213(77)90384-4.

[61] J. C. Collins, D. E. Soper and G. F. Sterman. "Factorization of Hard Processes in QCD". In: *Adv. Ser. Direct. High Energy Phys.* 5 (1989), pp. 1–91. DOI: 10.1142/9789814503266_0001. arXiv: hep-ph/0409313.

[62] A. Buckley et al. "General-purpose event generators for LHC physics". In: *Phys. Rept.* 504 (2011), pp. 145–233. DOI: 10.1016/j.physrep.2011.03.005. arXiv: 1101.2599 [hep-ph].

[63] C. Quigg. "Unanswered Questions in the Electroweak Theory". In: *Ann. Rev. Nucl. Part. Sci.* 59 (2009), pp. 505–555. DOI: 10.1146/annurev.nucl.010909.083126. arXiv: 0905.3187 [hep-ph].

[64] B. C. Allanach. "Beyond the Standard Model Lectures for the 2016 European School of High-Energy Physics". In: *2016 European School of High-Energy Physics*. 2017, pp. 123–152. DOI: 10.23730/CYRSP-2017-005.123. arXiv: 1609.02015 [hep-ph].

[65] A. D. Sakharov. "Violation of CP Invariance, C asymmetry, and baryon asymmetry of the universe". In: *Pisma Zh. Eksp. Teor. Fiz.* 5 (1967), pp. 32–35. DOI: 10.1070/PU1991v034n05ABEH002497.

[66] J. H. Christenson et al. "Evidence for the 2π Decay of the K_2^0 Meson". In: *Phys. Rev. Lett.* 13 (1964), pp. 138–140. DOI: 10.1103/PhysRevLett.13.138.

[67] Planck Collaboration. "Planck 2018 results. IV. Diffuse component separation". In: *Astron. Astrophys.* 641 (2020), A4. DOI: 10.1051/0004-6361/201833881. arXiv: 1807.06208 [astro-ph.CO].

[68] V. C. Rubin and W. K. Ford Jr. "Rotation of the Andromeda Nebula from a Spectroscopic Survey of Emission Regions". In: *Astrophys. J.* 159 (1970), pp. 379–403. DOI: 10.1086/150317.

[69] K. G. Begeman. "H I rotation curves of spiral galaxies. I - NGC 3198". In: *Astron. Astrophys.* 223 (1989), pp. 47–60.

[70] D. Walsh, R. F. Carswell and R. J. Weymann. "0957 + 561 A, B - Twin quasistellar objects or gravitational lens". In: *Nature* 279 (1979), pp. 381–384. DOI: 10.1038/279381a0.

[71] R. Massey, T. Kitching and J. Richard. "The dark matter of gravitational lensing". In: *Rept. Prog. Phys.* 73 (2010), p. 086901. DOI: 10.1088/0034-4885/73/8/086901. arXiv: 1001.1739 [astro-ph.CO].

[72] A. Einstein. "The Foundation of the General Theory of Relativity". In: *Annalen Phys.* 49.7 (1916), pp. 769–822. DOI: 10.1002/andp.19163540702.

[73] ESA/Hubble/NASA. Copyright. URL: https://apod.nasa.gov/apod/ap111221.html (visited on 2nd Mar. 2022).

[74] D. Clowe, A. Gonzalez and M. Markevitch. "Weak-Lensing Mass Reconstruction of the Interacting Cluster 1E 0657-558: Direct Evidence for the Existence of Dark Matter". In: *Astrophys. J.* 604.2 (2004), pp. 596–603. DOI: 10.1086/381970.

[75] D. Clowe et al. "A direct empirical proof of the existence of dark matter". In: *Astrophys. J. Lett.* 648 (2006), pp. L109–L113. DOI: 10.1086/508162. arXiv: astro-ph/0608407.

[76] C. S. Kochanek et al. "Clusters of galaxies in the local universe". In: *Astrophys. J.* 585 (2003), pp. 161–181. DOI: 10.1086/345896. arXiv: astro-ph/0208168.

[77] S. W. Allen, R. W. Schmidt and A. C. Fabian. "Cosmological constraints from the x-ray gas mass fraction in relaxed lensing clusters observed with Chandra". In: *Mon. Not. Roy. Astron. Soc.* 334 (2002), p. L11. DOI: 10.1046/j.1365-8711.2002.05601.x. arXiv: astro-ph/0205007.

[78] A. Vikhlinin et al. "Chandra sample of nearby relaxed galaxy clusters: Mass, gas fraction, and mass-temperature relation". In: *Astrophys. J.* 640 (2006), pp. 691–709. DOI: 10.1086/500288. arXiv: astro-ph/0507092.

[79] *NASA Finds Direct Proof of Dark Matter*. X-ray: NASA/CXC/CfA/M. Markevitch et al.; Optical: NASA/STScI; Magellan/U.Arizona/D. Clowe et al.; Lensing Map: NASA/STScI; ESO WFI; Magellan/U.Arizona/D. Clowe et al. URL: https://chandra.harvard.edu/photo/2006/1e0657/1e0657_scale.jpg (visited on 7th Mar. 2022).

[80] M. Schumann. "Direct Detection of WIMP Dark Matter: Concepts and Status". In: *J. Phys. G* 46.10 (2019), p. 103003. DOI: 10.1088/1361-6471/ab2ea5. arXiv: 1903.03026 [astro-ph.CO].

[81] D. J. Fixsen. "The Temperature of the Cosmic Microwave Background". In: *Astrophys. J.* 707 (2009), pp. 916–920. DOI: 10.1088/0004-637X/707/2/916. arXiv: 0911.1955 [astro-ph.CO].

[82] J. A. Tauber et al. "Planck Pre-Launch Status: The Planck Mission". In: *Astron. Astrophys.* 520 (2010), A1. DOI: 10.1051/0004-6361/200912983.

[83] C. Bambi and A. D. Dolgov. *Introduction to Particle Cosmology*. UNITEXT for Physics. Springer, 2015. ISBN: 978-3-662-48077-9. DOI: 10.1007/978-3-662-48078-6.

[84] D. Larson et al. "Seven-Year Wilkinson Microwave Anisotropy Probe (WMAP) Observations: Power Spectra and WMAP-Derived Parameters". In: *Astrophys. J. Suppl.* 192 (2011), p. 16. DOI: 10.1088/0067-0049/192/2/16. arXiv: 1001.4635 [astro-ph.CO].

[85] E. W. Kolb and M. S. Turner. "The Early Universe". In: *Front. Phys.* 69 (1990), pp. 1–547. DOI: 10.1201/9780429492860.

[86] B. J. Carr and S. W. Hawking. "Black holes in the early Universe". In: *Mon. Not. Roy. Astron. Soc.* 168 (1974), pp. 399–415.

[87] A. M. Green and B. J. Kavanagh. "Primordial Black Holes as a dark matter candidate". In: *J. Phys. G* 48.4 (2021), p. 043001. DOI: 10.1088/1361-6471/abc534. arXiv: 2007.10722 [astro-ph.CO].

[88] B. J. Kavanagh. *bradkav/PBHbounds: Release version*. Version 1.0. Nov. 2019. DOI: 10.5281/zenodo.3538999. URL: https://doi.org/10.5281/zenodo.3538999.

[89] V. Springel, C. S. Frenk and S. D. M. White. "The large-scale structure of the Universe". In: *Nature* 440 (2006), p. 1137. DOI: 10.1038/nature04805. arXiv: astro-ph/0604561.

[90] M. Boylan-Kolchin et al. "Resolving Cosmic Structure Formation with the Millennium-II Simulation". In: *Mon. Not. Roy. Astron. Soc.* 398 (2009), p. 1150. DOI: 10.1111/j.1365-2966.2009.15191.x. arXiv: 0903.3041 [astro-ph.CO].

[91] T. Di Matteo et al. "Direct cosmological simulations of the growth of black holes and galaxies". In: *Astrophys. J.* 676 (2008), p. 33. DOI: 10.1086/524921. arXiv: 0705.2269 [astro-ph].

[92] P. J. E. Peebles. "Large scale background temperature and mass fluctuations due to scale invariant primeval perturbations". In: *Astrophys. J. Lett.* 263 (1982), pp. L1–L5. DOI: 10.1086/183911.

[93] VIRGO Collaboration. "Evolution of structure in cold dark matter universes". In: *Astrophys. J.* 499 (1998), p. 20. DOI: 10.1086/305615. arXiv: astro-ph/9709010.

[94] G. R. Farrar. *A precision test of the nature of Dark Matter and a probe of the QCD phase transition*. 2018. arXiv: 1805.03723 [hep-ph].

[95] C. Gross et al. "Dark Matter in the Standard Model?" In: *Phys. Rev. D* 98.6 (2018), p. 063005. DOI: 10.1103/PhysRevD.98.063005. arXiv: 1803.10242 [hep-ph].

[96] R. D. Peccei and H. R. Quinn. "CP Conservation in the Presence of Pseudoparticles". In: *Phys. Rev. Lett.* 38 (1977), pp. 1440–1443. DOI: 10.1103/PhysRevLett.38.1440.

[97] K. Schmieden. "Searches for Axion Like Particles at the LHC". In: *Proc. Sci.* LHCP2021 (2021), p. 005. DOI: 10.22323/1.397.0005.

[98] ADMX Collaboration. "Extended Search for the Invisible Axion with the Axion Dark Matter Experiment". In: *Phys. Rev. Lett.* 124.10 (2020), p. 101303. DOI: 10.1103/PhysRevLett.124.101303. arXiv: 1910.08638 [hep-ex].

[99] K. Ehret et al. "New ALPS Results on Hidden-Sector Lightweights". In: *Phys. Lett. B* 689 (2010), pp. 149–155. DOI: 10.1016/j.physletb.2010.04.066. arXiv: 1004.1313 [hep-ex].

[100] S. Dodelson and L. M. Widrow. "Sterile-neutrinos as dark matter". In: *Phys. Rev. Lett.* 72 (1994), pp. 17–20. DOI: 10.1103/PhysRevLett.72.17. arXiv: hep-ph/9303287.

[101] ATLAS Collaboration. "Search for heavy neutral leptons in decays of W bosons produced in 13 TeV pp collisions using prompt and displaced signatures with the ATLAS detector". In: *JHEP* 10 (2019), p. 265. DOI: 10.1007/JHEP10(2019)265. arXiv: 1905.09787 [hep-ex].

[102] P. B. Denton. "Sterile Neutrino Search with MicroBooNE's Electron Neutrino Disappearance Data". In: *Phys. Rev. Lett.* 129.6 (2022), p. 061801. DOI: 10.1103/PhysRevLett.129.061801. arXiv: 2111.05793 [hep-ph].

[103] M. I. Vysotsky, A. D. Dolgov and Y. B. Zeldovich. "Cosmological Restriction on Neutral Lepton Masses". In: *JETP Lett.* 26 (1977), pp. 188–190.

[104] P. Hut. "Limits on Masses and Number of Neutral Weakly Interacting Particles". In: *Phys. Lett. B* 69 (1977), p. 85. DOI: 10.1016/0370-2693(77)90139-3.

[105] B. W. Lee and S. Weinberg. "Cosmological Lower Bound on Heavy Neutrino Masses". In: *Phys. Rev. Lett.* 39 (1977), pp. 165–168. DOI: 10.1103/PhysRevLett.39.165.

[106] G. Steigman and M. S. Turner. "Cosmological Constraints on the Properties of Weakly Interacting Massive Particles". In: *Nucl. Phys. B* 253 (1985), pp. 375–386. DOI: 10.1016/0550-3213(85)90537-1.

[107] E. W. Kolb and M. S. Turner. "The Early Universe". In: *Nature* 294 (1981), p. 521. DOI: 10.1038/294521a0.

[108] M. Srednicki, R. Watkins and K. A. Olive. "Calculations of Relic Densities in the Early Universe". In: *Nucl. Phys. B* 310 (1988), p. 693. DOI: 10.1016/0550-3213(88)90099-5.

[109] P. Gondolo and G. Gelmini. "Cosmic abundances of stable particles: Improved analysis". In: *Nucl. Phys. B* 360 (1991), pp. 145–179. DOI: 10.1016/0550-3213(91)90438-4.

[110] M. Milgrom. "A Modification of the Newtonian dynamics as a possible alternative to the hidden mass hypothesis". In: *Astrophys. J.* 270 (1983), pp. 365–370. DOI: 10.1086/161130.

[111] M. Milgrom. "A Modification of the Newtonian dynamics: Implications for galaxies". In: *Astrophys. J.* 270 (1983), pp. 371–383. DOI: 10.1086/161131.

[112] M. Milgrom. "A modification of the Newtonian dynamics: implications for galaxy systems". In: *Astrophys. J.* 270 (1983), pp. 384–389. DOI: 10.1086/161132.

[113] J. D. Bekenstein. "Relativistic gravitation theory for the MOND paradigm". In: *Phys. Rev. D* 70 (2004). [Erratum: Phys.Rev.D 71, 069901 (2005)], p. 083509. DOI: 10.1103/PhysRevD.70.083509. arXiv: astro-ph/0403694.

[114] B. Famaey and S. McGaugh. "Modified Newtonian Dynamics (MOND): Observational Phenomenology and Relativistic Extensions". In: *Living Rev. Rel.* 15 (2012), p. 10. DOI: 10.12942/lrr-2012-10. arXiv: 1112.3960 [astro-ph.CO].

[115] J. S. Bullock and M. Boylan-Kolchin. "Small-Scale Challenges to the ΛCDM Paradigm". In: *Ann. Rev. Astron. Astrophys.* 55 (2017), pp. 343–387. DOI: 10.1146/annurev-astro-091916-055313. arXiv: 1707.04256 [astro-ph.CO].

[116] A. Del Popolo. "Nonbaryonic Dark Matter in Cosmology". In: *Int. J. Mod. Phys. D* 23 (2014), p. 1430005. DOI: 10.1142/S0218271814300055. arXiv: 1305.0456 [astro-ph.CO].

[117] H. Baer et al. "Dark matter production in the early Universe: beyond the thermal WIMP paradigm". In: *Phys. Rept.* 555 (2015), pp. 1–60. DOI: 10.1016/j.physrep.2014.10.002. arXiv: 1407.0017 [hep-ph].

[118] M. Dutra. "Origins for dark matter particles : from the 'WIMP miracle' to the 'FIMP wonder'". PhD thesis. U. Paris Saclay (COmUE), 2019.

[119] SuperCDMS Collaboration. "Results from the Super Cryogenic Dark Matter Search Experiment at Soudan". In: *Phys. Rev. Lett.* 120.6 (2018), p. 061802. DOI: 10.1103/PhysRevLett.120.061802. arXiv: 1708.08869 [hep-ex].

[120] EDELWEISS Collaboration. "Constraints on low-mass WIMPs from the EDELWEISS-III dark matter search". In: *JCAP* 05 (2016), p. 019. DOI: 10.1088/1475-7516/2016/05/019. arXiv: 1603.05120 [astro-ph.CO].

[121] XENON Collaboration. "The XENON1T Dark Matter Experiment". In: *Eur. Phys. J. C* 77.12 (2017), p. 881. DOI: 10.1140/epjc/s10052-017-5326-3. arXiv: 1708.07051 [astro-ph.IM].

[122] LUX Collaboration. "The Large Underground Xenon (LUX) Experiment". In: *Nucl. Instrum. Meth. A* 704 (2013), pp. 111–126. DOI: 10.1016/j.nima.2012.11.135. arXiv: 1211.3788 [physics.ins-det].

[123] DAMA Collaboration. "The DAMA/LIBRA apparatus". In: *Nucl. Instrum. Meth. A* 592 (2008), pp. 297–315. DOI: 10.1016/j.nima.2008.04.082. arXiv: 0804.2738 [astro-ph].

[124] R. Bernabei et al. "First model independent results from DAMA/LIBRA-phase2". In: *Nucl. Phys. Atom. Energy* 19.4 (2018), pp. 307–325. DOI: 10.15407/jnpae2018.04.307. arXiv: 1805.10486 [hep-ex].

[125] K. K. Boddy et al. "Lines and Boxes: Unmasking Dynamical Dark Matter through Correlations in the MeV Gamma-Ray Spectrum". In: *Phys. Rev. D* 94.9 (2016), p. 095027. DOI: 10.1103/PhysRevD.94.095027. arXiv: 1606.07440 [hep-ph].

[126] Fermi-LAT Collaboration. "The Large Area Telescope on the Fermi Gamma-ray Space Telescope Mission". In: *Astrophys. J.* 697 (2009), pp. 1071–1102. DOI: 10.1088/0004-637X/697/2/1071. arXiv: 0902.1089 [astro-ph.IM].

[127] IceCube Collaboration. "The IceCube Neutrino Observatory: Instrumentation and Online Systems". In: *JINST* 12.03 (2017), P03012. DOI: 10.1088/1748-0221/12/03/P03012. arXiv: 1612.05093 [astro-ph.IM].

[128] Super-Kamiokande Collaboration. "The Super-Kamiokande detector". In: *Nucl. Instrum. Meth. A* 501 (2003), pp. 418–462. DOI: 10.1016/S0168-9002(03)00425-X.

[129] Super-Kamiokande Collaboration. "An Indirect Search for WIMPs in the Sun using 3109.6 days of upward-going muons in Super-Kamiokande". In: *Astrophys. J.* 742 (2011), p. 78. DOI: 10.1088/0004-637X/742/2/78. arXiv: 1108.3384 [astro-ph.HE].

[130] IceCube Collaboration. "Search for GeV-scale dark matter annihilation in the Sun with IceCube DeepCore". In: *Phys. Rev. D* 105.6 (2022), p. 062004. DOI: 10.1103/PhysRevD.105.062004. arXiv: 2111.09970 [astro-ph.HE].

[131] S. W. Barwick et al. "The high-energy antimatter telescope (HEAT): An instrument for the study of cosmic ray positrons". In: *Nucl. Instrum. Meth. A* 400 (1997), pp. 34–52. DOI: 10.1016/S0168-9002(97)00945-5.

[132] M. Boezio et al. "The space experiment PAMELA". In: *Nucl. Phys. B Proc. Suppl.* 134 (2004), pp. 39–46. DOI: 10.1016/j.nuclphysbps.2004.08.006.

[133] AMS Collaboration. "First Result from the Alpha Magnetic Spectrometer on the International Space Station: Precision Measurement of the Positron Fraction in Primary Cosmic Rays of 0.5-350 GeV". In: *Phys. Rev. Lett.* 110 (2013), p. 141102. DOI: 10.1103/PhysRevLett.110.141102.

[134] H.E.S.S. Collaboration. "H.E.S.S. contributions to the 28th international cosmic ray conference". In: *28th International Cosmic Ray Conference*. 2003. arXiv: astro-ph/0307452.

[135] J. J. Beatty et al. "New measurement of the cosmic-ray positron fraction from 5 to 15 GeV". In: *Phys. Rev. Lett.* 93 (2004), p. 241102. DOI: 10.1103/PhysRevLett.93.241102. arXiv: astro-ph/0412230.

[136] PAMELA Collaboration. "An anomalous positron abundance in cosmic rays with energies 1.5-100 GeV". In: *Nature* 458 (2009), pp. 607–609. DOI: 10.1038/nature07942. arXiv: 0810.4995 [astro-ph].

[137] H.E.S.S. Collaboration. "Probing the ATIC peak in the cosmic-ray electron spectrum with H.E.S.S". In: *Astron. Astrophys.* 508 (2009), p. 561. DOI: 10.1051/0004-6361/200913323. arXiv: 0905.0105 [astro-ph.HE].

[138] PAMELA Collaboration. "Cosmic-Ray Positron Energy Spectrum Measured by PAMELA". In: *Phys. Rev. Lett.* 111 (2013), p. 081102. DOI: 10.1103/PhysRevLett.111.081102. arXiv: 1308.0133 [astro-ph.HE].

[139] Fermi-LAT Collaboration. "Cosmic-ray electron-positron spectrum from 7 GeV to 2 TeV with the Fermi Large Area Telescope". In: *Phys. Rev. D* 95.8 (2017), p. 082007. DOI: 10.1103/PhysRevD.95.082007. arXiv: 1704.07195 [astro-ph.HE].

[140] AMS Collaboration. "Towards Understanding the Origin of Cosmic-Ray Positrons". In: *Phys. Rev. Lett.* 122.4 (2019), p. 041102. DOI: 10.1103/PhysRevLett.122.041102.

[141] V. V. Mikhailov et al. "Galactic Cosmic Ray Electrons and Positrons over a Decade of Observations in the PAMELA Experiment". In: *Bull. Russ. Acad. Sci. Phys.* 83.8 (2019), pp. 974–976. DOI: 10.3103/S1062873819080288.

[142] O. Buchmueller, C. Doglioni and L. T. Wang. "Search for dark matter at colliders". In: *Nature Phys.* 13.3 (2017), pp. 217–223. DOI: 10.1038/nphys4054. arXiv: 1912.12739 [hep-ex].

[143] ATLAS Collaboration. *Dark matter summary plots for s-channel, 2HDM+a and Dark Higgs models*. Tech. rep. ATL-PHYS-PUB-2022-036. 2022. URL: https://cds.cern.ch/record/2816368.

[144] H. Georgi. "Effective field theory". In: *Ann. Rev. Nucl. Part. Sci.* 43 (1993), pp. 209–252. DOI: 10.1146/annurev.ns.43.120193.001233.

[145] M. Beltran et al. "Maverick dark matter at colliders". In: *JHEP* 09 (2010), p. 037. DOI: 10.1007/JHEP09(2010)037. arXiv: 1002.4137 [hep-ph].

[146] Q.-H. Cao et al. "Effective Dark Matter Model: Relic density, CDMS II, Fermi LAT and LHC". In: *JHEP* 08 (2011), p. 018. DOI: 10.1007/JHEP08(2011)018. arXiv: 0912.4511 [hep-ph].

[147] J. Goodman et al. "Constraints on Light Majorana Dark Matter from Colliders". In: *Phys. Lett. B* 695 (2011), pp. 185–188. DOI: 10.1016/j.physletb.2010.11.009. arXiv: 1005.1286 [hep-ph].

[148] Y. Bai, P. J. Fox and R. Harnik. "The Tevatron at the Frontier of Dark Matter Direct Detection". In: *JHEP* 12 (2010), p. 048. DOI: 10.1007/JHEP12(2010)048. arXiv: 1005.3797 [hep-ph].

[149] J. Goodman et al. "Constraints on Dark Matter from Colliders". In: *Phys. Rev. D* 82 (2010), p. 116010. DOI: 10.1103/PhysRevD.82.116010. arXiv: 1008.1783 [hep-ph].

[150] P. J. Fox et al. "Missing Energy Signatures of Dark Matter at the LHC". In: *Phys. Rev. D* 85 (2012), p. 056011. DOI: 10.1103/PhysRevD.85.056011. arXiv: 1109.4398 [hep-ph].

[151] G. Busoni et al. "On the Validity of the Effective Field Theory for Dark Matter Searches at the LHC". In: *Phys. Lett. B* 728 (2014), pp. 412–421. DOI: 10.1016/j.physletb.2013.11.069. arXiv: 1307.2253 [hep-ph].

[152] G. Busoni et al. "On the Validity of the effective field theory for dark matter searches at the LHC, Part II: Complete analysis for the *s*-channel". In: *JCAP* 1406 (2014), p. 060. DOI: 10.1088/1475-7516/2014/06/060. arXiv: 1402.1275 [hep-ph].

[153] G. Busoni et al. "On the validity of the effective field theory for dark matter searches at the LHC Part III: analysis for the *t*-channel". In: *JCAP* 1409 (2014), p. 022. DOI: 10.1088/1475-7516/2014/09/022. arXiv: 1405.3101 [hep-ph].

[154] O. Buchmueller, M. J. Dolan and C. McCabe. "Beyond Effective Field Theory for Dark Matter Searches at the LHC". In: *JHEP* 01 (2014), p. 025. DOI: 10.1007/JHEP01(2014)025. arXiv: 1308.6799 [hep-ph].

[155] J. Abdallah et al. *Simplified Models for Dark Matter and Missing Energy Searches at the LHC*. Tech. rep. FERMILAB-FN-0990-PPD. 2014. arXiv: 1409.2893 [hep-ph].

[156] M. R. Buckley, D. Feld and D. Goncalves. "Scalar Simplified Models for Dark Matter". In: *Phys. Rev. D* 91 (2015), p. 015017. DOI: 10.1103/PhysRevD.91.015017. arXiv: 1410.6497 [hep-ph].

[157] J. Abdallah et al. "Simplified Models for Dark Matter Searches at the LHC". In: *Phys. Dark Univ.* 9-10 (2015), pp. 8–23. DOI: 10.1016/j.dark.2015.08.001. arXiv: 1506.03116 [hep-ph].

[158] D. Abercrombie et al. "Dark Matter benchmark models for early LHC Run-2 Searches: Report of the ATLAS/CMS Dark Matter Forum". In: *Phys. Dark Univ.* 27 (2020), p. 100371. DOI: 10.1016/j.dark.2019.100371. arXiv: 1507.00966 [hep-ex].

[159] F. Kahlhoefer et al. "Implications of unitarity and gauge invariance for simplified dark matter models". In: *JHEP* 02 (2016), p. 016. DOI: 10.1007/JHEP02(2016)016. arXiv: 1510.02110 [hep-ph].

[160] S. Ipek, D. McKeen and A. E. Nelson. "A Renormalizable Model for the Galactic Center Gamma Ray Excess from Dark Matter Annihilation". In: *Phys. Rev. D* 90.5 (2014), p. 055021. DOI: 10.1103/PhysRevD.90.055021. arXiv: 1404.3716 [hep-ph].

[161] J. M. No. "Looking through the pseudoscalar portal into dark matter: Novel mono-Higgs and mono-Z signatures at the LHC". In: *Phys. Rev. D* 93.3 (2016), p. 031701. DOI: 10.1103/PhysRevD.93.031701. arXiv: 1509.01110 [hep-ph].

[162] D. Goncalves, P. A. N. Machado and J. M. No. "Simplified Models for Dark Matter Face their Consistent Completions". In: *Phys. Rev. D* 95.5 (2017), p. 055027. DOI: 10.1103/PhysRevD.95.055027. arXiv: 1611.04593 [hep-ph].

[163] N. F. Bell, G. Busoni and I. W. Sanderson. "Self-consistent Dark Matter Simplified Models with an s-channel scalar mediator". In: *JCAP* 1703.03 (2017), p. 015. DOI: 10.1088/1475-7516/2017/03/015. arXiv: 1612.03475 [hep-ph].

[164] M. Bauer, M. Klassen and V. Tenorth. *Universal Properties of Pseudoscalar Mediators*. 2017. arXiv: 1712.06597 [hep-ph].

[165] U. Haisch and A. Malinauskas. "Let there be light from a second light Higgs doublet". In: *JHEP* 03 (2018), p. 135. DOI: 10.1007/JHEP03(2018)135. arXiv: 1712.06599 [hep-ph].

[166] G. Arcadi et al. "Pseudoscalar Mediators: A WIMP model at the Neutrino Floor". In: *JCAP* 03 (2018), p. 042. DOI: 10.1088/1475-7516/2018/03/042. arXiv: 1711.02110 [hep-ph].

[167] N. F. Bell, G. Busoni and I. W. Sanderson. "Two Higgs Doublet Dark Matter Portal". In: *JCAP* 1801.01 (2018), p. 015. DOI: 10.1088/1475-7516/2018/01/015. arXiv: 1710.10764 [hep-ph].

[168] T. D. Lee. "A Theory of Spontaneous T Violation". In: *Phys. Rev. D* 8 (1973), pp. 1226–1239. DOI: 10.1103/PhysRevD.8.1226.

[169] G. C. Branco et al. "Theory and phenomenology of two-Higgs-doublet models". In: *Phys. Rept.* 516 (2012), pp. 1–102. DOI: 10.1016/j.physrep.2012.02.002. arXiv: 1106.0034 [hep-ph].

[170] J. F. Gunion and H. E. Haber. "The CP conserving two Higgs doublet model: The Approach to the decoupling limit". In: *Phys. Rev. D* 67 (2003), p. 075019. DOI: 10.1103/PhysRevD.67.075019. arXiv: hep-ph/0207010 [hep-ph].

[171] S. L. Glashow and S. Weinberg. "Natural Conservation Laws for Neutral Currents". In: *Phys. Rev. D* 15 (1977), p. 1958. DOI: 10.1103/PhysRevD.15.1958.

[172] E. A. Paschos. "Diagonal Neutral Currents". In: *Phys. Rev. D* 15 (1977), p. 1966. DOI: 10.1103/PhysRevD.15.1966.

[173] ATLAS Collaboration. "Constraints on mediator-based dark matter and scalar dark energy models using $\sqrt{s} = 13$ TeV pp collision data collected by the ATLAS detector". In: *JHEP* 05 (2019), p. 142. DOI: 10.1007/JHEP05(2019)142. arXiv: 1903.01400 [hep-ex].

[174] ATLAS Collaboration. "Search for invisible Higgs-boson decays in events with vector-boson fusion signatures using 139 fb^{-1} of proton-proton data recorded by the ATLAS experiment". In: *JHEP* 08 (2022), p. 104. DOI: 10.1007/JHEP08(2022)104. arXiv: 2202.07953 [hep-ex].

[175] CMS Collaboration. "Search for invisible decays of the Higgs boson produced via vector boson fusion in proton-proton collisions at $\sqrt{s} = 13$ TeV". In: *Phys. Rev. D* 105 (2022), p. 092007. DOI: 10.1103/PhysRevD.105.092007. arXiv: 2201.11585 [hep-ex].

[176] S. Argyropoulos and U. Haisch. *Benchmarking LHC searches for light 2HDM+$\boldsymbol{a}$ pseudoscalars*. 2022. arXiv: 2202.12631 [hep-ph].

[177] U. Haisch and G. Polesello. "Searching for heavy Higgs bosons in the $t\bar{t}Z$ and tbW final states". In: *JHEP* 09 (2018), p. 151. DOI: 10.1007/JHEP09(2018)151. arXiv: 1807.07734 [hep-ph].

[178] C. F. Uhlemann and N. Kauer. "Narrow-width approximation accuracy". In: *Nucl. Phys. B* 814 (2009), pp. 195–211. DOI: 10.1016/j.nuclphysb.2009.01.022. arXiv: 0807.4112 [hep-ph].

[179] P. Pani and G. Polesello. "Dark matter production in association with a single top-quark at the LHC in a two-Higgs-doublet model with a pseudoscalar mediator". In: *Phys. Dark Univ.* 21 (2018), pp. 8–15. DOI: 10.1016/j.dark.2018.04.006. arXiv: 1712.03874 [hep-ph].

[180] G. Rovelli. "Searches for Dark Matter production in events with top quarks in the final state with the ATLAS detector at the LHC". PhD thesis. Pavia U., 2021.

[181] R. Assmann, M. Lamont and S. Myers. "A brief history of the LEP collider". In: *Nucl. Phys. B Proc. Suppl.* 109 (2002), pp. 17–31. DOI: 10.1016/S0920-5632(02)90005-8.

[182] E. Mobs. *The CERN accelerator complex - August 2018. Complexe des accélérateurs du CERN - Août 2018*. General Photo. 2018. URL: https://cds.cern.ch/record/2636343 (visited on 3rd June 2022).

[183] L. Arnaudon et al. *Linac4 Technical Design Report*. Tech. rep. CERN-AB-2006-084, CARE-Note-2006-022-HIPPI. 2006. URL: https://cds.cern.ch/record/1004186.

[184] J. Vollaire et al. *Linac4 design report*. Ed. by M. Vretenar. Vol. 6/2020. CERN Yellow Reports: Monographs. Geneva: CERN, 2020. ISBN: 978-92-9083-579-0. DOI: 10.23731/CYRM-2020-006.

[185] CMS Collaboration. "The CMS Experiment at the CERN LHC". In: *JINST* 3 (2008), S08004. DOI: 10.1088/1748-0221/3/08/S08004.

[186] LHCb Collaboration. "The LHCb Detector at the LHC". In: *JINST* 3 (2008), S08005. DOI: 10.1088/1748-0221/3/08/S08005.

[187] ALICE Collaboration. "The ALICE experiment at the CERN LHC". In: *JINST* 3 (2008), S08002. DOI: 10.1088/1748-0221/3/08/S08002.

[188] R. Alemany-Fernandez et al. *Operation and Configuration of the LHC in Run 1*. Tech. rep. 2013. URL: https://cds.cern.ch/record/1631030.

[189] J. Wenninger. *Operation and Configuration of the LHC in Run 2*. Tech. rep. 2019. URL: https://cds.cern.ch/record/2668326.

[190] *Large Hadron Collider restarts*. URL: https://home.web.cern.ch/news/news/accelerators/large-hadron-collider-restarts (visited on 8th June 2022).

[191] M. Schaumann et al. "First Xenon-Xenon Collisions in the LHC". In: *9th International Particle Accelerator Conference*. June 2018. DOI: 10.18429/JACoW-IPAC2018-MOPMF039.

[192] W. Herr and B. Muratori. "Concept of luminosity". In: *CERN Accelerator School at DESY Zeuthen: Accelerator Physics*. 2003, pp. 361–377.

[193] H. Burkhardt and P. Grafstrom. *Absolute luminosity from machine parameters*. Tech. rep. CERN-LHC-PROJECT-REPORT-1019. 2007. URL: https://cds.cern.ch/record/1056691/files/lhc-project-report-1019.pdf.

[194] S. van der Meer. *Calibration of the Effective Beam Height in the ISR*. Tech. rep. CERN-ISR-PO-68-31. 1968. URL: https://cds.cern.ch/record/296752.

[195] ATLAS Collaboration. "Luminosity Determination in *pp* Collisions at $\sqrt{s}$ = 7 TeV Using the ATLAS Detector at the LHC". In: *Eur. Phys. J. C* 71 (2011), p. 1630. DOI: 10.1140/epjc/s10052-011-1630-5. arXiv: 1101.2185 [hep-ex].

[196] ATLAS Collaboration. "Luminosity determination in pp collisions at $\sqrt{s}$ = 8 TeV using the ATLAS detector at the LHC". In: *Eur. Phys. J. C* 76.12 (2016), p. 653. DOI: 10.1140/epjc/s10052-016-4466-1. arXiv: 1608.03953 [hep-ex].

[197] ATLAS Collaboration. *Luminosity determination in pp collisions at $\sqrt{s} = 13$ TeV using the ATLAS detector at the LHC*. Tech. rep. ATLAS-CONF-2019-021. 2019. URL: https://cds.cern.ch/record/2677054.

[198] G. Avoni et al. "The new LUCID-2 detector for luminosity measurement and monitoring in ATLAS". In: *JINST* 13.07 (2018), P07017. DOI: 10.1088/1748-0221/13/07/P07017.

[199] ATLAS Collaboration. *Luminosity public results run-II*. URL: https://twiki.cern.ch/twiki/bin/view/AtlasPublic/LuminosityPublicResultsRun2 (visited on 3rd June 2022).

[200] ATLAS Collaboration. "ATLAS data quality operations and performance for 2015-2018 data-taking". In: *JINST* 15.04 (2020), P04003. DOI: 10.1088/1748-0221/15/04/P04003. arXiv: 1911.04632 [physics.ins-det].

[201] ATLAS Collaboration. *E_T^{miss} performance in the ATLAS detector using 2015-2016 LHC pp collisions*. Tech. rep. ATLAS-CONF-2018-023. 2018. URL: https://cds.cern.ch/record/2625233.

[202] P. Billoir and S. Qian. "Fast vertex fitting with a local parametrization of tracks". In: *Nucl. Instrum. Meth. A* 311 (1992), pp. 139–150. DOI: 10.1016/0168-9002(92)90859-3.

[203] ATLAS Collaboration. "ATLAS b-jet identification performance and efficiency measurement with $t\bar{t}$ events in pp collisions at $\sqrt{s} = 13$ TeV". In: *Eur. Phys. J. C* 79.11 (2019), p. 970. DOI: 10.1140/epjc/s10052-019-7450-8. arXiv: 1907.05120 [hep-ex].

[204] L. de Nooij. "The $\Phi(1020)$-meson production cross section measured with the ATLAS detector at $\sqrt{S}$ = 7 TeV". PhD thesis. U. Amsterdam, IHEF, 2014.

[205] ATLAS Collaboration. *Track Reconstruction Performance of the ATLAS Inner Detector at $\sqrt{s} = 13$ TeV*. Tech. rep. ATL-PHYS-PUB-2015-018. 2015. URL: https://cds.cern.ch/record/2037683.

[206] ATLAS Collaboration. *ATLAS Insertable B-Layer Technical Design Report*. Tech. rep. CERN-LHCC-2010-013, ATLAS-TDR-19. 2010. URL: https://cds.cern.ch/record/1291633.

[207] ATLAS Collaboration. *ATLAS Insertable B-Layer Technical Design Report Addendum*. Tech. rep. CERN-LHCC-2012-009, ATLAS-TDR-19-ADD-1. 2012. URL: https://cds.cern.ch/record/1451888.

[208] ATLAS IBL Collaboration. "Production and Integration of the ATLAS Insertable B-Layer". In: *JINST* 13.05 (2018), T05008. DOI: 10.1088/1748-0221/13/05/T05008. arXiv: 1803.00844 [physics.ins-det].

[209] ATLAS Collaboration. *Approved Plots of the Tracking Combined Performance Group*. Tech. rep. IDTR-2015-007. 2015. URL: https://atlas.web.cern.ch/Atlas/GROUPS/PHYSICS/PLOTS/IDTR-2015-007 (visited on 4th June 2022).

[210] ATLAS TRT Collaboration. "The ATLAS Transition Radiation Tracker (TRT) proportional drift tube: Design and performance". In: *JINST* 3 (2008), P02013. DOI: 10.1088/1748-0221/3/02/P02013.

[211] H. Kolanoski and N. Wermes. *Teilchendetektoren: Grundlagen und Anwendungen*. Springer, 2016. ISBN: 978-3-662-45349-0. DOI: 10.1007/978-3-662-45350-6.

[212] A. Artamonov et al. "The ATLAS forward calorimeters". In: *JINST* 3 (2008), P02010. DOI: 10.1088/1748-0221/3/02/P02010.

[213] ATLAS Collaboration. "Performance of the ATLAS Trigger System in 2015". In: *Eur. Phys. J. C* 77.5 (2017), p. 317. DOI: 10.1140/epjc/s10052-017-4852-3. arXiv: 1611.09661 [hep-ex].

[214] ATLAS Collaboration. "Operation of the ATLAS trigger system in Run 2". In: *JINST* 15.10 (2020), P10004. DOI: 10.1088/1748-0221/15/10/P10004. arXiv: 2007.12539 [physics.ins-det].

[215] T. Gleisberg et al. "Event generation with SHERPA 1.1". In: *JHEP* 02 (2009), p. 007. DOI: 10.1088/1126-6708/2009/02/007. arXiv: 0811.4622 [hep-ph].

[216] S. Catani et al. "QCD matrix elements + parton showers". In: *JHEP* 11 (2001), p. 063. DOI: 10.1088/1126-6708/2001/11/063. arXiv: hep-ph/0109231.

[217] S. Frixione and B. R. Webber. "Matching NLO QCD computations and parton shower simulations". In: *JHEP* 06 (2002), p. 029. DOI: 10.1088/1126-6708/2002/06/029. arXiv: hep-ph/0204244.

[218] S. Frixione, P. Nason and C. Oleari. "Matching NLO QCD computations with Parton Shower simulations: the POWHEG method". In: *JHEP* 11 (2007), p. 070. DOI: 10.1088/1126-6708/2007/11/070. arXiv: 0709.2092 [hep-ph].

[219] B. R. Webber. "A QCD Model for Jet Fragmentation Including Soft Gluon Interference". In: *Nucl. Phys. B* 238 (1984), pp. 492–528. DOI: 10.1016/0550-3213(84)90333-X.

[220] J. Alwall et al. "The automated computation of tree-level and next-to-leading order differential cross sections, and their matching to parton shower simulations". In: *JHEP* 07 (2014), p. 079. DOI: 10.1007/JHEP07(2014)079. arXiv: 1405.0301 [hep-ph].

[221] P. Nason. "A new method for combining NLO QCD with shower Monte Carlo algorithms". In: *JHEP* 11 (2004), p. 040. DOI: 10.1088/1126-6708/2004/11/040. arXiv: hep-ph/0409146.

[222] S. Alioli et al. "A general framework for implementing NLO calculations in shower Monte Carlo programs: the POWHEG BOX". In: *JHEP* 06 (2010), p. 043. DOI: 10.1007/JHEP06(2010)043. arXiv: 1002.2581 [hep-ph].

[223] T. Sjöstrand, S. Mrenna and P. Z. Skands. "A brief introduction to PYTHIA 8.1". In: *Comput. Phys. Commun.* 178 (2008), p. 852. DOI: 10.1016/j.cpc.2008.01.036. arXiv: 0710.3820 [hep-ph].

[224] M. Bahr et al. "Herwig++ Physics and Manual". In: *Eur. Phys. J. C* 58 (2008), pp. 639–707. DOI: 10.1140/epjc/s10052-008-0798-9. arXiv: 0803.0883 [hep-ph].

[225] J. Bellm et al. "Herwig 7.0/Herwig++ 3.0 release note". In: *Eur. Phys. J.* C76.4 (2016), p. 196. DOI: 10.1140/epjc/s10052-016-4018-8. arXiv: 1512.01178 [hep-ph].

[226] Sherpa Collaboration. "Event Generation with Sherpa 2.2". In: *SciPost Phys.* 7.3 (2019), p. 034. DOI: 10.21468/SciPostPhys.7.3.034. arXiv: 1905.09127 [hep-ph].

[227] J.-C. Winter, F. Krauss and G. Soff. "A Modified cluster hadronization model". In: *Eur. Phys. J. C* 36 (2004), pp. 381–395. DOI: 10.1140/epjc/s2004-01960-8. arXiv: hep-ph/0311085.

[228] ATLAS Collaboration. "The ATLAS Simulation Infrastructure". In: *Eur. Phys. J. C* 70 (2010), pp. 823–874. DOI: 10.1140/epjc/s10052-010-1429-9. arXiv: 1005.4568 [physics.ins-det].

[229] GEANT4 Collaboration. "GEANT4: A simulation toolkit". In: *Nucl. Instrum. Meth. A* 506 (2003), p. 250. DOI: 10.1016/S0168-9002(03)01368-8.

[230] C. Degrande et al. "UFO - The Universal FeynRules Output". In: *Comput. Phys. Commun.* 183 (2012), pp. 1201–1214. DOI: 10.1016/j.cpc.2012.01.022. arXiv: 1108.2040 [hep-ph].

[231] A. Alloul et al. "FeynRules 2.0 - A complete toolbox for tree-level phenomenology". In: *Comput. Phys. Commun.* 185 (2014), pp. 2250–2300. DOI: 10.1016/j.cpc.2014.04.012. arXiv: 1310.1921 [hep-ph].

[232] C. Degrande. "Automatic evaluation of UV and R2 terms for beyond the Standard Model Lagrangians: a proof-of-principle". In: *Comput. Phys. Commun.* 197 (2015), pp. 239–262. DOI: 10.1016/j.cpc.2015.08.015. arXiv: 1406.3030 [hep-ph].

[233] M. Bauer, U. Haisch and F. Kahlhoefer. *Two Higgs Doublet Model plus pseudoscalar extension UFO*. URL: https://github.com/LHC-DMWG/model-repository/tree/master/models/Pseudoscalar_2HDM (visited on 11th Oct. 2022).

[234] T. Sjöstrand, S. Mrenna and P. Z. Skands. "PYTHIA 6.4 Physics and Manual". In: *JHEP* 05 (2006), p. 026. DOI: 10.1088/1126-6708/2006/05/026. arXiv: hep-ph/0603175.

[235] T. Sjöstrand et al. "An introduction to PYTHIA 8.2". In: *Comput. Phys. Commun.* 191 (2015), pp. 159–177. DOI: 10.1016/j.cpc.2015.01.024. arXiv: 1410.3012 [hep-ph].

[236] NNPDF Collaboration. "Parton distributions for the LHC Run II". In: *JHEP* 04 (2015), p. 040. DOI: 10.1007/JHEP04(2015)040. arXiv: 1410.8849 [hep-ph].

[237] R. Harlander, M. Kramer and M. Schumacher. *Bottom-quark associated Higgs-boson production: reconciling the four- and five-flavour scheme approach*. Tech. rep. CERN-PH-TH-2011-134, FR-PHENO-2011-009, TTK-11-17, WUB-11-04. 2011. arXiv: 1112.3478 [hep-ph].

[238] S. Frixione et al. "Angular correlations of lepton pairs from vector boson and top quark decays in Monte Carlo simulations". In: *JHEP* 04 (2007), p. 081. DOI: 10.1088/1126-6708/2007/04/081. arXiv: hep-ph/0702198.

[239] P. Artoisenet et al. "Automatic spin-entangled decays of heavy resonances in Monte Carlo simulations". In: *JHEP* 03 (2013), p. 015. DOI: 10.1007/JHEP03(2013)015. arXiv: 1212.3460 [hep-ph].

[240] R. D. Ball et al. "Parton distributions with LHC data". In: *Nucl. Phys. B* 867 (2013), pp. 244–289. DOI: 10.1016/j.nuclphysb.2012.10.003. arXiv: 1207.1303 [hep-ph].

[241] ATLAS Collaboration. *ATLAS Pythia 8 tunes to 7 TeV data*. Tech. rep. ATL-PHYS-PUB-2014-021. 2014. URL: https://cds.cern.ch/record/1966419.

[242] D. J. Lange. "The EvtGen particle decay simulation package". In: *Nucl. Instrum. Meth. A* 462 (2001), pp. 152–155. DOI: 10.1016/S0168-9002(01)00089-4.

[243] O. Mattelaer. "On the maximal use of Monte Carlo samples: re-weighting events at NLO accuracy". In: *Eur. Phys. J. C* 76.12 (2016), p. 674. DOI: 10.1140/epjc/s10052-016-4533-7. arXiv: 1607.00763 [hep-ph].

[244] ATLAS Collaboration. "Search for dark matter produced in association with bottom or top quarks in $\sqrt{s} = 13$ TeV pp collisions with the ATLAS detector". In: *Eur. Phys. J. C* 78.1 (2018), p. 18. DOI: 10.1140/epjc/s10052-017-5486-1. arXiv: 1710.11412 [hep-ex].

[245] *Simplied DM model with (pseudo-)scalar mediator UFO*. URL: https://github.com/LHC-DMWG/model-repository/tree/master/models/HF_S%2BPS (visited on 11th Oct. 2022).

[246] M. Backovic et al. "Higher-order QCD predictions for dark matter production at the LHC in simplified models with s-channel mediators". In: *Eur. Phys. J. C* 75.10 (2015), p. 482. DOI: 10.1140/epjc/s10052-015-3700-6. arXiv: 1508.05327 [hep-ph].

[247] S. Schumann and F. Krauss. "A Parton shower algorithm based on Catani-Seymour dipole factorisation". In: *JHEP* 03 (2008), p. 038. DOI: 10.1088/1126-6708/2008/03/038. arXiv: 0709.1027 [hep-ph].

[248] S. Hoeche et al. "A critical appraisal of NLO+PS matching methods". In: *JHEP* 09 (2012), p. 049. DOI: 10.1007/JHEP09(2012)049. arXiv: 1111.1220 [hep-ph].

[249] S. Hoeche et al. "QCD matrix elements and truncated showers". In: *JHEP* 05 (2009), p. 053. DOI: 10.1088/1126-6708/2009/05/053. arXiv: 0903.1219 [hep-ph].

[250] S. Hoeche et al. "QCD matrix elements + parton showers: The NLO case". In: *JHEP* 04 (2013), p. 027. DOI: 10.1007/JHEP04(2013)027. arXiv: 1207.5030 [hep-ph].

[251] S. Frixione et al. "Single-top hadroproduction in association with a W boson". In: *JHEP* 07 (2008), p. 029. DOI: 10.1088/1126-6708/2008/07/029. arXiv: 0805.3067 [hep-ph].

[252] ATLAS Collaboration. *Studies on top-quark Monte Carlo modelling for Top2016*. Tech. rep. ATL-PHYS-PUB-2016-020. 2016. URL: https://cds.cern.ch/record/2216168.

[253] A. Denner, R. Feger and A. Scharf. "Irreducible background and interference effects for Higgs-boson production in association with a top-quark pair". In: *JHEP* 04 (2015), p. 008. DOI: 10.1007/JHEP04(2015)008. arXiv: 1412.5290 [hep-ph].

[254] O. Bessidskaia Bylund. "Top quark and heavy vector boson associated production at the ATLAS experiment : Modelling, measurements and effective field theory". PhD thesis. Stockholm U., 2017. ISBN: 978-91-7649-344-1.

[255] ATLAS Collaboration. *Modelling of rare top quark processes at $\sqrt{s} = 13$ TeV in ATLAS*. Tech. rep. ATL-PHYS-PUB-2020-024. 2020. URL: https://cds.cern.ch/record/2730584.

[256] ATLAS Collaboration. *The Pythia 8 A3 tune description of ATLAS minimum bias and inelastic measurements incorporating the Donnachie-Landshoff diffractive model*. Tech. rep. ATL-PHYS-PUB-2016-017. 2016. URL: https://cds.cern.ch/record/2206965.

[257] S. Frixione, P. Nason and G. Ridolfi. "A Positive-weight next-to-leading-order Monte Carlo for heavy flavour hadroproduction". In: *JHEP* 09 (2007), p. 126. DOI: 10.1088/1126-6708/2007/09/126. arXiv: 0707.3088 [hep-ph].

[258] M. Beneke et al. "Hadronic top-quark pair production with NNLL threshold resummation". In: *Nucl. Phys. B* 855 (2012), pp. 695–741. DOI: 10.1016/j.nuclphysb.2011.10.021. arXiv: 1109.1536 [hep-ph].

[259] M. Cacciari et al. "Top-pair production at hadron colliders with next-to-next-to-leading logarithmic soft-gluon resummation". In: *Phys. Lett. B* 710 (2012), pp. 612–622. DOI: 10.1016/j.physletb.2012.03.013. arXiv: 1111.5869 [hep-ph].

[260] P. Bärnreuther, M. Czakon and A. Mitov. "Percent Level Precision Physics at the Tevatron: First Genuine NNLO QCD Corrections to $q\bar{q} \to t\bar{t}+X$". In: *Phys. Rev. Lett.* 109 (2012), p. 132001. DOI: 10.1103/PhysRevLett.109.132001. arXiv: 1204.5201 [hep-ph].

[261] M. Czakon and A. Mitov. "NNLO corrections to top-pair production at hadron colliders: the all-fermionic scattering channels". In: *JHEP* 12 (2012), p. 054. DOI: 10.1007/JHEP12(2012)054. arXiv: 1207.0236 [hep-ph].

[262] M. Czakon and A. Mitov. "NNLO corrections to top pair production at hadron colliders: the quark-gluon reaction". In: *JHEP* 01 (2013), p. 080. DOI: 10.1007/JHEP01(2013)080. arXiv: 1210.6832 [hep-ph].

[263] M. Czakon, P. Fiedler and A. Mitov. "Total Top-Quark Pair-Production Cross Section at Hadron Colliders Through $O(\alpha_S^4)$". In: *Phys. Rev. Lett.* 110 (2013), p. 252004. DOI: 10.1103/PhysRevLett.110.252004. arXiv: 1303.6254 [hep-ph].

[264] M. Czakon and A. Mitov. "Top++: A Program for the Calculation of the Top-Pair Cross-Section at Hadron Colliders". In: *Comput. Phys. Commun.* 185 (2014), p. 2930. DOI: 10.1016/j.cpc.2014.06.021. arXiv: 1112.5675 [hep-ph].

[265] E. Re. "Single-top Wt-channel production matched with parton showers using the POWHEG method". In: *Eur. Phys. J. C* 71 (2011), p. 1547. DOI: 10.1140/epjc/s10052-011-1547-z. arXiv: 1009.2450 [hep-ph].

[266] R. Frederix, E. Re and P. Torrielli. "Single-top t-channel hadroproduction in the four-flavour scheme with POWHEG and aMC@NLO". In: *JHEP* 09 (2012), p. 130. DOI: 10.1007/JHEP09(2012)130. arXiv: 1207.5391 [hep-ph].

[267] S. Alioli et al. "NLO single-top production matched with shower in POWHEG: s- and t-channel contributions". In: *JHEP* 09 (2009). [Erratum: JHEP 02, 011 (2010)], p. 111. DOI: 10.1088/1126-6708/2009/09/111. arXiv: 0907.4076 [hep-ph].

[268] N. Kidonakis. "Two-loop soft anomalous dimensions for single top quark associated production with a W^- or H^-". In: *Phys. Rev. D* 82 (2010), p. 054018. DOI: 10.1103/PhysRevD.82.054018. arXiv: 1005.4451 [hep-ph].

[269] N. Kidonakis. "NNLL resummation for s-channel single top quark production". In: *Phys. Rev. D* 81 (2010), p. 054028. DOI: 10.1103/PhysRevD.81.054028. arXiv: 1001.5034 [hep-ph].

[270] N. Kidonakis. "Next-to-next-to-leading-order collinear and soft gluon corrections for t-channel single top quark production". In: *Phys. Rev. D* 83 (2011), p. 091503. DOI: 10.1103/PhysRevD.83.091503. arXiv: 1103.2792 [hep-ph].

[271] N. Kidonakis. "Top Quark Production". In: *Helmholtz International Summer School on Physics of Heavy Quarks and Hadrons*. 2014, pp. 139–168. DOI: 10.3204/DESY-PROC-2013-03/Kidonakis. arXiv: 1311.0283 [hep-ph].

[272] ATLAS Collaboration. *Modelling of the $t\bar{t}H$ and $t\bar{t}V$ ($V = W, Z$) processes for $\sqrt{s} = 13$ TeV ATLAS analyses*. Tech. rep. ATL-PHYS-PUB-2016-005. 2016. URL: https://cdsweb.cern.ch/record/2120826.

[273] D. de Florian et al. *Handbook of LHC Higgs Cross Sections: 4. Deciphering the Nature of the Higgs Sector*. Vol. 2/2017. CERN Yellow Reports: Monographs. Geneva: CERN, 2016. DOI: 10.23731/CYRM-2017-002. arXiv: 1610.07922 [hep-ph].

[274] ATLAS Collaboration. *ATLAS simulation of boson plus jets processes in Run 2*. Tech. rep. ATL-PHYS-PUB-2017-006. 2017. URL: https://cds.cern.ch/record/2261937.

[275] T. Gleisberg and S. Hoeche. "Comix, a new matrix element generator". In: *JHEP* 12 (2008), p. 039. DOI: 10.1088/1126-6708/2008/12/039. arXiv: 0808.3674 [hep-ph].

[276] F. Cascioli, P. Maierhofer and S. Pozzorini. "Scattering Amplitudes with Open Loops". In: *Phys. Rev. Lett.* 108 (2012), p. 111601. DOI: 10.1103/PhysRevLett.108.111601. arXiv: 1111.5206 [hep-ph].

[277] A. Denner, S. Dittmaier and L. Hofer. "Collier: a fortran-based Complex One-Loop LIbrary in Extended Regularizations". In: *Comput. Phys. Commun.* 212 (2017), pp. 220–238. DOI: 10.1016/j.cpc.2016.10.013. arXiv: 1604.06792 [hep-ph].

[278] F. Buccioni et al. "OpenLoops 2". In: *Eur. Phys. J. C* 79.10 (2019), p. 866. DOI: 10.1140/epjc/s10052-019-7306-2. arXiv: 1907.13071 [hep-ph].

[279] C. Anastasiou et al. "High precision QCD at hadron colliders: Electroweak gauge boson rapidity distributions at NNLO". In: *Phys. Rev. D* 69 (2004), p. 094008. DOI: 10.1103/PhysRevD.69.094008. arXiv: hep-ph/0312266.

[280] S. Catani et al. "Vector boson production at hadron colliders: a fully exclusive QCD calculation at NNLO". In: *Phys. Rev. Lett.* 103 (2009), p. 082001. DOI: 10.1103/PhysRevLett.103.082001. arXiv: 0903.2120 [hep-ph].

[281] ATLAS Collaboration. *Multi-Boson Simulation for 13 TeV ATLAS Analyses*. Tech. rep. ATL-PHYS-PUB-2017-005. 2017. URL: https://cds.cern.ch/record/2261933.

[282] H. B. Hartanto et al. "Higgs boson production in association with top quarks in the POWHEG BOX". In: *Phys. Rev. D* 91.9 (2015), p. 094003. DOI: 10.1103/PhysRevD.91.094003. arXiv: 1501.04498 [hep-ph].

[283] R. Frederix, D. Pagani and M. Zaro. "Large NLO corrections in $t\bar{t}W^{\pm}$ and $t\bar{t}t\bar{t}$ hadroproduction from supposedly subleading EW contributions". In: *JHEP* 02 (2018), p. 031. DOI: 10.1007/JHEP02(2018)031. arXiv: 1711.02116 [hep-ph].

[284] T. Cornelissen et al. *Concepts, Design and Implementation of the ATLAS New Tracking (NEWT)*. Tech. rep. ATL-SOFT-PUB-2007-007, ATL-COM-SOFT-2007-002. 2007. URL: https://cds.cern.ch/record/1020106.

[285] ATLAS Collaboration. "Muon reconstruction and identification efficiency in ATLAS using the full Run 2 *pp* collision data set at $\sqrt{s} = 13$ TeV". In: *Eur. Phys. J. C* 81.7 (2021), p. 578. DOI: 10.1140/epjc/s10052-021-09233-2. arXiv: 2012.00578 [hep-ex].

[286] ATLAS Collaboration. "Electron and photon performance measurements with the ATLAS detector using the 2015-2017 LHC proton-proton collision data". In: *JINST* 14.12 (2019), P12006. DOI: 10.1088/1748-0221/14/12/P12006. arXiv: 1908.00005 [hep-ex].

[287] ATLAS Collaboration. "Optimisation of large-radius jet reconstruction for the ATLAS detector in 13 TeV proton-proton collisions". In: *Eur. Phys. J. C* 81.4 (2021), p. 334. DOI: 10.1140/epjc/s10052-021-09054-3. arXiv: 2009.04986 [hep-ex].

[288] ATLAS Collaboration. "Performance of top-quark and W-boson tagging with ATLAS in Run 2 of the LHC". In: *Eur. Phys. J. C* 79.5 (2019), p. 375. DOI: 10.1140/epjc/s10052-019-6847-8. arXiv: 1808.07858 [hep-ex].

[289] ATLAS Collaboration. "Performance of the ATLAS Track Reconstruction Algorithms in Dense Environments in LHC Run 2". In: *Eur. Phys. J. C* 77.10 (2017), p. 673. DOI: 10.1140/epjc/s10052-017-5225-7. arXiv: 1704.07983 [hep-ex].

[290] R. Frühwirth. "Application of Kalman filtering to track and vertex fitting". In: *Nucl. Instrum. Meth. A* 262 (1987), pp. 444–450. DOI: 10.1016/0168-9002(87)90887-4.

[291] G. Piacquadio, K. Prokofiev and A. Wildauer. "Primary vertex reconstruction in the ATLAS experiment at LHC". In: *J. Phys. Conf. Ser.* 119 (2008), p. 032033. DOI: 10.1088/1742-6596/119/3/032033.

[292] ATLAS Collaboration. *Performance of primary vertex reconstruction in proton-proton collisions at $\sqrt{s}$ =7 TeV in the ATLAS experiment*. Tech. rep. ATLAS-CONF-2010-069. 2010. URL: https://cdsweb.cern.ch/record/1281344.

[293] ATLAS Collaboration. "Reconstruction of primary vertices at the ATLAS experiment in Run 1 proton-proton collisions at the LHC". In: *Eur. Phys. J. C* 77.5 (2017), p. 332. DOI: 10.1140/epjc/s10052-017-4887-5. arXiv: 1611.10235 [physics.ins-det].

[294] ATLAS Collaboration. *Vertex Reconstruction Performance of the ATLAS Detector at $\sqrt{s} = 13$ TeV*. Tech. rep. ATL-PHYS-PUB-2015-026. 2015. URL: https://cds.cern.ch/record/2037717.

[295] R. Frühwirth, W. Waltenberger and P. Vanlaer. "Adaptive vertex fitting". In: *J. Phys. G* 34 (2007), N343. DOI: 10.1088/0954-3899/34/12/N01.

[296] ATLAS Collaboration. "Topological cell clustering in the ATLAS calorimeters and its performance in LHC Run 1". In: *Eur. Phys. J. C* 77 (2017), p. 490. DOI: 10.1140/epjc/s10052-017-5004-5. arXiv: 1603.02934 [hep-ex].

[297] ATLAS Collaboration. "Electron reconstruction and identification in the ATLAS experiment using the 2015 and 2016 LHC proton-proton collision data at $\sqrt{s} = 13$ TeV". In: *Eur. Phys. J. C* 79.8 (2019), p. 639. DOI: 10.1140/epjc/s10052-019-7140-6. arXiv: 1902.04655 [physics.ins-det].

[298] ATLAS Collaboration. "Electron and photon energy calibration with the ATLAS detector using 2015-2016 LHC proton-proton collision data". In: *JINST* 14.03 (2019), P03017. DOI: 10.1088/1748-0221/14/03/P03017. arXiv: 1812.03848 [hep-ex].

[299] ATLAS Collaboration. "Muon reconstruction performance of the ATLAS detector in proton-proton collision data at $\sqrt{s}$ =13 TeV". In: *Eur. Phys. J. C* 76.5 (2016), p. 292. DOI: 10.1140/epjc/s10052-016-4120-y. arXiv: 1603.05598 [hep-ex].

[300] M. Cacciari, G. P. Salam and G. Soyez. "The anti-k_t jet clustering algorithm". In: *JHEP* 04 (2008), p. 063. DOI: 10.1088/1126-6708/2008/04/063. arXiv: 0802.1189 [hep-ph].

[301] G. Corcella et al. *HERWIG 6.5 release note*. Tech. rep. CAVENDISH-HEP-02-17, DAMTP-2002-124, KEK-TH-850, MPI-PHT-2002-55, CERN-TH-2002-270, IPPP-02-58, MC-TH-2002-7. 2002. arXiv: hep-ph/0210213.

[302] I. Neutelings. *Top jet*. URL: https://tikz.net/jet_top/ (visited on 23rd Aug. 2022).

[303] ATLAS Collaboration. "Jet reconstruction and performance using particle flow with the ATLAS Detector". In: *Eur. Phys. J. C* 77.7 (2017), p. 466. DOI: 10.1140/epjc/s10052-017-5031-2. arXiv: 1703.10485 [hep-ex].

[304] ATLAS Collaboration. "Jet energy scale and resolution measured in proton-proton collisions at $\sqrt{s} = 13$ TeV with the ATLAS detector". In: *Eur. Phys. J. C* 81.8 (2021), p. 689. DOI: 10.1140/epjc/s10052-021-09402-3. arXiv: 2007.02645 [hep-ex].

[305] ATLAS Collaboration. "Jet energy scale measurements and their systematic uncertainties in proton-proton collisions at $\sqrt{s} = 13$ TeV with the ATLAS detector". In: *Phys. Rev. D* 96.7 (2017), p. 072002. DOI: 10.1103/PhysRevD.96.072002. arXiv: 1703.09665 [hep-ex].

[306] M. Cacciari, G. P. Salam and G. Soyez. "FastJet user manual". In: *Eur. Phys. J. C* 72 (2012), p. 1896. DOI: 10.1140/epjc/s10052-012-1896-2. arXiv: 1111.6097 [hep-ph].

[307] ATLAS Collaboration. "Performance of pile-up mitigation techniques for jets in pp collisions at $\sqrt{s} = 8$ TeV using the ATLAS detector". In: *Eur. Phys. J. C* 76.11 (2016), p. 581. DOI: 10.1140/epjc/s10052-016-4395-z. arXiv: 1510.03823 [hep-ex].

[308] ATLAS Collaboration. *Forward jet vertex tagging using the particle flow algorithm*. Tech. rep. ATL-PHYS-PUB-2019-026. 2019. URL: https://cds.cern.ch/record/2683100.

[309] ATLAS Collaboration. "Identification and rejection of pile-up jets at high pseudorapidity with the ATLAS detector". In: *Eur. Phys. J. C* 77.9 (2017). [Erratum: Eur.Phys.J.C 77, 712 (2017)], p. 580. DOI: 10.1140/epjc/s10052-017-5081-5. arXiv: 1705.02211 [hep-ex].

[310] I. Neutelings. *B tagging jets*. URL: https://tikz.net/jet_btag/ (visited on 18th Aug. 2022).

[311] ATLAS Collaboration. *Optimisation and performance studies of the ATLAS b-tagging algorithms for the 2017-18 LHC run*. Tech. rep. ATL-PHYS-PUB-2017-013. 2017. URL: https://cds.cern.ch/record/2273281.

[312] ATLAS Collaboration. *Identification of Jets Containing b-Hadrons with Recurrent Neural Networks at the ATLAS Experiment*. Tech. rep. ATL-PHYS-PUB-2017-003. 2017. URL: https://cds.cern.ch/record/2255226.

[313] ATLAS Collaboration. *Secondary vertex finding for jet flavour identification with the ATLAS detector*. Tech. rep. ATL-PHYS-PUB-2017-011. 2017. URL: https://cds.cern.ch/record/2270366.

[314] ATLAS Collaboration. *Topological b-hadron decay reconstruction and identification of b-jets with the JetFitter package in the ATLAS experiment at the LHC*. Tech. rep. ATL-PHYS-PUB-2018-025. 2018. URL: https://cds.cern.ch/record/2645405.

[315] ATLAS Collaboration. *Expected performance of the 2019 ATLAS b-taggers*. Tech. rep. FTAG-2019-005. 2019. URL: https://atlas.web.cern.ch/Atlas/GROUPS/PHYSICS/PLOTS/FTAG-2019-005/.

[316] ATLAS Collaboration. "Measurement of the c-jet mistagging efficiency in $t\bar{t}$ events using pp collision data at $\sqrt{s} = 13$ TeV collected with the ATLAS detector". In: *Eur. Phys. J. C* 82.1 (2022), p. 95. DOI: 10.1140/epjc/s10052-021-09843-w. arXiv: 2109.10627 [hep-ex].

[317] ATLAS Collaboration. *Calibration of light-flavour jet b-tagging rates on ATLAS proton-proton collision data at $\sqrt{s} = 13$ TeV*. Tech. rep. ATLAS-CONF-2018-006. 2018. URL: https://cds.cern.ch/record/2314418.

[318] ATLAS Collaboration. "In situ calibration of large-radius jet energy and mass in 13 TeV proton-proton collisions with the ATLAS detector". In: *Eur. Phys. J. C* 79.2 (2019), p. 135. DOI: 10.1140/epjc/s10052-019-6632-8. arXiv: 1807.09477 [hep-ex].

[319] D. Krohn, J. Thaler and L.-T. Wang. "Jet Trimming". In: *JHEP* 02 (2010), p. 084. DOI: 10.1007/JHEP02(2010)084. arXiv: 0912.1342 [hep-ph].

[320] ATLAS Collaboration. "Performance of jet substructure techniques for large-R jets in proton-proton collisions at $\sqrt{s} = 7$ TeV using the ATLAS detector". In: *JHEP* 09 (2013), p. 076. DOI: 10.1007/JHEP09(2013)076. arXiv: 1306.4945 [hep-ex].

[321] S. D. Ellis and D. E. Soper. "Successive combination jet algorithm for hadron collisions". In: *Phys. Rev. D* 48 (1993), pp. 3160–3166. DOI: 10.1103/PhysRevD.48.3160. arXiv: hep-ph/9305266.

[322] ATLAS Collaboration. "Identification of boosted, hadronically decaying W bosons and comparisons with ATLAS data taken at $\sqrt{s} = 8$ TeV". In: *Eur. Phys. J. C* 76.3 (2016), p. 154. DOI: 10.1140/epjc/s10052-016-3978-z. arXiv: 1510.05821 [hep-ex].

[323] ATLAS Collaboration. *Jet mass reconstruction with the ATLAS Detector in early Run 2 data*. Tech. rep. ATLAS-CONF-2016-035. 2016. URL: https://cds.cern.ch/record/2200211.

[324] M. Cacciari and G. P. Salam. "Pileup subtraction using jet areas". In: *Phys. Lett. B* 659 (2008), pp. 119–126. DOI: 10.1016/j.physletb.2007.09.077. arXiv: 0707.1378 [hep-ph].

[325] M. Cacciari, G. P. Salam and G. Soyez. "The Catchment Area of Jets". In: *JHEP* 04 (2008), p. 005. DOI: 10.1088/1126-6708/2008/04/005. arXiv: 0802.1188 [hep-ph].

[326] ATLAS Collaboration. *Measurement of the ATLAS Detector Jet Mass Response using Forward Folding with 80 fb^{-1} of $\sqrt{s} = 13$ TeV pp data*. Tech. rep. ATLAS-CONF-2020-022. 2020. URL: https://cds.cern.ch/record/2724442.

[327] ATLAS Collaboration. "Search for high-mass diboson resonances with boson-tagged jets in proton-proton collisions at $\sqrt{s} = 8$ TeV with the ATLAS detector". In: *JHEP* 12 (2015), p. 055. DOI: 10.1007/JHEP12(2015)055. arXiv: 1506.00962 [hep-ex].

[328] A. J. Larkoski, G. P. Salam and J. Thaler. "Energy Correlation Functions for Jet Substructure". In: *JHEP* 06 (2013), p. 108. DOI: 10.1007/JHEP06(2013)108. arXiv: 1305.0007 [hep-ph].

[329] A. J. Larkoski, I. Moult and D. Neill. "Power Counting to Better Jet Observables". In: *JHEP* 12 (2014), p. 009. DOI: 10.1007/JHEP12(2014)009. arXiv: 1409.6298 [hep-ph].

[330] ATLAS Collaboration. *Boosted hadronic vector boson and top quark tagging with ATLAS using Run 2 data*. Tech. rep. ATL-PHYS-PUB-2020-017. 2020. URL: https://cds.cern.ch/record/2724149.

[331] J. Küchler. "Search for Partners of the Top Quark with the ATLAS Experiment". PhD thesis. Wuppertal U., 2018.

[332] ATLAS Collaboration. "Search for top-squark pair production in final states with one lepton, jets, and missing transverse momentum using 36 fb^{-1} of $\sqrt{s}$ = 13 TeV pp collision data with the ATLAS detector". In: *JHEP* 06 (2018), p. 108. DOI: 10.1007/JHEP06(2018)108. arXiv: 1711.11520 [hep-ex].

[333] ATLAS Collaboration. "Performance of the missing transverse momentum triggers for the ATLAS detector during Run-2 data taking". In: *JHEP* 08 (2020), p. 080. DOI: 10.1007/JHEP08(2020)080. arXiv: 2005.09554 [hep-ex].

[334] ATLAS Collaboration. *2015 start-up trigger menu and initial performance assessment of the ATLAS trigger using Run-2 data*. Tech. rep. ATL-DAQ-PUB-2016-001. 2016. URL: https://cds.cern.ch/record/2136007.

[335] ATLAS Collaboration. "Performance of electron and photon triggers in ATLAS during LHC Run 2". In: *Eur. Phys. J. C* 80.1 (2020), p. 47. DOI: 10.1140/epjc/s10052-019-7500-2. arXiv: 1909.00761 [hep-ex].

[336] ATLAS Collaboration. "Performance of the ATLAS muon triggers in Run 2". In: *JINST* 15.09 (2020), P09015. DOI: 10.1088/1748-0221/15/09/p09015. arXiv: 2004.13447 [physics.ins-det].

[337] ROOT Collaboration. *HistFactory: A tool for creating statistical models for use with RooFit and RooStats*. Tech. rep. CERN-OPEN-2012-016. 2012. URL: https://cds.cern.ch/record/1456844.

[338] G. Cowan et al. "Asymptotic formulae for likelihood-based tests of new physics". In: *Eur. Phys. J. C* 71 (2011). [Erratum: Eur.Phys.J.C 73, 2501 (2013)], p. 1554. DOI: 10.1140/epjc/s10052-011-1554-0. arXiv: 1007.1727 [physics.data-an].

[339] T. Junk. "Confidence level computation for combining searches with small statistics". In: *Nucl. Instrum. Meth. A* 434 (1999), pp. 435–443. DOI: 10.1016/S0168-9002(99)00498-2. arXiv: hep-ex/9902006.

[340] A. L. Read. "Modified frequentist analysis of search results (The CL(s) method)". In: *Workshop on Confidence Limits*. 2000, pp. 81–101. DOI: 10.5170/CERN-2000-005.

[341] A. L. Read. "Presentation of search results: The CL_S technique". In: *J. Phys. G* 28 (2002), pp. 2693–2704. DOI: 10.1088/0954-3899/28/10/313.

[342] ATLAS, CMS, LHC Higgs Combination Group Collaboration. *Procedure for the LHC Higgs boson search combination in Summer 2011*. Tech. rep. CMS-NOTE-2011-005, ATL-PHYS-PUB-2011-011. 2011. URL: https://cds.cern.ch/record/1379837/.

[343] ATLAS Collaboration. "Combined search for the Standard Model Higgs boson in *pp* collisions at $\sqrt{s}$ = 7 TeV with the ATLAS detector". In: *Phys. Rev. D* 86 (2012), p. 032003. DOI: 10.1103/PhysRevD.86.032003. arXiv: 1207.0319 [hep-ex].

[344] A. Armbruster. "Discovery of a Higgs Boson with the ATLAS Detector". PhD thesis. Michigan U., 2013.

[345] S. Williams. "Searching for weakly produced supersymmetric particles using the ATLAS detector at the LHC". PhD thesis. Cambridge U., 2013.

[346] R. D. Cousins, J. T. Linnemann and J. Tucker. "Evaluation of three methods for calculating statistical significance when incorporating a systematic uncertainty into a test of the background-only hypothesis for a Poisson process". In: *Nucl. Instrum. Meth. A* 595.2 (2008), pp. 480–501. DOI: 10.1016/j.nima.2008.07.086. arXiv: physics/0702156.

[347] ATLAS Collaboration. *Formulae for Estimating Significance*. Tech. rep. ATL-PHYS-PUB-2020-025. 2020. URL: https://cds.cern.ch/record/2736148.

[348] ATLAS Collaboration. "Search for new phenomena with top quark pairs in final states with one lepton, jets, and missing transverse momentum in pp collisions at $\sqrt{s} = 13$ TeV with the ATLAS detector". In: *JHEP* 04 (2021), p. 174. DOI: 10.1007/JHEP04(2021)174. arXiv: 2012.03799 [hep-ex].

[349] P. C. Bhat et al. "Optimizing Event Selection with the Random Grid Search". In: *Comput. Phys. Commun.* 228 (2018), pp. 245–257. DOI: 10.1016/j.cpc.2018.02.018. arXiv: 1706.09907 [hep-ph].

[350] K. Sastry, D. Goldberg and G. Kendall. "Genetic Algorithms". In: *Search Methodologies: Introductory Tutorials in Optimization and Decision Support Techniques*. Ed. by E. K. Burke and G. Kendall. Boston, MA: Springer US, 2005, pp. 97–125. ISBN: 978-0-387-28356-2. DOI: 10.1007/0-387-28356-0_4.

[351] F. Jorge et al. *Top squark signal significance enhancement by different Machine Learning Algorithms*. 2021. arXiv: 2106.06813 [hep-ph].

[352] ATLAS Collaboration. "Measurements of the top quark branching ratios into channels with leptons and quarks with the ATLAS detector". In: *Phys. Rev. D* 92.7 (2015), p. 072005. DOI: 10.1103/PhysRevD.92.072005. arXiv: 1506.05074 [hep-ex].

[353] G. Brooijmans et al. *Les Houches 2017: Physics at TeV Colliders New Physics Working Group Report*. FERMILAB-CONF-17-664-PPD. 2018. arXiv: 1803.10379 [hep-ph].

[354] P. Konar et al. "Dark Matter Particle Spectroscopy at the LHC: Generalizing MT2 to Asymmetric Event Topologies". In: *JHEP* 04 (2010), p. 086. DOI: 10.1007/JHEP04(2010)086. arXiv: 0911.4126 [hep-ph].

[355] C. G. Lester and B. Nachman. "Bisection-based asymmetric M_{T2} computation: a higher precision calculator than existing symmetric methods". In: *JHEP* 03 (2015), p. 100. DOI: 10.1007/JHEP03(2015)100. arXiv: 1411.4312 [hep-ph].

[356] C. Lester and D. Summers. "Measuring masses of semi-invisibly decaying particles pair produced at hadron colliders". In: *Phys. Lett.* B 463 (1999), pp. 99–103. DOI: 10.1016/S0370-2693(99)00945-4. arXiv: hep-ph/9906349.

[357] A. Barr, C. Lester and P. Stephens. "m_T2: the truth behind the glamour". In: *J. Phys. G* 29 (2003), pp. 2343–2363. DOI: 10.1088/0954-3899/29/10/304. arXiv: hep-ph/0304226.

[358] ATLAS Collaboration. *Object-based missing transverse momentum significance in the ATLAS detector*. Tech. rep. ATLAS-CONF-2018-038. ATLAS-CONF-2018-038. 2018. URL: https://cds.cern.ch/record/2630948.

[359] ATLAS Collaboration. "Search for a scalar partner of the top quark in the all-hadronic $t\bar{t}$ plus missing transverse momentum final state at $\sqrt{s} = 13$ TeV with the ATLAS detector". In: *Eur. Phys. J. C* 80.8 (2020), p. 737. DOI: 10.1140/epjc/s10052-020-8102-8. arXiv: 2004.14060 [hep-ex].

[360] ATLAS Collaboration. "Measurement of the $t\bar{t}$ production cross-section and lepton differential distributions in $e\mu$ dilepton events from pp collisions at $\sqrt{s} = 13\,\text{TeV}$ with the ATLAS detector". In: *Eur. Phys. J. C* 80.6 (2020), p. 528. DOI: 10.1140/epjc/s10052-020-7907-9. arXiv: 1910.08819 [hep-ex].

[361] ATLAS Collaboration. "Search for new phenomena in events with two opposite-charge leptons, jets and missing transverse momentum in pp collisions at $\sqrt{s}$ = 13 TeV with the ATLAS detector". In: *JHEP* 04 (2021), p. 165. DOI: 10.1007/JHEP04(2021)165. arXiv: 2102.01444 [hep-ex].

[362] ATLAS Collaboration. "Measurements of the inclusive and differential production cross sections of a top-quark-antiquark pair in association with a Z boson at $\sqrt{s} = 13$ TeV with the ATLAS detector". In: *Eur. Phys. J. C* 81.8 (2021), p. 737. DOI: 10.1140/epjc/s10052-021-09439-4. arXiv: 2103.12603 [hep-ex].

[363] U. Haisch and G. Polesello. "Searching for production of dark matter in association with top quarks at the LHC". In: *JHEP* 02 (2019), p. 029. DOI: 10.1007/JHEP02(2019)029. arXiv: 1812.00694 [hep-ph].

[364] ATLAS Collaboration. "Measurement of the top quark-pair production cross section with ATLAS in pp collisions at $\sqrt{s} = 7$ TeV". In: *Eur. Phys. J. C* 71 (2011), p. 1577. DOI: 10.1140/epjc/s10052-011-1577-6. arXiv: 1012.1792 [hep-ex].

[365] ATLAS Collaboration. "Measurement of the top quark pair production cross section in pp collisions at $\sqrt{s} = 7$ TeV in dilepton final states with ATLAS". In: *Phys. Lett. B* 707 (2012), pp. 459–477. DOI: 10.1016/j.physletb.2011.12.055. arXiv: 1108.3699 [hep-ex].

[366] ATLAS Collaboration. "Search for dark matter in events with a hadronically decaying vector boson and missing transverse momentum in pp collisions at $\sqrt{s} = 13$ TeV with the ATLAS detector". In: *JHEP* 10 (2018), p. 180. DOI: 10.1007/JHEP10(2018)180. arXiv: 1807.11471 [hep-ex].

[367] ATLAS Collaboration. *Combination and summary of ATLAS dark matter searches using 139 fb-1 of $\sqrt{s}$ = 13 TeV p p collision data and interpreted in a two-Higgs-doublet model with a pseudoscalar mediator*. Tech. rep. ATLAS-CONF-2021-036. 2021. URL: https://cds.cern.ch/record/2777863.

[368] ATLAS Collaboration. *Dark matter summary plots for s-channel and 2HDM+a models*. Tech. rep. ATL-PHYS-PUB-2021-045. 2021. URL: https://cds.cern.ch/record/2798737.

[369] ATLAS Collaboration. "Search for charged Higgs bosons decaying into a top quark and a bottom quark at $\sqrt{s} = 13$ TeV with the ATLAS detector". In: *JHEP* 06 (2021), p. 145. DOI: 10.1007/JHEP06(2021)145. arXiv: 2102.10076 [hep-ex].

[370] ATLAS Collaboration. *Combination of searches for invisible Higgs boson decays with the ATLAS experiment*. Tech. rep. ATLAS-CONF-2020-052. 2020. URL: https://cds.cern.ch/record/2743055.

[371] ATLAS Collaboration. "Searches for scalar leptoquarks and differential cross-section measurements in dilepton-dijet events in proton-proton collisions at a centre-of-mass energy of $\sqrt{s} = 13$ TeV with the ATLAS experiment". In: *Eur. Phys. J. C* 79.9 (2019), p. 733. DOI: 10.1140/epjc/s10052-019-7181-x. arXiv: 1902.00377 [hep-ex].

[372] ATLAS Collaboration. *Measurements of W^+W^- production in decay topologies inspired by searches for electroweak supersymmetry*. CERN-EP-2022-087. 2022. arXiv: 2206.15231 [hep-ex].

[373] J. M. Butterworth et al. "Constraining new physics with collider measurements of Standard Model signatures". In: *JHEP* 03 (2017), p. 078. DOI: 10.1007/JHEP03(2017)078. arXiv: 1606.05296 [hep-ph].

[374] A. Buckley et al. "Testing new physics models with global comparisons to collider measurements: the Contur toolkit". In: *SciPost Phys. Core* 4 (2021), p. 013. DOI: 10.21468/SciPostPhysCore.4.2.013. arXiv: 2102.04377 [hep-ph].

[375] I. Zurbano Fernandez et al. *High-Luminosity Large Hadron Collider (HL-LHC): Technical design report*. Ed. by I. Béjar Alonso et al. Vol. 10/2020. CERN Yellow Reports: Monographs. Geneva: CERN, 2020. DOI: 10.23731/CYRM-2020-0010.

[376] A. Dainese et al., eds. *Report on the Physics at the HL-LHC,and Perspectives for the HE-LHC*. Vol. 7/2019. CERN Yellow Reports: Monographs. Geneva: CERN, 2019. ISBN: 978-92-9083-549-3. DOI: 10.23731/CYRM-2019-007.

[377] ATLAS and CMS Collaboration. *Addendum to the report on the physics at the HL-LHC, and perspectives for the HE-LHC: Collection of notes from ATLAS and CMS*. Vol. 7. CERN Yellow Reports: Monographs. Geneva: CERN, 2019, Addendum. DOI: 10.23731/CYRM-2019-007.Addendum. arXiv: 1902.10229 [hep-ex].

[378] "IPCC, 2021: Summary for Policymakers". In: *Climate Change 2021: The Physical Science Basis. Contribution of Working Group I to the Sixth Assessment Report of the Intergovernmental Panel on Climate Change*. Ed. by V. Masson-Delmotte et al. Cambridge University Press. DOI: 10.1017/9781009157896.001. URL: https://www.ipcc.ch/report/ar6/wg1/downloads/report/IPCC_AR6_WGI_SPM.pdf (visited on 9th Sept. 2022).

[379] U.S. Environmental Protection Agency. *Definition of CO2e*. URL: https://www3.epa.gov/carbon-footprint-calculator/tool/definitions/co2e.html (visited on 9th Sept. 2022).

[380] K. Bloom et al. "Climate impacts of particle physics". In: *2022 Snowmass Summer Study*. Mar. 2022. arXiv: 2203.12389 [physics.soc-ph].

[381] K. Bos et al. *LHC computing Grid. Technical design report*. Tech. rep. CERN-LHCC-2005-024. 2005. URL: https://cds.cern.ch/record/840543.

[382] ATLAS Collaboration. "PanDA: Distributed production and distributed analysis system for ATLAS". In: *J. Phys. Conf. Ser.* 119 (2008), p. 062036. DOI: 10.1088/1742-6596/119/6/062036.

[383] ATLAS Collaboration. "ATLAS WORLD-cloud and networking in PanDA". In: *J. Phys. Conf. Ser.* 898.5 (2017), p. 052011. DOI: 10.1088/1742-6596/898/5/052011.

[384] D. Thain, T. Tannenbaum and M. Livny. "Distributed computing in practice: the Condor experience." In: *Concurrency - Practice and Experience* 17.2-4 (2005), pp. 323–356.

[385] L. Lannelongue, J. Grealey and M. Inouye. "Green Algorithms: Quantifying the Carbon Footprint of Computation". In: *Adv. Sci.* 8.12 (2021), p. 2100707. DOI: 10.1002/advs.202100707.

[386] *Kibana Dashboard*. URL: https://atlas-kibana.mwt2.org/app/dashboards#/view/00a4a6d0-24f9-11ec-bc4b-6bc59948c109 (visited on 9th Sept. 2022).

[387] *Electricity Maps*. URL: https://app.electricitymaps.com (visited on 12th Sept. 2022).

[388] *CO_2 Emissions Calculator*. URL: https://www.carboncare.org/en/co2-emissions-calculator.html (visited on 9th Sept. 2022).

[389] M. Schelewsky, R. Follmer and C. Dickmann. *CO2-Fußabdrücke im Alltagsverkehr*. 224/2020. 2020. URL: https://www.umweltbundesamt.de/publikationen/co2-fussabdruecke-im-alltagsverkehr (visited on 9th Sept. 2022).

[390] *CERN Environment Report*. Vol. 2. CERN Environment Report. 2021. DOI: 10.25325/CERN-Environment-2021-002.

Appendix A

Thesis work CO_2e emission

The anthropological emission of greenhouse gases causes an increase of the average temperature on planet earth [378]. This global warming poses a threat to many species inhabiting the planet. The global warming will cause the sea-level to rise, increase the risk of extreme weather events such as flooding or drought and may potentially reduce the crop yields. The more the global temperature increases, the stronger the mentioned effects will likely impact all species on the planet, among them humans. It is therefore paramount to keep the temperature increase with respect to the pre-industrial era as small as possible. As immediate net-zero emissions are not feasible, two scenarios of the global temperature increase are currently under consideration: a temperature increase below 1.5 °C and a temperature increase below 2 °C. Both necessitate a significant reduction of greenhouse gas emissions in the upcoming years. For a temperature increase below 1.5 °C, the greenhouse gas emissions, quantified in CO_2e units[1], must, with a confidence of 83 %, be reduced to below roughly 1.1 t CO_2e per person per year from now until 2050 [378, 380].

The CO_2e emissions of the work performed in this thesis are evaluated in this appendix. Only direct emissions from the author due to the use of computers, servers and computing grids are considered. The emissions arise from producing datasets and samples of reduced sizes ("ntuple production"), the statistical analysis of the tW+DM search, the combination of the 0L, 1L and 2L channel regions as well as the usage of individual personal and network computers to produce plots and presentations and to optimise the tW+DM search regions. In addition, emissions due to long-distance travelling (> 150 km) are considered as a comparison. Emissions from other sources, e.g. due to the computer usage of other people involved in the tW+DM search, the production of the full-size samples, earlier sample size reductions ("DAOD"), the detector and accelerator operation, office and laboratory infrastructure and operation, etc., are not accounted for. The aim of this appendix is to draw attention to the greenhouse gas emissions that are produced directly from the work of a single PhD student.

The following CO_2e emitting sources are accounted for:

- "grid computing": the production of smaller size samples from larger size ones ("ntuple production") was conducted using the Worldwide LHC computing grid (WLCG) [381], accessed via the Production and Distributed Analysis system (`PanDA`) [382, 383].
- "batch system": the statistical analysis of the tW+DM analysis and the combination of the 0L, 1L and 2L channels was carried out on the DESY computer

[1] CO_2e abbreviates CO_2 equivalent and is the amount of greenhouse gas emitted with the same global warming potential as one metric ton of CO_2 [379]. It is calculated according to Equation A-1 in 40 CFR Part 98.

cluster batch system. It was accessed via the `HTCondor` software [384].

- "local computing": summarises all the sources originating from the usage of the personal computer and from using DESY network computers to produce e.g. plots and presentations, as well as used to define the search regions.

The CO_2e emissions are estimated by determining the single-core CPU usage time of the described sources. The power consumption due to the non-stop availability of the grid and network resources is not accounted for. The obtained usage times are input into the `Green Algorithms` tool [385] version 2.1, assuming a generic, single-core CPU (setting "any") and a RAM of 2 GB per computer. Note that the CO_2e emission increases with the size of the RAM and given that many computers have a RAM greater than 2 GB, the estimate gives a lower bound of the greenhouse gas emissions.

The particularities of calculating the CO_2e emissions of the grid computing are discussed in the following. The grid computing executes computing jobs on servers all over the world. The CO_2e emissions depend on the power-station infrastructure ("energy mix") in the different countries in which the jobs are executed. For example, a high fraction of electricity produced by coal-fired power-stations leads to a large CO_2e emission per usage hour of a single-core CPU compared to a high fraction of electricity from renewable sources. The single-core computing time is therefore determined per country for the grid computing. The computing time per country in the PhD time of the author is obtained using the webpage in Reference [386] and input into the `Green Algorithms` [385] tool to obtain CO_2e emissions per country. The average energy mix per country is used in the CO_2e calculation, opposed to e.g. a further division into (federal) states or provinces. Note that this assumption comes with a high uncertainty. If assuming that all the grid computers in the United States were situated in California for example, the CO_2e emissions of the thesis work from the grid computers in the United States are reduced by more than 50 % from $\simeq$ 21 t to $\simeq$ 9 t. A breakdown of the grid computing emissions of the thesis work per country is shown in Table A.1. The highest emissions stem from the grid computing jobs executed in the United States, which sum to 20.91 t of CO_2e with a single-core CPU usage of 329.9 y. The emissions caused by grid computers in Germany are roughly 4.5 times higher than the ones caused in France, even though the CPU usage time is roughly double in France. This is due to the energy mix in France being dominated by atomic power-stations with a relatively low CO_2e emission per kW h of electricity, compared to the large fraction of coal-, gas- and biomass-fired power-stations in Germany, which have a much higher CO_2e emission per kW h [387]. The total CO_2e emission from grid computing amounts to roughly 39 t.

The greenhouse gas emissions from grid computing are compared to the emissions from the other computing sources in Table A.2. Compare to the grid computing, the CO_2e emissions of the batch system as well as the personal and network computing are negligible with 0.31 t, 0.12 t and 0.07 t, respectively. The batch system single-core CPU usage time is obtained from `HTCondor` using the `condor_userprio -allusers` command. The CO_2e emissions from the personal and network computers are estimated by assuming that two CPU cores are used for nine hours per day over a timespan of 4 years and 2.5 years, respectively, with 210 working days per year. This roughly corresponds to the usage time of these resources during the PhD time of the author.

The comparably large CO_2e emissions of the grid computing are due to the long single-core computing time, which sums to roughly 1200 y. This long computing time is due to a memory leak in the used software, a robust retry management of `PanDA` if an executed computing job failed, and inexperienced usage of the grid resources.

	CPU usage [y]	CO_2e emission [t]
CERN (France)	130.59	0.71
Canada	73.97	1.34
France	248.38	1.35
Germany	118.86	6.29
Italy	28.65	1.36
Netherlands	13.45	0.85
Norway	99.47	0.16
Russia	13.37	0.61
Spain	26.98	0.83
Taiwan	12.34	0.88
United Kingdom	103.26	3.66
United States	329.90	20.91
Total	1199.22	38.95

Table A.1: Single-core CPU usage time in years and CO_2e emission due to grid computing from the author during his PhD work. The emissions are divided into the different countries and CERN. The electricity used by CERN is assumed to mainly origin from France.

Item	CPU usage [y]	CO_2e emission [t]
Grid computing	1199.22	38.95
Batch system	4.46	0.31
Personal computer	0.86	0.12
Network computers	0.54	0.07
Total	1204.98	39.45

Table A.2: Single-core CPU usage time in years and CO_2e emission due to computing resources directly used by the author during his PhD work.

Source	CO_2e emission [t]
Computing - Grid	38.95
Computing - Batch	0.31
Computing - Local	0.19
Travelling - Train	1.05
Travelling - Plane	0.75
Total	41.25

Table A.3: CO_2e emissions due to computing and travelling during the PhD thesis time of the author.

The single-core computing time of the author on the grid computers has been compared to other users. It must be regarded as an extreme case, caused by the memory leak. The single-core CPU computing time of other users executing comparable tasks in a comparable timespan was found to be in the range of 80 y–230 y, corresponding to CO_2e emissions of roughly 3 t–8 t, assuming the same distribution of the computing time across the countries. In any case, assuming a PhD time period of three years, the greenhouse gas emissions are comparable to or exceed the 1.1 t of CO_2e emission per person to remain within the 1.5 °C increase of the global temperature until 2050 [378, 380]. More elaborate code testing before accepting tasks on the grid computing system and a more strict job retrial policy may help to avoid grid computing CO_2e emissions as high as caused by the author. In general though, the CO_2e emissions of computing must be reduced by using less CO_2e emitting energy sources to power the computers and by making the computations more efficient.

The greenhouse gas emissions due to the PhD-related long-distance travelling of the author are also calculated and compared to the emissions from computing. Because of the restrictions during the Corona pandemic, the travelling possibilities of the author were limited compared to students without any travelling restrictions within their PhD time. The travelling CO_2e emissions of other PhD students not affected by the pandemic may therefore be higher, though the exact emissions depend a lot on the geographic location of the student, their interest in travelling and the travel budget.

For the author, the distances travelled by train and by plane were estimated using Reference [388] and converted into CO_2e emissions using the numbers published in Reference [389]. The resulting CO_2e emissions are compared to those from computing in Table A.3. The CO_2e emissions due to train and plane travelling sum to 1.05 t and 0.75 t, respectively. Whilst the ratio of these two numbers is roughly 1.4, the number of kilometres travelled by train (20 870 km) is roughly the 4.7-fold of the distance travelled by plane (4400 km). The total travelling CO_2e emissions sum to 1.8 t. This is negligible compared to the CO_2e emissions due to computing, which sum to 39.45 t.

Split across the PhD time of the author of four years, the CO_2e emissions due to travelling do not exceed the 1.1 t of CO_2e emission per person per year. These numbers are however impacted by the pandemic travelling restrictions, which came into action 1.5 y after the author started his PhD. Students not limited by the pandemic may have produced the double amount of CO_2e emissions due to travelling within their three year PhD period. This would yield a total of 3.6 t CO_2e emission or 1.2 t per PhD year, exceeding the 1.1 t CO_2e emission per person per year. In any case, travelling is not the only source of greenhouse gas emission and emissions due to travelling should be kept as low as possible. For every travel, the purpose, distance and means must be considered and traded off against the alternative of a

virtual meeting.

In conclusion, the author emitted a total of roughly 41 t of CO_2e during his PhD thesis work. While this is a rather extreme case, CO_2e emissions must be reduced in computing and travelling to reach the goal of a global warming limited by 1.5 °C. The fraction of renewable energy sources must be increased and the necessity for in-person meetings must be traded off against virtual meetings. To increase the fraction of renewable energy sources, computing sites may want to consider installing solar panels or wind turbines in the vicinity. In spite of the emissions reductions necessary in computing and travelling, it is worth noting that more than 70 % of CERN's CO_2e emissions stem from gas detectors and detector cooling of the LHC experiments [390]. Such emissions have not been accounted for here. It is therefore indispensable to undertake massive immediate action in all parts of particle physics to reduce the greenhouse gas emissions such that the global temperature is not increased by more than 1.5 °C.

Acknowledgements

Doing a PhD would have not been possible for me without the help and support of several people.

Firstly, I would like to thank my supervisor, Dr. Priscilla Pani for her excellent support in the past four+ years! Without her expertise, clear mind and patience I would have not managed to perform my research and to write my thesis! I would also like to thank Dr. Claudia Seitz for supervising me while Priscilla was away, for her advice and support at all times and for reading a part of my thesis!

Thank you to Dr. Ingo Bloch for all of his help while qualifying as an ATLAS author on the ATLAS ITk Upgrade project and on any of the instrumentation projects I was involved in during my time as a PhD student.

I owe a dept or gratitude to Dr. Thorsten Kuhl for all of his comments on my work and for considerably improving the quality of this thesis by his critical comments!

Thank you to Prof. Dr. Johannes Albrecht and Prof. Dr. Thomas Lohse for being my thesis referees and thank you Prof. Dr. Christophe Grojean and Prof. Dr. Achim Peters for being part of my thesis committee!

I would like to thank Dr. Klaus Mönig, Prof. Dr. Ingrid Gregor and Prof. Dr. Cigdem Issever for keeping my back free from the administrative side and for all the support and advice concerning on-going and future projects.

Large parts of this thesis would have not been possible without my wonderful colleagues Dr. Alvaro Lopez-Solis and Paul Moder. Thank you for the great time we had while working on the tW+DM search, for always being available and for us being such a good team. I will truly miss working together with you! Thank you also for the critical comments on large parts of this thesis and all the mental support that I needed from time to time!

I would like to thank Dr. Sarah Williams for her stamina, motivation and large effort to perform a measurement of the W^+W^- cross-section in a SUSY search inspired phase space. I really enjoyed being part of the project and working together with you! Thank you also for proof-reading my thesis and all the discussion on how to improve it! Regarding cross-section measurements I also need to thank Dr. Yichen Li who introduced me to the challenges of unfolding and made all of this very interesting to me.

Big thanks go to all of those without the mentioned upper projects would have not been possible. Thank you to Paolo, Josep and Joseph for all of your hard work and your comments on the tW+DM project. Thank you to Matt, Giulia and Flavia for all the effort in the first tW+DM search! Thank you to Sebastian, Sonia and Francesco for all your work and excellent collaboration on the W^+W^- cross-section measurement!

Further, I would like to thank Ruchi, Edo, Carl, Martin R., Martin S. and all the technicians involved for their great work, collaboration and support on my efforts in the ATLAS ITk Upgrade project!

Thank you very much Alvaro, Paul, Marianna, Martin H., Filip, Eleonora, Marawan, Supriya, Akanksha, Christian, Bora, Timothee, Rickard, Judith and

Baishali for making the everyday life at DESY so much fun! Thank you for all the great discussions we had, all the input and mental support. Without people like you I would have not managed the PhD. Thank you also to the KiSelector team for all the effort and Judith for organising the coding seminar! An extra thank you goes to Martin, Marianna and Filip for the critical review of large parts of my thesis!

Thank you also to Dr. Philipp Gadow for reading large parts of my thesis!

Nils and Trine, thank you for organising the PhD seminar (Nils) with me and thank you for setting up the FH Sustainability Forum (both)! I think that they are truly necessary projects and I am curious to see how they will evolve.

A big thank you goes to my family and friends for their support and good words throughout all the years of studying, for their understanding when I was working long hours again, for hanging out, for the trips and holidays and for making all of this time so enjoyable!

Finally, I would like to thank Susi for her love, her endless patience and for the awesome bike tours!

Last but not least I would like to thank anyone I might have forgotten and hope that you feel recognised for your contribution to my PhD by these words. :)